Femtosecond time-resolved spectroscopy in polyatomic systems investigated by velocity-map imaging and high-order harmonic generation

David Staedter

To cite this version:

David Staedter. Femtosecond time-resolved spectroscopy in polyatomic systems investigated by velocity-map imaging and high-order harmonic generation. Atomic and Molecular Clusters [physics.atm-clus]. Université Paul Sabatier - Toulouse III, 2013. English. NNT : . tel-00922203

HAL Id: tel-00922203
https://theses.hal.science/tel-00922203v1

Submitted on 24 Dec 2013

Université
de Toulouse

THÈSE

En vue de l'obtention du

DOCTORAT DE L'UNIVERSITÉ DE TOULOUSE

Délivré par l'Université Toulouse III – Paul Sabatier
Discipline ou spécialité: Physique

Femtosecond time-resolved spectroscopy in polyatomic systems investigated by velocity-map imaging and high-order harmonic generation

---

Présenté et soutenue par
David STÄDTER

20. September 2013

JURY

M^{me}	Valérie BLANCHET	Chargée de recherche, CNRS LCAR, Toulouse	Directrice de Thèse
M.	Timo FLEIG	Professeur, LCPQ, Université Paul Sabatier Toulouse	Président de Jury
M.	Laurent NAHON	Chercheur, Synchrotron SOLEIL	Examinateur
M.	Andrew ORR-EWING	Professeur, School of Chemistry University of Bristol	Rapporteur
M.	Lionel POISSON	Chargé de recherche, CNRS IRAMIS, Paris	Rapporteur

École doctorale: Sciences de la Matière (SDM)
Unité de recherche: Laboratoire Collisions Agrégats Réactivité (LCAR IRSAMC UMR5589)
Directrice de Thèse: Valérie BLANCHET

Ph.D. Thesis

Femtosecond time-resolved spectroscopy in polyatomic systems investigated by velocity-map imaging and high-order harmonic generation

presented by:
David STÄDTER

A thesis submitted to the
Graduate School (Sciences de la Matière (SDM)) of the
Université Toulouse III – Paul Sabatier
in partial fulfillment of the requirements for the degree of
Doctor of Philosophy (Ph.D.) of the Univeristé de Toulouse

Toulouse, 20. September 2013

JURY

M^{me}	Valérie BLANCHET	Chargée de recherche, CNRS LCAR, Toulouse	Supervisor
M.	Timo FLEIG	Professor, LCPQ, Université Paul Sabatier Toulouse	President of the Jury
M.	Laurent NAHON	Chercheur CEA, Synchrotron SOLEIL	Examiner
M.	Andrew ORR-EWING	Professor, School of Chemistry University of Bristol	Reviewer
M.	Lionel POISSON	Chargé de recherche, CNRS IRAMIS, Paris	Reviewer

Graduate School: Sciences de la Matière (SDM)
Research laboratory: Laboratoire Collisions Agrégats Réactivité (LCAR IRSAMC UMR5589)
Supervisor: Valérie BLANCHET

Femtosecond time-resolved spectroscopy in polyatomic systems investigated by velocity-map imaging and high-order harmonic generation

Ph.D. thesis, 20. September 2013
Supervisor: Valérie BLANCHET
Reviewers: Andrew ORR-EWING and Lionel POISSON
Examiners: Timo FLEIG and Laurent NAHON

Université Toulouse III – Paul Sabatier
Sciences de la Matière (SDM)
Laboratoire Collisions Agrégats Réactivité (LCAR IRSAMC UMR5589)
118 Rue de Narbonne – 31062 Toulouse – France

UNIVERSITÉ
TOULOUSE III
PAUL SABATIER

Université
de Toulouse

MARIE CURIE ACTIONS

SEVENTH FRAMEWORK PROGRAMME

ICONIC

Imaging and **CON**trol **I**n **C**hemistry

Marie Curie Initial Training Network (ITN)
under the Seventh Framework Program of the European Union

IRSAMC
LCAR - LCPQ - LPCNO - LPT

CELIA

UNIVERSITÉ TOULOUSE III PAUL SABATIER

Université de Toulouse

UNIVERSITÉ DE BORDEAUX

UNIVERSITÉ BORDEAUX 1
Sciences Technologies

To my mother

Darkness cannot drive out darkness;
only light can do that.

– Martin Luther King, Jr.

Acknowledgments

My Ph.D. has been an incredible and wonderful, if often overwhelming, experience – a true marathon event from an academic, professional and personal perspective. It is not easy to pinpoint whether this has been due to engaging with the topic itself, dividing time between two universities and groups, working in a foreign country, staying in the lab until dawn, overcoming experimental setbacks or just staying on track..., to only mention a few. Regardless of the reasons, it is always the people around you who make the difference. One of the joys of completion, whatever the challenge – in this case my Ph.D. – is reflecting back on the journey, and remembering all the colleagues, friends and family who have helped and supported me along this long but fulfilling road. Without them I would not have been able to complete it and I am grateful to them for making the past three years exceptional and unforgettable.

First and foremost, this Ph.D. thesis would not have been possible without the continuous encouragement of my principal supervisor, Dr. Valérie Blanchet – not to mention her advice, patience, motivation, enthusiasm and unsurpassed knowledge. For all of this I would like to express my sincere gratitude. From the beginning, she apparently effortlessly managed to divide her time between two different labs in two different cities, closely supervising two Ph.D. students in Toulouse and helping out a third one in Bordeaux. Through all of this, without any complaint, she stayed late in the lab, always had time to talk, to share a joke, or help me with the French administration. I have appreciated her steady influence throughout my Ph.D. career, giving me orientation and support with promptness, forbearance and care, particularly during some of the more difficult periods of my time in her lab. Especially towards the end, during the writing of this manuscript, when she had already left the lab in Toulouse to move permanently to Bordeaux, she managed to come and see me regularly in Toulouse, as well as hosting me for my visits to Bordeaux. A particular thank-you goes to both her and her husband, Prof. David Dean, for their continued hospitality. I reflect fondly on the times we spent at their place in Bordeaux, discussing science and life, while drinking beer and making BBQ. I could not have imagined having a better advisor and mentor for my Ph.D. research.

I would like to thank all the members of my dissertation committee: Prof. Andrew Orr-Ewing, Dr. Lionel Poisson, Dr. Laurent Nahon, and Prof. Timo Fleig. I am especially grateful to Prof. Andrew Orr-Ewing and Dr. Lionel Poisson for agreeing to be the reviewers of my thesis, and for reading through my manuscript before, after and even during their summer holidays; to

Dr. Laurent Nahon for being an examiner and guest on my defense panel; and to Prof. Timo Fleig for kindly acting as the president of the jury, even though particularly as a theoretician it is no easy task to read an experimental thesis. I very much appreciate all the thoughtful and detailed comments, as well as the encouraging and constructive feedback, which the jury members have provided me with.

I want to thank as well the organizers of the ICONIC network for a wonderful experience. As a Ph.D. fellow within this network I was privileged to have the opportunity to learn first-hand about imaging techniques. In addition, the various training schools and network meetings all over Europe broadened my knowledge of the field and made networking easy. I recognize that the research carried out for this thesis would not have been possible without the financial assistance of grants from the Marie Curie ICONIC initial training network (ITN-ICONICPITN-GA-2009-238671) and from the ANR HARMODYN.

A particularly big thank-you goes to Dr. Yann Mairesse, who was not officially my co-supervisor in Bordeaux, but who definitely took me under his wing while I was there, and always made me feel at home even though I was only a guest there. I am indebted to him for his valuable advice in scientific discussions. Furthermore, Yann made a significant contribution to the experimental knowhow that I acquired over the course of my Ph.D. studies. I will always be very envious of his magic touch, with which he could make an experiment work in minutes, where I spent hours trying.

Special thanks go to Nico, who when I started my Ph.D. was in his last year of his own Ph.D. with Valerie. I owe him big time, not only because I learned from him what VMI is, how things work in the lab, and how to handle my boss, but also because he and his partner Amélie really helped me feel home away from home, especially outside of the lab. I have great memories of the *soirées* at his place with raclette, wine and other typical French food. *Merci beaucoup* for being so kind and patient with me and my poor French.

I am very grateful for the assistance given by the permanent staff of the Laboratoire Collision Agrégats et Réactivité at IRSAMC. I would particularly like to thank Elsa Baynard and Stéphane Faure, for their technical support during the experiments. As a *one woman show* Elsa managed the femtosecond laser system so that it was ready for me to use. I learned a great deal from her about femtosecond laser systems and all their little aches and pains. Without Stéphane I guess I would still be in the lab trying to take data. I am grateful for his help making the connection between computer and experiment run flawlessly, and for teaching me about efficient data acquisition. I appreciate his expertise and kindness, and thank him for always finding time for me in his busy schedule. Special thanks go to the secretary staff: Marie-France Rolland, who retired shortly after my arrival; Sylvie Boukhari; and Christine Soucasse, for taking on the burden of administrative work, and for being always kind and patient with me and my elementary French. I also received generous support from Laurent Polizzi, Gerard Trenec, William Volondat, Michel Gianesin and Daniel Castex, the engineering and technical staff, whom I thank for their expertise and professionalism. I apologize for all my last minute requests when something broke or had to be replaced in the lab - it always happens just before the end of the day. They did a wonderful job in designing, constructing and adapting the experimental setup which underwent a huge change and modernization during my Ph.D. time, which would have not been possible without their unwavering dedication. I would also like to thank Roland Lagarrigue and Emmanuelle Kierbel, our IT staff, for their technical computer support. Furthermore, I would like to express my gratitude to Dr. Beatrice Chatel, Prof. Jacques Vigué, Dr. Jean-Marc L'Hermite, Prof. Chirstoph Meier, Dr. Benoit Chalopin, Dr. Alexandre Gauguet, Dr. Sébastien Zamith, Dr. Julien Boulon, Dr. Jean-Philippe Champeaux, Dr. Peter Klüpfel and all other members of the LCAR for being friendly to me at all times. I also want to thank all of my fellow Ph.D. students at LCAR, both former and current, especially Arun, Jonathan, Gabriel, Charlotte, Marina and my office colleague Mina. A special thank-you goes to Ayhan my next-door office and lab colleague, who started his Ph.D. with Beatrice just one year before me. I owe my deepest gratitude to him for being not only a fellow Ph.D. student, but a perfect friend. He and his wife Neda were always kind to me, at times even feeding me, when I stayed another late night in the lab. I will always remember the wonderful and great evenings we spent together, talking about all aspects of life while having BBQ or typical iranian food.

Then there is the group in Bordeaux, my second home. Here besides Yann, whom I have already mentioned, I want to thank Prof. Eric Mevel and Prof. Eric Constant the group leaders of the Harmodyn group at the Centre Laser Intense et Application (CELIA) at the Université Bordeaux 1, and Dr. Baptiste Fabre for their kindness, help and support. I also want to thank Celine Oum, the secretary at CELIA, for her generous support and help with the administration while I was in Bordeaux. I would also like to thank the other members at CELIA, especially Dr. Dominique Descamps, for managing the laser system, and also being present in the lab, giving advise at anytime; Dr. Patrick Martin, for giving me a space in his office and Dr. Fabrice Catoire. Special thanks goes to Amélie, Charles and Hartmut, fellow Ph.D. students, with whom I worked closely. Charles and I worked on building the fs-VUV experiment, combining HHG and VMI and I do not know how many days and nights we spent together in the lab trying to get the experiment to work, but it was always fun working together. Hartmut, who I already knew from my undergraduate studies in Konstanz, is actually the reason I did my Ph.D. in France, and I am very grateful for his friendship. Having been doing his Ph.D. already for one year in Bordeaux in the Harmodyn group, he told me, in his words: “There is an open position in Toulouse, the guys are cool, so look at it” (Of course, he said this in German), and thats how I got there. A particular thank-you goes to him and his partner Félicité for being good friends, and for their hospitality, since they often gave me a place to stay while I was doing experiments in Bordeaux. I also want to thank Hartmut's flatmates who always welcomed me in their home. A final (Bordeaux) thank-you goes to the other Ph.D. students at CELIA, including Ondrei Hort, for their humor and for the nice atmosphere in the lab.

In general there are always more people involved besides your group members and I have been very privileged to get to know and to collaborate with many other great people during the course of my Ph.D. I owe a very important debt to Dr. Petros Samartzis. Sama (as he introduces himself), brought the ClN_3 project to Toulouse. During his three-month visit with us in Toulouse he introduced me to the world of real practical chemistry. His immense knowledge, and humor made working in the lab a blast. I was also lucky to meet him again in Heraklion, on the Greek island Crete, while I was visiting his own lab. Thank you for the fun and the encouraging discussions during my visit at the Institute of Electronic Structure and Laser at the Foundation for Research and Technology (Forth) lab. Here, I also want to thank Andreas and Pavle, fellow Ph.D. students in the ICONIC network, who were working with Sama, who not only assisted me in the lab and let me 'play' with their setup, but also made the visit to Crete outside of the lab a fun experience, with weekend trips and amazing Greek food – *ευχαριστὼ*. Many thanks also go to Dr. Catarina Vozzi and Prof. Salvatore Stagira, who I was fortunate to work with during a research visit at the Terawatt Laser Laboratory in Milan at the Dipartimento di Fisica at the Politecnico di Milano. A thank-you also goes to Matteo, who at this time was a Ph.D. student with Catarina – *mille grazie*. I have greatly benefited from working with Andras Bodi and Patrick Hemberger, the beamline scientists at the Swiss Light Source at the Paul Scherrer Institut, where Valerie and I spent one week with them using their iPEPICO setup. Unfortunately we dismantled the whole experiment during this time loosing valuable beamtime, but I learned a huge amount about the inside of this experiment and, nevertheless, we were able to produce some interesting results on TTF. For further collaboration on the TTF study, I want to thank Prof. Paul Mayer from the Chemistry Department at the University of Ottawa. For his collaboration on the azulene project, a thank-you goes also to Prof. Piotr Piecuch from the Department of Chemistry at the Michigan State University, who is one of the few people on this earth who can actually calculate doubly excited states.

I am also greatly indebted to many of my former teachers and I especially want to thank Klaus Stegele, for encouraging me to study Physics, and Prof. Jure Demsar, my Masters' thesis supervisor, who encouraged me to proceed to a Ph.D. even though I turned him down on his Ph.D. position offer.

I have dedicated this thesis to my mom who is a very special and important person in my life. If it wasn't for her strength in letting me go I would not have been able to come as far as I have. Whether it was leaving home to go to study in a different city, my travels to Australia, or now my more recent move to the South of France for this Ph.D., she has always encouraged me to chase my goals, even if this meant being geographically separated. Though, undoubtedly if I had remained in Freiburg all this time we would have driven each other crazy anyway. But I can always count on her wholehearted support and no words can describe my appreciation and love for her.

I have made many friends along the way, and they have helped me, one way or another, in my struggle to complete my Ph.D.. I would like to thank all of them, especially Chris; Dennis; Tom; Wolle; Susan; Yen: Koli; Sebastian and Kathrin; Uli and Regina; and my French flatmates, Fanny and Julien, for their help, support and understanding. Last but not least, I want to thank Sara who since she stepped into my life two plus years ago, completely changed it. Her intelligence, sometimes hurting honesty but constructive feedback, funny humor, strange taste, liveliness and beauty have enriched my life in countless ways. Without her encouragement, support and editing assistance, I would not have been able to finished this journey.

Abstract

Femtosecond time-resolved spectroscopy in polyatomic systems investigated by velocity-map imaging and high-order harmonic generation

presented by
David STÄDTER

Revealing the underlying ultrafast dynamics in molecular reaction spectroscopy demands state-of-the-art imaging techniques to follow a molecular process step by step.

Femtosecond time-resolved velocity-map imaging is used to study the photodissociation dynamics of chlorine azide (ClN_3). Here especially the co-fragments chlorine and N_3 are studied on the femtosecond timescale in two excitation energy regions around 4.67 eV and 6.12 eV, leading to the formation of a linear N_3 fragment and a cyclic N_3 fragment, respectively. This work is the first femtosecond spectroscopy study revealing the formation of cyclic N_3. Tetrathiafulvalene (TTF, $C_6H_4S_4$) electronic relaxation is studied, while scanning the electronic excitation around 4 eV, by time resolved mass and photoelectron spectroscopy. As only few is known about the ion continuum about TTF the imaging photoelectron photoion coincidence (iPEPICO) technique is used in order to disentangle the complex ionic dissociation.

The second part of the thesis is based on the generation and application of XUV light pulses by high-order harmonic generation with an intense femtosecond laser pulse in a molecular target. Two types of phase sensitive attosecond spectroscopy experiments were conducted to study the vibrational dynamics of SF_6: one using strong field transient grating spectroscopy, where high-order harmonic generation takes place in a grating of excitation, and the second experiment using high-order harmonic interferometry using two intense XUV probe pulses. The temporal dependencies in phase and amplitude reveal the vibrational dynamics in SF_6 and demonstrate that high-order harmonic generation is sensitive to the internal excitations. Last but not least, the use of high-order harmonics as a XUV photon source for the velocity-map imaging spectrometer is investigated. Using time-resolved photoelectron imaging, the relaxation dynamics initiated with 15.5 eV in argon and 9.3 eV in acetylene are revealed.

Contents

List of Figures

List of Tables

List of Abbreviations

as	attosecond, 10^{-18} seconds
ATAS	absorption transient attosecond spectroscopy
ATI	above threshold ionization
BBO	Beta-Barium Borate, β-BaB_2O_4
BSI	barrier-suppressed ionization
CCD	charged coupled devide
CEP	carrier envelope phase
CI	conical intersection
CMB	crossed molecular beams
CPL	chirped pulse amplification
CRATI	channel resolved above threshold ionization
cw	continuous wave
ENLOS	extreme nonlinear optical spectroscopy
EUV	extreme ultra-violet
FEL	free-electron laser
fs	femtosecond, (10^{-15}sec)
FTL	Fourier-transform limited
FWHM	full width at half maximum
GDD	group delay dispersion
HEF	high energy form
HHG	high-order harmonic generation
HOMO	highest occupied molecular orbital
HX	harmonix X, i.e. H5 = harmonic 5
I_p	ionization potential (IP) or ionization energy (IE)
iPEPICO	imaging photo- electron photoion coincidence spectroscopy
IR	infrared
KER	kinetic energy release
KLM	Kerr-lens mode locking
LUMO	lowest unoccupied molecular orbital
MB	molecular beam
MCP	micro channel plate
MI	multiphoton ionization
MSX	intersystem crossing
NOPA	nonlinear optical parametric amplification
ns	nanosecond, 10^{-12} seconds
ps	picosecond, 10^{-12} sec.
REMPI	resonance enhanced multiphoton ionization
SAE	single active electron approximation
SB	side band
SFA	strong field approximation
TDSE	time-dependent Schrödinger equation
TER	translational energy release
TI	tunnel ionization
Ti:Sa	Titanium-Sapphire
TKER	total kinetic energy release
TOF	time-of-flight
TOF-MS	Wiley-McLaren time-of-flight mass spectrometer
TS	transition state
VMI	velocity-map imaging
VUV	vacuum ultra-violet
XUV	= EUV

Introduction

The gaps between the fields of physics, chemistry, and biology are bridged by the motion of molecules in complex structures, atoms in molecules, and electrons within atoms and molecules [1]. Diverse tools appeared in the last decades which have enabled the direct probing of time-averaged, static structure of matter, such as electron and neutron diffraction, X-ray absorption and diffraction, NMR spectroscopy and electron microscopy [2]. Using these techniques it is possible to determine three-dimensional structures with atomic scale resolution. However, to form a complete understanding of chemical reactions, phase transitions, or biological functions, the actual events have to be resolved in real-time. These changes follow different timescales and proceed through different transition states and intermediates. These dynamics and structural changes are naturally linked through the laws of quantum mechanics [1]. For example, the solution of the Schrödinger equation for a particle's wave function yields an oscillatory motion with the oscillation period $T_{osc} = 2\pi(\hbar/\Delta E)$ where ΔE is the energy difference between two eigenstates. The larger the energy separation between the two eigenstates, the faster is the particle's motion in the superposition state. The energy spacing and the change from one state to another is closely connected with the absorption and emission of photons. The energy spacing of vibrational energy levels is on the order of tenth to several hundred milli-electron volts for instance, which implies that molecular vibrations occur on a timescale of tens to hundreds of femtoseconds (fs = 10^{-15} sec, 0.000 000 000 000 001 seconds or one quadrillionth, or one millionth of one billionth, of a second). This defines the characteristic timescale for the motion of atoms in a molecule, including those resulting in irreversible structural changes during chemical reactions like isomerization.

The invention of short pulsed laser systems provided the possibility of detecting these processes in real time. Spectroscopy, mass spectrometry, and diffraction techniques play the modern day role of 'ultrahigh-speed photography' in the investigation of molecular processes to capture the involved steps. One of the earliest examples of high-speed photography experiments was the 'horse in motion' in 1878 by Eadweard Muybridge. Using a row of cameras with tripwires, he was bale to capture the motion of a galloping horse. In a sense this is considered the birth of photographic studies of motion and motion-picture projection. Since nuclear motion within molecules occurs on a femtosecond timescale, femtosecond lasers have the appropriate 'shutter speed' to capture the evolution of important nuclear rearrangements such as

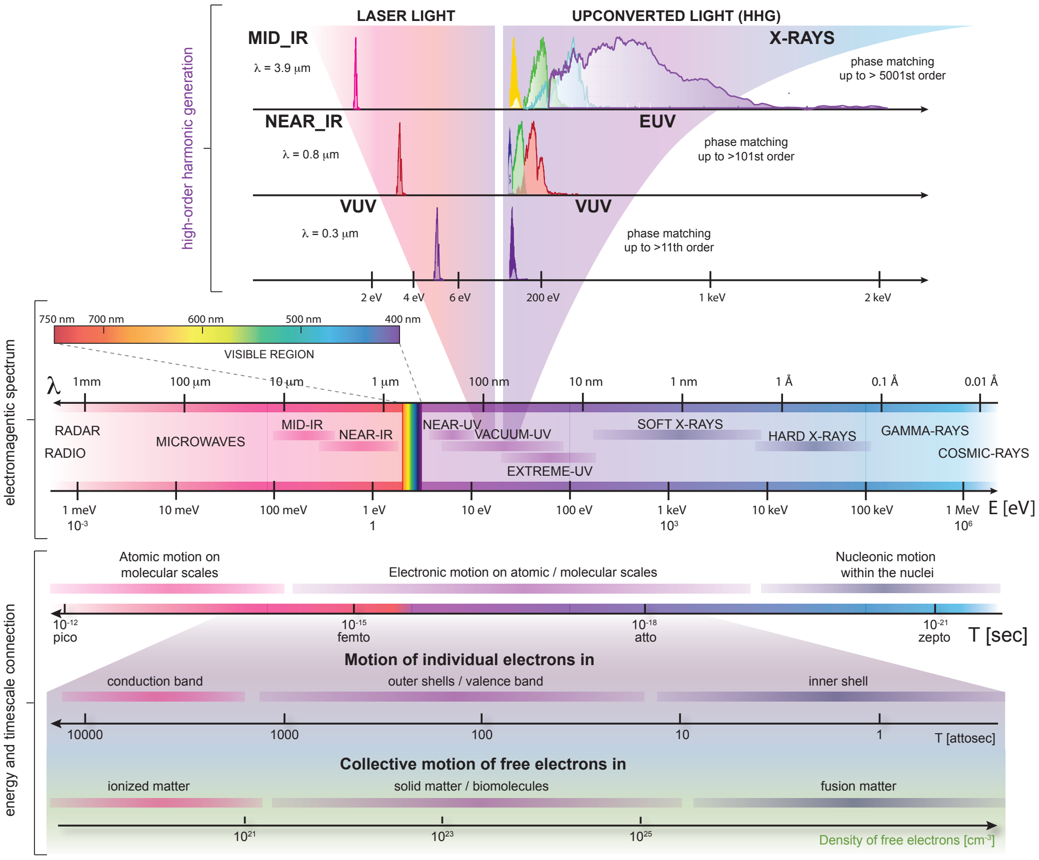

Figure 1: Illustration of the electromagnetic spectrum, the connection between energy and timescales for molecular dynamics. Adapted from [1]. The top shows the spectrum reachable by high-order harmonic generation depending on the driving laser frequency. Adapted from [3].

izomerisation and dissociation (see Chapter 2). Femtosecond spectroscopy is like following a ‘movie’ that will show the elementary steps leading to the products of a chemical reaction. Time-resolved experiments with femtosecond resolution deal in general with unimolecular processes induced by a pump pulse in a parent molecule. The details of relaxation processes, such as decay time, energy balance or branching ratios can be revealed by time-resolved spectroscopy, which is the field of femtochemistry.

Figure 1 shows the electromagnetic spectrum and summarizes the characteristic timescales of microscopic motion and their connection with energy spacing between the relevant stationary states. According to Ahmed Zewail, who is regarded as the founder of femtochemistry, the field of femtochemistry tries to answer for example the following questions: How does the energy put into a reactant molecule redistribute among the different degrees of freedom, and how fast does this happen? What are the speeds of the chemical changes connecting individual quantum states in the reactants and products? What are the detailed nuclear motions that chart the reaction through its transition states, and how rapid are these motions? [4]. However, life is never that easy. Actually, to understand the elementary steps one has to compare the observables of the experiment with theoretical models produced by ab-initio calculations to eventually reconstruct the transition state dynamics from the results of investigations of the kinetics of the reactants and products. Furthermore, the molecules have to be ideally in a free environment, for instance produced in gas phase. Now the main puzzling question is how to detect such drastic nuclear changes and what will be the observables in gas phase. On even shorter timescales than the motion of atoms and molecules is the motion of electrons. The characteristic timescales for the motion of one or several electrons and for the collective motion of an electronic ensemble are shown in Figure 1. Atomic distances are on the order of a few Angtröm and therefore one obtains oscillation periods of valence electron wave packets in bound atomic or molecular systems on the order of a few to hundreds of attoseconds (as = 10^{-18} sec.) [1]. As femtochemisty is the science of the motion of atoms and molecules, attosecond physics is the science of the motion of electrons. To produce light pulses in the attosecond regime one has to go to photon energies with 100 eV up to keV, meaning to the ultraviolet and vacuum ultraviolet region in the electromagnetic spectrum. This is where high-order harmonic generation comes into the picture as a tool to upconvert the near-IR femtosecond laser light into the VUV or even up to the soft X-ray region.

In this manuscript, two pump-probe techniques with two different observables are developed; one based on the traditional femtochemistry and one based on high-order harmonic generation. Generally, pump-probe experiments using two femtosecond laser pulses, the relative delay between them will be the main controllable of the experiment. The pump pulse switches on dynamics by fulfilling a resonance. This first laser light-molecule interaction determines time 'zero' with the precision of the pump pulse duration by generating a wave packet that will start to oscillate and/or relax over time. The resonances presented in this manuscript are mostly electronic resonances (excitation in the UV range, see Chapter 2, Chapter 3 and Chapter 5) and vibrational resonances (Raman excitation in the IR, see Chapter 4). The probe pulse is the second light-molecule interaction that will produce the observable. The most important issue in such pump-probe experiments is to detect the wave packet created by the pump whatever the potential surfaces on which it evolves. One of most widely used probe steps in gas-phase studies is ionization, since ions can be readily detected. Two kinds of ionization are used in this manuscript. The first type is the traditional ionization with observables such as the angular and energy distributions of the products of ionization (electrons, parent ions, ionized fragments). The energy and angular distributions of photoelectrons and photofragments are recorded through an imaging technique collecting charged particals, in particular velocity-map imaging (VMI). Ionization potentials (I_p) for the parent molecules are in general larger than 7 eV and even higher for the fragments. These high energies have been reached up to now by multiphoton ionization (see Chapter 2) with the unavoidable complication related to resonances and weak efficiencies. This has motivated the development of a universal ionization technique, namely a fs-VUV pulse which will be addressed in Chapter 5. The second type of ionization uses tunnel ionization with its main observable being the XUV emission produced by the recombination of the electron emitted by the cationic core. This process is called high-order harmonic generation which can be described in three steps (the three step model): tunnel ionization, acceleration of the the electron in the continuum dressed by the intense laser field and then recombination with XUV emission. This new pump-probe femtochemistry is based on XUV photon detection and is attractive due to its phase sensitivity compared to VMI detection. A key ingredient in this all-optical technique has been the tunnel ionization by a strong laser field with the prevailing approximation that only one electron – the less bound one to the cation (HOMO = highest occupied molecular orbital) – is emitted by tunnel ionization. Furthermore, any dynamics in the cation or effects by the strong laser field on the cationic core during the high-order harmonic generation process are generally disregarded, and will be addressed in Chapter 4.

The manuscript is organized as follows.
Chapter 1 introduces the two main experimental techniques which have been employed to investigate the molecular dynamics that will be discussed in this thesis, namely femtosecond velocity-map imaging and high-order harmonic generation.

A study of femtosecond time-resolved photodissociation of ClN_3 after electronic excitation in two different energy regions will be presented in Chapter 2. The main observables are the co-fragments N_3 and Cl. The goal of the experiment is to elucidate the ultrafast dynamics that lead to a cyclic-N_3 production. Indeed at 4.5 eV, only linear N_3 is expected to be produced whereas around 6.17 eV (201 nm) mainly cyclic-N_3 is produced. Using the technique of velocity-map imaging not only allows the identification of the co-fragments by their energy balance but also gives access to their angular distribution and the femtosecond time resolution reveals the timescale of the dissociation. Using a multiphoton ionization process to detect the fragments, we are able for the first time to directly image the N_3 fragments with femtosecond time-resolution and give further insight into the production of linear and cyclic N_3.

Tetrathiafulvalene (TTF, $C_6H_4S_4$) electronic relaxation is studied in Chapter 3, while scanning the electronic excitation around 4 eV, by time resolved mass and photoelectron spectroscopy. To enhance the sensitivity, the photoionization is achieved at different probe wavelengths (266 nm, 400 nm and 800 nm). The pump wavelength has been varied from 322 nm to 307 nm to reveal a possible change of the electronic character via a change of in the decay measured time. With an intense 800 nm pulse the ATI photoionization of TTF is studied. Within this internal energy a variety of dissociation channels are accessible in the ion continuum. In order to disentangle the complex ionic dissociation, the imaging photoelectron photoion coincidence (iPEPICO) technique is used. Above the dissociation threshold, iPEPICO results show that the molecular ion (m/z = 204) dissociates into seven product ions, six of which compete in a 1.0 eV internal energy window.

In Chapter 4, the diffracted XUV spectrum generated by high-order harmonic generation in vibrationally excited SF_6 is studied in two phase sensitive high-order harmonic spectroscopy (HHS) setups. The XUV emission from SF_6 is suspected to take place not mainly from the HOMO as observed in all rare gas atoms, and N_2, CO_2, NO_2 and N_2O_4, but from the HOMO-2 and HOMO-3. By changing the geometry in the ground state of SF_6 through a vibrational excited state prepared by a Raman transition, we aim to shed light into the process of high-order harmonic generation in SF_6. Two sophisticated experimental set-ups, both based on an heterodyne detection are implemented to not only measure the amplitude but also the phase of the high-order harmonic emission. One setup uses two pump pulses to create a grating of vibrational excitation in the gas jet through which the probe pulse generates high-order harmonics. The diffracted XUV light is the main observable with its efficiency depending on the geometry of SF_6. The second experiment uses two spatially separated probe pulses, both generating a XUV beam which interfere spatially in far field. The interferences in amplitude and phase carry information about the vibrational excitations induced by the a pump pulse overlapped with only one of the two probes.

Chapter 5 makes a link between Chapter 2 / Chapter 3 and Chapter 4, since here the high-order harmonic emission is used as a secondary source lying in the XUV range to realize a universal detection scheme. For this a new XUV spectrometer was built and coupled to a velocity-map imaging spectrometer. After a description and characterization of the new setup the first time-resolved ionization made on Argon and C_2H_2 are presented. Here the observables are sideband photoelectrons that are produced by two quantum paths involving different resonances.

The thesis concludes with a summary about the presented work and a discussion about future implications and perspectives.

References

[1] Krausz, F. *Attosecond physics*. Rev. Mod. Phys. **81**:1 163–234 (2009) (cited p. 1–3).

[2] Zewail, AH. *The new age of structural dynamics*. Acta Cryst. **66**:2 135–136 (2010) (cited p. 1).

[3] Popmintchev, T, Chen, MC, Popmintchev, D, Arpin, P, Brown, S, Alisauskas, S, Andriukaitis, G, Balciunas, T, Mucke, OD, Pugzlys, A, Baltuska, A, Shim, B, Schrauth, SE, Gaeta, A, Hernandez-Garcia, C, Plaja, L, Becker, A, Jaron-Becker, A, Murnane, MM, and Kapteyn, HC. *Bright Coherent Ultrahigh Harmonics in the keV X-ray Regime from Mid-Infrared Femtosecond Lasers*. Science **336**:6086 1287–1291 (2012) (cited p. 2).

[4] Zewail, AH. *Femtochemistry: Atomic-scale dynamics of the chemical bond*. J. Phys. Chem. A **104**:24 5660–5694 (2000) (cited p. 2).

1

From femtosecond to attosecond imaging

Contents

Abstract

The chapter gives an introduction to the two main experimental setups used in this thesis to investigate molecular dynamics, namely femtosecond velocity-map imaging and high-order harmonic generation. After introducing the general concept of imaging in molecular dynamics and the pump-probe technique in Section 1.1, Section 1.2 illustrates the fundamental concepts of velocity-map imaging. In Section 1.3 the concept of high-order harmonic generation is described.

Keywords: molecular dynamics, femtosecond, attosecond, photoinduced dynamics, pump-probe technique, velocity-map imaging, Newton spheres, Abel transformation, kinetic energy release, angular distribution, high-order harmonic generation, three-step model, phase matching, extreme nonlinear optical spectroscopy, fs-XUV spectroscopy

1.1 Introduction

1.1.1 Imaging in molecular dynamics

The technique of ion and electron imaging has become a versatile tool in the study of molecular dynamic processes [1] where most of these processes are simple two-body events that end with the particles departing from each other with a fixed amount of kinetic and internal energy and a fixed direction. The product angular (direction) and velocity (energy) distributions provide insight into some of the most basic chemical phenomena: the breaking and forming of chemical bonds and is essential for a fundamental understanding of chemical reactivity. One can distinguish two experimental directions in imaging molecular dynamics, crossed molecular beam (CMB) and photoinduced experiments:

1. **Crossed molecular beam experiments (CMB)** are studying bimolecular reactions [2] or molecular scattering [3] as presented by the following reactions:

    - bimolecular reactions: $\mathrm{A} + \mathrm{BC} \rightarrow \mathrm{ABC}^* \rightarrow \mathrm{AB} + \mathrm{C}$
    - inelastic scattering: $\mathrm{AB}(v,J) + \mathrm{C} \rightarrow \mathrm{ABC}^* \rightarrow \mathrm{AB}(v',J') + \mathrm{C}$

    where ABC^* is a collision complex. CMB experiments, invented by Taylor and Daz 1955 [4, 5], were the first experiments used to measure the product angular and velocity distributions. The basic principle underlying these experiments is very simple. Two molecular beams containing the reactants are crossed, usually at right angles, reaction occurs at the point of intersection, and products scattered at a particular angle are detected by a mass spectrometer equipped with an electron-impact ion source. The flight time from the crossing region to the detector yields the product velocity, and by stepping the detector through the possible scattering angles, the entire product velocity-angle distribution may be obtained. The success of the research area of CMB reactions led to the 1986 Nobel Prize in Chemistry to three of the leaders in this field, Dudley R Herschbach [6], Yuan T Lee [5, 7] and John C Polanyi [8, 9] for their incisive experimental and interpretative work on the dynamics of elementary gas-phase reactions. However in bimolecular reactions, the inherent distribution of the impact parameter leads to a distribution, in the picosecond domain, of the time (t=0) at which the reaction starts. To be able to have access to dynamics on faster timescales this technique is not suitable.

2. **Photoinduced molecular dynamic experiments** are using light for photoionization and photodissociation. After absorption of one or more photons a hypothetical bound molecule AB can undergo the following reactions:

    - photodissociation: $\mathrm{AB} + n\hbar\omega \rightarrow \mathrm{AB}^* \rightarrow \mathrm{A} + \mathrm{B}$
    - photoionization: $\mathrm{AB} + n\hbar\omega \rightarrow \mathrm{AB}^* \rightarrow \mathrm{AB}^+ + \mathrm{e}^-$
    - dissociative ionization: $\mathrm{AB} + n\hbar\omega \rightarrow \mathrm{AB}^* \rightarrow \mathrm{A}^+ + \mathrm{B} + \mathrm{e}^-$

    where AB^* is photo-excited complex.

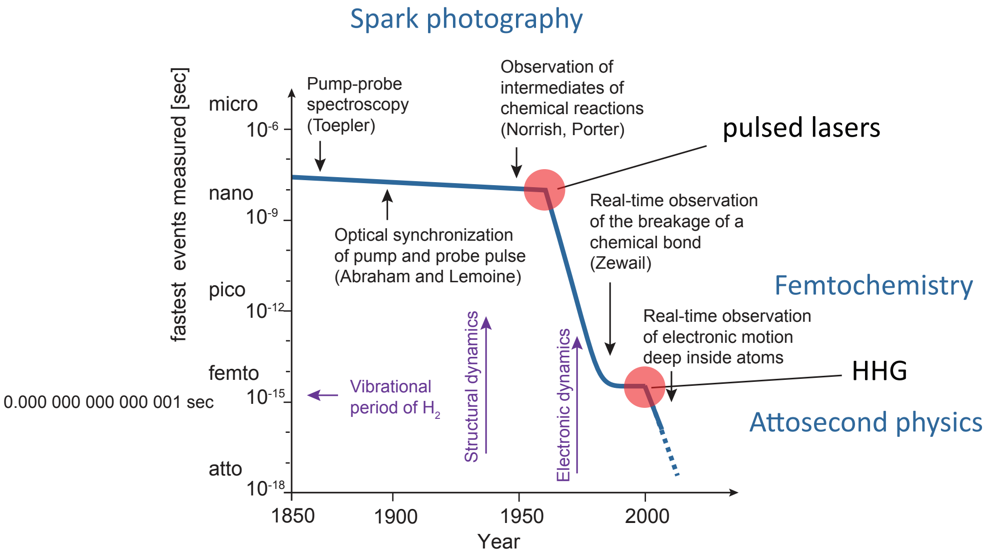

Figure 1.1: Evolution of techniques for time-resolved observation of microscopic processes. Discontinuities in the slope of fasted measured events vs years indicate revolutions in technology. Adapted from [12].

1.1.2 Photoinduced Dynamics and the pump-probe technique

In a photodissociation process, the bond between A–B will break and the molecule will fly apart resulting in fragments A and B. The photon energy is then converted into external degrees of freedom like translation and rotation and in internal degrees of freedom like vibration and excitation of the molecular fragments A and B. If the molecule is excited to a repulsive state, direct dissociation will occur but even if the molecule is excited to a bound state, dissociation can occur if the intermediate state AB* couples to a repulsive state (predissociation [10]). Especially the radial photofragment distribution has always been of great interest for chemists and was first realized by Solomon [11] by applying photochemical etching inside a glass hemisphere. This method measured the flux of fragments at the wall of a hemisphere when plane-polarized light photodissociated a molecular gas.

But how to freeze certain steps to be able to follow the reaction over time? As mentioned in the introduction, one of the first records of capturing motion or of a too fast process for the human eye, was Muybridge 1878, who was able to record snapshots of a galloping horse via spark photography. Around the same time Toepler extended this kind of spark photography to study microscopic dynamics by generating sound waves with a short light spark (pump) and subsequently photographing them with an electronically delayed second spark (probe) [13]. This technique is now known as the 'pump-probe' (time-resolved) spectroscopy. Since then sophisticated experimental innovations improved this technique. First Abraham and Lemoine (1899) introduced optical synchronization by deriving the pump and probe flash from the same spark with a variable optical path length between them and thereby improving the temporal resolution with the limit set by the flash light duration [12]. The progress in these time-resolved measurements was driven by the development of light sources with shorter light flashes. The first who observed chemical reaction intermediates with the pump-probe technique were Norrish and Porter who received the Nobel prize in 1949 for *'their studies of extremely fast chem-*

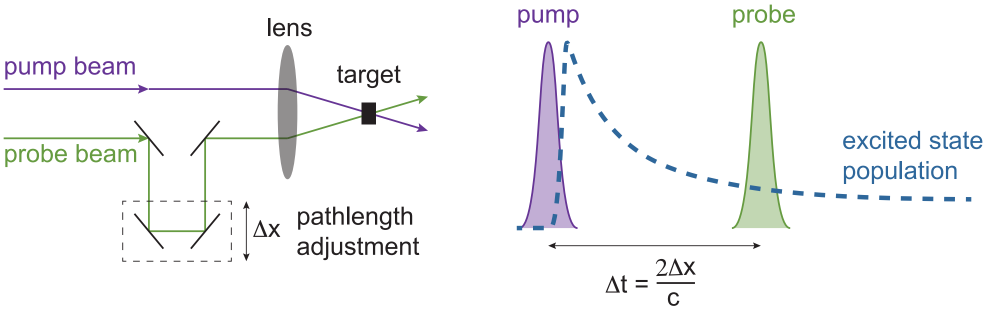

Figure 1.2: Two color pump-probe experiment principle. Two femtosecond laser beams are delayed with respect to each other using a translation stage (four mirror arrangement) and focused into a target. The first pump beam (purple) produces an excited state population in the target (blue dashed line), which the second probe beam (green) probes at different pump-probe delays Δt. Adapted from [17].

ical reactions, effected by disturbing the equilibrium by means of very short pulses of energy', which at this time referred to reaction occurring on the microsecond timescale [12]. The biggest milestone in improving the time resolution was the invention of tunable lasers, especially pulsed lasers, which opened a whole new range of experimental techniques. Ultrashort laser pulses brought the pump-probe spectroscopy from several nanoseconds down to several femtoseconds, six orders of magnitude within merely two and a half decades. Figure 1.1 shows the development and evolution of techniques for time-resolved spectroscopy. The invention of femtosecond technology permitted Ahmed Zewail and coworkers to observe for the first time the breakage and formation of chemical bonds in real time with this technology and opened the field of femtochemistry [14, 15]. He was awarded with the Nobel Prize in Chemistry 1999 [16].

The principle of pump-probe spectroscopy is quite simple and illustrated in Figure 1.2. The first ('pump') laser pulse initiates a reaction, for instance creates an excited state population, and a short time later the second ('probe') laser detects the evolution of this initiated disturbance using various available spectroscopic techniques of which ion or photoelectron imaging is only one. The time resolution to investigate this kind of molecular dynamics is simple given by the time duration of the two laser pulses and the possibility to presicely adjust the delay between them. The technical advances in the last decades has made femtosecond lasers commercially available giving us a time resolutions down to several femtoseconds. The pump pulse will switch on dynamics by fulfilling a resonance. This first light–molecule interaction determines time 'zero-time' at the precision of the pump pulse duration by generating a wave packet that will start to oscillate or/and relax over time. The resonances presented in this manuscript are mostly electronic resonances (excitation in the UV range, see Chapter 2 and Chapter 5) and vibrational resonances (Raman excitation in the IR, see Chapter 4). The probe pulse is the second light–molecule interaction that will produce the observable. The most important issue in such pump-probe experiments is to detect the wave packet created by the pump whatever the potential surfaces on which it evolves. One of most widely used probe steps in gas-phase studies is ionization, since ions can be readily detected.

In this manuscript, two kinds of ionization are used. The first one is the traditional ionization with observables such as the angular and energy distributions of the products of ionization (electrons, parent ions, ionized fragments). The energy and angular distributions of photoelectrons and photofragments are recorded through an imaging technique, in particular velocity-map imaging (VMI) which will be described in the following section in more detail. This method has enabled a number of remarkable advances over the past few years due to its simple implementation for all polarities and to the 4π-steradian detection volume that compensates the weak probability of pump-probe interactions. The second type of ionization uses tunnel ionization with its main observable the XUV emission produced by the recombination of the electron emitted by the cationic core. This is called high-order harmonic generation which can be described in three steps (the three step model), with tunnel ionization, acceleration of the the electron in the continuum dressed by the intense laser field and then recombination with XUV emission and will be discussed in Section 1.3. In this second kind of probe step, the condition on the laser is that it needs to be very short ($<$30 fs) and very intense ($\sim 10^{14}$W/cm^2). This new pump-probe femtochemistry is based on XUV photon detection and is attractive via its phase sensitivity compared to VMI detection.

1.2 Velocity-map imaging

1.2.1 Introduction

The next step forward twenty years after the invention of ion imaging by Solomon [11] was made by Chandler and Houston [18], introducing a technique in which the three-dimensional spatial distribution of a photofragment, measured at a certain time after photodissociation, is projected onto a two-dimensional surface (detector). This technique combined the use of position sensitive ion detection with a Charge-Coupled Device (CCD), a camera, to provide a more sensitive detection technique. The principle idea was to intersect a molecular beam by a photolysis and a probe laser beam at a position between two electrostatic plates called repeller and extractor. The photolysis laser (pump beam) ruptures the molecular bond, while the probe laser ionizes the photofragment. The potential between the electrodes was such, that the ion cloud was accelerated along the time-of-flight axis and compressed perpendicular to it at the same time through a Wiley-McLaren Time-of-Flight Mass Spectrometer (TOF-MS) [19] on to the detector so that all ions arrive at the position sensitive detector simultaneously as a ‘pancake’. The detector consists of a pair of microchannel plates (MCP) coupled to a phosphor screen. An ion hitting the MCP’s gives rise to a burst of electrons at the back face (gain $\sim 10^6$), which produces a flash of light when it strikes the phosphor screen. This can be captures as an image by a CCD camera for processing and analysis in a PC.

This technique of ion imaging has been improved and modified by Eppink and Parker in 1997 [20] through the use of an electrostatic lens. This is now known as velocity-map imaging (VMI), which constitutes a state-of-the-art spectroscopy method. The key improvement to the imaging technique involves the ion optics used to direct ions towards the imaging detector. In the original experiments, the repeller and extractor plates consisted of a pair of grids that provided a uniform extraction field, ensuring a direct spatial mapping of photofragment ions

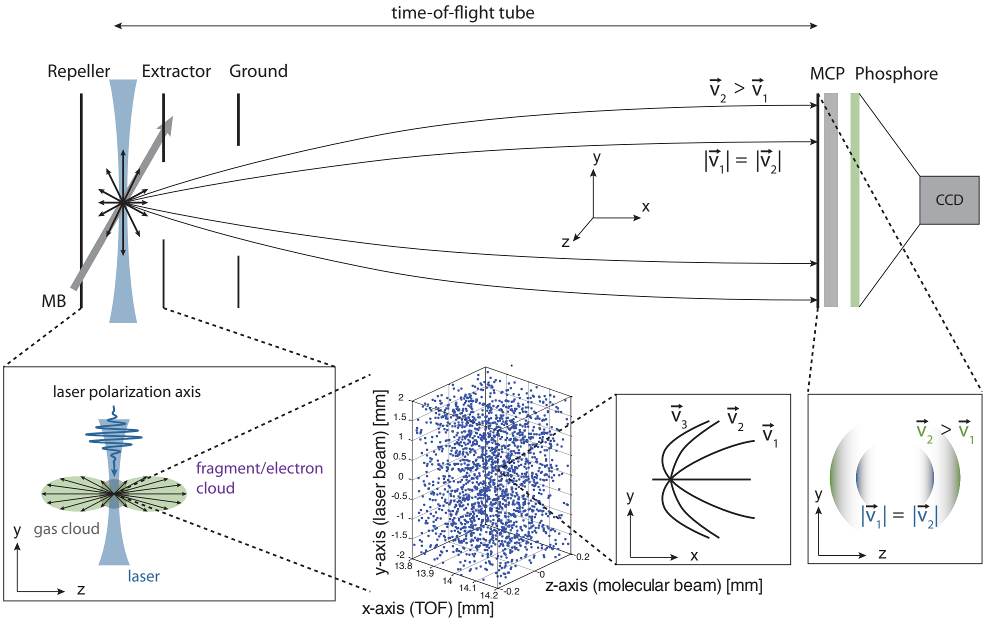

Figure 1.3: Velocity-map Principle. (TOP) side view of the electrode tube with the intersection of molecular beam and laser between the electrodes. Ions formed are accelerated past the ground electrode and fly through the time-of-flight tube to the imaging detector (MCP+Phosphor), which is monitored by a CCD camera. (bottom) Trajectories e.g at 45 degrees in the xy plane calculated from a volume defined by the laser waist size (< 400 µm) and the molecular beam size (< 4 mm). These trajectories are begin quickly bend in the field direction and are focused at the velocity mapping focal plane in the case of $|\vec{v}_1| = |\vec{v}_2| = |\vec{v}_3| = \ldots$ with the same radius.

onto the detector. But as in real life the finite dimensions of the molecular beam and photolysis laser are not producing a single point in space, this leads to blurring of the image. Minimizing the interaction volume reduces the blurring, but also leads to a reduction in signal strength. Additionally, the grids used in the ion lenses are distorting the images. In the modified version of Eppink and Parker the grids are removed which not only got rid of the grid distortions, but also opened the possibility to use the electrostatic lenses in such a way that ions with the same initial velocity are mapped onto the same point on the detector, whatever their initial spatial position, hence the name 'velocity mapping'. The principle is shown in Figure 1.3. As for the original ion imaging experiment the laser and molecular beam are intersected between the repeller and extractor electrodes. The voltages on the repeller and extractor are chosen in such a way that the electrodes function as a lens. All ion fragments produced in the interaction volume defined by the laser beam focus waist (< 400 µm) and the molecular beam diameter (< 4 mm) are focused on the same spot on the detector at the end of the time-of-flight (TOF) tube if they had the same initial velocity. As we will see in the next section, in photon-initiated reactions, the reference direction is usually the polarization vector ε_L of the pump laser pulse for a quick dissociation compared to the rotational period of the parent molecule. The angular distribution of photofragments is well defined relative to this direction due to the fact that absorption of a photon requires overlap between ε and the transition dipole μ for the electronic transition involved in the dissociation. The result is an image of the angular and velocity distribution as shown in Figure 1.3 lower right corner. A larger initial velocity results

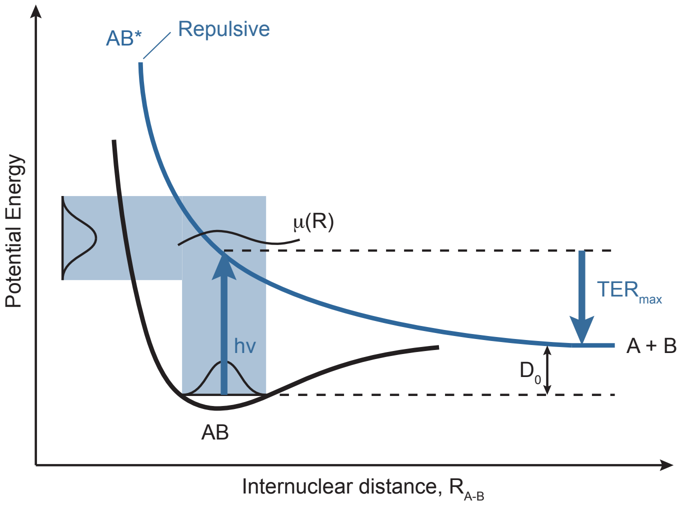

Figure 1.4: Schematic energy potential surface for translational spectroscopy. The translational energy release TER for a photolysis reaction $AB + \hbar\nu \rightarrow A + B$ is determined by measuring the velocity of product A or B. Absorption strength is governed by the projection of the AB wave-function combined with the transition dipole moment function $\mu(R)$ (an arbitrary $\mu(R)$ is shown) onto the repulsive excited state. Adapted from [17].

in a distribution further away from the center whereas the angular distributions comes from all ions with the same initial velocity but different initial velocity directions.

1.2.2 Newton spheres and the VMI experiment

As mentioned before for photodissociation in general a 'pump-probe' configuration is used. In this case the photodissociation is initiated by the first 'pump' laser and the photolysis reaction can be written as

$$\mathrm{AB} + \hbar\omega \rightarrow \mathrm{AB}^* \rightarrow \mathrm{A}(v,J) + \mathrm{B}(v,J) \tag{1.1}$$

where $\hbar\omega$ is the photon energy used to dissociate and v and J are vibrational and rotational quantum numbers of the molecular fragments. When a molecule AB, where A-B may be polyatomic, absorbs a photon and undergoes fragmentation, both energy and momentum must be conserved. A certain amount of energy is required to dissociate the bond, the so called bond energy D_0 as illustrated in the schematic potential energy surface plot in Figure 1.4. Normally the photon energy will be higher than D_0 and the remaining energy after dissociation is released into translational and internal energy of the products as

$$\hbar\omega - D_0 = E_{i,A} + E_{i,B} + TER \tag{1.2}$$

where E_i are the internal energies of the fragments A and B and TER is the translational energy release or total kinetic energy release (TKER) relative to the center of mass. Assuming A and B are produced in the ground state with no internal energies gives us an upper limit for the kinetic energy by:

$$TER_{max} = \hbar\omega - D_0. \tag{1.3}$$

The translational energy release in the center of mass frame is given by:

$$TER = \frac{1}{2}\mu' \mathrm{v}'^2_{rel} = \frac{1}{2}m_A \mathrm{v}_A^2 + \frac{1}{2}m_B \mathrm{v}_B^2 \tag{1.4}$$

where m_A, m_B, v_A and v_B are the mass and velocity of the fragments A and B, respectively. μ' is the reduced mass and v'_{rel} the relative velocity in the center of mass frame for the molecule AB. Conservation of momentum given by

$$m_A \vec{\mathrm{v}}_A + m_B \vec{\mathrm{v}}_B = 0 \tag{1.5}$$

results in the kinetic energy partitioning where the kinetic energy release (KER) of each fragment is given by

$$KER_A = \frac{m_B}{m_{AB}} TER \qquad \text{and} \qquad KER_B = \frac{m_A}{m_{AB}} TER. \tag{1.6}$$

In order to detect the fragments a second laser is used for ionization, the so called 'probe' laser. The interaction of this probe laser for instance with fragment A can be written in the same manner as

$$A + \hbar\omega \rightarrow A^+ + e^- + TER \tag{1.7}$$

The photoionization process with $m_e^- \ll m_A$ and Eq. (1.6) results in a photoelectron receiving essentially all the translational energy TER, leaving the ion A$^+$ in the state defined by the first 'pump' laser process. Each photodissociation or photoionization event yields two partner fragments flying with equal momentum in opposite directions in the centre-of-mass frame due to the conservation of momentum. For a given photon energy and given product quantum states (internal energies) the photofragment speeds (kinetic energy) are well defined. Repeating the same event for many times, the fragments build up a spherical distributions in velocity space. These are the so-called *Newton (velocity) spheres* for the process. The size of the Newton sphere tells us about the balance of internal and translational energy in the reaction and the surface pattern of the Newton sphere tells us about the electronic transitions involved in the dissociation.

Figure 1.5 shows the schematic pump-probe VMI setup. The pump and probe laser pulses are intersected with the molecular beam between the repeller and extractor. The newton spheres of the ions are then velocity mapped on to a 2D position sensitive detector which consists of a microchannel plate (MCP), a phosphor and a charged coupled device (CCD) camera. As this sphere is pushed towards the detector it is magnified and squeezed and ends up as a 2D projection of this 3D sphere on the detector. A single photodissociation event where mass A < mass B creates the Newton spheres shown in Figure 1.6. Over time, the photodissociation will produce two nested spheres with a radii ratio of

$$\frac{R_A}{R_B} = \sqrt{\frac{m_A}{m_B}} \tag{1.8}$$

The radius is directly proportional to the initial velocity in the yz-direction except for a mag-

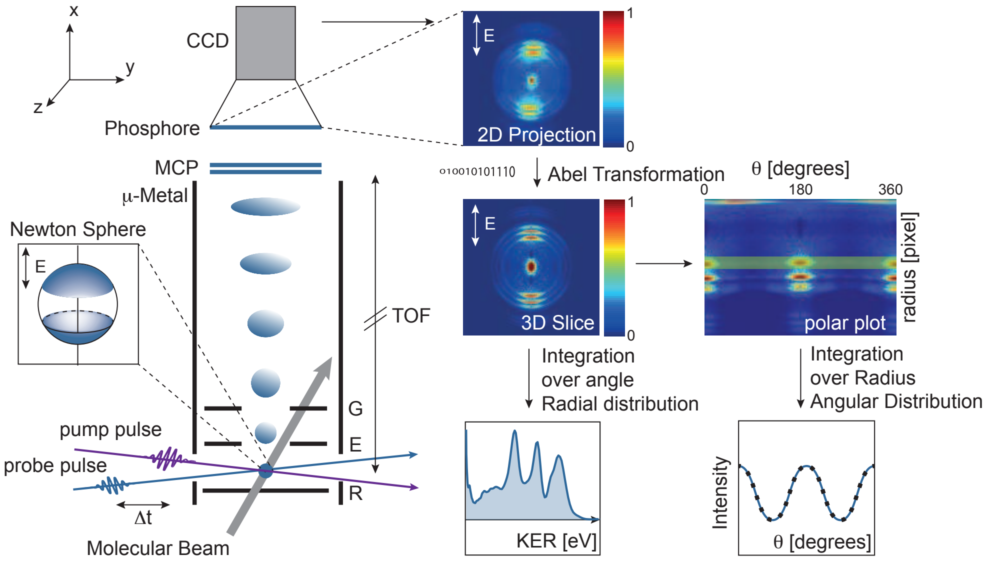

Figure 1.5: Schematic pump-probe VMI setup. The left part shows the electrode system with repeller (R), extrator (E) and ground (G) to accelerate the photo-products towards the detector which consists of a microchannel plate (MCP) a phosphor and a charged-coupled-device CCD to image the phosphor and to send a digitized picture to the PC. Two laser pulses with a variable delay between them are intersected in the molecular beam between the repeller end extractor electrodes. The time-of-flight (TOF) which is shielded by a μ-metal, is in the μsec range and gives enough time to separate the fragments in mass and to stretch the Newton spheres in the yz-plane. Consequently the 3D distribution of the photo products in projected on to a 2D image on the detector, shown on the left. An Abel transformations allows the reconstruction of the 3D distribution and by integrating this reconstructed image over the angle and the radius one obtains the radial or energy distribution (KER) and the angular distributions, respectively.

nification factor caused by the electric field component in the yz-direction and can be written as

$$R = M\mathrm{v}_{yz}t \tag{1.9}$$

where t is the time-of-flight and M a magnification factor [20]. The time-of-flight t is given by the velocity in x direction (TOF-axis) and the length L of the TOF, which is in our case 42 cm. v_x is the velocity of the charged particle gained in the electric field given by $\mathrm{v}_x = \sqrt{2Vq/m}$ where q is the charge and V the potential in which the charged particle is accelerated, which is given by the potential difference of the repeller and extrator voltages (V_{rep} - V_{ex}). If the electric field component in the yz-direction is neglected and the acceleration region is small compared to the total length L of the spectrometer (here 42 cm / 4 cm), the time-of-flight can be written as

$$t \approx \frac{L}{\mathrm{v}_x} = L\sqrt{\frac{m}{2qV}} \tag{1.10}$$

From this one can get the relationship between the radius R and the initial kinetic energy KER of the fragments, which is given by:

$$R = ML\sqrt{\frac{KER}{qV}} = \alpha\sqrt{KER} \tag{1.11}$$

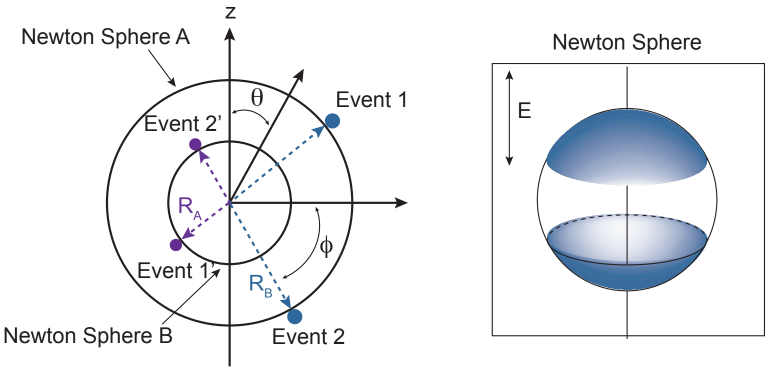

Figure 1.6: Nested Newton spheres from photofragments A and B where $m_A > m_B$. The polar angle θ is defined with respect to the z-axis, the azimuthal angle is φ, and the radius is given by R. Adapted from [1].

where $\alpha = ML/\sqrt{qV}$ is a calibration factor for the experimental setup, which has to be determined experimentally (see Section 1.2.5). Eq. (1.10) and Eq. (1.11) are correct for all charged particles, regardless of their mass or charge. In other words, with the detector time-gated at the TOF time t for the certain mass, any species with the same kinetic energy will appear at the same radius R on the detector. This is quite helpful in calibrating the VMI as one can do the calibration with photoelectrons even if molecular fragments are detected later.

1.2.3 Back conversion of 2D projected images to Newton spheres

As mentioned before the Newton sphere is a 3D distribution which will be squeezed by the electric field to a 2D projections onto the 2D detector. The physical information about the distribution is a center slice through this 3D distribution. In order to extract the kinetic energy and angular distribution information from the images, it is necessary to reconstruct the original 3D distributions. Figure 1.7 outlined the experimental steps in photofragment imaging:

- (A) creation of the Newton spheres by photodissociation
- (B) conversion of the photofragments to ions by laser ionization
- (C) projection of the ionic Newton spheres onto a 2D detector
- (D) recovery of the three-dimensional information from the 2D image using a mathematical transformation

There are two different approaches to the inversion [21]. The first one is a mathematical approach. One can distinguish basically two mathematical concepts (a) inversion methods and (b) forward convolution methods. The inversion methods assume that if the 3D distribution has an axis of cylindrical symmetry (in general fixed by the laser polarization) and therefore if a 2D-central slice is taken through the 3D distribution, the slice contains all the information required to reconstruct the original distribution. From this slice, the 3D projection can be obtained by rotation around the cylindrical axis, which is known as the *Abel transformation* [22]. Hence, the *inverse Abel transform* can be used to obtain the slice from the projection of the 3D distribution. But also so called onion peeling and filtered backprojections methods are available [23]. As in our analyzing step we use a program based on inverse Abel Transformation Appendix B gives an overview over this method. However, if there is no cylindrical

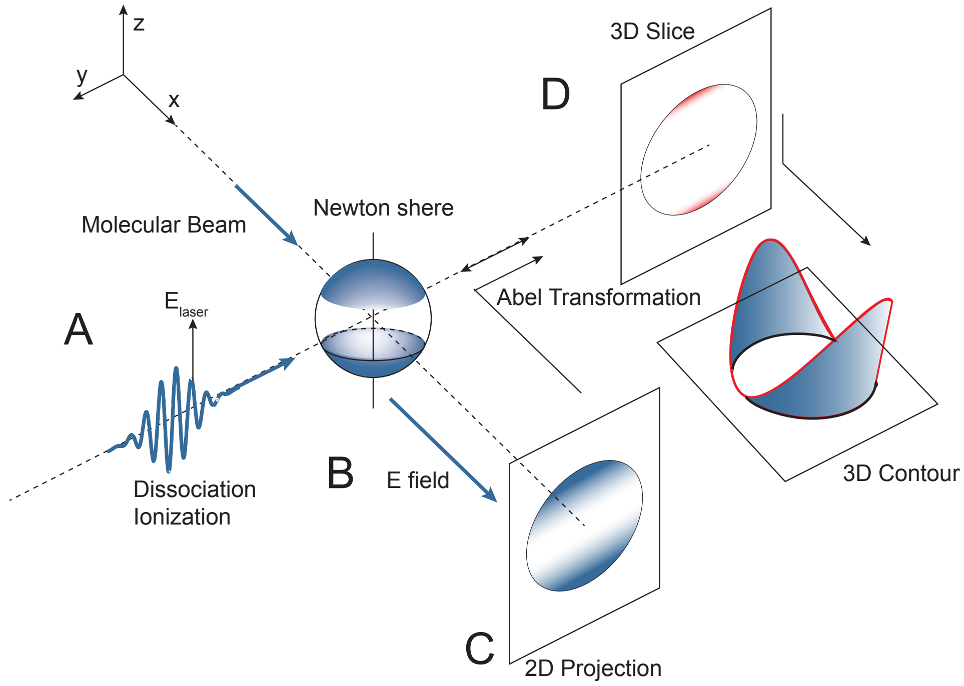

Figure 1.7: Experimental steps in photofragment imaging to measuring Newton spheres from photodissociation. (A) Photodissociation of molecules in a molecular beam by using a linearly polarized laser with the polarization direction parallel to the detector face. (B) Conversion of the photofragment molecules making up the Newton spheres into ions by laser ionization. (C) Projection of the ion spheres onto a 2D detector. (D) Mathematical transformation of the 2D image back to the three-dimensional data of step (A). This slice through the middle of the Newton sphere is displayed in (D) as either a color 2D diagram or 3D contour diagram. With experimental slicing techniques it is possible to avoid step (C). Adapted from [1].

symmetry in the experiment, a forward convolution method is necessary [24–26]. Here, the experiment is simulated in a computer model that produces 2D data that are then compared with the experimental data. By iteratively optimizing parameters in the computer model the best reconstruction of the experimental data is found.

The second approach relies on experimental techniques to sample only the central 2D slice of the expanding Newton sphere and therefore avoid step (C) and (D). This has been achieved by Tonokura and Suzuki [27] using laser sheet ionization, where the shape of the laser beam ionizes only the center slice and by DC-slicing techniques [28–31]. In the Latter case the ion optics are optimized to rather stretch the distribution along the TOF axis than compress them. The ions then arrive at the detector over a wide range of times, and selected slices of the scattering distribution can be imaged simply by applying a suitably narrow time gate voltage to the detector.

1.2.4 Energy and Angular Distributions

The energy distribution as seen in the previous section is proportional to the radius square (see Eq. (1.11)). Therefore the radial distribution obtained from the VMI can be converted to a kinetic energy distribution by integration over the angular coordinates (see Figure 1.5). The kinetic energy is related to the mass and the speed of the fragment. Following the conservation of momentum from Eq. (1.5) and the energy partitioning from Eq. (1.6) we can predict the kinetic energy of its co-fragment and even determine if two observed fragments are coming from the same dissociation channel, meaning they are co-fragments. The maximum translational energy is given by

$$TER_{max} = \hbar\omega - D_0 \tag{1.12}$$

where $\hbar\nu$ is the photon energy used for the dissociation and D_0 the bond energy needed to break the molecule. By conservation of energy, any energy that is not released into product translational degrees of freedom is released in the form of internal degrees of freedom like vibrational and rotational excitation of the co-fragments. This results in a broadening of the energy distribution to lower energy than the upper limit given by Eq. (1.12). Random gas-phase collisions create Newton spheres with homogeneous (isotropic) surface patterns. An anisotropic surface pattern is the result of a selected directionality in the process. A directionality can be introduced in several ways: by crossing a molecular beam at a specified angle with another molecular beam, by selecting special reactant molecular angular momenta, molecular axis alignment and/or orientation or by using a linearly polarized laser beam. In latter case, which is the case in photoselection the directionality is due to the polarization vector of the incident photon beam we use for photodissociation.

For photodissociation, the directionality of the ejected A and B fragments yields information on the direction of the transition dipole with respect to the bond-breaking axis and thus the nature of the excited electronic state. Herschbach and Zare first pointed out that the vector correlation between the parent's transition dipole moment, $\vec{\mu}$, and the recoil velocity of the product, $\vec{v}$, can lead to an anisotropic distribution of photofragments [32]. Looking at an ensemble of molecules with a transition dipole moment μ randomly oriented in the laboratory frame the probability of absorbing one photon is given by the product of the transition dipole moment $\vec{\mu}$ and the polarization vector $\vec{\varepsilon_p}$ of the electric field via:

$$P = |\vec{\mu}\vec{\varepsilon_p}|^2 \tag{1.13}$$

Is the electric field linear polarized, it will preferable excite molecules with their transition dipole moment $\vec{\mu}$ parallel to $\vec{\varepsilon_p}$. This relationship establishes the relationship between the molecular frame and the laboratory axes. In the following, only the axial recoil of a diatomic molecule as illustrated in Figure 1.8 (recoil velocity of the fragments is along the direction of molecular axis which is in this case the bond axis) is considered. In this case for each product velocity the angular distribution is given by [33]:

$$\begin{aligned} I(\theta) &= \frac{1}{4\pi}\int_0^{2\pi} |\vec{\mu}\vec{\varepsilon_p}|^2 \, d\Phi \\ &= \frac{(\mu\varepsilon_p)^2}{4\pi} \times [1 + 2P_2(\cos\chi)P_2(\cos\theta)] \end{aligned} \tag{1.14}$$

where $P_2(x)$ is the second Legendre polynomial $P_2(x) = 1/2(3x^2 - 1)$. χ is the angle between the the transition dipole moment and the recoil velocity and θ the angle between the elec-

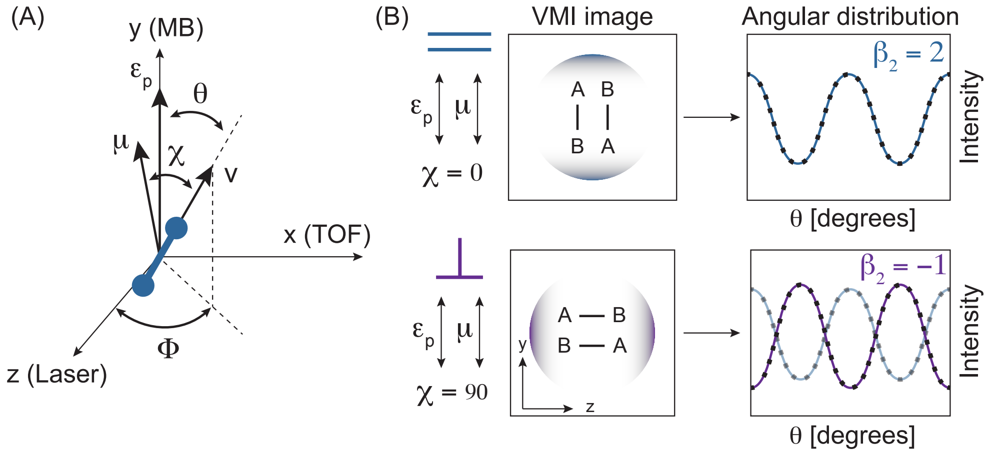

Figure 1.8: Photofragment spectroscopy – angular distribuiton. (A) Geometry. Axial recoil of a diatomic molecule is assumed. Detector (VMI) is in the x-direction. ε_p: polarization vector of the electric field of the exciting laser pulse. μ: transition dipole moment. v: velocity vector of the photofragment. θ: angle between the the recoil velocity and and the polarization vector of the exciting laser field. χ: angle between the recoil velocity and the transition dipole moment. Adapted from [33]. (B) The two extreme cases for $\chi = 0°$ (parallel transition) and 90° (perpendicular transition) with the corresponding angular distribution expected characterized by a anisotropy parameter $\beta_2 = 2$ or -1, respectively.

tric field vector and the recoil velocity. $\beta_2 = 2P_2(\cos\chi)$ is called the *anisotropy parameter*. Looking at a simple diatomic molecule A-B as illustrated in Figure 1.8 one can see that the transition dipole moment $\vec{\mu}$ can make an angle χ with the recoil velocity and we can distinguish two extreme cases:

- **parallel transition** ($\chi = 0°$) The transition dipole moment $\vec{\mu}$ is lying along the dissociating bond (molecular axis) and therefore parallel to the relative recoil velocity $\vec{v}$. The fragments A and B will be emitted parallel to the dissociation laser polarization. This is characterized by an anisotropy parameter $\beta = 2$ and leads to a distribution $\propto \cos^2\theta$.

- **perpendicular transition** ($\chi = 90°$) In this case the transition dipole moment $\vec{\mu}$ is perpendicular to the dissociating bond. The maximum probability of absorbing in his case is given when the molecular bond axis is perpendicular to the polarization of the laser and the fragments A and B will be emitted perpendicular to the dissociating laser polarization yielding β_2 = -1 and the distribution will be $\propto \sin^2\theta$.

It has to be noted that these are extreme cases for one photon absoprtion. First only the second Legendre polynomial is considered and no higher orders. In general the angular distribution is given by the sum over higher orders. For the scope of this thesis this will be sufficient, for higher orders of the Legendre polynomials and their correlation to the angular distribution see Appendix C. Secondly in this picture the asymptotic recoil velocity is along the bond axis of the dissociating bond. In the general case with an angle α between them, β_2 will be given by $\beta_2 = 2P_2(\cos\chi)P_2(\cos\alpha)$. All this implies that the dissociation timescale is significantly shorter than the timescale of the molecular rotational motion. If this is not given the correlation between the angular distribution and the transition dipole moment is lost and the angular distribution is blurred. Thus, one can tell from the experimentally determined value of β_2, if the

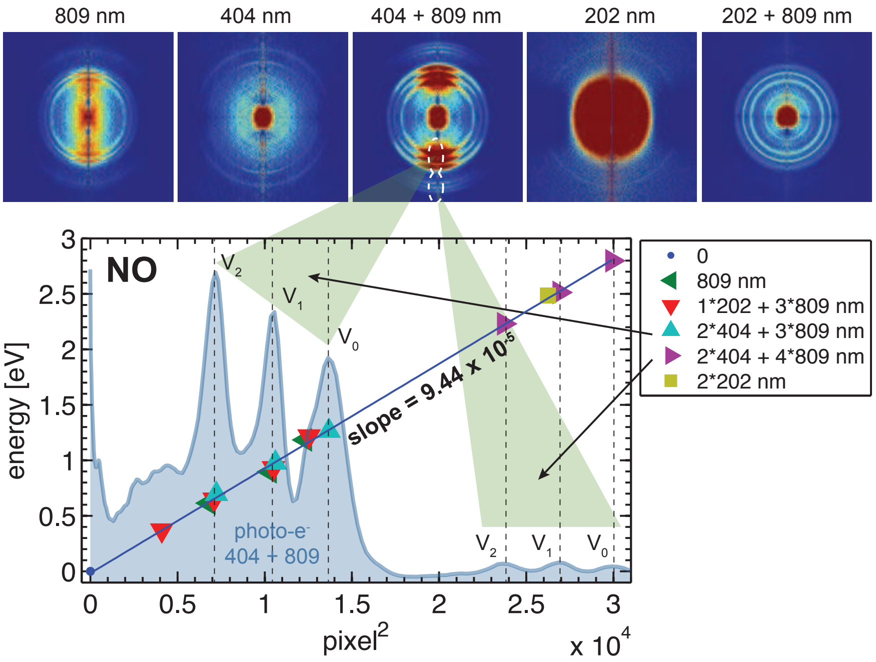

Figure 1.9: Photo-electron spectra of NO at various ionization wavelength to determine the calibration factor of the VMI setup for a repeller and extractor voltage of 2 kV and 1.42 kV, respectively.

dissociation is direct, meaning the molecule has little time to rotate before the dissociation act, and if the relevant excited state is associated with a parallel or perpendicular transition. Doing the experiment on the femtosecond timescale, instead of pico or nanosecond scales means that we are naturally on a timescale shorter then the rotational period of the parent molecule and this degree of freedom is frozen for most of the time delay.

1.2.5 VMI calibration

Eq. (1.11) from Section 1.2

$$R = ML\sqrt{\frac{KER}{qV}} = \alpha\sqrt{KER} \quad \rightarrow \quad E_{kin} = \alpha R^2$$

gave us the relationship between the radius where the fragments are observed on the detector and their kinetic energy. The proportionality factor α depends on the experimental setup and the alignment of the laser beams relative to the molecular beam and the repeller and extractor plate for a fixed repeller voltage and has to be determined through a calibration. In general, in femtolaser facilities where narrow bandwidth laser are not available, this is done detecting photoelectrons of a system for which the spectroscopy is well known. In our case we used NO or Xenon which posseses the advantage of having very close electronic states which are well known. Figure 1.9 shows the Abel-inverted photo-electron images of NO obtained for different ionization wavelengths. The graph shows the extracted spectrum at 404 + 809 nm at Δt = 0 between these two lasers pulses (center image). Plotted is the intensity versus pixel square (blue line). NO$^+$ is detected in its ground electronic state ($X^1\Sigma^+$) by ionizing NO from

Table 1.1: Calibration factor for various repeller (extractor) set voltages determined on the photoelectron spectra of NO with the typical resolution obtained from Figure 1.9 as ΔE at E.

repeller	extractor (focused)	calibration factor α	resolution
2 kV	1.42 kV	9.44×10^{-5}	90 meV at 1 eV 135 meV at 2.5 eV
4 kV	2.84 kV	2.28×10^{-4}	200 meV at 1 eV 210 meV at 2.5 eV
5.5 kV	3.91 kV	2.63×10^{-5}	220 meV at 1 eV 266 meV at 2.5 eV

it ground state ($X^2\Pi_r$) which has an I_p of 9.26 eV [34]. The sets of peaks are identified as the $v = 0, 1, 2$ vibrational modes of NO$^+$. We also observe a second set of three peaks 1.53 eV higher resulting from the absorption of an extra 809 nm photon. The vibrational quantum for NO$^+$ in the ($X^1\Sigma^+$) state is 0.295 eV [35]. Using the knowledge of the I_p and the spacing of the peaks one can plot now the peak position versus the energy calculated from:

$$E_{kin}^{v_i} = n\hbar\omega - I_p^{NO} - E(v_i), \qquad i = 0, 1, 2 \tag{1.15}$$

where n is the number of photons, I_p the ionization energy of NO and $E(v_i)$ the energy of the vibrational level. As the relation ship between energy and pixel square (see Eq. (1.11)) this can then be fitted by a linear function where the slope of this fit corresponds to the calibration factor α. Figure 1.9 shows as well the values for the peaks of the photoelectrons of NO using 202, 404, and 809 nm alone, and as well in pump-probe configuration for 202 + 809 nm and 404 + 809 nm. The calibration factor in the case of a repeller (extractor) voltage of 2 kV (1.42 kV) is determined to be $\alpha = 9.44 \times 10^{-5}$. The photo-electron spectra has also be recorded for repeller (extractor) set voltages of 4 kV (2.84 kV) and 5.5 kV (3.91 kV). Table 1.1 gives an overview over the determined calibration factors.

Most of the experiments on the photodissociation of ClN$_3$ have been done with a repeller voltage of 2 kV. As this calibration factor depends on the position of the laser between the electrodes the alignment procedure on a day to day basis is quite important, if one doesn't want to do a calibration each day. The alignment procedure is explained in the experimental section of the photodissociation of ClN$_3$ (see Section 2.2.3)

1.2.6 The VMI vacuum system

Figure 1.10 shows the vacuum setup for the VMI experiment in Toulouse. During my Ph.D. we redesigned the VMI vacuum system to be more compact and updated the electrode focusing system and the MCP detector. It consist of three main vacuum chambers. In the source chamber the molecular beam is produced. A new designed manipulator allows us not only to change easily the position of the MB source in all three dimensions without braking the vacuum but we also have the ability to change between a continuous and pulsed molecular

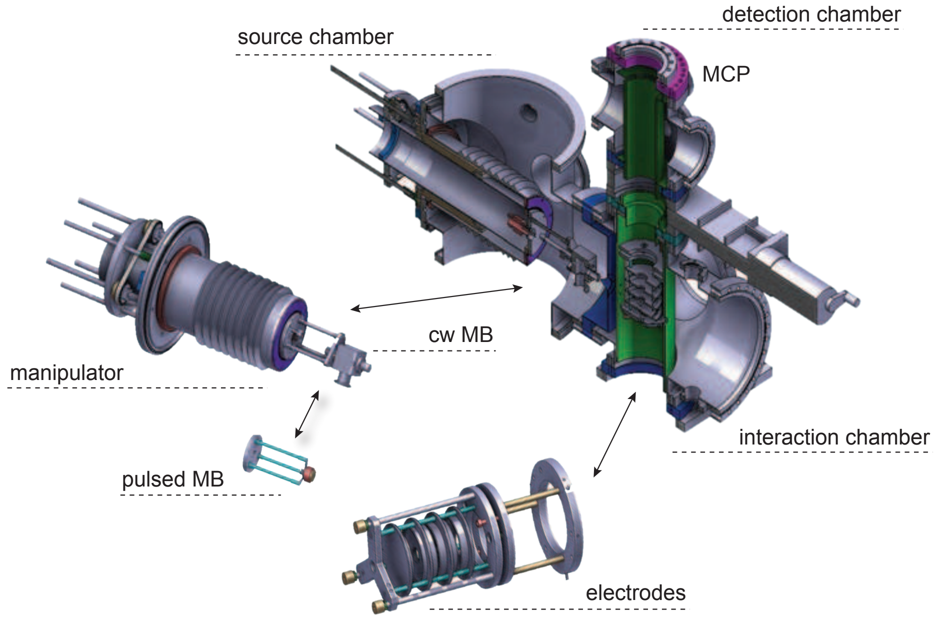

Figure 1.10: Schematic drawing of the experimental vacuum setup for the VMI spectrometer in Toulouse.

beam source. We are able to mount an Even-Lavie pulsed valve[1] [36] and a piezo pulsed valve designed by Maurice Janssen [37, 38]. The molecular beam is then send into the interaction chamber through a skimmer, where it is send in between the repeller and extractor plates and intersected by the two laser pulses. The skimmer is mounted on a rotation plate which allows us to mount up to three different skimmers and which can be controlled from outside to change the skimmer without braking the vacuum. On top of the interaction chamber is the detection chamber, consisting of a time-of-flight tube shielded by a μ-metal (green part in Figure 1.10) and finishing with the detector. The detector is a MCP and phosphor screen combination from Photek (VID275). It consist of two MCP plates with a diameter of 75 mm mounted in a z-configuration on a CF-flange and a P43 phosphor. On top of the MCP a digital CCD camera C8484-05G form Hamamatsu is mounted. The camera is equipped with a high-resolution sensor featuring an effective pixel count of 1344x1023 pixels and a frame rate of about 10 Hz.

The vacuum chambers are pumped by four turbo pumps backed up by two primary pumps. A magnetic turbo pump with a capacity of 3200l/s is used to pump the source chamber. The interaction chamber is pumped by two turbo molecular pumps, one mounted in the direction of the molecular beam with a capacity of 300l/s and one mounted underneath the TOF with 500 l/s. A fourth small turbo pump is mounted just below the detector with 300 l/s. In the source chamber typically a pressure of 10^{-7}mbar is reached and in the detection chamber 10^{-8} mbar. If the gas jet is switched on we typically measure a few 10^{-4} mbar in the source chamber

---

[1] Evan-Lavie valve website

by maintaining a pressure in the interaction chamber of a few 10^{-6} to 10^{-7} mbar. The two backing pumps consist each of a root pump connected to a primary pump with have a capacity of 160 m^3/h for the roots and 63 m^3/h for the primary pump. This insures a backing pressure behind the turbo pumps of $\sim 10^{-3}$ mbar.

1.3 High-order harmonic generation

High-order harmonic generation (HHG) is an extreme form of nonlinear frequency conversion which goes way beyond the standard nonlinear optics like second or third order harmonic generation (SHG/THG) in nonlinear crystals as seen in Appendix A.3. In general HHG is obtained when a very intense ($I \sim 10^{14} W/cm^2$) and short (tens of fs) laser pulse is focused into a gas. It was observed the first time in the late 80's in experiments to characterize perturbative low-order harmonic generation [39, 40]. Instead they observed a large number of odd harmonics of the fundamental driving laser evenly spaced in frequency as shown in Figure 1.11 A. The intensity of these successively higher harmonic orders is not decreasing significantly like in second order harmonic generation in crystals [41, 42] and therefore cannot be explained by perturbative nonlinear optics [43]. The spectrum can be decomposed into 3 parts, first the intensity decreases rapidly for the lower harmonics as expected form perturbation theory but then the conversion efficiency is almost constant in the plateau region until it drops down quickly in the so called 'cut-off' region [40, 44]. Harmonics can be generated with photon energies of several eV [45–48] up to more than 1.6 keV [49, 50] and therefore spanning from the ultraviolet up to the soft X-ray region of the electromagnetic spectrum. The large bandwidth of these spectra reveals directly one of the unique characteristics of HHG, namely allowing us, in principle, the generation of pulses shorter than the driving laser [51–53] and even down to a few attoseconds ($10^{-18} sec$) [50, 54, 55], where the shortest measured pulses up to now were 63 as [56]. Slight disadvantage is that the attosecond pulses are emitted from pulse trains and not as single attosecond pulses but there are methods already in place to isolate a single attosecond pulse [57–60]. As the generating laser radiation, this new radiation is coherent, has a limited divergence angle (2-12 mrad) and a well defined polarization which makes it a versatile tool in VUV spectroscopy.

A number of basic aspects can be already explained with a 'simple man's model' presented in the beginning of the 90's by Kulander et al. [61, 62], and Corkum [63], describing how an electron under the influence of a strong electromagnetic field can leave the atom though tunnel ionization, be accelerated in the laser field and later recombines with the ionic core, thereby emitting harmonic radiation. Thus, in this quasi-classical theory there are three steps involved: tunnel ionization, propagation in the laser field, and recombination and is therefore called 'the three step model'.

1.3.1 The three step model: a quasi classical description of HHG

As mentioned before HHG can be already understood in a 'simple man's model' the three step model [63]

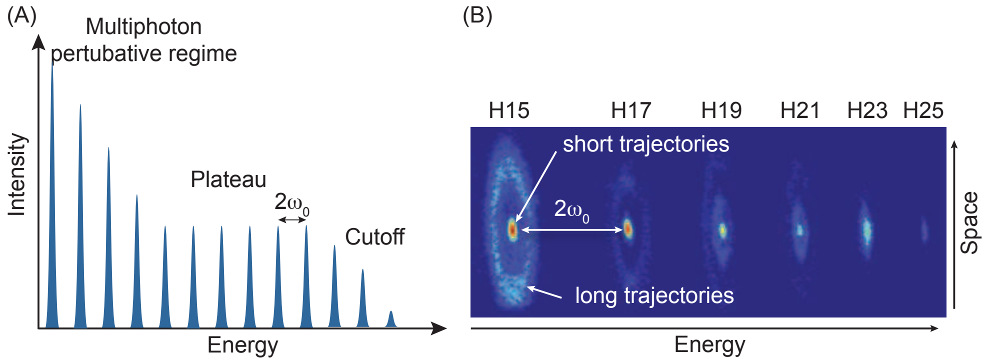

Figure 1.11: High harmonic spectrum. (A) schematic spectrum of a typical high harmonic radiation showing 3 part, rapid decrease of the intensity for the first harmonics in the multiphoton pertubative regime, followed by an plateau where the emission efficiency is almost constant until the signal drops suddenly in the cut off region. (B) Harmonic spectrum produced in argon at a fundamental laser wavelength of 800 nm. Visible here is the spacial structure of HHG as two different ring structures referred to as short and long trajectories.

1. **Tunnel Ionization**

   The strong focused electric field is bending the Coulomb potential and the outer valence electron can tunnel from the ground state of the atom or molecule through the potential barrier.

2. **Acceleration in the laser field**

   The electron is accelerated and driven back to the parent ion as the electric field reverses, in less time than half of the optical period.

3. **Recombination**

   The electron recombines radiatively with its parent ion onto the ground state. This continuum-bound transition converts the kinetic energy of the electron into an extreme ultraviolet (EUV) photon.

which are graphically shown in Figure 1.12. In the following each step will be introduced.

1. Tunnel Ionization

There are basically 3 types of ionization due to an intense laser if the photon energy is lower than the ionization energy (I_p) of the atom or molecule: multiphoton ionization (MI), tunnel ionization (TI) and barrier-suppressed ionization (BSI) depending on the laser intensity as shown in Figure 1.13. The first one is regarded as non-perturbative where the Coulomb potential is not deformed. Ionization occurs by absorbing n photons to reach the IP. This technique is used in femtochemistry as we will see later. HHG in contrary is a regime where the ionization doesn't happen through multiphoton absorption but through tunnel ionization. This happens when the oscillating electric field of the laser given by $|\vec{E}_L(t)| = E_0\, cos(\omega_L t)$, becomes comparable to the intra-atomic field strength ($\sim 10^8$ V/cm). This leads to deformation of the coulomb potential and can lower the barrier so much that tunneling becomes possible. The

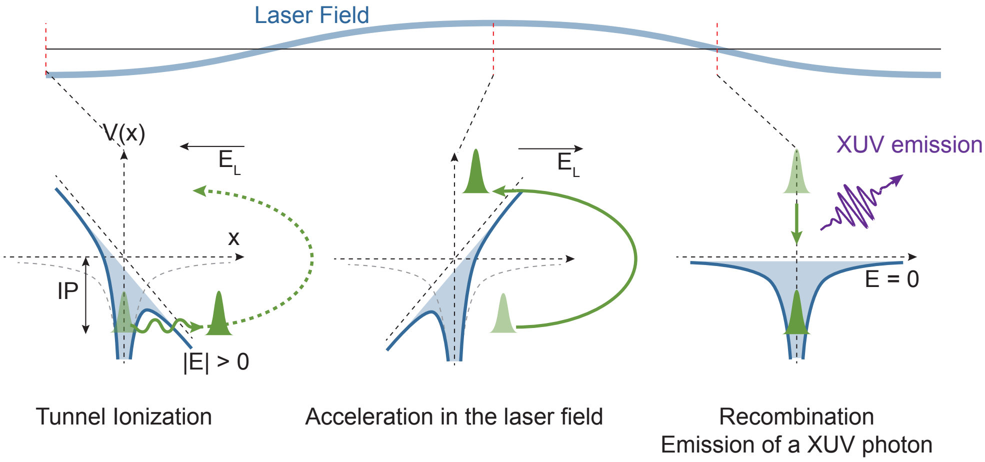

Figure 1.12: The three step model of HHG. The electric field of a focused laser first ionizes an outer valence electron from the ground state of an atom or molecule. This electron is then accelerated by the electric field of the laser. If it returns to the vicinity of the parent ion, the electron can radiatively recombine into the ground state.

total time-dependent potential $V(\vec{r},t)$ felt by a single electron can be written

$$V(\vec{r},t) = V_0(\vec{r}) + V_L(\vec{r},t) = -\frac{Z_{eff}}{|\vec{r}|} + e\vec{E}_L(t)\vec{r} \tag{1.16}$$

where $V_0(\vec{r})$ is the effective ionic coulomb potential and $V_L(\vec{r},t)$ the dipole interaction with the laser electric field. Z_{eff} is the effective charge of the nucleus[1]. Keldysh was the first in 1965 to give an unified picture of nonlinear ionization for atoms in the field of a strong electromagnetic wave whose frequency is lower than the ionization potential, known as the Keldysh theory [64]. This allows to identify the two limiting cases leading to multiphoton ionization or tunnel ionization, distinguished by the Keldysh adiabatic parameter γ_K given by:

$$\gamma_k = \frac{\omega_L\sqrt{2m_eI_p}}{eE_0} = \sqrt{\frac{I_p}{2U_p}} = \frac{\tau}{T_L} \tag{1.17}$$

where e and m_e are the charge and the mass of the electron, I_p the ionization potential, $U_p = e^2E_0^2/4m_e\omega_L^2 \sim I\lambda^2$ the ponderomotive energy, which is the average kinetic energy of the electron in the oscillating electric field and proportional to the laser intensity and the wavelength square. The Keldysh parameter can also be correlated to the timescales involved where τ is the ionization time the electron needs to tunnel through the barrier and is given by

$$\tau = 2\pi\frac{\sqrt{2m_eI_p}}{eE_0} \tag{1.18}$$

$T_L = 2\pi/\omega_L$ is the period of the oscillating electric field which is typically 2.67 fs for a titanium-sapphire laser (Ti:Sa-Laser) at $\lambda = 800$ nm. Consequently we can see that the Keldysh parameter is the ratio between the tunnel time τ and the optical period T_L.

---

[1] $Z_{eff}(Ar, Kr) = 1$

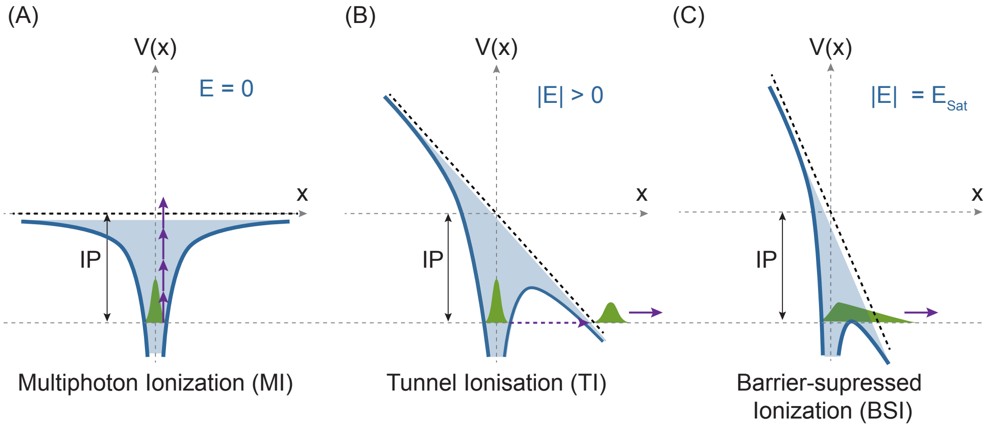

Figure 1.13: Regimes of strong-field ionization. Exposing an atom to an intense laser field will result in a modified potential (solid line) composed of the Coulomb potential (dashed line) and the time dependent effective potential of the optical pulse (see also Eq. (1.16)). At moderate intensities, the resulting potential is close to the unperturbed Coulomb potential and an electron can be liberated only upon simultaneous absorption of n photons, resulting in perturbative, multiphoton ionization. The ionization rate in this case scales with the n-th power of the laser intensity. In this scenario, there is insufficient time for the electron to tunnel through the barrier during each laser cycle, and the electron is bounced back and forth by the time-dependent potential. (B) At sufficiently high-field strengths the Coulomb barrier becomes narrow, allowing optical tunnel ionization to take over and resulting in a tunneling current that follows adiabatically the variation of the resultant potential. (C) At very high fields, the electric field amplitude reaches values sufficient to suppress the Coulomb barrier below the energy level of the ground state, opening way to above-barrier ionization. In the tunnel and above-barrier scenarios, ionization can be considered quasi-static.

$\omega_L \rightarrow \infty$ Is the laser frequency ω_L high the Keldysh parameter is $\gamma_k \gg 1$ and multiphoton ionization will be the dominant part (see Figure 1.13 A). This also means that $\tau \gg T_L$ and the electron will have insufficient time to tunnel through the barrier during each laser cycle. The electron is bounced back and forth by the oscillating potential until it absorbs enough photons to become a free electron [65]. The ionization rate ω_i is proportional to E_0^{2q}, where q is the order of the non-linear process.

$\omega_L \rightarrow 0$ In this case the Keldysh parameter is $\gamma_k \ll 1$ and $\tau \ll T_L$. This is called the tunneling limit. The electron will have enough time to tunnel through the barrier during one laser cycle and the potential will not change drastically during this time (see Figure 1.13 B) so that the ionization can be seen as quasi static. If $\gamma_k \lesssim 1$, tunneling still takes place but becomes inefficient. The tunnel ionization rate for an hydrogen atom was already calculated by Keldysh in 1965 and later 1986 generalized by Ammosov, Delone and Krainov to an arbitrary electronic state of complex atoms and ions in an oscillating electric field [66]. The calculated ionization rate is now known as the ADK ionization rate and given by

$$\omega_{ADK}(t) = \sqrt{\frac{3E_L(t)}{\pi(2I_p)^{3/2}}} A_{n*l*} B_{l,|m|} I_p \left(\frac{2(2I_p)^{3/2}}{E_L(t)}\right)^{2n*-|m|-1} \exp\left(-\frac{2(2I_p)^{3/2}}{3E_L(t)}\right) \tag{1.19}$$

where the factors A_{n*l*} and $B_{l,|m|}$ are defined by the principle quantum number n, angular quantum number l and the magnetic quantum number m of the electron. In general we can say

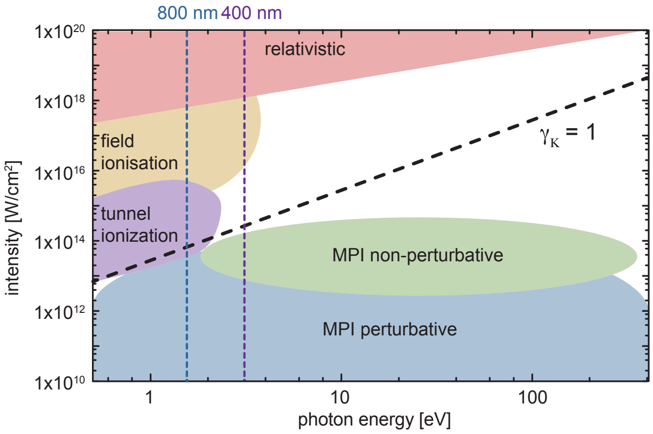

Figure 1.14: Different photoionisation regimes as a function of the laser intensity and photon energy. For the rather low laser intensities ionization proceeds either by a multiphoton perturbative process for the lowest intensities or a multiphoton non-perturbative process [67]. If the laser frequency is quite low but the laser intensity is moderately strong, ionization occurs via tunneling [68]. Field ionisation happens at even higher laser intensity when the potential barrier is completely suppressed by the laser field. At extremely hight laser intensities relativistic effects play an important role [69]. The vertical dotted blue and purple lines indicate the photon energies related to the laser wavelength of 800 nm and 400 nm, respectively, which are used in this manuscript. The dashed black line shows the case of $\gamma_k = 1$ for argon. Adapted from [70].

that the tunnel ionization depends exponentially on the electric field strength and the ionization potential:

$$\omega_{ADK}(t) \propto I_p^{0.25} \exp\left(-\frac{5.65(I_p)^{3/2}}{3E_L(t)}\right) \tag{1.20}$$

One also sees that the Keldysh parameter depends on both the strength of the electric field E_L and the frequency of the laser ω_L, which is graphically shown in Figure 1.14. At the intensity of 10^{14} W/cm^2 and at 800 nm, the Keldysh parameter is around 1 for example in the case of argon. Thus we are in the intermediate region between tunnel and multiphoton ionization. When the electric field becomes much stronger than the regime of tunnel ionization the coulomb potential can be bent so much that the barrier becomes significantly lower than the I_p, and the electron is then ripped off the parent ion as shown in Figure 1.13 C. This is called barrier-supressed ionization (BSI) [68]. In between these two regimes we will have an electric field intensity for which we saturate the tunnel ionization. The total probability of ionization p_I can be calculated by integrating the ionization rate over the pulse duration of the electric field:

$$p_I = 1 - \exp\left(-\int_{-\infty}^{\infty} \omega_{ADK}(t)\, dt\right) \tag{1.21}$$

The tunnel ionization will increase exponentially with increasing the laser intensity until the probability reaches one. This is defined as the saturation intensity I_{sat} which depends on the laser duration and the spacial profile. If one assumes that the potential $V(\vec{r},t)$ from Eq. (1.16) is mainly one dimensional along the z-polarization of the laser $V(\vec{r},t) = V(z) = -Z_{eff}/|z| - eE_z$, at the threshold the derivative of the potential has to be zero, $V'(z_0) = 0$ which leads to $z_0 = \sqrt{Z_{eff}/(eE_L)}$ and the saturation potential itself is given by $V_{sat} = -I_p$. With this we can estimate the saturation energy and intensity as function of the ionization potential to:

$$E_{sat} = \frac{I_p^2}{4Z_{eff}} \tag{1.22a}$$

$$I_{sat} = \frac{I_p^4}{16Z_{eff}^2} \tag{1.22b}$$

$$I_{sat}\,[W/cm^2] = 4.02 \times 10^9\, \frac{I_p^4}{Z_{eff}^2}\,[eV] \tag{1.22c}$$

Note that the electric field needed to lower the potential barrier has a quadratic dependence on the ionization potential. For a given laser intensity, the ionization regime may be totally different depending on the gas used. Table 1.2 shows the intensities needed to suppress the barrier in rare gases, calculated from equation Eq. (1.22b).

Table 1.2: Calculation of the saturation energy (barrier suppression) for different rare gases.

gaz	He	Ne	Ar	Kr	Xe
I_p [eV]	24.59	21.56	15.76	14.00	12.13
I_{sat} [10^{14} W/cm^2]	14.62	8.65	2.47	1.54	0.87

While in atoms it is clear that it is the least bound electron which participates in the tunnel ionization process, in molecules one of the challenges is to determine which molecular orbital participates and how it depends on the geometry of the molecule. This issue will be discussed in Chapter 4 about the HHG spectroscopy of SF_6.

2. Acceleration in the laser field

This is the part of the semiclassical theory which is treated classically. In the context of the strong field approximation (SFA) the coulomb potential of the atom is neglected and the electron is regarded as a free electron whose motion is governed only by the external laser field given by $|\vec{E}_L(t)| = E_0\, cos(\omega_L t)$. The differential equation for the motion of the electron can then be written as:

$$\ddot{x}(t) = -\frac{eE_0}{m_e}\cos(\omega_L t) = -\frac{eE_0}{m_e}\cos(\varphi) \tag{1.23}$$

where $\varphi = \omega_0 t$. We consider an electron which is *ab initio* bound to an atom and appears in the continuum at time zero t_i with an initial velocity of approximately $\mathrm{v}_0 = \dot{x}(t_i) = 0$. Furthermore, by neglecting the distance between the electron and the nucleus and puting $x(t_i) = 0$, the velocity $v(t)$ and the position $x(t)$ of the free electron, born at an arbitrary phase ϕ of the oscillating electric field, can be calculated to be:

$$\mathrm{v}(t) = \int_0^t -\frac{e}{m_e} E_L(t')\,dt' = -\frac{eE_0}{m_e\omega_L}\left[\sin(\omega_L t + \phi) - \sin(\phi)\right] \tag{1.24a}$$

$$x(t) = \int_0^t v(t')\,dt' = \frac{eE_0}{m_e\omega_L^2}\left[\cos(\omega_L t + \phi) - \cos(\phi) + \sin(\phi)t\right] \tag{1.24b}$$

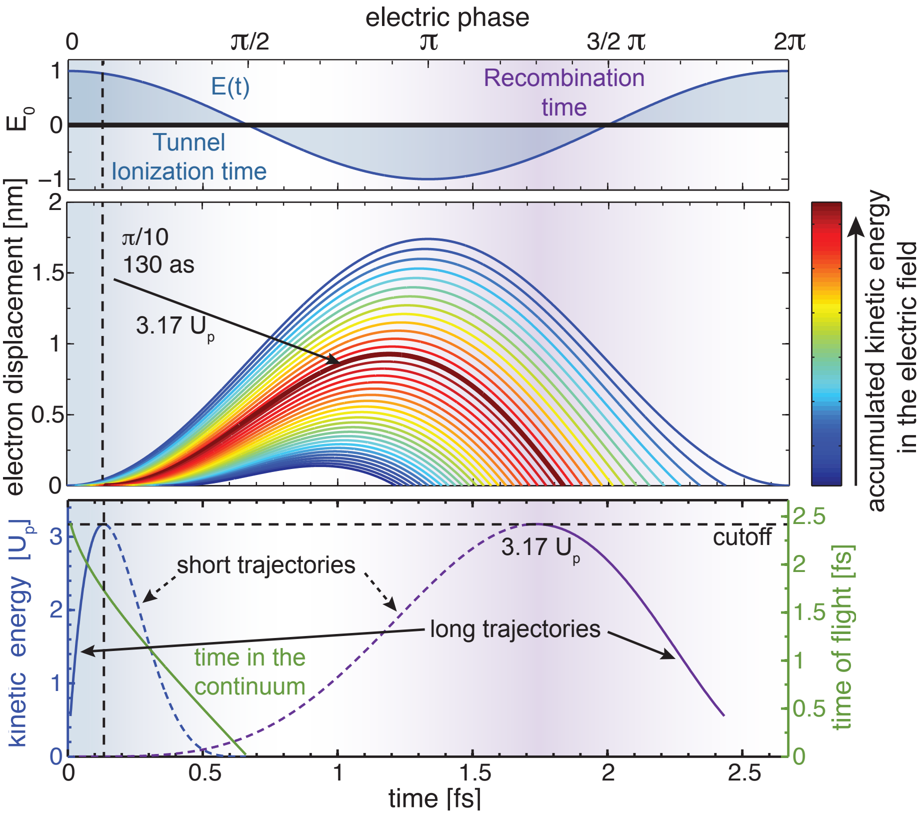

Figure 1.15: Calculated electron trajectories after ionization of argon with a laser intensity of 10^{14} W/cm^2 at 800 nm. The oscillating laser field is displayed on the top of the figure as function of the phase. The trajectories are plotted in the center figure. The kinetic energy of electrons while recolliding with the parent ion is strongest for red and weakest for blue trajectories. The thickest trajectory is where the kinetic energy is maximum (E_{kin} = 3.17 U_p). The lower part of the figure shows the kinetic energy versus the ionization time (blue area) and versus the recombination time (purple area) inside one laser cycle. A different recombination time (purple) is attributed to each ionization time (blue). Below the 3.17 U_p we can identify the short (dashed) and long (solid) trajectories. The green line shows the time the electron spends in the continuum depending on when it is emitted.

The amplitude of this oscillating electron trajectory

$$\frac{eE_0}{m_e\omega_L^2} = R_0 \tag{1.25}$$

is also called the ponderomotive radius R_0. These radii are on the order of a few nanometers considering a typical ionization radiation of $I_L \sim 10^{14}$ W/cm^2 and therefore much larger than the atomic radius. In Figure 1.15 the electron trajectories following Eq. (1.24b) with respect to the ionization time are shown for one laser cycle. Depending on the time when the atom is ionized inside this period, it is possible that the electron will reverse its direction and return to the core and gain different amounts of kinetic energy. Before the electric field reaches its maximum, the electrons will not return to the parent ion. Only electrons emitted in the phase regime $[0 - \pi/2]$ or in time $(0 \leqslant t_i \leqslant 0.67$ fs) and $[\pi - 3\pi/2]$ (time) will return to the core, while electrons emitted at any other phases of the cycle will not return and veer away from the point of birth in the continuum. Electrons emitted exactly at the maximum of the laser intensity will have no kinetic energy when they return, whereas the electron emitted at $\approx \pi/10$ ($t_i = 130$ as) will gain the maximum kinetic energy which is given by 3.17 U_p, where U_p is the ponderomotive energy. Its trajectory refers to the cut-off trajectory. In Figure 1.15 lower part the kinetic energy the electron is gaining during the time in the laser field is plotted versus the ionization (blue area) and recombination time (purple) area. If the return kinetic energy of the electron is below 3.17 U_p, two different electron trajectories (solid and dashed lines) can be associated with this kinetic energy having different time of flight values. These two trajectories are refeered to as long (solid) and short (dashed) trajectories:

- short trajectories identifies electrons emitted after $\pi/10$, they don't travel far away from the ionic core and the propagation time in the continuum is short and increases with harmonic order.

- long trajectories in contrary identifies electrons emitted before $\pi/10$ near the maximum of the laser field, they can travel up to 2 nm away form the ionic core and the time of propagation in the continuum is rather long and decreases with harmonic order.

The earlier an electron is emitted during a laser cycle, the longer it will remain in the continuum and will acquire a phase shift with respect to the electron-hole left behind in the ionic core. This phase shift is proportional to the average time delay between ionization and recombination and the ionization potential:

$$\Delta\varphi_q \approx -\alpha_q \Delta I_L \tag{1.26}$$

As the time-of-flight is larger for long compared to short trajectories so will be the phase difference when electron and ion recombine. This will effect each harmonic order and can be used to identify spatially different ionization channels [71, 72]. For instance in argon $\alpha_{short} = 12 \times 10^{-14}$ rad.cm^2/W and $\alpha_{long} = 25 \times 10^{-14}$ rad.cm^2/W with an laser intensity of 1.5 10^{-14} W/cm^2 [73].

3. Recombination

In the case the electron returns to the parent ion one can observe several processes. The electron can be scattered inelastically by the ion core, transferring part of its energy to another electron. Thus, a second electron may be ejected from the ionic ground state to the continuum. This process is called *non-sequential double ionisation (NSDI)* [74–77]. Alternatively, the electron can be elastically scattered by the ion core. In this case, it can acquire drift energies up to 10 U_p. Such effect is referred to as *high order above threshold ionisation (HATI)* [78–80]. And finally, the electron can recombine with the ion emitting its energy in form of a high energy photon which we know as *high harmonic generation (HHG)*. In the latter case the excess energy gained by the electron in the external oscillating field is carried away by emitting a high energy photon. This energy can be expressed as:

$$\hbar\omega = E_{kin} + I_p \tag{1.27}$$

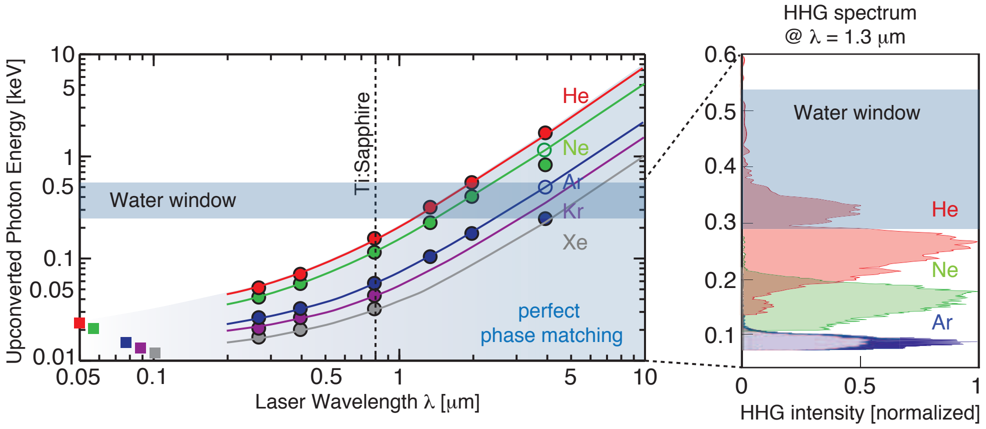

Figure 1.16: Predicted and observed HHG phase-matching cutoffs as a function of laser wavelength from the UV to the mid-IR for the rare gases. Solid circles show the observed cutoffs, open circles show the predicted cutoffs for Ar and Ne, which cannot be reached due to inner-shell absorption [50, 81–84]. On the right experimental phase-matched soft-X-ray super-continua achieved at 1.3 μm. By increasing the driving laser wavelength it is possible to generate light in the water window (x-ray energies of 280 to 530 eV). Water is transparent to these x-rays while nitrogen and other elements found in biological specimens are absorbing. These wavelengths could be used in a x-ray microscope for viewing living specimens [85]. Adapted from [50, 86].

where E_{kin} is the kinetic energy of the electron and I_p the ionization potential of the generating medium. Solving Eq. (1.24b) with $x(t_0) = 0$ we can obtain the maximum kinetic energy of 3.17 U_p and therefore the maximum of photon energy is given by:

$$(\hbar\omega)_{max} = 3.17 U_p + I_p \tag{1.28}$$

known as the cutoff-law of high harmonic generation. In units of electron volts U_p can be expressed as $U_p = 9.33 \times E_0[10^{14} W/cm^2] \times \lambda^2[\mu m^2]$. Using media with higher I_p or larger driving laser wavelength the cutoff can be pushed further to higher energies. Figure 1.16 shows a summary of predicted and observed HHG phase-matched cutoffs for the rare gases with an example of an soft x-ray continuum generated with an driving laser wavelength at 1.3 μm.

The structure of HHG emission

With the three-step model we can now also easily understand the spectral and temporal structure of the HHG emission. The recollision process repeats itself each half laser cycle, generating a burst of EUV-radiation. As momentum needs to be conserved, the polarization between the absorbed and emitted photons are strongly correlated. High harmonics generated in a linear polarized laser field are themselves linearly polarized [87]. In the time domain, this forms a pulse train synchronized with the fundamental laser, as shown in Figure 1.17. Since the EUV burst is confined to each half laser cycle, the pulse duration of each burst is in the attosecond regime and intrinsically coherent to the fundamental field due to momentum conservation. In the spectral domain, this corresponds to a comb with a spacing of twice the fundamental laser frequency. This leads directly to an understanding of the observation that the HHG peaks ap-

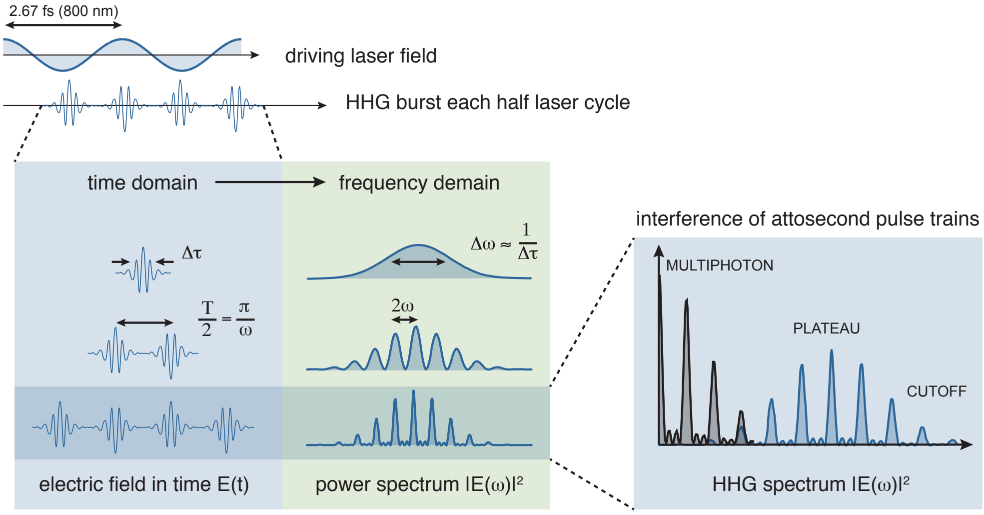

Figure 1.17: Temporal and spectral structure of HHG emission: from the time to the frequency domain. HHG spectrum as interference of attosecond pulse trains.

pear only at odd integer multiples of the fundamental frequency. Looking at the second order nonlinear polarizability $P^{(2)}(\omega_3)$ given for an interaction of an electric field with a medium with nonzero second order susceptibility:

$$P_i^{(2)} = \chi_{ijk}^{(2)}(-\omega_3;\omega_1,\omega_2)E_j^{\omega_1}E_k^{\omega_2} \tag{1.29}$$

where $\chi^{(2)}$ is the 2nd order susceptibility tensor, the indices i, j, k denote cartesian components of the electric field oscillating at $\omega_3, \omega_2, \omega_1$. In the case of second order harmonic generation the frequencies are related $\omega_3 = (\omega_1 + \omega_2)$, where ω_3 is the 'output' frequency and ω_1 and ω_2 are the frequencies of the incident electric field. If the conversion medium has a inversion symmetry, $P_i^{(2)}(\omega_3) = -P_i^{(2)}(\omega_3)$ should be fulfilled. This only works if $P^{(2)} \equiv 0$. This means that in centrosymmetric media one cannot observe nonlinearities of even order. Randomly aligned gases are inversion symmetric. In a macroscopic generation medium one will always find an inversion symmetric pendant such that harmonics of even order are suppressed in the spectrum.

Up to now we always considered a linear polarized electric field. Using a circular or elliptic polarized driving laser field the electron trajectories should not lead back to the ionic core. This is not 100% true because the electronic wave-packet will get broadened while traveling. This can be described by the intrinsic dispersion of a free electron wave-packet. In quantum mechanics the free electron wave-packet can be written as a superposition of plane waves as first approximation. From the Schrödinger equation one gets the group (v_g) and phase (v_p) velocities

$$v_p = \frac{\hbar k}{2m_e} \qquad v_g = \frac{\hbar k}{m_e} \tag{1.30}$$

of the electron wavepacket. These are fundamentally different. As we can see an electron with a classical momentum $\vec{p} = \hbar\vec{k}$ moves with the group velocity v_g but the phase velocity is only half of v_g and introduces a dispersion and therefore a spread of the electron wave-packet. The recombination of the electron with the ionic core is given by the overlap of the wave functions and therefore if the ellipticity of the driving laser is small ($\varepsilon_L < 15\%$) there can still be an overlap. But the HHG emission yield is decreasing rapidly with increasing ellipticity of the driving laser. This effect is not so drastic in molecules [88] and clusters [89] because of the extension of the molecular orbital (see Section 1.3.4)

1.3.2 The quantum model of HHG

The three step model explains all basic concept of HHG and agrees often with the experimental observations. It allows us even to determine phase information and can distinguish between electrons emitted at different times during the laser cycle. But looking for example at the tunnel ionization time we find a huge discrepancy between the predictions and the experimental results [90], for instance in the case of elliptical polarized driving laser field. In the quantum mechanical picture the returning free electron is regarded as a wave function and not as a particle and this wave function has to overlap with the initial wave function in order to recombine. Due to the quantum-mechanical nature of the electron, which suffers from dispersion when not bound to a potential the rescattering electron wave-function spreads spatially which leads to smaller overlap with the parent ion than classically expected.

To deal with the strong field response of atoms and molecules in general and HHG in particular in a quantum mechanical picture, one has to solve the time-dependent Schrödinger equation (TDSE):

$$i\hbar\frac{\delta}{\delta t}\psi(\vec{r},t) = \hat{H}\psi(\vec{r},t) \tag{1.31}$$

where ψ is the wave function of the quantum system and $\hat{H}$ is the Hamiltonian operator, which characterizes the total energy of any given wave function. The Hamiltonian is given by:

$$\hat{H} = -\frac{\hbar^2}{2m}\nabla^2 + V(\vec{r},t) \tag{1.32}$$

where in this case the time-dependent potential $V(\vec{r},t)$ is given by the sum of the atomic coulomb potential and the dipole interaction with the electric field as seen in the three step model. Although the TDSE can be solved numerically for the simplest case of an hydrogen atom, it requires considerable computational time. To solve this equation for multielectron systems is almost impossible. Thus one has to consider approximations to derive an analytical solution. In the case of atoms in strong laser fields this has been done the first time in 1994 by Lewenstein and coworkers and is known as the strong field approximation (SFA) [91] which uses the single active electron approximation (SAE) developed by Keldysh in 1965 [64]. This quantum mechanical treatment of HHG is now known as the Lewenstein model of high harmonic generation. It allows to analyze the experimental results qualitative and quantitative and justifies the hypothesizes done in the three step model. As it it not necessary to understand the basic concept of HHG, it is not treated here but a summary can be found in the Appendix D of this manuscript.

1.3.3 Macroscopic high harmonic generation, phase matching and photon flux

More important than the quantum mechanical description of HHG is the macroscopic response. So far only one atom in a strong electric field has been considered with its microscopic response to an external strong electric field. Under experimental conditions high harmonics are generated typically in a gas which has a density (10^{17}-10^{18}cm^{-3}) and the driving laser has a focal length which is larger than zero (Rayleigh length) defining an interaction volume with a certain number of atoms. On one hand a certain density or volume is needed because like in second harmonic generation in crystals phase matching within a certain coherence length has to be sustained in order to improve the efficiency of the generation and to measure a macroscopic response. On the other hand, if the generation volume is longer than its absorption length, the emitted photons can be reabsorbed by the medium itself reducing the efficiency again. The typical low flux and the low efficiency of HHG ($\sim 10^{-7}$) is the most important technical bottleneck for attosecond science and HHG as a new XUV light source as an emerging field. Therefore to further enhance the conversion efficiency and photon flux the understanding of these macroscopic phenomena is important.

Phase matching conditions for HHG

The phase matching for constructive interference as schematically shown Figure 1.18 A is characterized by the phase mismatch Δk between the wave vectors k of the driving laser and of the qth harmonic order given by

$$\Delta k = k(q\omega_L) - qk(\omega_L) = \frac{\pi}{L_c} \tag{1.33}$$

where ω_L is the fundamental laser frequency and L_c is the coherence length over which the accumulated phase slip between the fundamental and the generated light is π. In an ideal situation Δk should be zero or at least very small for an efficient conversion. Or in other words, the different emitters should radiate in phase at any given point in the generation volume. The wave vector k is governed by four physical dispersion effects: atom, plasma, geometrical and atomic dipole phase dispersions which add to the gaussian beam vector $k_{vac}(\omega)$ in vacuum and can be written as a sum of these:

$$k(\omega) = k_{vac}(\omega) + k_{atoms}(\omega) + k_{plasma}(\omega) + k_{geom}(\omega) + k_{ADphase}(\omega) \tag{1.34}$$

where $k_{vac} = 2\pi/c$ is the wave vector in vacuum. In vacuum phase matching is always achieved ($\Delta k_{vac} = 0$) and the phase mismatch can be written as:

$$\Delta k = \Delta k_{atoms} + \Delta k_{plasma} + \Delta k_{geom} + \Delta k_{ADphase} \tag{1.35}$$

- **neutral atom dispersion:** The neutral gas used for HHG has typically a frequency dependent index of refraction which can be written as $n(\lambda, \rho) = 1 + \delta n_d(\lambda)\rho$, where $\delta n_d(\lambda)$ is the dispersion per unit of atomic density. For a partially ionized medium one gets $n(\lambda, \rho, I) = 1 + \delta n_d(\lambda)\rho\,(1 - \eta(I))$. The nonlinear component of the index is found negligible for experimental pressures and intensities and can be omitted and thus the resulting wave vector mismatch is given by

$$\Delta k_{atom}(\rho, I) = -q\frac{2\pi}{\lambda_L}\left[\delta n_d(\lambda_0) - \delta n_d(\lambda_q)\right]\rho(1-\eta(I)) \tag{1.36}$$

where λ_0 is the fundamental wavelength and λ_q the wavelength of the q's harmonic, η is the ionization probability and ρ the atomic density [92]. Dispersion is caused by resonances of the medium and depends on the spectral position of absorption lines or bands in the medium. In general the refractive index is larger than 1 in the visible or the near- and mid-infrared (the driving laser spectral region) and smaller than 1 (but very close to 1) in the extreme ultraviolet (where typically the harmonics are generated). Therefore one obtains $\Delta k_{atoms} < 0$.

- **plasma dispersion:** The rapid ionization induced by this strong field interaction inevitably leads to the generation of free electrons, where the majority of electrons do not recombine in the third step of HHG [93]. The generated plasma gives rise to a collective plasma resonance. The plasma dispersion can be written as

$$\Delta k_{plasma}(\rho, I) = \frac{\omega_p^2(q^2-1)}{2qc\omega_L} = \rho\eta\, r_e\lambda_L\frac{q^2-1}{q} \tag{1.37}$$

where $\omega_p = \sqrt{e^2 n_e/(\varepsilon_0 m_e)}$ is the plasma resonance frequency with n_e the free electron density and ε_0 the dielectric constant of the vacuum and r_e is the classical electron radius. All these factors are positive and therefore $\Delta k_{plasma} > 0$.

- **geometric dispersion:** This phase results from the propagation of a gaussian beam in a confined space, like the focus of a gaussian beam or a guided propagation in hollow fiber or plasma and is referred to as the Gouy phase Φ_{Gouy}. For a focused gaussian beam the Gouy wave vector is given by[1]

$$k_{Gouy}(z) = \frac{d\Phi_{Gouy}}{dz} = \frac{d}{dz}\left[-\arctan\left(\frac{\lambda_L z}{\pi\omega_0^2}\right)\right] = \frac{d}{dz}\left[-\arctan\left(\frac{2z}{b}\right)\right] \simeq -\frac{2}{b} \tag{1.38}$$

where $b = 2z_R$ is the confocal parameter with $z_R = \pi\omega_0^2/\lambda_L$ the Rayleight length of the gaussian beam focus and $\omega_0 = f\lambda_L/(\pi d)$ the beam waist with the focal length f and the beam radius d. The axis of the laser propagation is z [94–96]. Figure 1.18 C shows a geometrical interpretation of this phase shift. Assuming that the harmonics are produced with the same confocal parameter b than the driving laser we get:

$$\Delta k_{Gouy} = \frac{2(q-1)}{b} > 0 \tag{1.39}$$

The arctan dependency of the Gouy phase leads to a phase difference before and after the focus of exactly π as shown in Figure 1.18 C.

---

[1] $\frac{d}{dx}\arctan x = \frac{1}{x^2+1} \underbrace{\Rightarrow}_{x=2z/b} \frac{1}{(2z/b)^2+1}\frac{2}{b} \underbrace{\simeq}_{z\approx 0} \frac{2}{b}$, $z \approx 0$ means in the focus

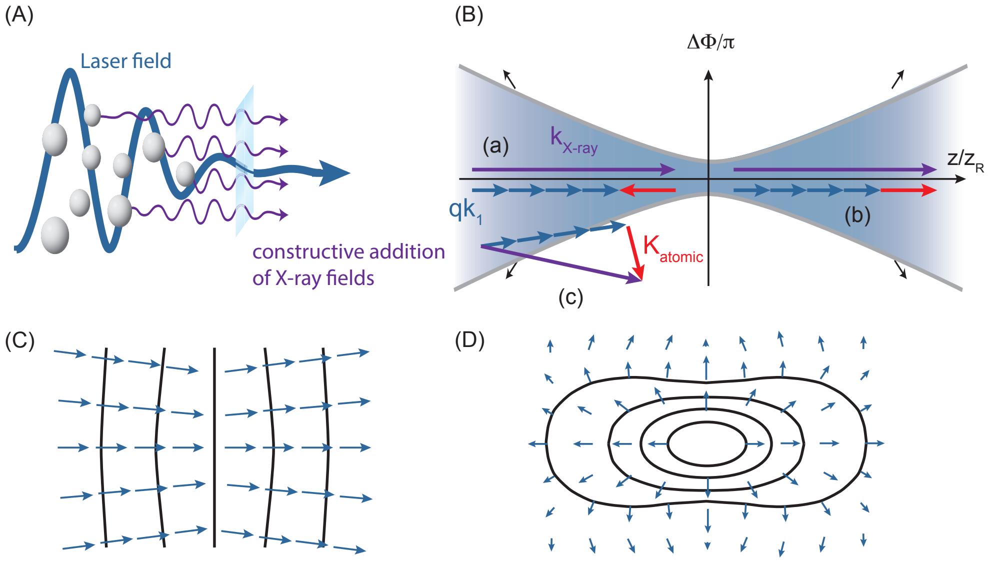

Figure 1.18: High harmonic phase matching conditions. (A) Illustration of phase matching for constructive addition of the X-ray fields. (B) Phase matching conditions for different points of the focal region: (a) On axis at focus before focus, (b) on axis after the focus, (c) off-axis before the focus. Adapted form [86, 100]. (C) Wave vector k_1 of the fundamental laser beam going through a focus including the effect of the Gouy phase shift. (D) The effective dipole phase wave vector K_{atomic} in the focal region. Adapted from [100].

- **atomic dipole dispersion:** The origin of this phase is the trajectory acquired by the electron leading to the emission of the qth harmonic in the continuum. It is proportional to the laser intensity

  $$\Delta k_{ADphase} = \alpha \nabla I_L(r,z) \tag{1.40}$$

  The laser intensity can vary spatially in both the longitudinal and radial directions. Therefore, the atom dipole phase also varies axially as well as radially. This leads to a reduced harmonic emission as well as strong spatial distortion [97–99]

The relative importance of these terms depends on the geometry of the generation of HHG. With tight focusing and long pulses, the efficiency of HHG is limited by the geometrical phase shift [100] and/or by defocusing due to the large density of free electrons [101]. Loose focusing reduces the effect of the Gouy shift and ultrashort pulses minimize the ionization effect and increase the atomic response as required to optimize HHG [47, 85, 102, 103] Guiding the fundamental beam in hollow-core fibers has been shown to have extraordinary spatial coherence properties [104] as it acts as a spatial filter. This can be used to further reduce the defocusing and to optimize the phase matching and has been studied extensively [105–109].

In our case, a Gaussian laser beam is focused into a thin gas jet (for HHG used as a probe process) or a gas cell (for HHG used as a secondary VUV light source). Therefore the intensity dependent atomic dipole phase and the Gouy phase are the dominant terms. Neglecting the other terms we can already make some qualitative conclusions [100]. The phase matching condition for Eq. (1.33) can be summarized as:

$$k_{X-ray} = \underbrace{k_{Gouy} + qk(\omega_L)}_{qk_1} + \underbrace{K_{atomic}}_{\sim \Delta k_{ADphase} = \alpha \nabla I_L} \tag{1.41}$$

where k_{X-ray} is the wave vector of the emitted harmonic, k_1 is the sum of the fundamental wave vector and the Gouy phase shift (Figure 1.18 C) and K_{atomic} an effective wave vector which represents the atomic dipole phase [100], illustrated in Figure 1.18 D. There are basically four different conditions depending on the position of the beam focus relative to the gas jet as shown in Figure 1.18 B:

- Directly in focus $z = 0$ the phase matching cannot be fulfilled.
- for points located on axis and after the focus ($z > 0$) the effective wave vector K compensates for the focusing phase mismatch and thus realizing collinear phase matching (Figure 1.18 (B-b)).
- for points located on axis but before the focus ($z < 0$) the effective wave vector K further deteriorates phase matching, so that the harmonic generation is very inefficiently (Figure 1.18 (B-a))
- non-collinear phase matching is achieved, if one considers points off axis but the efficiency is less than in the collinear regime. This is the condition of phase matching that leads to long trajectories (Figure 1.18 (B-c)).

As we have seen the relative position of the jet and the focus leads to different HHG as the intensity changes along the propagation direction z. One observes a different spatial distribution of the harmonic intensity whether the jet is placed before or after the focus [110]. The emission angle is essentially linked to the vector K_{atomic} whose norm itself is proportional to the term α (see Eq. (1.40)). Especially since the phase of long and short trajectories differ in intensity dependence, the short trajectories can only be phase-matched on axis when the laser is focused before the gas jet, while the long trajectories can be phase matched off axis before and after the gas jet [97].

As summary, phase-matching condition can be fulfilled by i.e:

- tuning the gas density (modification of gas density leads to modification of the index of reflection), using gas jets or gas cells.
- changing position of the focus with respect to the gas resulting in minimization of Gouy phase-shift influence
- in the hollow-fiber geometry modification of the fiber parameters can develop perfect phase-matching
- free electron density can be controlled by the changing intensity and time duration of laser pulse

The free electron density and therefore the plasma dispersion we neglected at the beginning is at the end, after optimizing the geometry, the ultimate limit for phase matching for multi-cycle

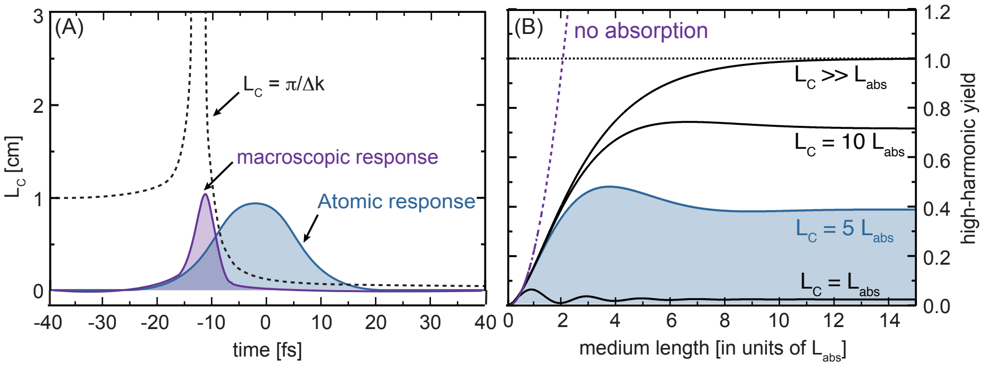

Figure 1.19: (A) Photon yield of the atomic response (dotted dashed line) for a 40 fs laser pulse with a peak intensity of 10^{14} W/cm^2 using a 4 cm long, 200 µm core diameter capillary filled with 8 mbar of Xe. Phase matching reduces the HHG to a much shorter time interval leading to a macroscopic response (purple solid line) (adapted from [92]. Note that both the atomic and macroscopic responses are shifted slightly to negative delays as at Δt = 0 ionization starts to dominate. (B) Number of on-axis emitted photos at different coherence length and absorption length ratios. Adapted from [111].

lasers. With ionization, the plasma mismatch provides an additional positive contribution that tends to overbalance the neutral gas dispersion effect when starting from the optimum pressure. But when a higher neutral gas pressure is used, transient phase matching is achieved through time dependent ionization at the time the plasma exactly compensates the initial wave vector mismatch. Calculations show that the time dependent harmonic field at the output of the medium is strongly peaked at the time for which phase matching is reached (see Figure 1.19 A). It is of crucial importance that phase matched harmonic generation could be achieved in presence of ionization allowing the use of high intensities required to increase the atomic response. Another important consequence is the shortening of the harmonic pulse duration due to the transient phase matching. This can be seen on Figure 1.19 where the macroscopic response is much shorter than the single atom response [92].

Reabsorption of the generated light

The generated EUV-light is typically in the range of 10-100 eV for a standard Ti:saphhire laser at 800 nm. The same reason that makes this wavelength region so interesting for molecular dynamics also produces a drawback in the efficiency: the valence electrons of many materials are bound with energies of $\sim$ 10 eV and above. Therefore a strong absorption efficiency characterizes this energy region, but so does as well the generating gas. In the absence of reabsorption the high harmonic flux would grow quadratically with the pressure length product $\rho_{opt} L_{med}$ where ρ_{opt} is the optimal pressure and L_{med} the length of the generating medium (see Figure 1.19 B). The critical length at which reabsorption plays a role is given by the absorption length $L_{abs} = 1/(\sigma\rho)$, where σ is the single photon ionization cross section and ρ the gas density. This length corresponds to the distance at which the harmonic intensity is attenuated by a factor $1/e$. With absorption the HHG flux will saturate. The saturation level depends on the coherence length, and becomes very low if the coherence length becomes equal to the absorption length [92, 111]. The optimizing conditions for HHG can be summarized as:

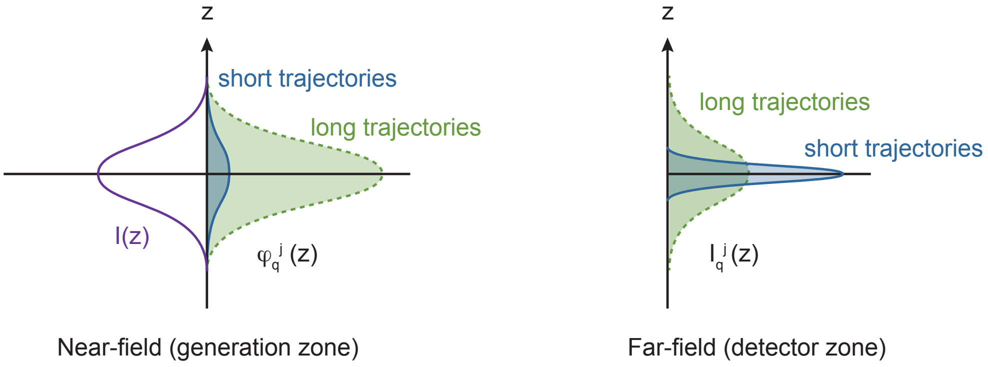

Figure 1.20: The HHG far field spatial profile is obtained by a Fourier transform of the near field profile at generation. The stronger the phase ($\propto \alpha_q^i I_L(r,z,t)$) the stronger the divergence of the emitted harmonics. Adapted from [114].

$$L_{med} > 3\, L_{abs} \tag{1.42a}$$

$$L_c > 5\, L_{abs} \tag{1.42b}$$

which is also shown in Figure 1.19 B.

Short and long trajectories in the far-field

Looking at the high harmonic spectrum in Figure 1.11 B we actually see that we are able to spatially separate the two different trajectories on the detector. These structure can be explained beginning with the linear intensity dependence of the atomic dipole phase as seen in Eq. (1.40) [112]:

$$\varphi_q = -\alpha_q^i I(t) \tag{1.43}$$

with i for short or long trajectory. Suppose that the driving laser pulse shows an gaussian temporal profile $I_L(t) = I_0 e^{-t^2/\tau^2}$. At a point in the generation volume, we can write the amplitude of the harmonic emission q as:

$$E_q = A_q(t) e^{i(\omega_q t - \varphi_q(t))} = A_q(t) e^{i(\omega_q t + \alpha_q I(t))} = A_q(t) e^{i\Phi(t)} \tag{1.44}$$

From this equation, we can go back to the expression of instantaneous harmonic frequency Ω [113]:

$$\Omega(t) = \frac{d\Phi(t)}{dt} = \omega_q + \alpha_q^i \frac{dI(t)}{dt} = \omega_q - \alpha_q^i \frac{2tI_0 e^{-t^2/\tau^2}}{\tau^2} \tag{1.45}$$

As $\alpha_q^i > 0$ this equation says that the XUV emission in the leading edge is blue-shifted and the XUV emission at the trailing edge is red-shifted. We know that $\alpha_q^{short} \approx 1$ - 5×10^{-14} cm^2/W for short trajectories and $\alpha_q^{long} \approx 20$ - 25×10^{-14} cm^2/W for long trajectories and therefore $\alpha_q^{long} > \alpha_q^{short}$ [112], which means that this frequency chirp is stronger for the long and weaker for short trajectories. This leads to a XUV pulse duration per harmonic of around 15 fs for a 30 fs fundamental pulse. The α_q^i dependency produces as well a spatial dependence illustrated in Figure 1.20. The short trajectory signal remains closer on axis whereas the long trajectory signal is very divergent.

1.3.4 HHG as extreme nonlinear optical spectroscopy

The three major properties of HHG which are: a coherent light source in the XUV, a self-probing mechanism and the generation of attosecond pulses, makes HHG as versatile tool in spectroscopy. These properties can basically be used in two ways to study molecular dynamics. The most straightforward is to consider it as a source of femtosecond pulses in the VUV which can be used to photoionize excited molecules as fragments with a direct one photon ionization, the fs-VUV Spectroscopy. Alternatively, high-harmonic generation process itself can be used as a probe of the structure of the emitting medium, the Extreme Non-Linear Optical Spectroscopy (ENLOS). In this manuscript, I will present results using both applications (see Chapter 4 and Chapter 5).

HHG form molecules: ENLOS

Non-Linear Optical Spectroscopy is commonly used to study ultrafast dynamics in matter. In general, one or several pump pulses first excite a sample then a delayed probe pulse interacts with this sample, resulting in the emission of light through a low (second or third) order nonlinear process. The emitted light carries structural information on the sample which is used to retrieve dynamical information. The principle of ENLOS is similar but the nonlinear process that is used is HHG. HHG from molecules can be understood by the same three-step model as in atomic gases. However, the orbital structure of molecules and thus the description of the mechanism of HHG in this case is significantly different. The fact that the electron leaves and comes back to the same atom or molecule (recombination step) can be seen as a self-probing technique. Due to the wave-particle dualism of matter, this electron can be seen as a matter wave with a de Broglie wavelength $\lambda_B = \hbar/p$, where $\hbar$ is the Planck constant and p the momentum of the particle. Harmonic 31[1] from a fundamental wavelength of 800 nm for instance would correspond to a de Broglie wavelength of 2 Å and therefore be able to probe the structure of atomic and molecular orbitals[2]. HHG can be seen as a spectroscopic tool to extract structural and dynamical information about the generating medium encoded in the HHG radiation. A schematic diagram of a ENLOS setup as used in Bordeaux is shown in Figure 1.21 A.

The most interesting feature of HHG in molecules is that the efficiency of particular harmonic orders depend drastically on the polarization ellipticity of the driving laser and its orientation with the respect to the molecular axis. The fact that HHG efficiency depends on the orientation of the molecule [115], suggests that the HHG process is strongly affected by the shape of the molecular orbitals and the polarization of the laser especially the laser ellipticity [116]. HHG from molecules was already reported in 1995 on N_2 [117]. But it was in 2004 when Itatani et al.

---

[1] at 800 nm (1.55 eV) and argon with an I_p = 15.76 eV this corresponds for instance to a kinetic energy of the of the electron E_{kin} = 32.24 eV. With $\lambda_B = \hbar/p = \hbar/\sqrt{2m_eE_{kin}}$ this corresponds to 2.13 Å

[2] for instance the van der Waals radius of argon is 1.88 Å

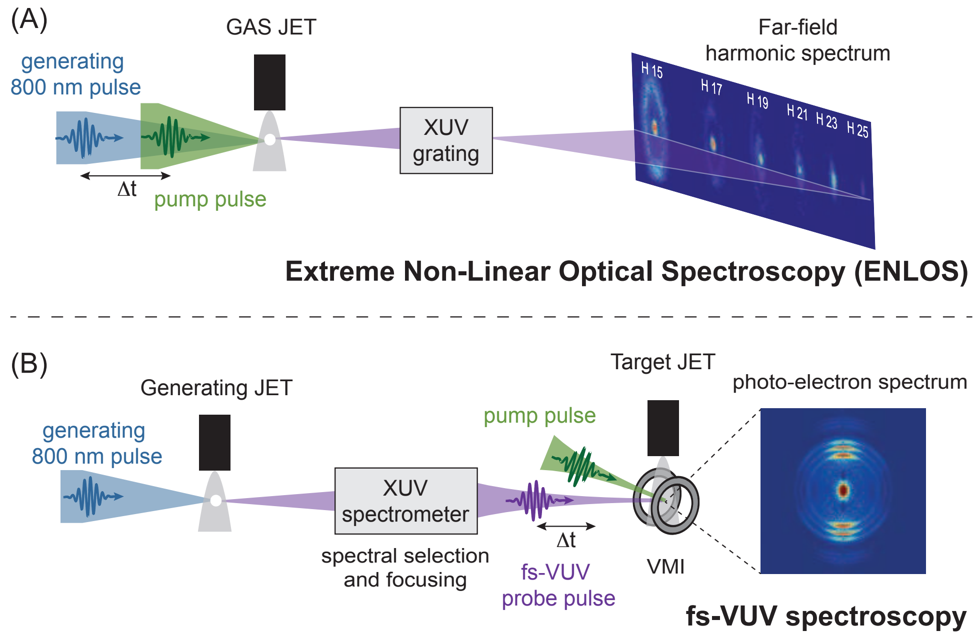

Figure 1.21: Schematic high harmonic spectroscopy setup. (A) Experimental setup for spectroscopically resolving a high harmonic spectrum in the ENLOS configuration. (B) fs-VUV spectroscopy setup using HHG as a source of XUV light for pump-probe experiments in the velocity-map imaging spectromter.

was able to make a connection between the orientation of the molecule and spectral intensities of the harmonics that the full power of HHG in molecules was revealed [118]. By performing inverse calculation Itatani and co-workers were able to obtain a tomographic reconstruction of the most-outer orbital of the N_2 molecule. This was the first time to image molecular orbitals with a potential to resolve changes in the structure on a femto or even attosecond timescale. The outer most valence orbitals are responsible for the chemical properties and therefore are the most interesting ones in terms of understanding chemical bond formation. This was a big step to making the 'molecular movie', showing the time-resolved process of the creation of a chemical bond.

It has been successfully used to topographically image molecular orbitals and electronic wave packets [72, 118–120] and combined with pump-probe techniques it can resolve molecular dynamics on an attosecond timescale [121]. The molecular structural information is not only encoded in the spectrum of the emitted light but also in its polarization state and especially the phase of the high harmonic emission. More versatile techniques has been proposed like polarization-resolved pump-probe spectroscopy [122, 123], transient grating spectroscopy [124] and high harmonic interferometry [119]. The latter two are used in this thesis and will be explained later on (see Chapter 4).

HHG as a XUV light source: fs-VUV spectroscopy

Apart from using HHG as a structural tool due to its fascinating characteristics, HHG it is also a new source of radiation giving easily access to the the electromagnetic spectrum from ultraviolet region (NUV/EUV) down to the soft X-ray regime which is normally only accessible through synchrotrons and free-electron lasers (FEL). It can be used to construct Table-top tunable EUV sources. The extreme ultraviolet (EUV/XUV) region, sometimes also called the vacuum ultraviolet (VUV) region is from special interest. In conventional spectroscopy the ionization of atoms and molecules is usually done by a multiphoton absorption process due to the lack of laser light with energies in the region of the ionization energy ($\sim$ 10 eV). This EUV-region with wavelength of 200 nm down to 10 nm, thus photon energies of 6 eV up to 100 eV is therefore suitable for the implementation of direct (one photon) ionization processes, namely an 'universal' ionization tool (Figure 1.21 B).

References

[1] Whitaker, BJ. *Imaging in Molecular Dynamics: Technology and Applications*. Cambridge: Cambridge Univ. Press, 2003 (cited p. 8, 16, 17).

[2] Houston, PL. *Snapshots of Chemistry: Product Imaging of Molecular Reactions*. Accounts of Chemical Research **28**:11 453–460 (1995) (cited p. 8).

[3] Houston, PL. *New Laser-Based and Imaging Methods for Studying the Dynamics of Molecular Collisions*. J. Phys. Chem. **100**:31 12757–12770 (1996) (cited p. 8).

[4] TAYLOR, EH and DATZ, S. *Study of Chemical Reaction Mechanisms with Molecular Beams - the Reaction of K with Hbr*. J. Chem. Phys. **23**:9 1711–1718 (1955) (cited p. 8).

[5] Lee, YT. *Molecular beam studies of elementary chemical processes.* Science **236**:4803 793–798 (1987) (cited p. 8).

[6] Herschbach, DR. *Molecular Dynamics of Elementary Chemical Reactions(Nobel Lecture)*. Angew. Chem. Int. Ed. Engl. **26**:12 1221–1243 (1987) (cited p. 8).

[7] Lee, YT. *Molecular Beam Studies of Elementary Chemical Processes(Nobel Lecture)*. Angew. Chem. Int. Ed. Engl. **26**:10 939–951 (1987) (cited p. 8).

[8] Polanyi, JC. *Some concepts in reaction dynamics.* Science **236**:4802 680–690 (1987) (cited p. 8).

[9] Polanyi, JC. *Some Concepts in Reaction Dynamics(Nobel Lecture)*. Angew. Chem. Int. Ed. Engl. **26**:10 952–971 (1987) (cited p. 8).

[10] Thiré, N, Cireasa, R, Staedter, D, Blanchet, V, and Pratt, ST. *Time-resolved predissociation of the vibrationless level of the B state of* CH_3I. Phys. Chem. Chem. Phys. **13**:41 18485–18496 (2011) (cited p. 9).

[11] Solomon, J. *Photodissociation as studied by Photolysis Mapping*. J. Chem. Phys. **47**: 889 (1967) (cited p. 9, 11).

[12] Krausz, F. *Attosecond physics*. Rev. Mod. Phys. **81**:1 163–234 (2009) (cited p. 9, 10).

[13] Krehl, P and Engemann, S. *August Toepler - The first who visualized shock waves.* Shock Waves **5**:1-2 1–18 (1995) (cited p. 9).

[14] Zewail, AH and Guo, H. *Femtosecond real-time probing of reactions. XIV. Rydberg states of methyl iodide*. Can. J. Chem. **72**:3 947–957 (1994) (cited p. 10).

[15] Zewail, AH. *Femtochemistry: Recent Progress in Studies of Dynamics and Control of Reactions and Their Transition States*. J. Phys. Chem. **100**:31 12701–12724 (1996) (cited p. 10).

[16] Zewail, AH. *Femtochemistry: Atomic-Scale Dynamics of the Chemical Bond Using Ultrafast Lasers (Nobel Lecture)*. Angew. Chem. Int. Ed. Engl. **104**:15 2586–2631 (2000) (cited p. 10).

[17] Brouard, M and Vallance, C. *Tutorials in molecular reaction dynamics*. Royal Society of Chemistry Cambridge, UK, 2010 (cited p. 10, 13).

[18] Chandler, DW and Houston, PL. *Two-dimensional imaging of state-selected photodissociation products detected by multiphoton ionization*. J. Chem. Phys. **87**: 1445 (1987) (cited p. 11).

[19] Wiley, WC and McLaren, H. *Time-of-Flight Mass Spectrometer with Improved Resolution*. Rev. Sci. Instr. **26**: 1150 (1955) (cited p. 11).

[20] Eppink, AT and Parker, DH. *Velocity map imaging of ions and electrons using electrostatic lenses: Application in photoelectron and photofragment ion imaging of molecular oxygen*. Rev. Sci. Instr. **68**:9 3477–3484 (1997) (cited p. 11, 15).

[21] Garcia, GA, Nahon, L, and Powis, I. *Two-dimensional charged particle image inversion using a polar basis function expansion*. Rev. Sci. Instr. **75**:11 4989 (2004) (cited p. 16).

[22] Heck, AJR and Chandler, DW. *Imaging Techniques for the Study of Chemical Reaction Dynamics*. Ann. Rev. Phys. Chem. **46**:1 335–372 (1995) (cited p. 16).

[23] Dasch, CJ. *One-dimensional tomography: a comparison of Abel, onion-peeling, and filtered backprojection methods*. Appl. Opt. **31**:8 1146–1152 (1992) (cited p. 16).

[24] Bontuyan, LS, Suits, AG, Houston, PL, and Whitaker, BJ. *State-resolved differential cross sections for crossed-beam argon-nitric oxide inelastic scattering by direct ion imaging*. J. Phys. Chem. **97**:24 6342–6350 (1993) (cited p. 17).

[25] Lorenz, KT, Westley, MS, and Chandler, DW. *Rotational state-to-state differential cross sections for the HCl–Ar collision system using velocity-mapped ion imaging*. Phys. Chem. Chem. Phys. **2**:4 481–494 (2000) (cited p. 17).

[26] Westley, MS, Lorenz, KT, Chandler, DW, and Houston, PL. *Differential cross sections for rotationally inelastic scattering of NO from He and* D_2. J. Chem. Phys. **114**:6 2669 (2001) (cited p. 17).

[27] Tonokura, K and Suzuki, T. *Slicing photofragment spatial distribution by laser sheet ionization*. Chem. Phys. Lett. **224**:1 1–6 (1994) (cited p. 17).

[28] Gebhardt, CR, Rakitzis, TP, Samartzis, PC, Ladopoulos, V, and Kitsopoulos, TN. *Slice imaging: A new approach to ion imaging and velocity mapping*. Rev. Sci. Instr. **72**:10 3848 (2001) (cited p. 17).

[29] Townsend, D, Minitti, MP, and Suits, AG. *Direct current slice imaging*. Rev. Sci. Instr. **74**:4 2530 (2003) (cited p. 17).

[30] Lin, JJ, Zhou, J, Shiu, W, and Liu, K. *Application of time-sliced ion velocity imaging to crossed molecular beam experiments*. Rev. Sci. Instr. **74**:4 2495–2500 (2003) (cited p. 17).

[31] Ryazanov, M and Reisler, H. *Improved sliced velocity map imaging apparatus optimized for H photofragments*. J. Chem. Phys. **138**:14 pages (2013) (cited p. 17).

[32] Zare, RN and Herschbach, DR. *Doppler line shape of atomic fluorescence excited by molecular photodissociation*. Proc. of the IEEE **51**:1 173–182 (1963) (cited p. 18).

[33] Sato, H. *Photodissociation of simple molecules in the gas phase*. Chem. Rev. **101**:9 2687–2726 (2001) (cited p. 18, 19).

[34] Reiser, G, Habenicht, W, Müller-Dethlefs, K, and Schlag, EW. *The ionization energy of nitric oxide*. Chem. Phys. Lett. **152**:2-3 119–123 (1988) (cited p. 21).

[35] Turner, DW. *Franck-Condon Factors in Ionization: Experimental Measurement Using Molecular Photoelectron Spectroscopy*. J. Chem. Phys. **45**:2 471 (1966) (cited p. 21).

[36] Even, U, Jortner, J, Noy, D, Lavie, N, and Cossart-Magos, C. *Cooling of large molecules below 1 K and He clusters formation*. J. Chem. Phys. **112**:18 8068–8071 (2000) (cited p. 22).

[37] Irimia, D, Kortekaas, R, and Janssen, MHM. *In situ characterization of a cold and short pulsed molecular beam by femtosecond ion imaging*. Phys. Chem. Chem. Phys. **11**:20 3958 (2009) (cited p. 22).

[38] Irimia, D, Dobrikov, D, Kortekaas, R, Voet, H, Ende, DA van den, Groen, WA, and Janssen, MHM. *A short pulse (7 microsec FWHM) and high repetition rate (dc-5kHz) cantilever piezovalve for pulsed atomic and molecular beams*. Rev. Sci. Instr. **80**:11 113303–113303 (2009) (cited p. 22).

[39] McPherson, A, Gibson, G, Jara, H, Johann, U, Luk, TS, MCINTYRE, IA, Boyer, K, and Rhodes, CK. *Studies of Multiphoton Production of Vacuum Ultraviolet-Radiation in the Rare-Gases*. J. Opt. Soc. Am. B **4**: 595–601 (1987) (cited p. 23).

[40] Ferray, M, L'Huillier, A, Li, XF, 'e, LAL, Mainfray, G, and Manus, C. *Multiple-harmonic conversion of 1064 nm radiation in rare gases*. J. Phys. B **21**:3 L31–L35 (1988) (cited p. 23).

[41] Franken, PA, Hill, AE, Peters, CW, and Weinreich, G. *Generation of Optical Harmonics*. Phys. Rev. Lett. **7**:4 118–119 (1961) (cited p. 23).

[42] Franken, P and Ward, J. *Optical Harmonics and Nonlinear Phenomena*. Rev. Mod. Phys. **35**:1 23–39 (1963) (cited p. 23).

[43] Armstrong, J, Bloembergen, N, Ducuing, J, and Pershan, P. *Interactions between Light Waves in a Nonlinear Dielectric*. Phys. Rev. **127**:6 1918–1939 (1962) (cited p. 23).

[44] Li, X, L'Huillier, A, Ferray, M, Lompré, L, and Mainfray, G. *Multiple-harmonic generation in rare gases at high laser intensity*. Phys. Rev. A **39**:11 5751–5761 (1989) (cited p. 23).

[45] L'Huillier, A and Balcou, P. *High-order harmonic generation in rare gases with a 1-ps 1053-nm laser*. Phys. Rev. Lett. **70**:6 774–777 (1993) (cited p. 23).

[46] Macklin, JJ, Kmetec, JD, and Gordon III, CL. *High-order harmonic generation using intense femtosecond pulses*. Phys. Rev. Lett. **70**:6 766–769 (1993) (cited p. 23).

[47] Chang, Z, Rundquist, A, Wang, H, Murnane, M, and Kapteyn, H. *Generation of Coherent Soft X Rays at 2.7 nm Using High Harmonics*. Phys. Rev. Lett. **79**:16 2967–2970 (1997) (cited p. 23, 36).

[48] Vozzi, C, Calegari, F, Frassetto, F, Poletto, L, Sansone, G, VILLORESI, P, NISOLI, M, De Silvestri, S, and Stagira, S. *Coherent continuum generation above 100 eV driven by an ir parametric source in a two-color scheme*. Phys. Rev. A **79**:3 033842 (2009) (cited p. 23).

[49] Seres, J, Seres, E, Verhoef, AJ, Tempea, G, Streli, C, Wobrauschek, P, Yakovlev, V, Scrinzi, A, Spielmann, C, and Krausz, F. *Laser technology: Source of coherent kiloelectronvolt X-rays*. Nature **433**:7026 596–596 (2005) (cited p. 23).

[50] Popmintchev, T, Chen, MC, Popmintchev, D, Arpin, P, Brown, S, Alisauskas, S, Andriukaitis, G, Balciunas, T, Mucke, OD, Pugzlys, A, Baltuska, A, Shim, B, Schrauth, SE, Gaeta, A, Hernandez-Garcia, C, Plaja, L, Becker, A, Jaron-Becker, A, Murnane, MM, and Kapteyn, HC. *Bright Coherent Ultrahigh Harmonics in the keV X-ray Regime from Mid-Infrared Femtosecond Lasers*. Science **336**:6086 1287–1291 (2012) (cited p. 23, 31).

[51] Sekikawa, T, Ohno, T, Yamazaki, T, Nabekawa, Y, and Watanabe, S. *Pulse Compression of a High-Order Harmonic by Compensating the Atomic Dipole Phase*. Phys. Rev. Lett. **83**:13 2564–2567 (1999) (cited p. 23).

[52] Toma, ES, Muller, HG, Paul, PM, Breger, P, Cheret, M, Agostini, P, Le Blanc, C, Mullot, G, and Cheriaux, G. *Ponderomotive streaking of the ionization potential as a method for measuring pulse durations in the XUV domain with fs resolution*. Phys. Rev. A **62**:6 061801 (2000) (cited p. 23).

[53] Drescher, M. *X-ray Pulses Approaching the Attosecond Frontier*. Science **291**:5510 1923–1927 (2001) (cited p. 23).

[54] Papadogiannis, N, Witzel, B, Kalpouzos, C, and Charalambidis, D. *Observation of Attosecond Light Localization in Higher Order Harmonic Generation*. Phys. Rev. Lett. **83**:21 4289–4292 (1999) (cited p. 23).

[55] Paul, PM, Toma, ES, Breger, P, Mullot, G, Balcou, P, Muller, HG, and Agostini, P. *Observation of a Train of Attosecond Pulses from High Harmonic Generation*. Science **292**:5522 1689–1692 (2001) (cited p. 23).

[56] Ko, DH, Kim, KT, Park, J, Lee, J, and Nam, CH. *Attosecond chirp compensation over brandband hight-order harmonics to generate near transform-linited 63 as pulses*. New Jour. Phys. **12**:6 063008 (2010) (cited p. 23).

[57] Goulielmakis, E, Schultze, M, Hofstetter, M, Yakovlev, VS, Gagnon, J, Uiberacker, M, Aquila, AL, Gullikson, EM, Attwood, DT, Kienberger, R, Krausz, F, and Kleineberg, U. *Single-Cycle Nonlinear Optics*. Science **320**:5883 1614–1617 (2008) (cited p. 23).

[58] Feng, X, Gilbertson, S, Mashiko, H, Wang, H, Khan, SD, Chini, M, Wu, Y, Zhao, K, and Chang, Z. *Generation of Isolated Attosecond Pulses with 20 to 28 Femtosecond Lasers*. Phys. Rev. Lett. **103**:18 183901 (2009) (cited p. 23).

[59] Ferrari, F, Calegari, F, Lucchini, M, Vozzi, C, Stagira, S, Sansone, G, and NISOLI, M. *High-energy isolated attosecond pulses generated by above-saturation few-cycle fields*. Nature Photonics **4**:12 875–879 (2010) (cited p. 23).

[60] Vincenti, H and Quere, F. *Attosecond Lighthouses: How To Use Spatiotemporally Coupled Light Fields To Generate Isolated Attosecond Pulses*. Phys. Rev. Lett. **108**:11 113904 (2012) (cited p. 23).

[61] Krause, J, Schafer, K, and Kulander, K. *High-order harmonic generation from atoms and ions in the high intensity regime*. Phys. Rev. Lett. **68**:24 3535–3538 (1992) (cited p. 23).

[62] Kulander, KC, Schafer, KJ, and Krause, JL. *Dynamics of Short-Pulse Excitation, Ionization and Harmonic Conversion*. Super-Intense Laser-Atom Physics **316**:Chapter 10 pages (1993) (cited p. 23).

[63] Corkum, PB. *Plasma Perspective on Strong-Field Multiphoton Ionization*. Phys. Rev. Lett. **71**:13 1994–1997 (1993) (cited p. 23).

[64] Keldysh, LV. *Ionization in the field of a strong electromagnetic wave*. Sov. Phys. JETP **20**:5 1307–1314 (1965) (cited p. 25, 33).

[65] Ivanov, MY, Spanner, M, and Smirnova, O. *Anatomy of strong field ionization*. J. Mod. Opt. **52**:2-3 165–184 (2005) (cited p. 26).

[66] Ammosov, MV, Delone, NB, and Krainov, VP. *Tunnel ionization of complex atoms and atomic ions in electromagnetic field*. Sov. Phys. JETP **64**: 1191 (1986) (cited p. 26).

[67] Mainfray, G and Manus, G. *Multiphoton ionization of atoms*. Rep. Prog. Phys. **54**:10 1333–1372 (1999) (cited p. 27).

[68] Augst, S, Strickland, D, Meyerhofer, D, Chin, S, and Eberly, J. *Tunneling ionization of noble gases in a high-intensity laser field*. Phys. Rev. Lett. **63**:20 2212–2215 (1989) (cited p. 27).

[69] Joachain, CJ and Kylstra, NJ. *Relativistic effects in laser-atom interactions*. Laser Phys. **11**:2 212–215 (2001) (cited p. 27).

[70] Shchatsinin, I. *Free clusters and free molecules in strong, shaped laser fields*. PhD thesis. Freie Universität Berlin, 2009 (cited p. 27).

[71] Kanai, T, Takahashi, EJ, Nabekawa, Y, and Midorikawa, K. *Destructive Interference during High Harmonic Generation in Mixed Gases*. Phys. Rev. Lett. **98**:15 153904 (2007) (cited p. 30).

[72] Smirnova, O, Patchkovskii, S, Mairesse, Y, Dudovich, N, and Ivanov, MY. *Strong-field control and spectroscopy of attosecond electron-hole dynamics in molecules*. Proc. Natl. Acad. Sci. **106**:39 16556–16561 (2009) (cited p. 30, 41).

[73] Gaarde, M and Schafer, K. *Quantum path distributions for high-order harmonics in rare gas atoms*. Phys. Rev. A **65**:3 031406 (2002) (cited p. 30).

[74] Fittinghoff, D, Bolton, P, Chang, B, and Kulander, K. *Observation of nonsequential double ionization of helium with optical tunneling*. Phys. Rev. Lett. **69**:18 2642–2645 (1992) (cited p. 30).

[75] Walker, B, Sheehy, B, DiMauro, LF, Agostini, P, Schafer, KJ, and Kulander, KC. *Precision measurement of strong field double ionization of helium*. Phys. Rev. Lett. **73**:9 1227–1230 (1994) (cited p. 30).

[76] Weber, T, Giessen, H, Weckenbrock, M, Urbasch, G, Staudte, A, Spielberger, L, Jagutzki, O, Mergel, V, Vollmer, M, and Dörner, R. *Correlated electron emission in multiphoton double ionization*. Nature **405**:6787 658–661 (2000) (cited p. 30).

[77] Weber, T, Weckenbrock, M, Staudte, A, Spielberger, L, Jagutzki, O, Mergel, V, Afaneh, F, Urbasch, G, Vollmer, M, and Giessen, H. *Recoil-ion momentum distributions for single and double ionization of helium in strong laser fields*. Phys. Rev. Lett. **84**:3 443–446 (2000) (cited p. 30).

[78] Agostini, P, Fabre, F, Mainfray, G, Petite, G, and Rahman, NK. *Free-Free Transitions Following Six-Photon Ionization of Xenon Atoms*. Phys. Rev. Lett. **42**:17 1127–1130 (1979) (cited p. 30).

[79] Paulus, G, Nicklich, W, Xu, H, Lambropoulos, P, and Walther, H. *Plateau in above threshold ionization spectra*. Phys. Rev. Lett. **72**:18 2851–2854 (1994) (cited p. 30).

[80] Milosevic, DB, Paulus, GG, and Becker, W. *High-order above-threshold ionization with few-cycle pulse: a meter of the absolute phase*. Opt. Express **11**:12 1418–1429 (2003) (cited p. 30).

[81] Popmintchev, T, Chen, MC, Cohen, O, Grisham, ME, Rocca, JJ, Murnane, MM, and Kapteyn, HC. *Extended phase matching of high harmonics driven by mid-infrared light*. Opt. Lett. **33**:18 2128–2130 (2008) (cited p. 31).

[82] Popmintchev, T, Chen, MC, Bahabad, A, Gerrity, M, Sidorenko, P, Cohen, O, Christov, IP, Murnanea, MM, and Kapteyn, HC. *Phase matching of high harmonic generation in the soft and hard X-ray regions of the spectrum*. Proc. Natl. Acad. Sci. **106**:26 10516–10521 (2009) (cited p. 31).

[83] Takahashi, EJ, Kanai, T, Ishikawa, KL, Nabekawa, Y, and Midorikawa, K. *Coherent Water Window X Ray by Phase-Matched High-Order Harmonic Generation in Neutral Media*. Phys. Rev. Lett. **101**:25 253901 (2008) (cited p. 31).

[84] Chen, MC, Arpin, P, Popmintchev, T, Gerrity, M, Zhang, B, Seaberg, M, Popmintchev, D, Murnane, MM, and Kapteyn, HC. *Bright, Coherent, Ultrafast Soft X-Ray Harmonics Spanning the Water Window from a Tabletop Light Source*. Phys. Rev. Lett. **105**:17 173901 (2010) (cited p. 31).

[85] Spielmann, C, Burnett, N, Sartania, S, Koppitsch, R, Schnurer, M, Kan, C, Lenzner, M, Wobrauschek, P, and Krausz, F. *Generation of Coherent X-rays in the Water Window Using 5-Femtosecond Laser Pulses*. Science **278**:5338 661–664 (1997) (cited p. 31, 36).

[86] Popmintchev, T, Chen, MC, Arpin, P, Murnane, MM, and Kapteyn, HC. *The attosecond nonlinear optics of bright coherent X-ray generation*. Nature Photonics **4**:12 822–832 (2010) (cited p. 31, 36).

[87] Antoine, P, Carré, B, L'Huillier, A, and Lewenstein, M. *Polarization of high-order harmonics*. Phys. Rev. A **55**:2 1314 (1997) (cited p. 31).

[88] Wong, MCH, Brichta, JP, and Bhardwaj, VR. *Signatures of symmetry and electronic structure in high-order harmonic generation in polyatomic molecules*. Phys. Rev. A **81**:6 061402 (2010) (cited p. 33).

[89] Ruf, H, Handschin, C, Cireasa, R, Thiré, N, Ferré, A, Petit, S, Descamps, D, Mevel, E, Constant, E, Blanchet, V, Fabre, B, and Mairesse, Y. *Inhomogeneous High Harmonic Generation in Krypton Clusters*. Phys. Rev. Lett. **110**:8 083902 (2013) (cited p. 33).

[90] Shafir, D, Soifer, H, Bruner, BD, Dagan, M, Mairesse, Y, Patchkovskii, S, Ivanov, MY, Smirnova, O, and Dudovich, N. *Resolving the time when an electron exits a tunnelling barrier*. Nature **485**:7398 343–346 (2012) (cited p. 33).

[91] Lewenstein, M, Balcou, P, Ivanov, MY, L'Huillier, A, and Corkum, PB. *Theory of High-Harmonic Generation by Low-Frequency Laser Fields*. Phys. Rev. A **49**:3 2117–2132 (1994) (cited p. 33).

[92] Mével, E, Constant, ', Garzella, D, Breger, P, Dorrer, C, Le Blanc, C, Salin, F, and Agostini, P. *Optimizing high order harmonic generation in absorbing gases*. AIP Conference Proceedings **525**:1 373–384 (2000) (cited p. 35, 38).

[93] Brabec, T and Krausz, F. *Intense few-cycle laser fields: Frontiers of nonlinear optics*. Rev. Mod. Phys. **72**:2 545–591 (2000) (cited p. 35).

[94] Pfeifer, T, Spielmann, C, and Gerber, G. *Femtosecond x-ray science*. Rep. Prog. Phys. **69**:2 443–505 (2006) (cited p. 35).

[95] Rubinowicz, A. *On the Anomalous Propagation of Phase in the Focus*. Phys. Rev. **54**:11 931–936 (1938) (cited p. 35).

[96] Paschotta, R. *Beam quality deterioration of lasers caused by intracavity beam distortions*. Opt. Express **14**:13 6069–6074 (2006) (cited p. 35).

[97] Salières, P, L'Huillier, A, and Lewenstein, M. *Coherence Control of High-Order Harmonics*. Phys. Rev. Lett. **74**:19 3776–3779 (1995) (cited p. 36, 37).

[98] Peatross, J, Fedorov, MV, and Kulander, KC. *Intensity-dependent phase-matching effects in harmonic generation*. J. Opt. Soc. Am. B **12**:5 863–870 (1995) (cited p. 36).

[99] Peatross, J and Meyerhofer, D. *Intensity-dependent atomic-phase effects in high-order harmonic generation*. Phys. Rev. A **52**:5 3976–3987 (1995) (cited p. 36).

[100] Balcou, P, Sali eres, P, L'Huillier, A, and Lewenstein, M. *Generalized phase-matching conditions for high harmonics: The role of field-gradient forces*. Phys. Rev. A **55**:4 3204–3210 (1997) (cited p. 36, 37).

[101] Altucci, C, Starczewski, T, Mevel, E, Wahlstrom, CG, Carre, B, and L'Huillier, A. *Influence of atomic density in high-order harmonic generation*. J. Opt. Soc. Am. B **13**:1 148–156 (1996) (cited p. 36).

[102] Schafer, K and Kulander, K. *High harmonic generation from ultrafast pump lasers*. Phys. Rev. Lett. **78**:4 638–641 (1997) (cited p. 36).

[103] Kan, C, Burnett, N, Capjack, C, and Rankin, R. *Coherent XUV Generation from Gases Ionized by Several Cycle Optical Pulses*. Phys. Rev. Lett. **79**:16 2971–2974 (1997) (cited p. 36).

[104] Bartels, RA, Paul, A, Green, H, Kapteyn, HC, Murnane, MM, Backus, S, Christov, IP, Liu, YW, Attwood, D, and Jacobsen, C. *Generation of spatially coherent light at extreme ultraviolet wavelengths*. Science **297**:5580 376–378 (2002) (cited p. 36).

[105] NISOLI, M, De Silvestri, S, and Svelto, O. *Generation of high energy 10 fs pulses by a new pulse compression technique*. Appl. Phys. Lett. **68**:20 2793–2795 (1996) (cited p. 36).

[106] Rundquist, A. *Phase-Matched Generation of Coherent Soft X-rays*. Science **280**:5368 1412–1415 (1998) (cited p. 36).

[107] Durfee, CG, Rundquist, AR, Backus, S, Herne, C, Murnane, MM, and Kapteyn, HC. *Phase matching of high-order harmonics in hollow waveguides*. Phys. Rev. Lett. **83**: 2187–2190 () (cited p. 36).

[108] Schnuerrer, M, Cheng, Z, Sartania, S, Hentschel, M, Tempea, G, Brabec, T, and Krausz, F. *Guiding and high-harmonic generation of sub-10-fs pulses in hollow-core fibers at* $10^{1}5$ *W/cm*^{2}. Appl. Phys. B **67**:2 263–266 (1998) (cited p. 36).

[109] Durfee III, CG, Rundquist, A, Kapteyn, HC, and Murnane, MM. *Guided wave methods and apparatus for nonlinear frequency generation*. Patent **6151155**: (2000) (cited p. 36).

[110] Lewenstein, M, Salieres, P, and L'Huillier, A. *Phase of the atomic polarization in high-order harmonic generation*. Phys. Rev. A **52**:6 4747–4754 (1995) (cited p. 37).

[111] Constant, E, Garzella, D, Breger, P, M 'evel, E, Dorrer, C, Le Blanc, C, Salin, F, and Agostini, P. *Optimizing High Harmonic Generation in Absorbing Gases: Model and Experiment*. Phys. Rev. Lett. **82**:8 1668–1671 (1999) (cited p. 38).

[112] Varju, K, Mairesse, Y, 'e, BC, Gaarde, MB, Johnsson, P, Kazamias, S, Lopez-Martens, R, Mauritsson, J, Schafer, KJ, Balcou, P, L'Huillier, A, and eres, PS. *Frequency chirp of harmonic and attosecond pulses*. J. Mod. Opt. **52**:2-3 379–394 (2005) (cited p. 39).

[113] Gaarde, MB, Salin, F, Constant, E, Balcou, P, Schafer, KJ, Kulander, KC, and L'Huillier, A. *Spatiotemporal separation of high harmonic radiation into two quantum path components*. Phys. Rev. A **59**:2 1367–1373 (1999) (cited p. 39).

[114] Higuet, J. *Etudes structurelles et dynamiques de systèmes atomiques ou moléculaires par génération d'harmoniques d'ordre élevé*. PhD thesis. Université de Bordeaux, 2010 (cited p. 39).

[115] Kanai, T, Minemoto, S, and Sakai, H. *Ellipticity Dependence of High-Order Harmonic Generation from Aligned Molecules*. Phys. Rev. Lett. **98**:5 053002 (2007) (cited p. 40).

[116] Cireasa, R, Bhardwaj, R, Blanchet, V, Boguslavsky, A, Descamps, D, Fabre, B, Legare, F, Mairesse, Y, Patchkovskii, S, Pons, B, Ruf, H, Schmidt, B, Surarez, J, Thire, N, and Wong, M. *High-harmonic generation sensitive to chirality*. in preparation for Nature Physics (2013) (cited p. 40).

[117] Sakai, H and Miyazaki, K. *High-Order Harmonic-Generation in Nitrogen Molecules with Subpicosecond Visible Dye-Laser Pulses*. Appl. Phys. B **61**:5 493–498 (1995) (cited p. 40).

[118] Itatani, J, Levesque, J, Zeidler, D, Niikura, H, Pepin, H, Kieffer, JC, Corkum, PB, and Villeneuve, DM. *Tomographic imaging of molecular orbitals*. Nature **432**:7019 867–871 (2004) (cited p. 41).

[119] Smirnova, O, Mairesse, Y, Patchkovskii, S, Dudovich, N, Villeneuve, D, Corkum, P, and Ivanov, MY. *High harmonic interferometry of multi-electron dynamics in molecules*. Nature **460**:7258 972–977 (2009) (cited p. 41).

[120] Haessler, S, Caillat, J, Boutu, W, Giovanetti-Teixeira, C, Ruchon, T, Auguste, T, Diveki, Z, Breger, P, Maquet, A, 'e, BC, ieb, RT, and eres, PS. *Attosecond imaging of molecular electronic wavepackets*. Nature Phys. **6**: 200–206 (2010) (cited p. 41).

[121] Baker, S. *Probing Proton Dynamics in Molecules on an Attosecond Time Scale*. Science **312**:5772 424–427 (2006) (cited p. 41).

[122] Levesque, J, Mairesse, Y, Dudovich, N, Pépin, H, Kieffer, JC, Corkum, P, and Villeneuve, D. *Polarization State of High-Order Harmonic Emission from Aligned Molecules*. Phys. Rev. Lett. **99**:24 243001 (2007) (cited p. 41).

[123] Mairesse, Y, Haessler, S, Fabre, B, Higuet, J, Boutu, W, Breger, P, Constant, E, Descamps, D, Mevel, E, and Petit, S. *Polarization-resolved pump–probe spectroscopy with high harmonics*. New Jour. Phys. **10**:2 025028 (2008) (cited p. 41).

[124] Mairesse, Y, Zeidler, D, Dudovich, N, Spanner, M, Levesque, J, Villeneuve, DM, Corkum, and B, P. *High-Order Harmonic Transient Grating Spectroscopy in a Molecular Jet*. Phys. Rev. Lett. **100**:14 143903 (2008) (cited p. 41).

2

Photodissociation of chlorine azide (ClN_3)

Contents

Abstract

This chapter reports the first time-resolved study of photochemistry of ClN_3 by femtosecond velocity-map imaging (fs-VMI). Goal of the experiment is to elucidate the ultrafast dynamics that lead to a cyclic-N_3 production. The photodissociation of ClN_3 is studied at two different energies, namely around 4.63 eV (268 nm) where only linear N_3 is produced and around 6.17 eV (201 nm) where mainly cyclic-N_3 is produced. After an introduction to molecule ClN_3 and its spectroscopy and previous experiments in Section 2.1.1, the experimental setup with the alignment procedure and typical image analysis is explained in Section 2.2. Section 2.3 shows the experimental results from the time-of-flight data followed by the femtosecond time-resolved translational energy and angular distributions analysis of Cl and N_3 in Section 2.4. Section 2.5 discusses a phenomena observed on the chlorine fragments and Section 2.6 gives a short summary of the other fragments from the photodissociation of ClN_3 before the chapter is closed by a summary and conclusion in Section 2.7.

Keywords: velocity-map imaging, photodissociation, chlorine azide, linear N_3, cyclic N_3

2.1 Introduction

2.1.1 The route to a unique all nitrogen ring - cyclic N_3

The first synthesis of an azide compound was reported in 1864 [1]. Since then a variety of these compounds like X-N_3 where X can stand for hydrogen and all halogens (I, Cl, Br or F) have been made and studied and Azide UV photochemistry has become a popular topic of investigation. ClN_3 was first synthesized in 1908 [2] and will be the subject of this chapter. An overview of Azide (X-N_3) UV photochemistry can be found in the review articles by P. Samartzis and A. M. Wodtke [3] and Inis C. Tornieporth-Oetting [4]. The interest in the photochemistry of chlorine azide (ClN_3) comes from the fact that the primary photo-product NCl ($a^1\Delta$) has been successfully used to achieve the population inversion in Iodine lasers [5]. Therefore, the photolysis of ClN_3 by near-UV radiation has been studied extensively with the main focus on the NCl product [6–14]. But the primary photodissociation of ClN_3 not only produces NCl, it proceeds through two dissociation pathways: molecular elimination producing NCl + N_2 and through radical bond rupture leading to Cl + N_3. The latter pathway has been found to be much more important than previously suspected [15, 16]. Furthermore we now have compelling theoretical and experimental evidence that the N_3 fragment can appear in two forms: in the well known linear N_3 and a theoretically predicted cyclic-N_3 configuration, an unique all nitrogen ring [17]. The production of this new species, cyclic-N_3, is of great interest not only because of its simplicity in structure as the smallest molecular all-nitrogen ring but also because it could be used as a reactant in building larger polyatomic N_x compounds which could be used as propellants and energy storage systems [3, 18, 19]. Most of the interpretation in photodissociation experiments is based on translational energy release data (see Section 1.2) where one uses the maximum translational energy e.g from $ClN_3 + \hbar\nu \rightarrow Cl + N_3$ to identify the products. This is only possible if one knows the thermochemical data of the parent molecule as it can be achieved e.g in the iPEPICO [20] experiment, also used during my Ph.D. on TTF [21] and shown in Chapter 3. The dissociation energy D_0 is particularly important. Surprisingly the most accurate value of D_0(Cl-N_3) became available only recently [22]. Using high-resolution synchrotron radiation and a quadruple mass spectrometer Quinto-Hernandez et al. determined the bond energy to be 1.86 ± 0.05 eV for the linear-N_3 channel. This compared well with *ab initio* electronic structure calculations, which yield a value of $D_0(\text{Cl-N}_3) = 1.87$ eV.

The absorption spectrum of ClN_3 has four absorption bands in the ultraviolet centered at 350, 250, 210 and $<$ 170.nm [7, 23] Only three of these absorption bands are shown in Figure 2.1. The ClN_3 molecular symmetry belongs to the C_s point group. The character table of the C_s point group is shown in Appendix E. The longest wavelength (S_1–S_0) absorption at ~350 nm is assigned as the $1A'' \leftarrow 1A'$ and the (S_2–S_0) absorption peaking near 250 nm as $2A' \leftarrow 1A'$ transition. The absorption near 210 nm may be influenced by both (S_3–S_0) $2A'' \leftarrow 1A'$ as well as (S_4–S_0) $3A' \leftarrow 1A''$ absorptions. The fourth and strongest absorption extends beyond 170 nm and has not been assigned. In Figure 2.1 the blue and grey area separate the wavelength region for the production of linear and cyclic-N_3, which will be discussed later. The darker grey and blue lines indicate the wavelength used in the present work as pump pulses.

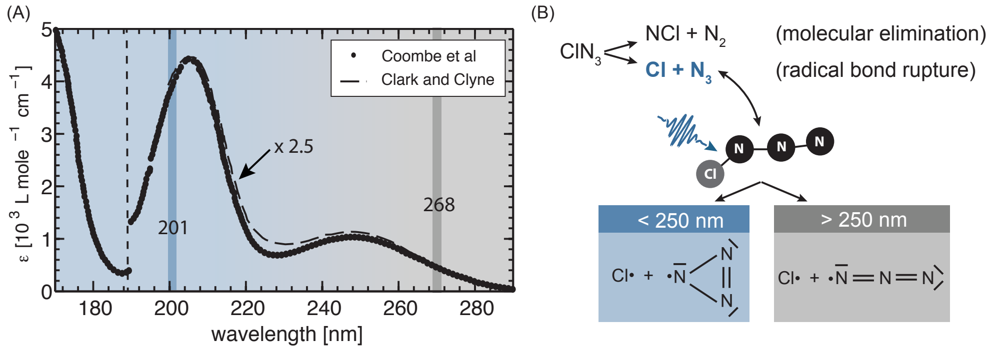

Figure 2.1: (A) The UV absorption spectrum of ClN_3 from 170 to 300 nm adapted from [7]. Three bands are observed centered at 250, 210 and 170 nm. The data in the region from 190 to 290 nm is multiplied by 2.5. The absorption spectrum is divided into two parts blue and grey area, showing the wavelength regions in which mainly cyclic (blue) or linear N_3 (grey) is produced. The darker grey and blue lines show the wavelengths used in this present work. (B) Illustration of the dissociation pathways after photolysis with different wavelengths.

As mentioned before, the primary dissociation channel of ClN_3 proceeds through two pathways, molecular elimination and radical bond rupture. The first one, molecular elimination, leading to NCl and N_2 fragments can produce these fragments through 4 different channels:

$$ClN_3(\tilde{X}^1A') + \hbar\nu \rightarrow NCl(a^1\Delta) + N_2(X^1\Sigma_g^+) \tag{2.1a}$$

$$ClN_3(\tilde{X}^1A') + \hbar\nu \rightarrow NCl(X^3\Sigma) + N_2(X^1\Sigma_g^+) \tag{2.1b}$$

$$ClN_3(\tilde{X}^1A') + \hbar\nu \rightarrow NCl(X^3\Sigma) + N_2(A^3\Sigma_u^+) \tag{2.1c}$$

$$ClN_3(\tilde{X}^1A') + \hbar\nu \rightarrow NCl(b^1\Sigma^+) + N_2(X^1\Sigma_g^+) \tag{2.1d}$$

From all four possible channels Eq. (2.1a) is the dominant one with Eq. (2.1b) being its spin forbidden analogue. The production of $N_2(A^3\Sigma_u^+)$ from the spin-allowed channel Eq. (2.1c) as well as $NCl(b^1\Sigma^+)$ from the second spin-allowed channel Eq. (2.1d) contribute only around 1% to the yield [7, 23]. Komissarov et al. examined the prompt and delayed production of $NCl(A^3\Sigma)$ using absorption spectroscopy after ClN_3 photolysis at λ = 248 nm [14]. They estimated that 80% of the primary NCl was formed in the $a^1\Delta$ state and, apart from the 1% of $NCl(b^1\Sigma^+)$, the remaining NCl was thought to be produced in the electronic ground state $(X^3\Sigma)$.

Recently, the ClN_3 photochemistry has received even more attention due to its second pathway, the radical bond rupture which leads to the products Cl and N_3. Although the production of cyclic-N_3 has been proposed since 1890 by T. Curtis [24], spectroscopic studies revealed mostly its linear geometry [25–28]. It was only in 2003 when Hansen and Wodtke reported a velocity-map ion imaging experiment of ClN_3 photodissociation at 235 nm under collision-free conditions that an alternative experimental outcome would be observed [17]. They showed that the translational energy distribution of the Cl fragment was bimodal (as shown in Figure 2.2 B). The lower transitional kinetic energy component and therefore higher energetic component found on Cl was first only called *high energy form* of N_3 (HEF-N_3). But this ex-

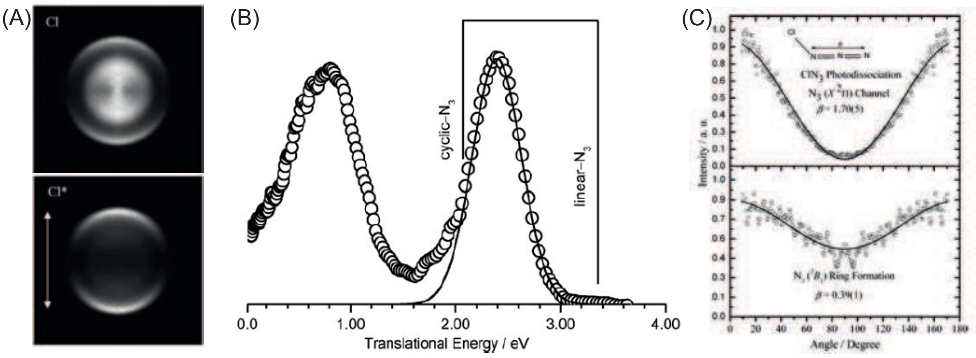

Figure 2.2: Velocity-map imaging evidence for cyclic-N$_3$ formation. (A) Images of Cl and Cl* photofragments from ClN$_3$ dissociation at 235 nm for which both (linear and cyclic) structures are expected to be produced. The arrow indicates the polarization direction of the laser. (B) Translational energy distribution of the Cl + N$_3$ pair extracted from the Cl image on the left. The vertical lines show the dissociation limit for cyclic- and linear-N$_3$. (C) Cl fragment angular distribution obtained from the images in A. Upper panel shows the angular distribution of Cl from the fast channel (linear N$_3$) and the lower panel from the HEF-N$_3$ channel. The lines are the fits yielding β_2 = 1.70(5), and β_2 = 0.39(1) for the fast and slow components, respectively. Adapted from [17].

periment also allowed the determination of the dissociation limit for HEF-N$_3$ + Cl and showed that it lies typically 1.34 eV higher in energy compared to the dissociation limit for N$_3$ in its linear configuration. This value was in good agreement with theoretical work performed the previous year regarding the prediction of the formation of an cyclic N$_3$ isomer [19]. Up to this point the cyclic form of N$_3$ existed only as a theoretical prediction mostly based on the Lewis dot structure [29] which satisfies the linear and cyclic form of N$_3$[1]. But in light of the good agreement between the experimental observations from Hansen and Wodtke with the theory, there was now substantial evidence that this radical channel leads to N$_3$ fragments that can appear not only in the well known linear geometry but also as a higher energetic cyclic isomer, an unique all-nitrogen ring. Therefore we can write that the radical dissociation pathway proceeds through these 2 channels:

$$\mathrm{ClN_3}(\tilde{X}^1A') + \hbar\nu \rightarrow \mathrm{Cl}(^2P_x) + \mathrm{N_3}(\tilde{X}^2\Pi) \qquad D_0^{lin} = 1.86\,\mathrm{eV}\ [22] \tag{2.2a}$$

$$\mathrm{ClN_3}(\tilde{X}^1A') + \hbar\nu \rightarrow \mathrm{Cl}(^2P_x) + \mathrm{N_3}(\mathsf{cyclic}) \qquad D_0^{cyc} = 3.16\,\mathrm{eV}\ [19] \tag{2.2b}$$

where x can be 3/2 and 1/2. This experimental observation triggered a variety of new experiments. So far experiments have been done with various dissociation wavelengths including 157.4, 193, 235, 248, 266 and 280 nm [15–17, 30–32]. Most of these experiments only detect the Cl fragment via ns-resonance enhanced multiphoton ionization (REMPI)[2], and they show evidence for this cyclic-N$_3$ fragment production at wavelength shorter then 250 nm (4.96 eV), with its yield increasing as wavelength is decreased (see Figure 2.3 and also blue and grey regions in Figure 2.1).

---

[1] The Lewis dot structures for N$_3$ are shown in Figure 2.1

[2] REMPI is a technique to enhance the ionization using when multiple photons are needed for ionization by going through a resonant state, often Rydberg states.

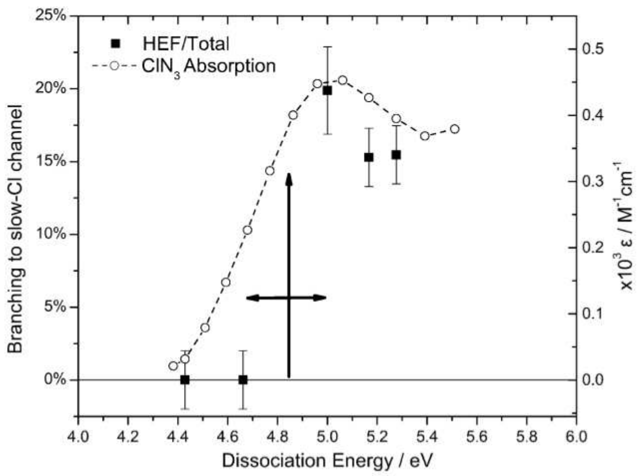

Figure 2.3: Energy threshold of slow Cl production. Filled squares with error bars represent the percentage of total Cl that is slow Cl. The best estimated value for the threshold is 4.83 ± 0.17 eV, indicated by an upward pointing arrow. Plotted as a line is the absorption spectrum of ClN_3 in this energy region. Adopted from [31].

Near-threshold photoionization with synchrotron radiation of N_3 photofragments produced by laser photodissociation of ClN_3 at 248 nm show two distinct ionization thresholds [33]. From this experiment a value of the ionization potential (I_p) of HEF-N_3 = 10.7 ± 0.2 eV was determined. This agrees well with the theoretically predicted value for cyclic N_3 of 10.58 eV [34]. Ionization energies from all fragments of ClN_3 are shown in Table 2.1. All this suggests that HEF-N_3 is indeed the cyclic N_3. But up to now there is no experimental proof of this cyclic structure except the agreement of D_0 and the I_p. This is mainly because all experiments have been done in the ns-time regime, namely on a timescale longer than the rotation of the parent and of the fragments (e.g N_3(B) ν_{rot} = 0.43 cm^{-1} ∼ 78 ps [35, 36], ClN_3 (A) T_{rot} = 13.4 ps[1]) which are in the ps time regime. The main interest of the present experiment is to build the energy and momentum balance on a timescale shorter than the rotation period. In contrast there are quite a few theoretical calculations relating to the parent molecule ClN_3 as well as the N_3 structure, excitations and stability.

Figure 2.4 (A) shows a schematic energy level diagram for the Cl-N-N-N system relative to ClN_3 ground state with all known dissociation pathways. It is divided into molecular elimination, radical bond rupture and the secondary dissociations with their electronic excitation configuration. Shown as well are the dissociative ionization channels which lie above 10 eV. As can be seen in Figure 2.4 (B), cyclic N_3 is stabilized by a spin-orbit forbidden dissociation onto $N_2(X^1\Sigma_g^+)$ + $N(^2D)$ and an endoenergetic barrier to $N_2(X^1\Sigma_g^+)$ + $N(^4S)$ of 1.42 and 1.22 eV, respectively. The relaxation onto its linear form is characterized by a frustrating barrier of 1.37 eV [19, 41]. This suggests that the cyclic form of N_3 is at least long lived. Indeed, in the synchrotron experiment that determined the ionization potential of N_3, some of the N_3

---

[1] The rotational period T_{rot} of ClN_3 was calculated as follows: $T_{rot} \sim 1/(2B)$, where B is the rotational constant given by $B = \hbar/(8\pi^2 cI)$ with $\hbar$: Planks constant, c: speed of light and I: momentum of inertia along the rotational axis. For ClN_3 we have three axis, A,B,C [37]. For the quickest one with A_0 = 37333 MHz we get T_{rot} = 13.4. For the slow axis T_{rot} ∼ 150 ps.

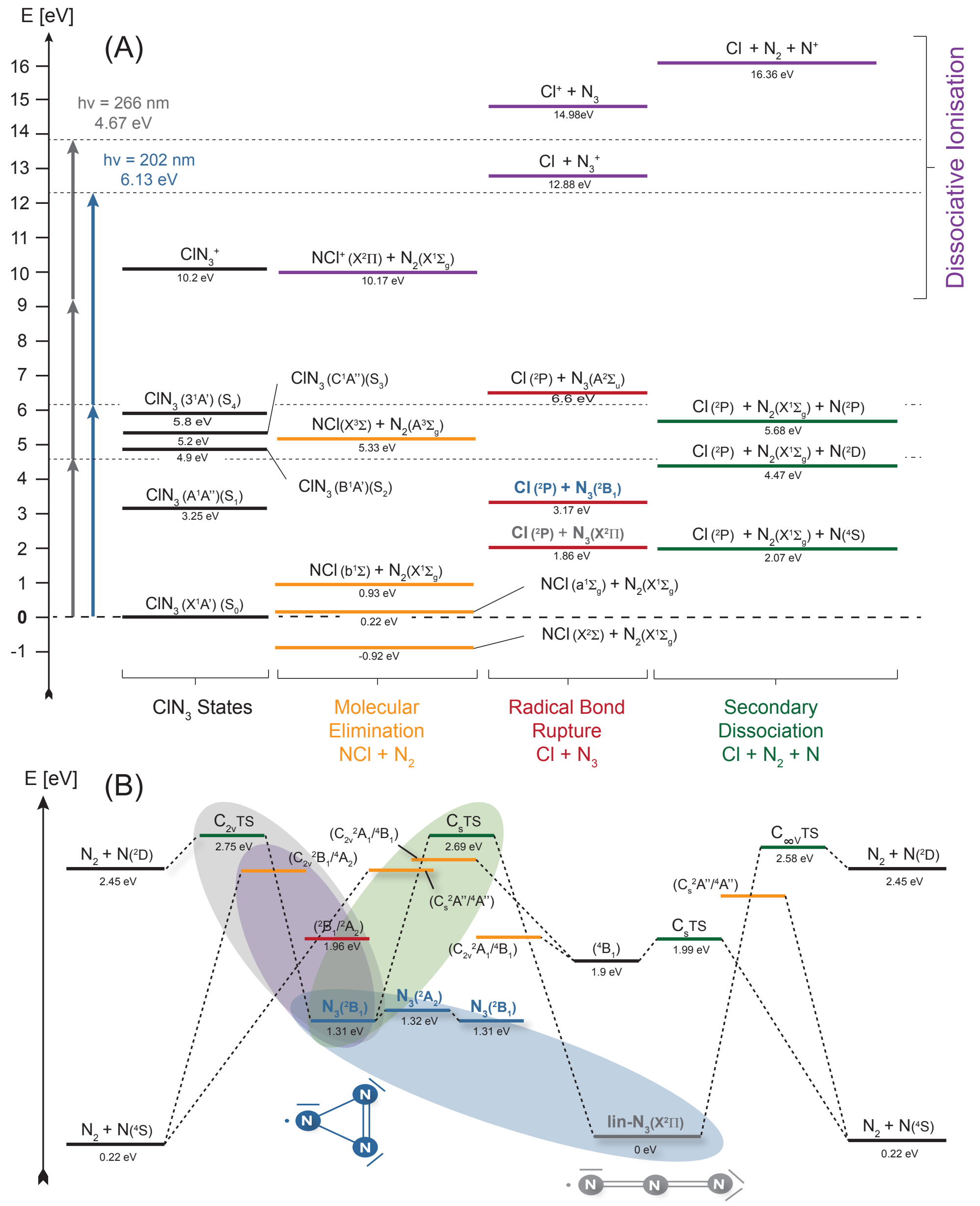

Figure 2.4: Energy-level diagram for the Cl-N-N-N system relative to ClN_3 ground state. All known dissociation pathways, divided into molecular elimination (orange), radical bond (red) rupture and secondary dissociations (green) with their electronic excitation configuration. Shown as well are the dissociative ionization channels (purple). Adapted from [16, 17, 22, 30, 40]. Energy-level diagram for N_3 system relative to N_3 in its linear geometry. Ground state species are shown as solid black lines and cyclic-N_3 as solid blue ones. Transition states (TS), intersystem crossings (MSX) and conical intersection (CI) are seen as green, orange, and red lines, respectively. N_3 cyclic is protected against relaxation to the linear geometry and dissociation to N_2 + N by $\sim$ 1 eV barriers. Adapted from [38, 41].

Table 2.1: Ionization energies (I_p) for all fragments of ClN_3

Species	I_p [eV]	**Source**
ClN_3	9.97	Quinto-Hernandez [38]
Cl	12.96	NIST
SO(Cl)	0.11	NIST
$N_3(X^2\Pi)$ [linear]	11.06	Dyke et al. [26]
$N_3(^2B_1, ^2A_2)$ [cyclic]	10.6	Hansen et al. [16]
$NCl(X^2\Sigma)$	11.47	Hansen et al. [39]
$NCl(a^1\Sigma_g)$	9.69	Hansen et al. [39]
N_2	15.58	NIST
N	14.53	NIST

fragments produced at 248 nm flew about 10 cm before to be ionized, and let imagine a µsec lifetime of N_3.

2.1.2 The Structure of ClN_3 and N_3

ClN_3, the C_s point group

It has only one symmetry plane σ_h which is the molecular plane (xy) and therefore belongs to the C_s point group as can be seen in Figure 2.5. This group has an A' and A'' symmetry. The transition dipole moment lying in the xy-plane has A' and along the z-axis a A'' symmetry. The C_s point group character and product tables are shown in Table E.1 in Appendix E. According to the C_s character table, going from an electronic state with A' symmetry to one with A' symmetry the transition dipole moment will also be A' and therefore lie in the molecular plane. Going form A' to A'' electronic state, the transition dipole moment will lie along the z-axis perpendicular to the molecular plane.

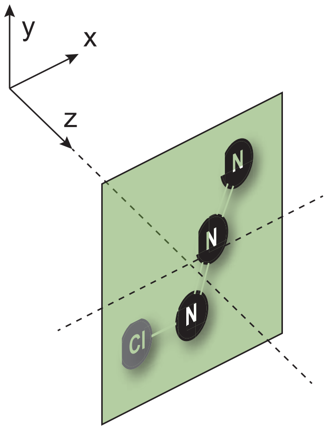

Figure 2.5: Molecular plane of ClN_3 (σ_h)

With a dissociation laser linearly polarized, parallel to the detector plane to fullfill the symmetry requirements for the inverse Abel-tranformation, we select molecules preferably with their transition dipole moment parallel or perpendicular to the dissociation laser polarization accordingly to the symmetry of the transition.

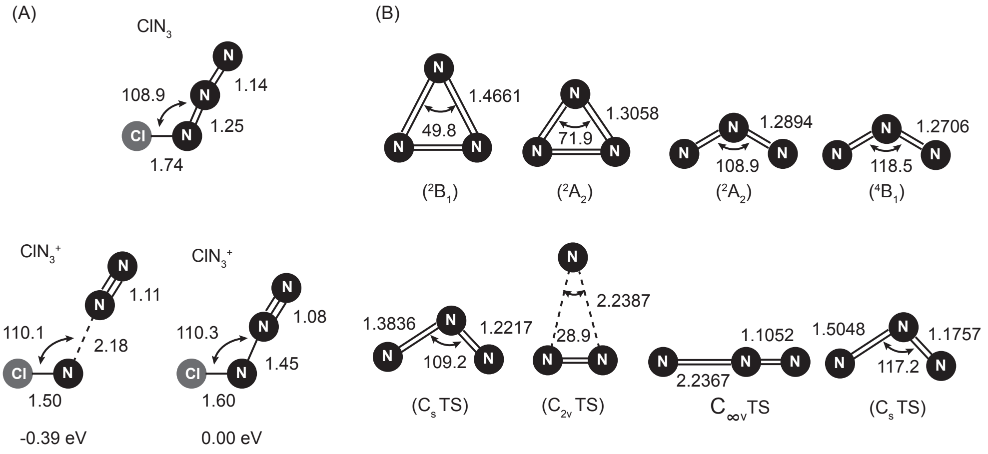

Figure 2.6: ClN_3 and N_3 molecular structure. (A) Geometries of ClN_3 and ClN_3^+ calculated at MP2/aug-cc-pVTZ and CCSD[T]/cc-pVTZ levels. row one: The structure of ClN_3 neutral. row tow: Two energy minima of ClN_3^+. Bond length are given in Å and angles in degrees. Adapted form [22]. (B) Stationary structures on the potential-energy surfaces for N_3. First row N_3 cyclic and linear, second row shows the transition states (compare to Figure 2.4 (B)). Adapted from [41].

Cyclic-N_3, the D_{3h} point group

Cyclic-N_3 is a Jahn-Teller molecule that exhibits a conical intersection at the D_{3h} (equilateral triangle) configuration. The D_{3h} point group and character tables are shown in Table E.4 in Appendix E. Kerkines et al. performed CASSCF *ab initio* potential energy surface and direct trajectory calculations and proposed a possible pathway to the formation of cyclic-N_3 following the photodissociation of ClN_3 using 157.4 nm [40]. The suggested scenario is as follows: (a) ClN_3 is excited to the 4 $^1A'$ (S_7) state. (b) This state dissociates after about 40 fs to $N_3(2^2A'$, with about 1.9 eV internal energy) + $Cl(^2P)$. (c) This vibrationally excited $N_3(2^2A')$ goes diabatically through a conical intersection at 44 fs onto $1^2A'$. (d) At 19 fs later and repeatedly after every 55 fs, $N_3(1^2A')$ crosses and trickles down via Coriolis coupling to $2^2A''(^2B_1)$ N_3, which has a potential minimum at the cyclic-N_3 structure. (e) Some fraction of $2^2A''(^2B_1)$ N_3 will lose kinetic energy quenched after vibrating in the well and will be found as the cyclic N_3, and some other fraction will eventually dissociate to $N(^2D)$ +N_2 over a high barrier found previously [41]. Figure 2.6 (B) shows the stationary structures on the potential-energy surface for N_3.

Figure 2.6 (A) shows the calculated ClN_3 geometry of the ground and first excited state from MP2/aug-cc-pVTZ and CCSD[T]/cc-pVTZ calculations with an angle of 109 degrees between Cl and N-N-N and the bond lengths of 1.74, 1.25 and 1.14 Å between Cl-N and N-N-N, respectively [22]. Experiments, supported by these calculations, show that the ClN_3^+ ion is unstable with an ionization energy of 10.2 ± 0.01 eV determined from dissociative ionization producing NCl^+ + N_2.

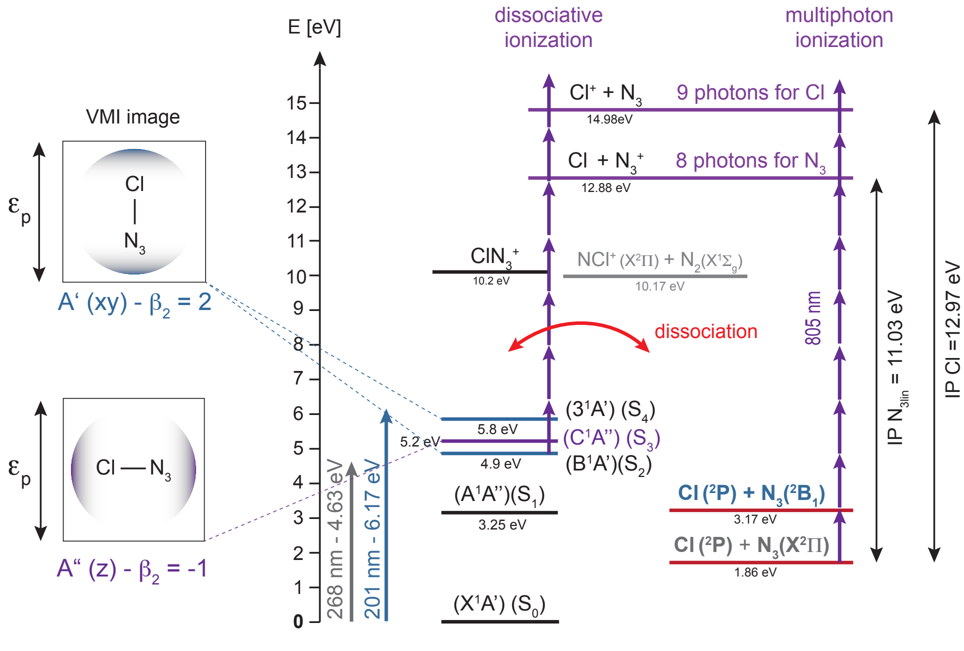

Figure 2.7: ClN_3 excitation scheme at 268 and 201 nm with only the dissociative ionization channels of Cl^+ and N_3^+. Shown are the electronic states of ClN_3 with their symmetry and the expected angular distribution for the possible electronic transitions.

2.2 Experimental

2.2.1 The excitation scheme for ClN_3 at 268 and 201 nm

Figure 2.7 shows the energy levels of ClN_3 which is a reduced version of Figure 2.4 focusing on the electronic states reachable by a one photon transition with 268 nm and 201 nm. We can see that in the two energy regions we can reach with these photon energies, there are three excited states of ClN_3. In the 250 nm absorption band there is the S_2 state with an A' symmetry and in the 210 nm absorption band there is the S_3 and S_4 state with an A'' and A' symmetry, respectively. The ground state of ClN_3 has an A' symmetry and therefore the two A' states should be reach from the ground state by an electronic transition of A'. This means that the linear polarized pump laser will excite preferably ClN_3 molecules with the molecular plane (xy) containing the laser field. Consequently the dissociation will lead to an angular distribution characterized by $\beta_2 = 2$. This will be the case for the S_2 and S_4 electronic states if the dissociation is fast compared to the rotation or out of plane bending modes of the molecule. The A'' transition to the S_3 electronic state leads to a selection of the molecular plane perpendicular to the laser polarization and to an angular distribution characterized by $\beta_2 = -1$.

The ionization potentials of N_3 cyclic/linear and Cl are 10.6/11.03 eV and 12.97 eV, respectively. Using an 803 nm pulse for ionizing we are using 8-9 photons to reach the ionization thresholds of the fragments. This extreme multiphoton ionization needs high laser intensities in the range of $> 10^{12}$ W/cm^2. High laser intensities also allows us to do dissociative ionization. This means we have enough intensity to ionize and dissociate at the same time. As we will see later the signal coming from this dissociative ionization is rather strong and can be

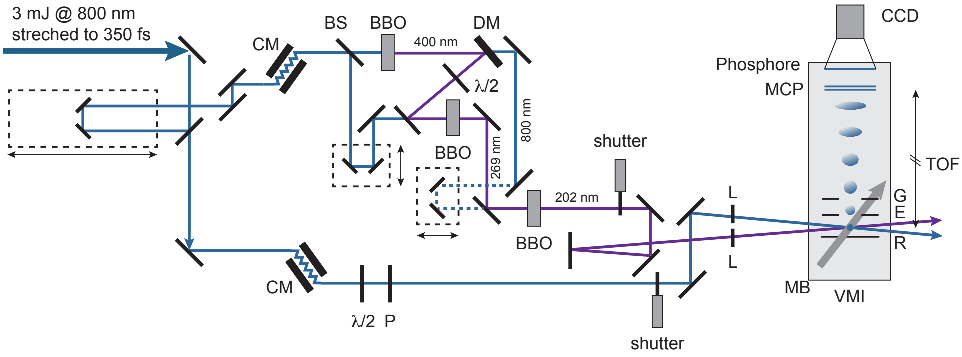

Figure 2.8: Schematic pump-probe fs-UV-VMI setup for the ClN_3 photodissociation experiment. The desired wavelengths of 268 and 201 nm are produced by third and fourth harmonic generation in Beta-Barium Borate (BBO) crystals, respectively. (BS: beamsplitter, BBO: Beta-Barium Borate, DM: dichroic mirror, P: polarizer, L: lens, $\lambda/2$: half-wave plate), CM: chirped mirrors.

even the dominant part. This is the main reason why we have to pay a little bit more attention to the subtraction of the background signals. This will be explained in Section 2.2.5

2.2.2 Femtosecond-UV-VMI setup

The photodissociation of ClN_3 has been studied in a pump-probe configuration using either 268 nm (4.63 eV) or 201 nm (6.17 eV) light to initiate the dissociation where mainly N_3 linear or cyclic is produced, respectively. The experimental setup consists of a standard continuous molecular beam (MB) chamber coupled to a velocity-map imaging (VMI) spectrometer. The Laser system employed was a 1 kHz Ti:Sapphire regenerative-amplified laser system (Amplitude System), delivering 3 mJ per pulse with a central wavelength of around 803 nm and a Fourier-transform limited full width at half-maximum (FWHM) duration of around 60 fs. An acousto-optical programmable dispersive filter (Dazzler) was inserted between the stretcher and amplifier to tune the fundamental wavelength and to compensate the second to fourth order dispersion. More details about the the VMI and the laser system can be found in Section 1.2 and Appendix A, respectively.

The schematic setup is shown in Figure 2.8. The output from the laser is chirped to 350 fs (introducing a GDD[1] $\sim 5000\ \mathrm{fs}^2$) and send to the experimental setup where is it recompressed by chirped mirrors before the frequency conversion. Propagating the laser chirped is reducing the B-Integral, which is a measure of the self focusing property of short laser pulses while traveling through a medium (see Appendix A). Before the experiment the laser beam is split into two beams to generate the pump and probe pulses. The pump beam is going through a long translation stage enabling time resolved measurements by varying the time delay between the two pulses. It is used to dissociate the molecule and the probe pulse to ionize the nascent fragments and to enable detection. To achieve the desired pump wavelengths we used the third and fourth harmonic of the fundamental wavelength (803 nm). The third harmonic (268 nm) is

---

[1] GDD, group delay dispersion, see Appendix A.3

produced by mixing the fundamental wavelength (803 nm) with the second harmonic (402 nm) in a Beta-Barium Borate (BBO) crystal. In the case of the fourth harmonic (201 nm) the third harmonic is again mixed with the fundamental wavelength in a BBO crystal. For 268 nm we achieve typically around 60 µJ/p with a FWHM bandwidth of 1.54 nm. These values depend largely on the crystal in use. The thicker the crystal the greater is the power but the bandwidth gets smaller and therefore the duration longer (see Appendix A). We tried to get the shortest pulses as possible by reducing the thickness but not loosing too much of the energy. Table 2.2 gives an overview of the crystals used and the achieved power conversions along with their bandwidths and expected theoretical pulse durations (Fourier-transform limited FTL).

The typical pump pulse energies were ~20 µJ and ~9µJ for the 268 and 201 nm, respectively. All results presented here have been detected by a multiphoton ionization process due to the fact that a probe pulse centered at 803 nm was used and all ionization energies of the detected fragments lie in the 10 eV region. Typically ~200 µJ was required for the ionization to effectively get the I_p from the fragments ($I_p > 10$ eV). The spectral bandwidths of the used pulses were measured to be 1.54 nm for the 268 nm, 0.85 nm for the 201 nm and 15.5 nm for the 803 nm. This corresponds to Fourier-transform limited bandwidths of 97 fs, 100 fs and 86 fs, respectively, and thus leading to a theoretical cross-correlation time between the pump and probe pulse of 92 fs (268 + 803 nm) and 93 fs (201 + 803 nm). The experimental values for the cross-correlation time measured in argon of 110 fs and 145 fs shown in Figure 2.9 is somewhat longer than the theoretical value due to high power effects, especially due to the viewport and the fact that no compression line is used after the last frequency conversion step to compress the UV beams. Indeed such a compression, e.g a prism compressor, would reduce the cross-correlation time but easily reduce the intensity output by a factor of two and introduce more spatial chirp. The beams were focused into the molecular beam by using 250 and 200 mm focal length lenses for the pump and probe beam, respectively. The dimensions of the laser spots were determined using a UV-CCD camera and the resulting pulse intensities were calculated to be $\sim 5 \times 10^{12}$ W/cm^2 for the 268 nm and $\sim 1 \times 10^{13}$ W/cm^2 for 803 nm radiation. The pump beam polarization was set parallel to the detector plane to provide the cylindrical symmetry required for the image reconstruction (see Section 1.2.3). The polarization of the probe beam was first also set to parallel and was later changed to perpendicular as comparison,

Table 2.2: Utilized BBO crystals for the generation of third (268 nm) and fourth (201 nm) harmonic with their characteristics and achieved conversion values. The beam is typically 7 mm is diameter.

λ [nm]	BBO type	dim [mm]	P [µJ]	$\Delta\lambda$ [nm]	ΔT (FTL) [fs]
403:	type1, $\theta = 35°$, $\phi = 90°$ P/P @ 500-700 nm	8x8x0.2	~250	8.44(15)	~40
268:	type1, $\theta = 44.3°$, $\phi = 90°$ P/P @ 400-803/266 nm	12x12x0.2	~60	1.542(3)	~97
201:	type1, $\theta = 64°$, $\phi = 90°$ P/P @ 266-803/201 nm	10x10x0.1	~12	0.841(8)	~100
803:			~300	15.55(7)	~86

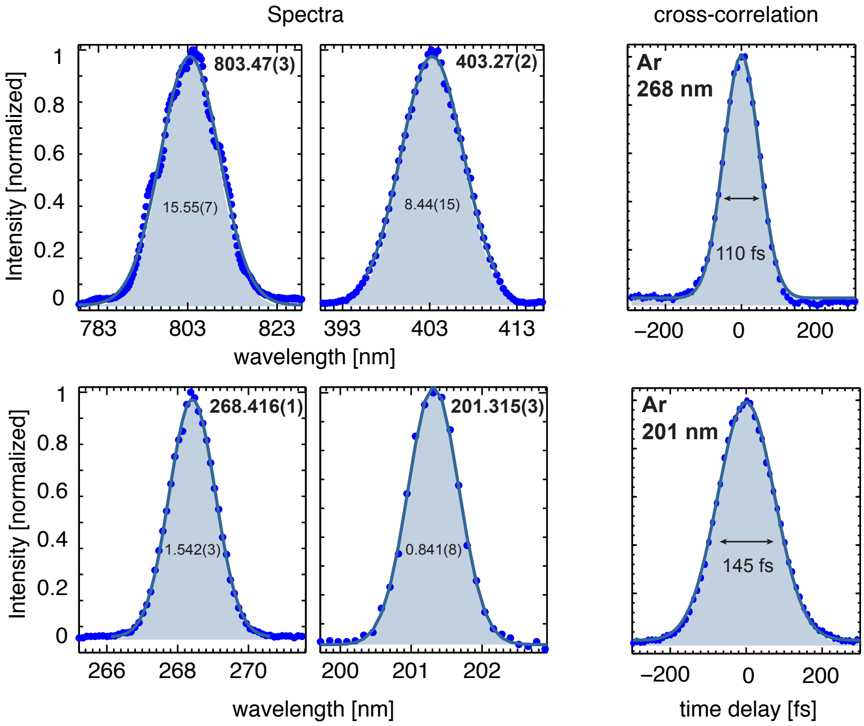

Figure 2.9: On the left: laser spectra for 803, 403, 268 and 201 nm. On the right cross-correlation times measured in argon between 268 + 803 nm and 201 + 803 nm.

which we will call parallel and perpendicular configuration. The ionized fragments were extracted in a direction perpendicular to the plane defined by the laser and the molecular beam, and detected at the end of a 40 cm time-of-flight (TOF) tube. The imaging detector consists of two micro-channel plates (MCPs) with a diameter of 7.5 cm in a z-configuration coupled to a phosphor screen and a 12-bit CCD camera. A more detailed explanation and a schematic drawing of the VMI setup can be found in Section 1.2. By pre-amplifying (× 200) and using a gated boxcar integrator to record the signal collected directly from the phosphor screen (P43) via a capacitor (100 pF) the transient ion signals are recorded as function of delay. At each pump-probe delay the signal was averaged over 1×10^4 laser shots. A typical ion fragment image selected in mass was obtained by accumulating 6×10^5 laser shots, whereas the images with one laser were only averaged over 2×10^5. Typically the images are obtained with a repeller plate voltage at 2 kV. In order to reconstruct the 3D distributions to extract the angular and kinetic energy distributions, the 2D projected raw images are Abel inverted. The calibration of the kinetic energy scale was performed by using photoelectron spectra obtained for NO (see Section 1.2.5). Typically, by using a repeller plate voltage of 2 kV, an energy resolution of 90 meV was obtained at 1.0 eV kinetic energy (see Table 1.1).

2.2.3 Alignment procedure

For time resolved pump-probe experiments the alignment and overlap of the two beams needs to be done spatially and temporally. The spacial alignment procedure is shown in Figure 2.10. The procedure is quite crucial as the pump-probe signal depends on the relative spatial overlap of the two laser beams, ideally done at the same focus voltage (extractor voltage) such that

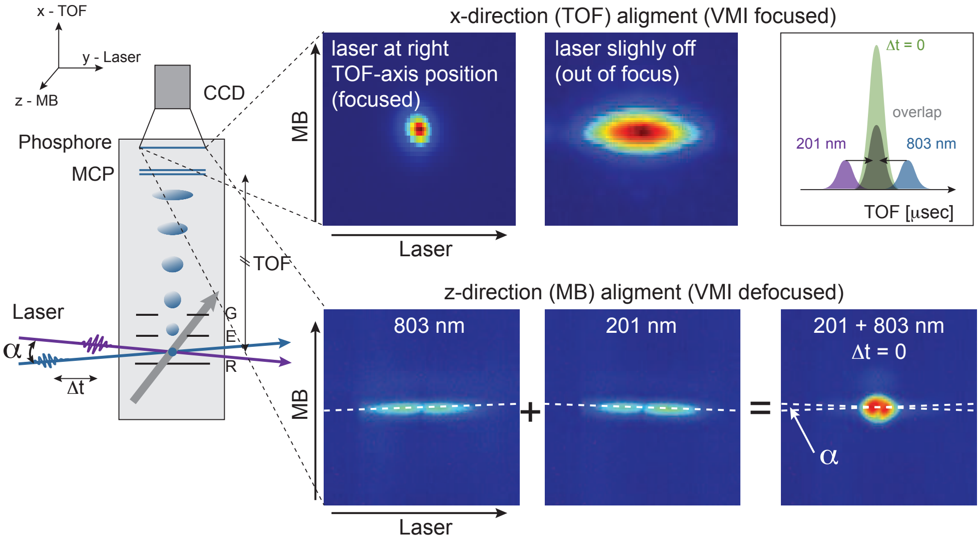

Figure 2.10: VMI laser alignment for the ClN_3 experiment using a molecular beam of NO. The top row shows the x-axis (TOF) alignment done with the focus voltage on the extractor plate. The bottom row shows the z-axis alignment (MB) with defocused voltage set on the extractor (100 V).

the calibration factor does not vary from day to day. As we are using for ClN_3 quite short focal lenses with 200 or 250 mm, the focal spots are only in the order of 50 - 100 μm and therefore the adjustment is quite sensitive. To avoid doing a calibration each day, the repeller and extractor voltages are kept exactly the same and the laser is accordingly adjusted and put to the right position in the x-axis which is the TOF axis and the z-axis which is the molecular beam axis (see Figure 2.10). Afterwards the time delay between the beams is adjusted to find Δt = 0 where both beams are overlapping also in time. Normally this alignment is preferable done on the system of interest for instance molecule AB. But this requires an ionization signal of AB^+ or a dissociative ionization signal A^+ from each laser beam. For ClN_3 this was not the case because of two reasons: the parent ion ClN_3^+ dissociates and the pump-probe contrast to be able to find the time zero between the two lasers is very tiny on the dissociative ionization signal. For these reasons we used NO as alignment molecule. Especially to find the time overlap between the pump and probe laser, the choice of the alignment system is important and depends largely on the wavelengths used in these two beams. To have a visible pump-probe contrast at Δt = 0 the ionization potential of the system should be high enough that multiphoton ionization is necessary but low enough to be able to do multiphoton ionization with the available laser intensities. NO has an I_p of 9.26 eV and therefore at 803 nm we need 6 photons to reach the I_p or two and three photons at 268 and 201 nm, respectively. At time zero when both lasers are overlapping in time to ionize NO we need only one photon at 268 nm and three photons at 803 nm or in the case of using 201 nm, one photon at 201 nm and only two photons at 803 nm. These numbers are drastically reduced compared to the multiphoton ionization with only one laser and therefore the probability of ionization is significantly increased which results in a huge increase in signal contrast at time zero compared to outside of the temporal overlap of the two pulses. For example the amount of NO^+ detected with each lasers was around 20 mV, given a background of 40 mV and at Δt = 0 the signal increased over 200 mV.

In the first step the two laser beams are adjusted in vertical and horizontal position before and after the entrance in the VMI by pinholes to ensure that the beams are going perfectly horizontal through voltage plates. Then the x-axis (TOF-axis, in our setup the vertical axis) is aligned by putting the extractor voltage to the value for which the calibration factor was determined. The laser beam is adjusted to be in focus on the camera which results in a signal spot on the detector as shown in Figure 2.10 on the right in the first row. If the beam is not exactly at the same vertical position the image will be out of focus for this particular set of voltages and the signal on the camera gets more diffuse (second image). In this case the focus voltage would be different and therefore also the calibration factor. The same is done with the second laser so that on the TOF monitored on the oscilloscope the two signals from each laser are overlapping (grey peak in Figure 2.10 first row on the right). To align the z-axis overlap, the MB direction and in our setup the horizontal axis, the VMI is defocused. In this case we are sensitive to the MB diameter and direction. As we can see in Figure 2.10 on the bottom row we now have a horizontal line on the detector where we are able to overlap both beams in the MB direction. We can even see that the line is slightly tilted with respect to the horizontal axis which is the laser direction. This corresponds to the small angle α between the two laser beams. After the alignment of both the TOF- and MB-axis the delay between the two beams is scanned to find the time zero. When both beams are overlapping in time we observe the increase in contrast on the CCD and on the oscilloscope as shown in Figure 2.10 on the outermost right plot. At this point fine adjustments on the MB- and TOF-axis can be done to increase the contrast further and to optimize the spatial overlap on the pump-probe signal directly. All adjustments are done with micrometer screws with the two last mirrors or with the lenses which are mounted in xyz translation stages. In the case where the VMI is defocused and we observe the horizontal line we can also adjust the lens position in the laser direction (y-axis) so that we observe a relatively homogeneous horizontal line, meaning that the laser waist is perfectly in the center of the VMI y-axis.

2.2.4 ClN_3 Production

ClN_3 is produced on site in a two-step reaction during the measurement. Typically $< 5\%$ of Cl_2 in an Ar/He (20/80%) mixture is lead through moist sodium azide (NaN_3 with water) in a reactor. The reactor setup is shown schematic in Figure 2.11.

Initially NaN_3 and water react to form HN_3 + NaOH. In the second step HN_3 reacts with Cl_2 to produce ClN_3 and HCl.

$$\begin{aligned} NaN_3 + H_2O &\rightarrow HN_3 + NaOH \\ HN_3 + Cl_2 &\rightarrow ClN_3 + HCl \end{aligned}$$

A standard drying agent (Drierite, anhydous $CaSO_4$) is used to remove water from the ClN_3/Ar/He mixture at the exit of the reactor. Helium is the preferred carrier gas to obtain very cold molecular beams with almost no internal energies. But because Helium is hard to ionize, especially

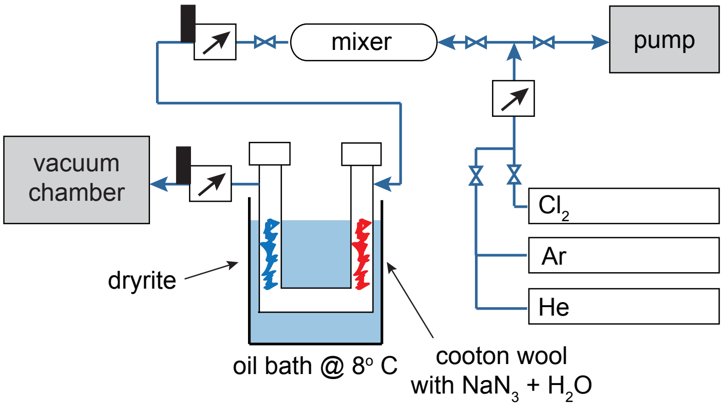

Figure 2.11: Schematic reactor setup for the ClN_3 -production.

in a multi-photon ionization configuration, argon was added to the mixture. Argon acts as a reference for the cross-correlation time and is used to determine the exact time zero between both laser pulses as shown in Figure 2.9. To maintain a stable reaction over a number of hours the whole reactor is cooled down to 8 degrees Celsius. Typically around 2g of NaN_3 was put on a cutton wool with about 80 drops of distilled water. These parameters assured a stable reaction over 8 hours. The continuous molecular beam was produced by expanding $\sim$140 Torr of the mixture through a 200 µm nozzle. Among all the vibrational modes of ClN_3 summarized in Table 2.3 we can assume that at most one quantum is populated in the molecular beam with less then 7%.

Table 2.3: Experimentally observed vibrational frequencies of ClN_3 [42]

	IR	Raman
Deformation mode in plane	223 cm^{-1}	223 cm^{-1}
Deformation mode out of plane	522 cm^{-1}	-
Cl-N_3 stretching mode	545 cm^{-1}	542 cm^{-1}

A longneck skimmer with an diameter of Ø = 0.7 mm was used to collimate the molecular beam to about 3 mm in width in the interaction region, where it is crossed by the pump and probe laser beams. It is worthy to note that we have noticed that the reaction is more stable with a continuous molecular flow rather than a pulsed nozzle.

2.2.5 Image analysis in the case of ClN_3

As we will see in the next chapter the main signal on ClN_3 comes from the dissociative ionization as stated in Figure 2.7 due to the high intensity of the 803 nm probe laser. The high intensity is needed to be able to detect the fragments by multiphoton ionization and the dissociative ionization should be well separated in energy in the TER plots. But high intensity means also a huge one color background with contributions in the TER regime of our expected fragments because the wavelength we are using are all multiple of 803 nm. To extract the important signals in pump-probe configuration of the fragments we are interested in, it is crucial

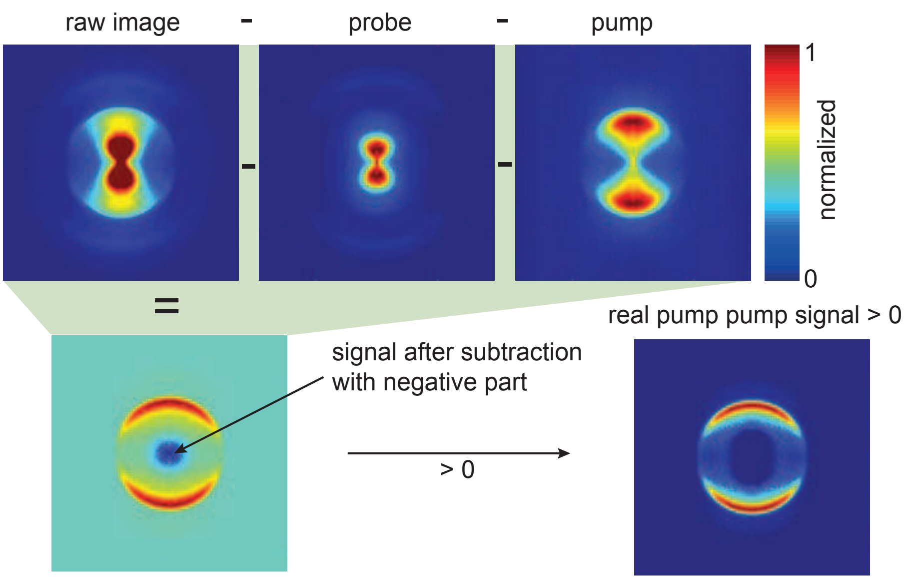

Figure 2.12: ClN_3 image analysis. Shown is the subtraction process as an example on raw images recorded on the N_3 fragment with an pump-probe delay of 1 ps.

to make a proper background subtraction. The important information is in the real pump-probe images, where the dissociation is done by the first pump pulse and the ionization to detect the fragment is done by the second probe pulse. The images recorded in the VMI are of course a superposition of both pulses. In order to reveal the important information all the images are background subtracted, meaning both single color signals are recorded as well and subtracted from the pump-probe image. Figure 2.12 illustrated the substraction process on the recorded images of the fragment N_3 at 268 nm plus 803 nm. The images are normalized to increase the contrast. Typically on an all-integrated image the pump and probe backgrounds are 10% and 85% of the pump-probe signal for N_3 as example. We see that the subtracted image sometimes has a negative component in the center of the image. This comes from the fact that even if the images are recorded with the same integration statistics, the signal from one color can be higher than in pump-probe configuration. Indeed the number of molecules available with one laser alone can be higher than in pump-probe configuration due to the depletion of the other laser beam. Moreover, saturation of the MCP and phosphor is easily achieved in the center of the image. As this contribution in the central part of the image is due to dissociative ionization and not in the area with TER > 0, the negative values are removed by setting them to zero. It is worthy to note that this effect can be observed as well on the full-integrated ion signals recorded from the capacitor.

As mentioned before to be able to make a proper background subtraction all images have to be taken with the same statistics. The main image is usually taken by averaging 5×10^6 laser shots leading to an acquisition time for one image of around 8-10 min. The time resolved studies contain usually 25 - 30 images leading to an total acquisition time of 4-5 hours for one scan. The background one color images are not delay dependent and taking one image for each one color should in theory be enough. As the laser intensity fluctuates quite strongly not only on a 5 hour timescale but already on a timescale comparable to the one image acquisition time,

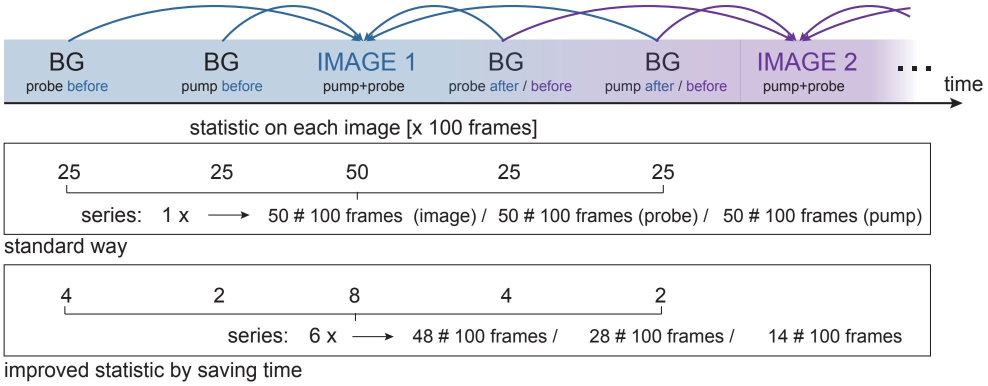

Figure 2.13: Schematic drawing of the new implemented acquisition statistic. One color backgrounds are taken before and after the pump-probe image. Statistics on each image can be reduced to reduce the influence of the laser fluctuations. The overall statistic is maintained by increasing the series. Choosing appropriate statistics for each image can reduce the total acquisition time. One frame corresponds to 100 ms aquisition time fixed by the CCD camera.

taking only one background image for a whole scan of 5 hours is not sufficient. Taking one color background images after each delay not only increases the acquisition time immensely but also was not enough to ensure a proper subtraction process. To improve the statistics with not increasing the acquisition time too much we implemented an acquisition procedure where we are able to take for one delay multiple images each followed by an one color background image with lower statistics which are summed up at the end to reach a sufficient statistic. The clue is to be able to choose different statistics for the main images and backgrounds according to the signal intensity. To be able to change between two color and one color backgrounds rapidly the beams have to be blocked fast and automatically. For this we implemented two beam shutters on the bases of magnetic hard drives. Our shutters were created according to the findings by Maguire et al. where they stated that voice-coil motors in computer hard disk drives show to make excellent mechanical shutters for light beams [43]. Shutter speeds in excess of 10 mm/ms are attained, allowing switching of a focused beam in under 10 µs [44]. These shutters are controlled by a labview program where we can set the statistics for each beam.

As the background signal for example for the 268 nm or 201 nm are quite low we don't need to take the same statistics on these images allowing us to reduce the overall acquisition time. For better statistic background images are taken before and after the pump-probe image. A schematic drawing of the new implemented acquisition statistic is shown in Figure 2.13. By decreasing the statistic of each image and increasing the number of series we are able to reduce the influence of the laser instabilities. The background 'after' the image is at the same time the background 'before' the next image. The labview program already does the subtraction with the right ratios and produced a so called treated images which is background substracted. All intermediate images are also saved for verification purposes. All images shown here on ClN_3 are taken with this acquisition process with a typical statistic shown in Figure 2.13.

2.3 Time-resolved transients of ClN_3 fragments

Because ClN_3 is produced in a reaction on site during the experiment as seen in the previous section it is important to check that one is not polluting the molecular beam with the intermediate products of this reaction. Both the UV and the 803 nm pulses are ideal sources to detect pollution due to the multiphoton processes easily achieved in the femtosecond time regime [45].

By pre-amplifying the signal extracted directly from the phosphor one is able the record the time-of-flight (TOF) mass spectrum of the species in the molecular beam using the VMI as a sophisticated mass spectrometer. In Figure 2.14 the time-of-flight (TOF) mass spectrum of ClN_3 is shown at both investigated wavelengths. Looking at the TOF spectrum it is evident that there is no measurable pollution of the intermediate products like HN_3, NaOH, HCl or Cl_2. Cl_2 from the seeding mixture is starting to appear when the mixture of NaN_3 and water on the cotton wool is depleted indicated that the reaction is coming to an end. Furthermore we observe that no parent ion ClN_3^+ is detected which would be expected at m/z = 77 amu. This indicates that the parent ion is not stable and dissociated directly to the $NCl^+(X^3\Sigma)$ + $N_2(X^1\Sigma_g^+)$. Indeed, N. Hansen et al. measured the NCl and N_2 fragments from ClN_3 photodissociation at 118 nm and 202 nm and they showed that ClN_3^+ is produced by 1 (118 nm) or 2 (202 nm) photon excitation probably in the first excited cation state [39]. They argument from the TER of NCl^+ is that the parent ion is short-lived requiring less than 0.28 eV to dissociate to NCl + N_2. They also showed quantum chemical calculations which suggest that the barrier to dissociation for this cation may be no greater than 0.09 eV. Electronic structure calculations on ClN_3^+ confirm that due to the large change in geometry compared to the parent neutral ClN_3 ionization leads to vibrational excited ClN_3^+ with more than enough energy to dissociate [22].

Even though we are not able the measure the decay of the parent ion ClN_3^+, a first guess of the typical time constants in our system can be done by recording this TOF mass spectrum for each fragment as a function of the delay between the dissociating (pump) and ionizing (probe) laser. The discrimination of the fragments is given by the flight time. All ions with the same mass and same TOF time are collected without energetic or angular discrimination by boxcar integrators. Our setup had six channels allowing us to record at the same time all five fragments plus argon as a reference. The signal out from the boxcar is an hardware average over 100 ms which means 100 laser shots. This signal is sent to the computer where one delay is typically integrated over 10-20 values in the computer. In addition 5 to 10 scans are acquired and averaged. Figure 2.15 shows the femtosecond time-resolved transients of each fragment coming from the dissociation of ClN_3 at 268 (top) and 201 nm (bottom). The argon reference is used to determine the exact time 'zero' and the time resolution between the two laser pulses, by fitting the argon transient with a gaussian function $y = y_0 + Ae^{-1/2*((t-t_0)/w)^2}$. The time 'zero' is given by the position t_0 and the time resolution, called the cross-correlation time T_{cc} given by the FWHM ($= 2\sqrt{2ln2}w$) of the gaussian fit. The transients of the fragments are then corrected according to this fit, shifting 'zero' to the one determined on argon. Intensities of 18 µJ and 9 µJ per pulse for the 268 and 201 nm dissociation laser pulse, respectively

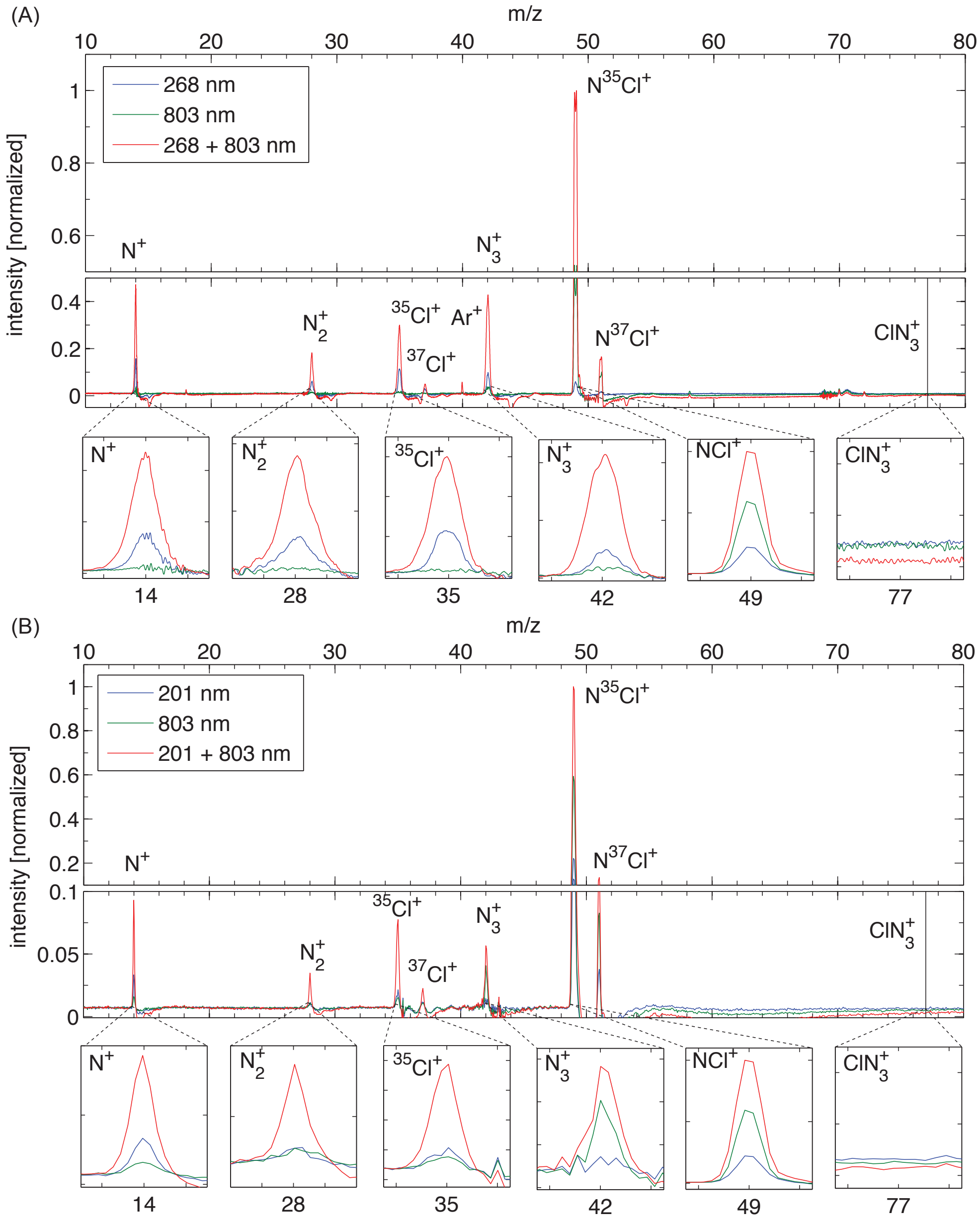

Figure 2.14: Time-of-flight mass spectrum of ClN_3. (A) at 268 and 803 nm. (B) at 201 and 803 nm. A vertical black line at $m/z = 77$ indicates where one would expect the parent ion ClN_3^+. The second line is a zoom on each mass given the exact mass position. Shown are the mass spectra with 268/201 and 803 nm alone in blue and green, respectively and red shows the mass spectra with both lasers at a time delay of 0 fs between the both lasers. The data is normalized to the NCl peak at $m/z = 49$ at time zero between the two lasers.

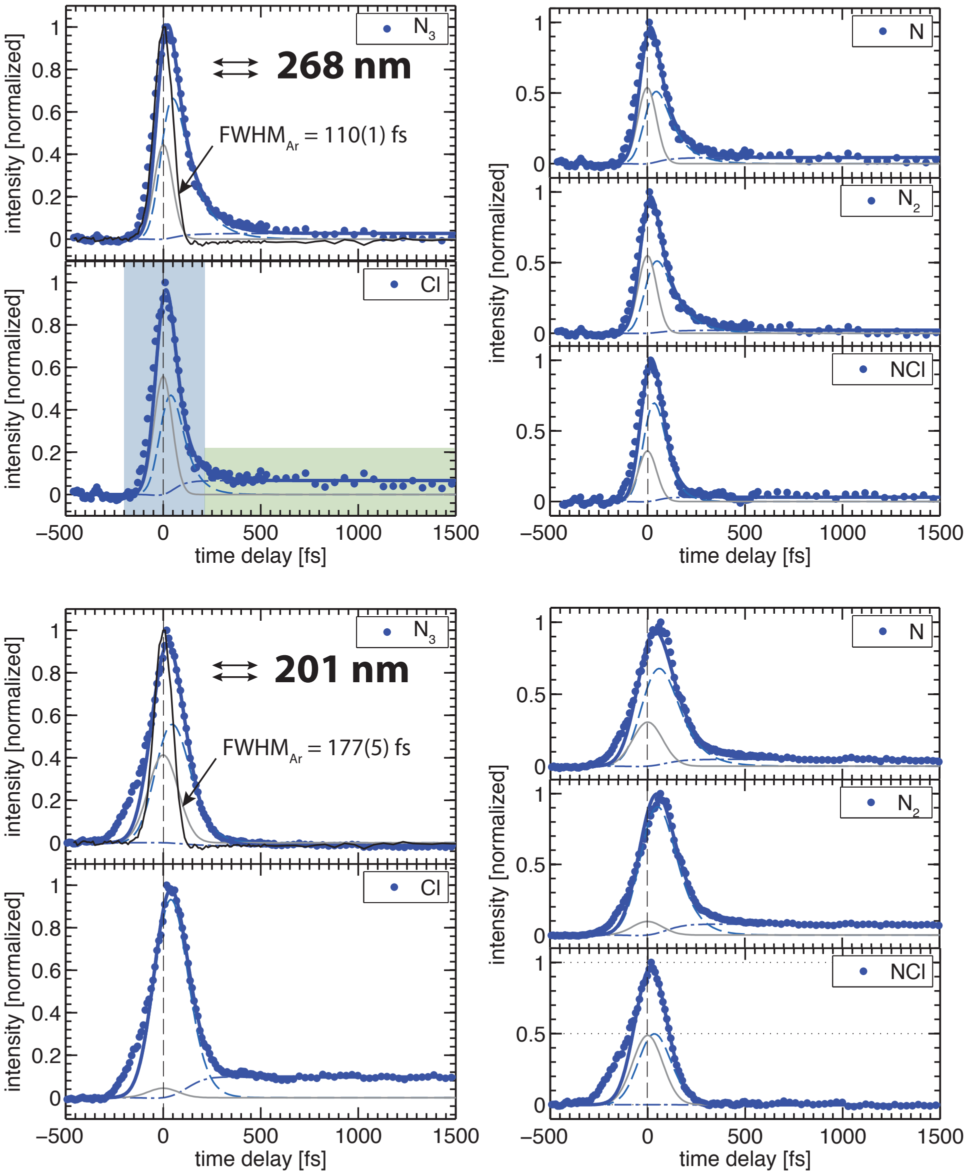

Figure 2.15: Integrated ion signals of all ClN_3 fragments as function of pump-probe delay after excitation with 268 (top) and 201 nm (bottom) with an 803 nm probe in parallel configuration. On the left N_3 and Cl and on the right N, N_2 and NCl. The blue and green area in the transient of Cl illustrates the dissociative ionization area and the area where the fragments are detected, respectively. For each transient, the fit is shown as a thick blue line that can be decomposed in a cross-correlation contribution (grey line), a decay component coming from the dissociative ionization of ClN_3^+ (long dashed blue line) and a rising part from the ionization of the neutral fragments (dash-doted blue line). The cross-correlation function determined on argon is shown in black.

were used, and 80 μJ per pulse for the 803 nm ionizing probe pulse. The maximum energy especially in the probe laser pulse is limited to not saturate the detector and the amplifier. The VMI is also used in a complete unfocused condition to avoid as well saturation. The strongest signal is coming from the NCl fragment and therefore is limiting the sensitivity on all other channels. The integrated amount of fragments produced at later delays is given by the step in the graphs as indicated by the green area in the transient of chlorine. The main contribution is coming from the dissociative ionization around time 'zero' due to the multiphoton ionization process shown in blue, limiting as well the sensitivity to detect the fragments at later times. To extract typical time constants the integrated ion signal of each fragment $S_{fragment}$ is fitted by an function of the form:

$$S_{fragment}(t) = y_0 + \Psi_{cc}(t) + \Psi_d(t) + \Psi_r(t) \tag{2.3}$$

where y_0 is an offset which corresponds to the backgound signal from pump and probe alone. For simplification of the fit this was set to zero. Ψ_{cc} is the cross-correlation function resulting from non-resonant ionization paths, shown in the Figure 2.15 as a grey line and given by a gaussian of the form

$$\Psi_{cc}(t) = a_0 \, e^{-\frac{1}{2}\left(\frac{\Delta t}{w}\right)^2} \tag{2.4}$$

with the width w determined on the argon reference. The decay and rising part, shown as dashed and dashed dotted lines respectively, are given by exponential functions of the form:

$$\Psi_d(t) = a_1 \, e^{-\frac{\Delta t}{T_d}} \times [1 + erf(\phi(\Delta t, T_d))] \tag{2.5}$$

$$\Psi_r(t) = a_2 \left(1 - e^{-\frac{\Delta t}{T_r}}\right) \times [1 + erf(\phi(\Delta t, T_r))] \tag{2.6}$$

where T_d and T_r are the decay and rising time, respectively. Δt is given by $t - t_0$ where t_0 is the time 'zero' between the two laser pulses determined by the cross-correlation on argon. The error function $\phi(\Delta t, T)$ is given by

$$\phi(\Delta t, T) = \frac{2\sqrt{ln2}}{T_{cc}} \left(\Delta t - \frac{T_{cc}^2}{8 \, ln2 \, T}\right) \tag{2.7}$$

which takes into account the width of cross-correlation function of argon T_{cc}. The most evident hypothesis is that $T_d = T_r$, meaning that the lifetime of the parent ion given by T_d is equal to the time the fragments need to appear (T_r). We already know because we are not detecting the parent ion as seen in the TOF mass spectrum that this is a very strong approximation and will give us only an estimation. Especially if electronic coupling takes place before the dissociation, the rising time of the fragments can be much longer than the decay of the parent ion as reported on fs dissociation of NO dimers for instance [46, 47].

Figure 2.16 shows the fit parameters for the transients of each fragment at 268 + 803 nm in grey and in blue at 201 + 803 nm.The amplitude a_2 from the rising part is very low compared to a_1 from the decay function, reflecting that we don't detect a huge amount of fragments. In the case of using 201 nm for the dissociation it is even less visible, especially for the fragments N_3 and NCl where the step is zero. The rising times $T_d = T_r$ are in the range of 50 to 80 fs for

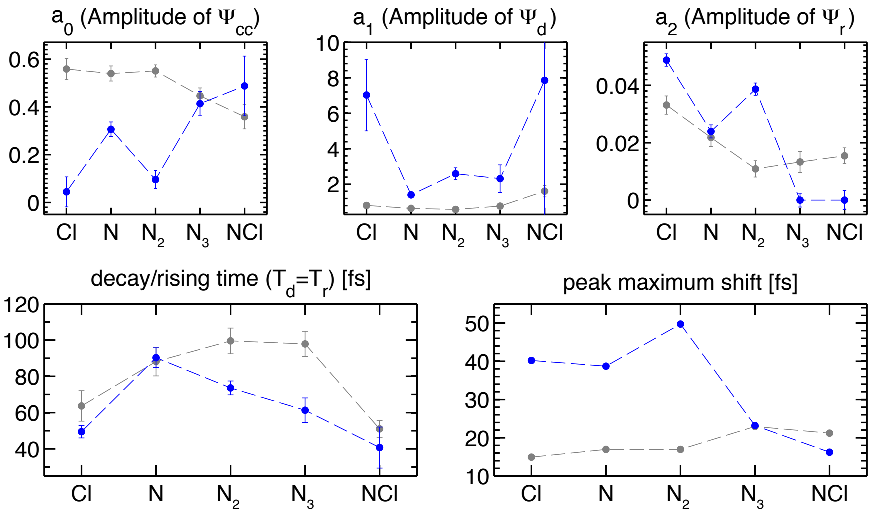

Figure 2.16: Fit parameters for the integrated ion signals of all ClN_3 fragments after excitation with 268 (grey) and 201 nm (blue) with an 803 nm probe pulse in parallel configuration. a_i with $i = 0, 1, 2$: amplitudes of the cross-correlation function, exponential decay and rising functions, respectively.

the dissociation at 268 nm and around 60 to 100 fs at 201 nm. Cl and NCl seems to have the fastest rising times whereas N, N_2 and N_3 have slightly longer rising times with a tendency of increasing with increasing number of N atoms at 268 nm and decreasing at 201 nm. The last graph in Figure 2.16 shows the shift of the maximum position of the transients relative to the ’zero’. This shift is not a parameter in the fit procedure but simply resulting from the decay time. In the case of 268 nm N_3 and NCl seem to be a bit more shifted than Cl, N, N_2. Whereas at the dissociation with 201 nm it is the contrary and Cl, N, N_2 are more than twice shifted compared to the dissociation at 268 nm.

As mentioned in Section 1.2 the polarization of the dissociation laser is fixed by the geometry of the VMI setup. As long an axis of cylindrical symmetry is maintained and that axis is parallel to the projection plane, one can apply the Abel transformation. In the VMI case, the axis of symmetry is the laser polarization and the projection plane is the detector, which means the polarization should be parallel to the detector to apply the Abel transform. This normally applies for both lasers, pump and probe. But one can get away with this requirement for the probe laser if the ionization process is spherically symmetric, for instant if one don’t favorably ionize along, or perpendicular to the pump laser polarization direction. We will see that this is true in our case for the multiphoton ionization detection process and we do not affect the $\cos^2$ angular distribution which is fully fixed by the first pump laser polarization. However it is important to keep in mind that this is not a general statement, for instance, it is not the case with the photoionization of CH_3I with the 800 nm [48]. Moreover with a narrow bandwidth laser, namely with nanosecond pulsed lasers, the *J* selection (rotational state selection) of the REMPI process will change this picture completely. But with a broadband femtosecond laser pulse, we are not selecting any rotational levels. In this case the dissociation process shouldn’t be affected by the ionization process. This means we can cross the pump and probe polarizations and use this to determine if our multiphoton ionization detection is not introducing an artefact

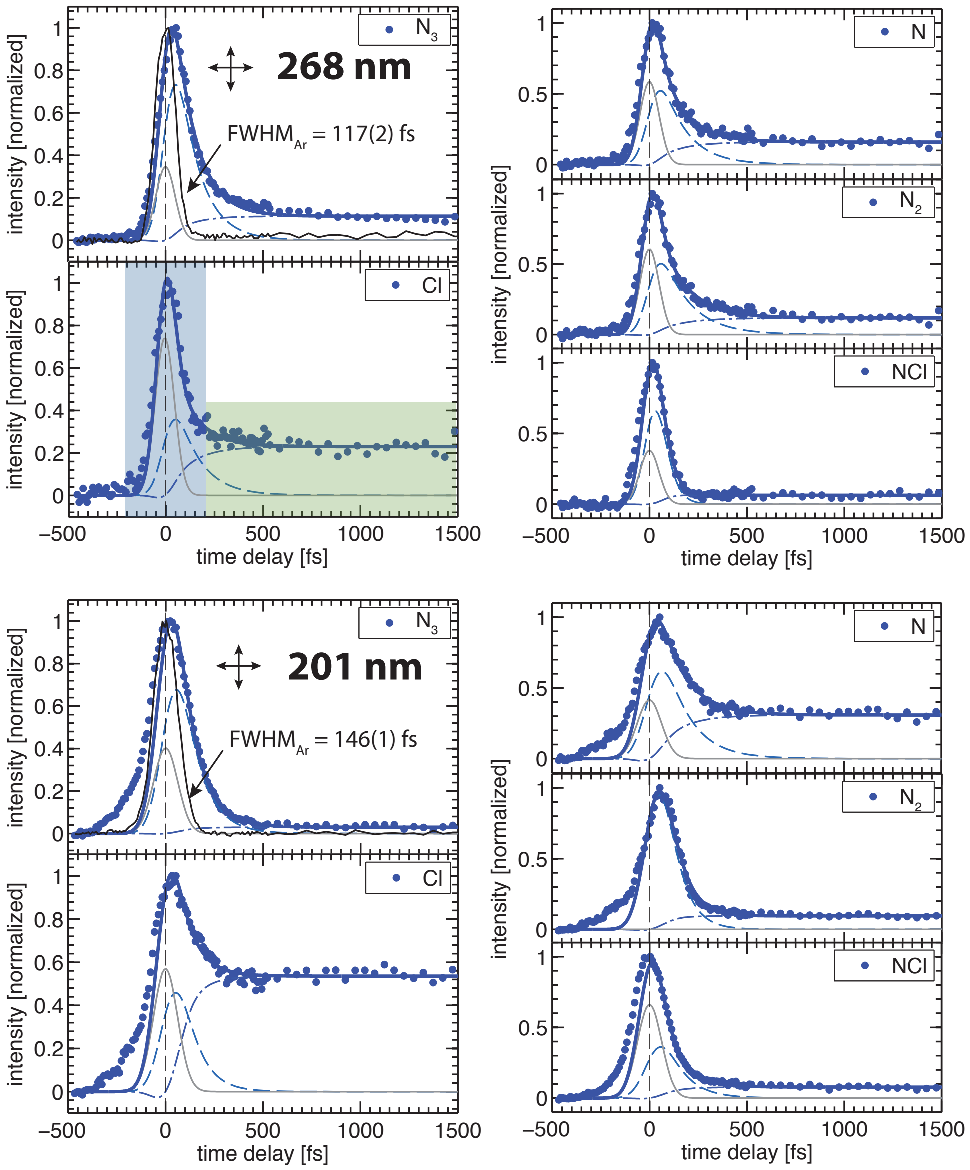

Figure 2.17: Integrated ion signals of all ClN$_3$ fragments as function of the pump-probe delay after excitation with 268 (top) and 201 nm (bottom) with an 803 nm probe pulse in perpendicular configuration. For each transient, the fit is shown as a thick blue line that can be decomposed in a cross-correlation contribution (grey line), a decay component coming from the dissociative ionization of ClN$_3^+$ (long dashed blue line) and a rising part from the ionization of the neutral fragments (dash-doted blue line). The cross-correlation function determined on argon is shown in black.

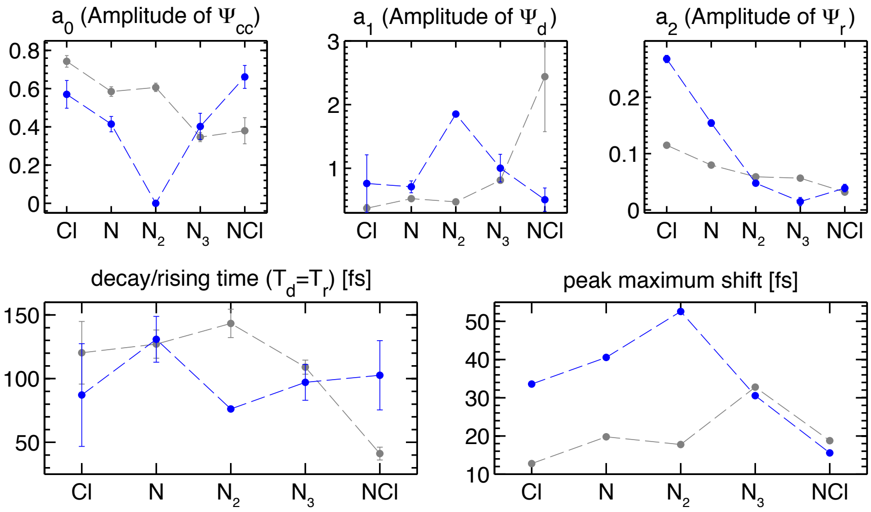

Figure 2.18: Fit parameters for the integrated ion signals of all ClN_3 fragments after excitation with 268 (grey) and 201 nm (blue) with an 803 nm probe pulse in perpendicular configuration. a_i with $i = 0, 1, 2$: amplitudes of the cross-correlation function, exponential decay and rising functions, respectively.

due to its high intensity. High laser intensities can introduce some alignment which would affect the outcome of the dissociation process like we have observed in the study of the CH_3I predissociation [48]. Figure 2.17 shows the femtosecond time-resolved transients of each fragment coming from the dissociation of ClN_3 at 268 (top) and 201 nm (bottom) with an 803 nm probe in perpendicular configuration. The transients are analyzed as described above. The difference to the parallel configuration is clearly observed on the transient of Cl. The ratio between the dissociative ionization (blue area) and the detection of the fragments (green area) is almost a factor five better, at least for Cl, N and N_2. For the fragments N_3 and NCl the step is again much smaller but also more visible. The time constants observed in perpendicular configuration are slightly larger but still around 80 - 100 fs. suggesting that the intense 803 nm probe pulse is not affecting the measurement drastically. Nevertheless, the dissociative ionization process with a perpendicular 803 nm probe pulse seems to be less efficient.

Instead of detecting the time-of-flight we will now use the VMI in its pulsed mode. This will allow us to increase the sensitivity for the detection of the fragments produced in small amounts, like N_3.

2.4 N_3 - Cl translational energy and angular distributions

In order to determine if we are able to detect the fragments coming from the right dissociation channel namely the radical bond rupture producing N_3 and Cl one can check the translational energy release TER of these fragments far away from the dissociation. Figure 2.19 on the right shows reconstructed velocity-map image slices of the three-dimensional velocity distribution of the fragments N_3 and Cl with a pump-probe delay of 1 ps obtained by using the inverse-Abel transformation. The single laser background images have been subtracted and the images are analyzed as discussed in Section 2.2.5. The first row shows the images recorded with a

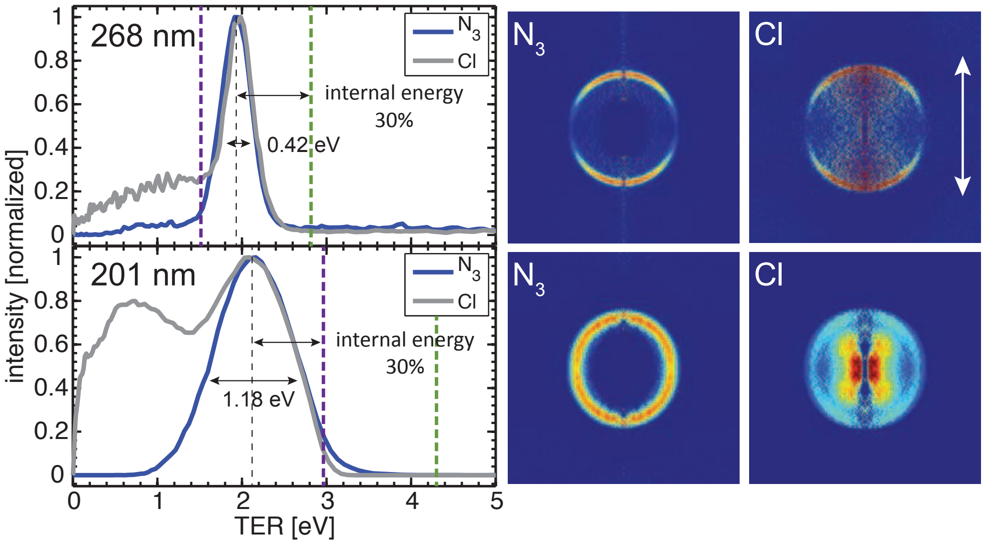

Figure 2.19: Translational energy release (TER) of the co-fragments Cl and N_3 at 1 ps for a dissociation wavelength of 268 (first row) and 201 nm (second row) with a probe intensity of ~200 µJ/p. The TER_{max} is indicated as green and purple dashed lines for the linear and cyclic N_3 limits, respectively. On the right the Abel inverted images of Cl and N_3 for these wavelengths and time delay are shown.

dissociation energy of 4.63 eV (268 nm) and the second row the images at 6.17 eV (201 nm). The arrow in the image of chlorine indicates the dissociation laser polarization. The translational energy release (TER) of N_3 and Cl obtained from these images are shown on the left. The TER for the dissociation in two fragments is given by.

$$TER_{fragment} = \hbar\nu - D_0 - E_{i,N_3} - E_{i,Cl}\,, \tag{2.8}$$

where $\hbar\nu$ is the dissociation laser energy, D_0 is the bond energy of ClN_3 and E_i the internal energy of the fragments. Both fragments show in both condition, meaning at 4.63 and 6.17 eV, the same TER distribution indicating that they are co-fragments and coming from the same dissociation channel. The dotted lines show the dissociation limits for producing N_3 linear (green) and N_3 cyclic (purple) obtained by:

$$TER_{max} = \hbar\nu - D_0 \qquad \text{with} \qquad \begin{aligned} D_0^{(lin)} &= 1.86\,\text{eV [22]} \\ D_0^{(cyc)} &= 3.16\,\text{eV [19]} \end{aligned} \tag{2.9}$$

at each dissociation wavelength.

At 268 nm TER_{max} is 2.77 eV and 1.47 eV for N_3 linear and cyclic, respectively and using 201 nm we obtain a TER_{max} of 4.31 eV and 3.01 eV for the case of linear and cyclic N_3 respectively. From the graph we see that both fragments are produced with a TER of 1.98 eV in the case of 268 nm and with a bandwidth of around 420 meV. This is well below the dissociation limit for N_3 linear at 268 nm but above the one for N_3 cyclic indicating that at 268 nm we are detecting N_3 in its linear configuration with ~ 420 meV of vibrational and rotational energy. In contrary at 201 nm the fragments are produced with an TER centered at 2.1 eV with a much larger bandwidth of 1.18 eV. Furthermore, the detected TER at 201 nm is more than 1 eV lower than the dissociation limit for N_3 linear indicated by the green dotted line and more in agreement with the dissociation limit of N_3 cyclic (purple line). Based on the energy threshold this is the first indication that N_3 at 201 nm is maybe produced in its cyclic form with a huge distribution (∼1.18 eV) of vibrational and rotational energy. Next we will discuss the time dependency of these components and as well the time dependency of the angular distributions seen in the Abel inverted images on the right of Figure 2.19.

2.4.1 The rising of N_3 linear and cyclic

Figure 2.20 shows the translational energy release TER of the fragment N_3 at 268 and 201 nm as function of the delay between the dissociation and ionizing laser for both, parallel and perpendicular configuration. Shown are the TER just outside the cross-correlation time (indicated by the shaded area around zero) at 150 fs and far away at 1 ps. Around zero up to 500 fs images were taken each 50 fs and sometimes even each 25 fs, whereas at longer delays the step was increased to 200 fs. As this makes the time-resolved data not equidistant, to plot the intensity maps the data was interpolated at longer delays where the step was not 50 fs and should be regarded for representation purposes only.

To determine the rising time of N_3 and therefore the dissociation time of ClN_3 at both dissociation wavelengths the area under the peak corresponding to this contribution (see blue area in Figure 2.20) was extracted. As one can see in the cuts shown in Figure 2.20 on the right at 150 fs, there are lower energetic components shown in green and purple. In order to get a more accurate rising time of the neutral fragments Cl and N_3, these components have to be taken into account. For this analysis the TER distribution is fit by

$$TER = \sum_{i=1}^{3} a_i e^{-\frac{1}{2}\left(\frac{x-x_{0i}}{w_i}\right)^2} \tag{2.10}$$

which is a sum of three gaussians where $i = 1,2,3$ corresponds to the three contributions we can identify in the TER distribution at short delays (purple, green, blue). The area under the third gaussian (blue) that corresponds to the ionization of the neutral N_3 fragment is shown in Figure 2.21 as function of the time delay. To extract the dissociation time, this transient is fitted by the same function introduced in Eq. (2.6) which was an exponential rising function corrected by an error function to take the cross-correlation into account. It is important to remind, that each study in the pulsed mode of the VMI is started by a quick ion scan over the TOF to record precisely the time zero between the two laser pulses and the cross-correlation time on argon.

The shaded blue area in the graph represents the FWHM of this cross-correlation function determined on Ar. The extracted dissociation time at 268 nm is 262 ± 38 fs and 252 ± 30 fs for parallel and perpendicular configuration, respectively. This refers again to the polarization of the 803 nm ionization laser polarization relative to the pump polarization. It is quite important to check that these values are the same to rule out any alignment of the fragments due to the intense probe pulse itself as mentioned before. The dissociation time at 201 nm is 178 ± 22 fs

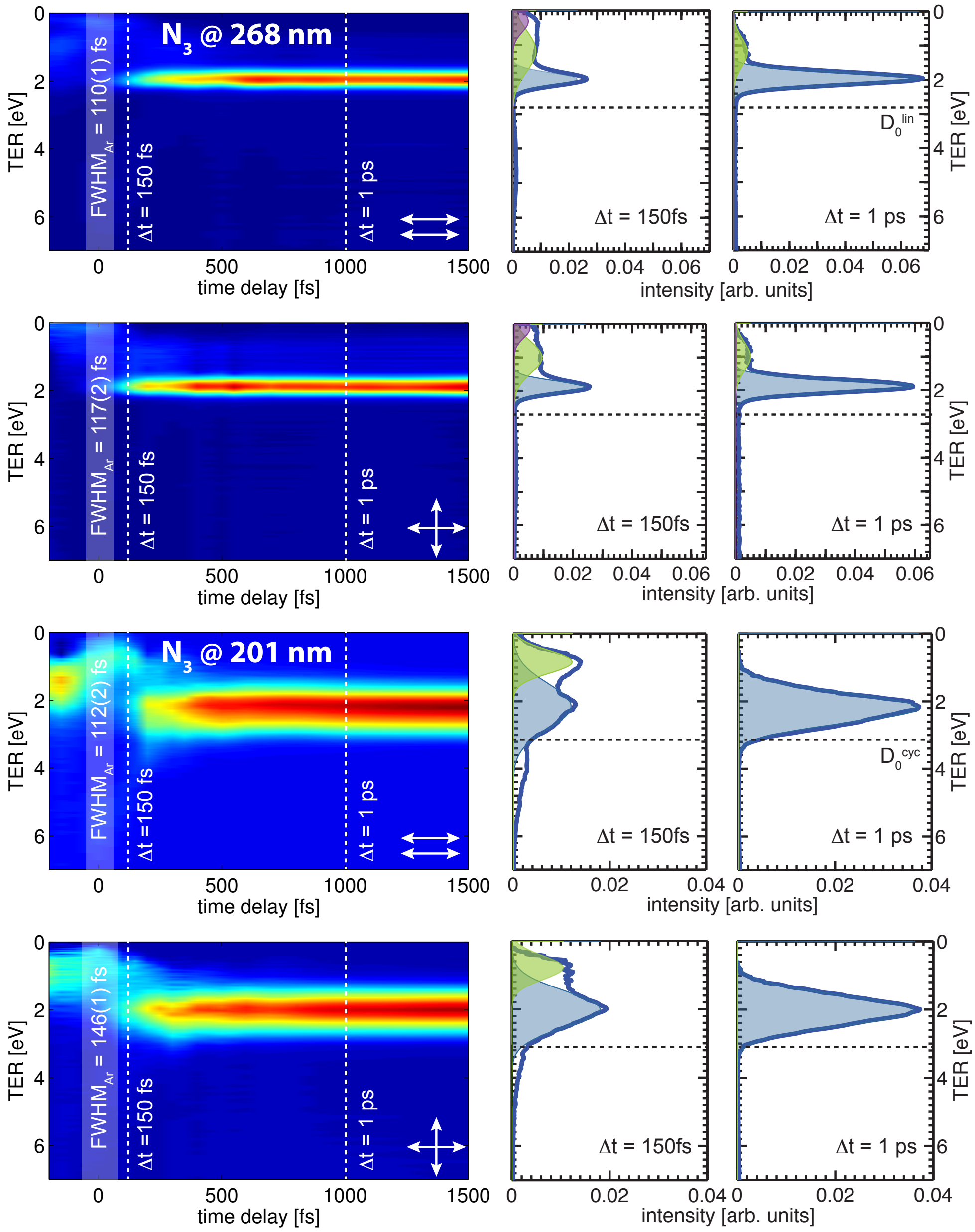

Figure 2.20: Translational energy release TER of the fragment N_3 at 268 and 201 nm as function of the delay between the dissociation and ionizing laser for both, parallel and perpendicular configuration.

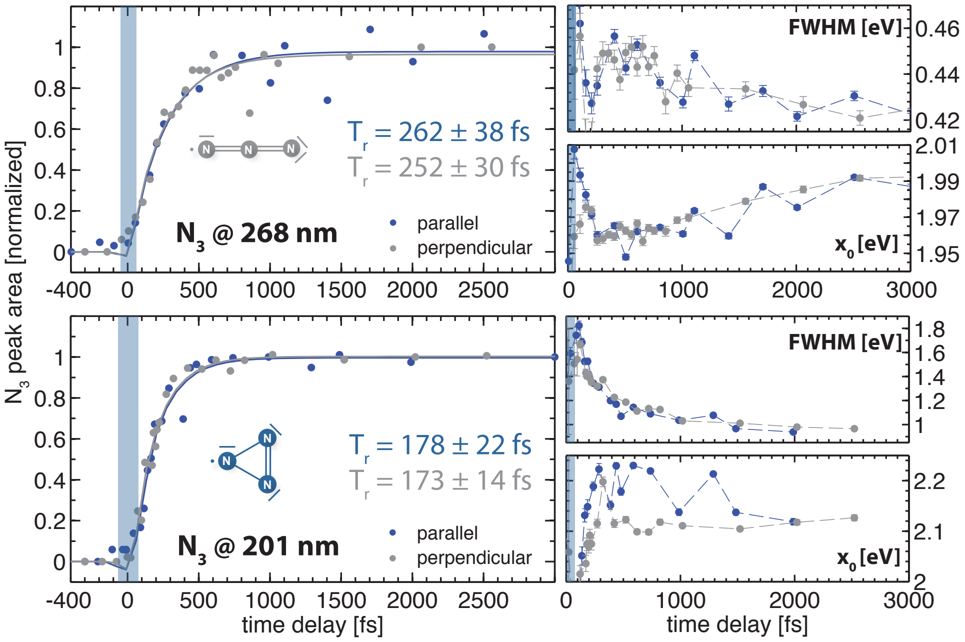

Figure 2.21: Time dependences of the N_3 fragments at 268 and 201 nm recorded two configurations, where the 803 nm probe polarization is either parallel or perpendicular to the pump polarization and detector plane. On the right: FWHM and peak position from the fit as function of the pump-probe delay.

and 173 ± 14 fs for parallel and perpendicular configuration, respectively, and therefore about 80 fs faster than in the case of dissociation with 268 nm. At both dissociation wavelengths the difference between parallel and perpendicular configuration is insignificant. It safe to say that the intense 803 nm probe pulse doesn't introduce any artifact. On the right side of Figure 2.21 the FWHM and the position of the maximum x_0 of the main contribution is shown. In the case of 268 nm the FWHM outside the cross-correlation is not changing a lot and an average of 0.437 ± 0.012 eV and 0.438 ± 0.012 eV for parallel and perpendicular configuration, respectively, can be obtained.

The position of the maximum of this main contribution seem to increase slightly with time but only by 1,7%, which is nevertheless slightly larger than the standard deviation of the average of the maximum given by 1.972 ± 0.014 eV. For cyclic N_3 at 201 nm the FWHM decreases during the dissociation time from 1.8 to 1 eV. Taking all values after the dissociation ($\sim$ 180 fs), from 200 fs till 2.5 ps we get an average FWHM of 1.12 ± 0.13 eV and 1.16 ± 0.15 eV in parallel and perpendicular configuration, respectively. The position of the maximum is given by 2.17 ± 0.05 eV in parallel and 2.03 ± 0.03 eV in perpendicular. However, it is important to note that in this energy region a $\Delta E \sim 0.02$ eV corresponds to $\sim$1 pixel shift in the radius of the image. As we don't have a pixel energy resolution the change of the position of the main peak observed here of $\sim$0.05 eV is negligible and in the resolution limit of our detection.

The lower energetic components

The fit parameters for the lower energetic components which were subtracted from the main peak around 2 eV are shown in Figure 2.22. The area under this gaussian fit is normalized to

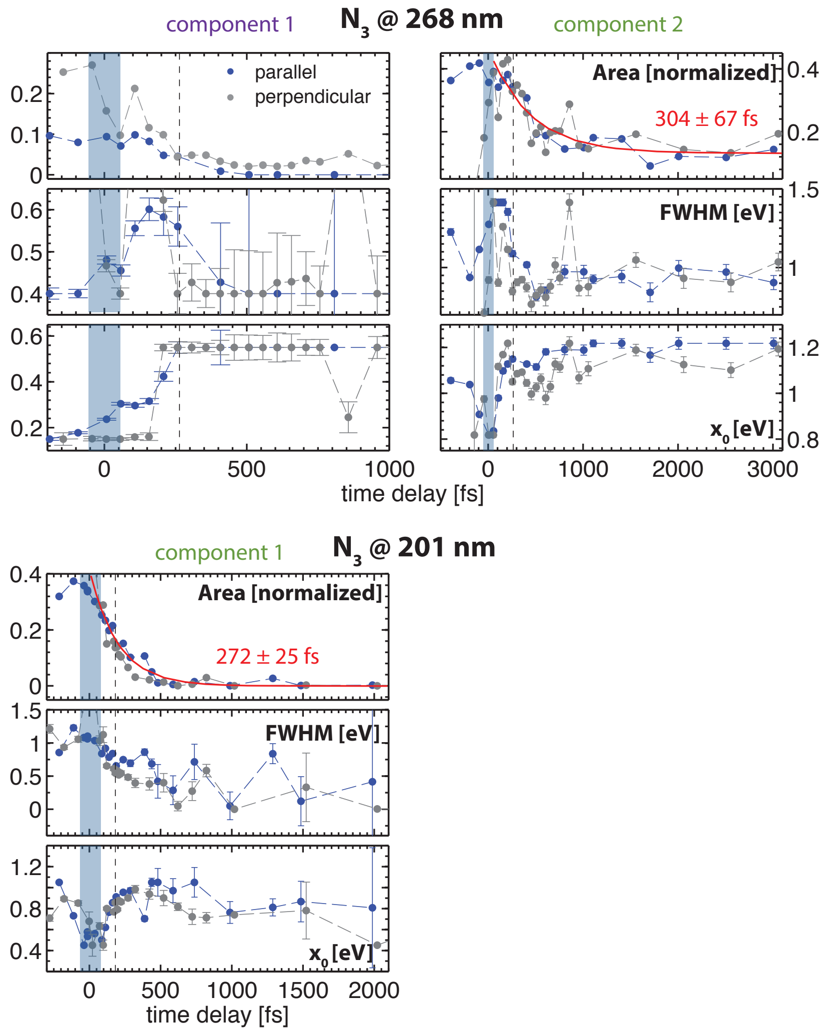

Figure 2.22: Time dependence of the lower energetic components. At 268 nm there are two components marked as purple and green and at 201 nm only one (green). Shown are the area under the curve, normalized to the area under the main peak, the FWHM and the position of this contribution.

the area of the main contribution. The first lower energetic component at 268 nm (purple, see Figure 2.20) has a TER of around 0.55 eV and is only around 10% of the main contribution around time zero. It disappears basically after the dissociation time indicated as dashed lines. The FWHM of the cross-correlation on Ar is again shown as the shaded blue area. The second component (green) around 1.2 eV doesn't go to zero but it only accounts 20% of the main contribution. The peak width (shown is the FWHM) and the peak position seem not to vary a lot with the time delay. At 201 nm we can observe only one lower energetic component (green) around 0.8 eV. Its contribution drops to zero during the dissociation time.

Energy analysis summary

The dissociation timescale observed on the neutral N_3 fragment is the same whatever the polarization configuration of the 803 nm probe pulse. We observe a faster dissociation time at 201 nm. Both dissociation times are more than twice longer than the time observed on the full integrated signal (Figure 2.16, Figure 2.18). This lets us conclude that in the case of detecting the TOF as function of time a detection threshold exists that limits the detection of all the masses produced. Indeed the maximal value on the MCP is fixed by the gain of the preamplifier and the largest signal (NCl^+). On the contrary for the pulsed mode, the choice of MCP voltage is mass dependent and in general was fixed to the maximum allowed namely 1500V. The extra components on the TER at lower energies are most likely due to dissociative ionization as they disappear on a similar timescale as the dissociation time. The long decay reveals that the dissociation is not a direct dissociation as suggested before [17]. Indeed, a direct dissociation would occur roughly on half of the Cl-N_3 stretching period which is only 30 fs ($\nu_{stretch}$ = 545 cm^{-1} = 61 fs). The fact that the relaxation dynamics can be followed whatever the electronic state encountered, means that dissociative ionization is not sensitive to the electronic character, but simply depending on the amount of excited parent molecules. Maybe an ionization experiment, recording the fragments and the photo-electrons at the same time could reveal properly the electronic states encountered.

2.4.2 Time-dependence of the N_3 photofragment angular distribution

More important than the time-dependency of the intensity of the fragment is the angular distribution. As we have seen in Section 1.2 the dissociation is sensitive to the relative alignments of the laser polarization and the molecular dipole moment. In general a linear polarized laser will preferentially excite molecules with their dipole moments parallel to its polarization. By looking at the angular distribution we can distinguish if the dissociation goes via an excited state with a parallel or perpendicular transition. Figure 2.23 (A) shows the Abel-inverted image of the N_3 fragment at the dissociation with 268 nm at a time delay of 1 ps outside of the dissociation time. The angular distribution is analyzed by first converting the radial image into a radius versus angle plot (Figure 2.23 (B)) by transforming it into polar-coordinates. After that the area of interest is selected corresponding to the FWHM of the peak in the energy distribution. The corresponding pixels are then averaged and plotted as seen in Figure 2.23 (C). The intensity variation as function of angle is afterwards fitted by:

$$I(\theta) = 1 + \beta_2 P_2(\cos\theta), \qquad P_2(x) = \frac{1}{2}(3x^2 - 1) \tag{2.11}$$

where β_2 is the anisotropy parameter and $P_2(x)$ the second Legendre polynomial. The anisotropy parameter β_2 can take values between -1 and 2 where the two extreme values corresponding to a perpendicular or parallel transition, respectively, as seen in Section 1.2.4.

Figure 2.24 shows the extracted β_2 parameter at a dissociation with 268 and 201 nm each using a parallel (blue) and perpendicular (grey) 803 nm probe pulse. One can identify three areas. The blue area in the graph represents again the FWHM of our cross-correlation time determined on Ar. Outside this cross-correlation time we can identify 2 areas, in which the β_2 parameter is changing with increasing time delay and one in which β_2 stays almost constant. The vertical dashed line represents the dissociation time determined in the previous section. In the case of linear N_3 at 268 nm one can extract a β_2 parameter of $\beta_2^{\parallel}$ = 1.61 ± 0.07 and $\beta_2^{\perp}$ = 1.67 ± 0.05 for a parallel and perpendicular 803 nm probe pulse, respectively by averaging

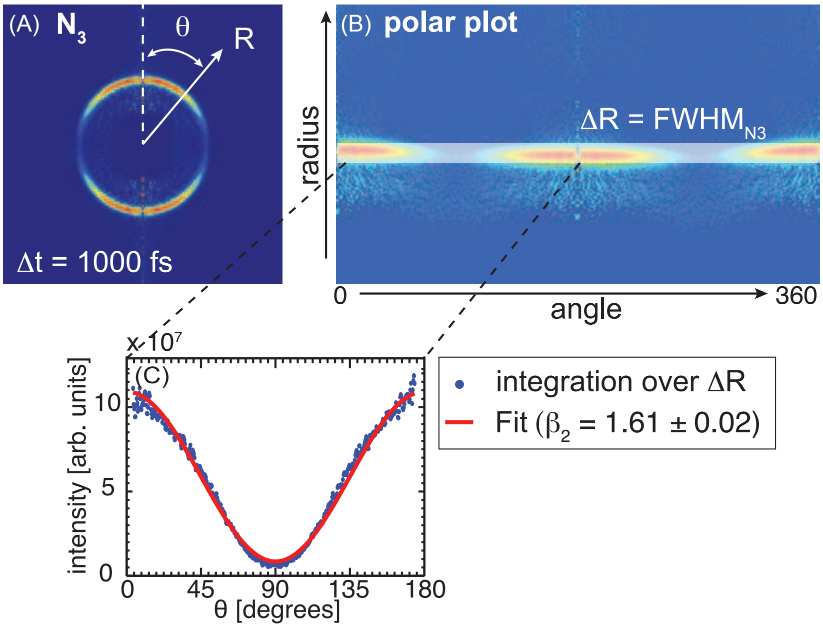

Figure 2.23: Angular distribution anlysis. Shown is the Abel inverted image of N_3 following dissociation at 268 nm at 1 ps. The image is converted into polar coordinates and the intensity of the relevant pixels are then fit by the anisotropy function from Eq. (2.11).

the data points after the dashed line. This compares quite well with the $\beta_2 \sim 1.71 \pm 0.1$ at 266 nm found previously on the chlorine fragment in the nanosecond time regime [31]. Shortly after the initiation of the dissociation we observe a higher β_2, changing rapidly during the dissociation time from 2 to 1.7. An exponential fit ($\beta_2(t) = y_0 + A\exp[-t/\tau]$) gives a time constant of this changing β_2 parameter at 268 nm of $\tau_{268} = 170 \pm 45$ fs and is therefore slightly faster than the dissociation time (~260 fs). The fact that it is starting at a $\beta_2 = 2$ suggests that this dissociation is initiated by a parallel transition $B^1A' \leftarrow X^1A'$ from the ground state to the second excited state of ClN_3 which is also in agreement with the results in the ns- regime on chlorine.

If the fact that we don't measure a $\beta_2 = 2$ but ~1.64 is coming from the rotation of the parent molecule, we can write the anisotropy parameter like[49]:

$$\beta_2 \approx 2P_2(\cos\chi)\frac{1+\omega^2\tau^2}{1+4\omega^2\tau^2} \tag{2.12}$$

where $\omega = (\pi kT/2I)^{1/2}$ is the angular velocity of the parent molecule, I the moment of inertia, and χ the angle between the internuclear axis and the direction of the transition dipole for the final state. Note that this equation assumes that the rotational period of the electronically excited ClN_3 is comparable to the dissociation time τ, thus taking into account the change of the orientation of the dissociation axis with respect to the direction of the polarization of the photolysis laser due to the rotation of the parent. With a measured dissociation time of ~ 257 fs and rotational periods for the parent molecule of ~13 ps for the fast axis and ~150 ps for the two slow axis, this is a tough assumption. Nevertheless, within this assumtion we can extract

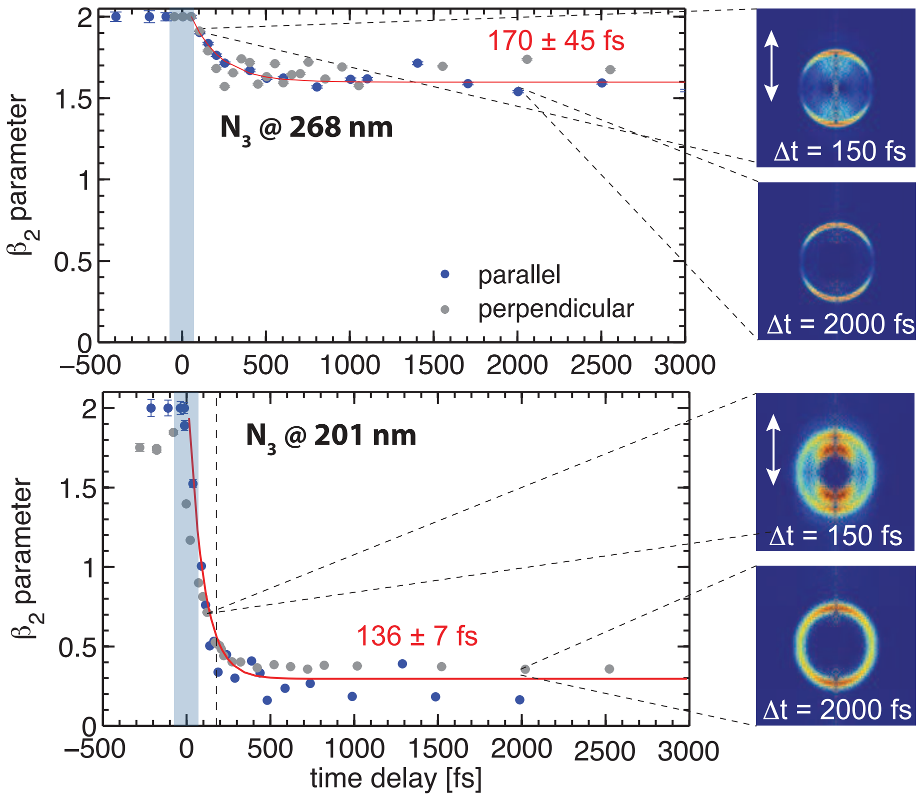

Figure 2.24: Anisotropy parameter β_2 as function of the time delay at 268 and 201 nm each using a parallel (blue) and perpendicular (grey) 803 nm probe pulse. Also shown are each 2 Abel inverted imaged at Δt = 150 and 2 ps. The red line is an exponential decay fit ($\beta_2(t) = y_0 + A\exp[-t/\tau]$) to extract the time dependency.

the rotational temperature given by

$$T_{rot} = \frac{2l}{\tau^2 \pi k}\left(\frac{2P_2 - \beta_2}{4\beta_2 - 2P_2}\right) \tag{2.13}$$

which are calculated to be ∼13 K and ∼141 K using the fast and slow axis, respectively. The ∼13 K rotational temperature is certainly not possible with a continuous molecular beam whereas the ∼141 K sounds plausible but with a 150 ps rotational period this might be too slow to have an impact on the β_2 dependancy. So it is fair to say that this broadening of the angular distribution is not coming from a rotation of the parent molecule, but has to be a signature of the potential energy surface instead.

For cyclic N_3 at 201 nm we can also identify three areas. Here the β_2 parameter reaches a value of $\beta_2^{\parallel} = 0.24 \pm 0.08$ and $\beta_2^{\perp} = 0.31 \pm 0.02$ for parallel and perpendicular configuration, taking the average of the data point after the dashed line (dissociation time). These values are as well in good agreement with the value found on Cl in the nanosecond regime in this wavelength region which is 0.38 ± 0.1 at 234 nm. Here as well it seems that this value is not observed directly, but starting from higher degrees of alignment. Outside the cross correlation we observe $\beta_2 \sim 1$, changing with a time constant of $\tau_{201} = 136 \pm 7$ fs to around 0.3. At long delays the angular distribution is almost isotropic ($\beta_2 \sim 0.3$). This result is

Table 2.4: Anisotropy parameter β_2 for linear and cyclic N_3 from the literature and in comparison to the values obtained in this work. The literature values are obtained detecting either only the chlorine fragments in a VMI in the ns time regime via a REMPI process$^{(a)}$ or by TOF photofragment translational spectroscopy$^{(b)}$. (para) and (perp) refers to the two experimental configurations used in this work.

wavelength [nm]	β_2 linear	β_2 cyclic	Detection	Reference
280	1.85 ± 0.1		Cl ns-REMPI VMI$^{(a)}$	[31]
268	1.61 ± 0.07 (para) 1.67 ± 0.05 (perp)		N_3 fs-VMI	this work
266	1.88 ± 0.1		Cl ns-REMPI VMI$^{(a)}$	[31]
248	1.75 ± 0.1	0.4 ± 0.05	Cl + N_3 TOF PTS$^{(b)}$	[16]
240	1.96 ± 0.1	0.38 ± 0.1	Cl ns-REMPI VMI$^{(a)}$	[31]
235	1.7 ± 0.05	0.39 ± 0.01	Cl ns-REMPI VMI$^{(a)}$	[17]
234	1.71 ± 0.1	0.38 ± 0.1	Cl ns-REMPI VMI$^{(a)}$	[31]
201		0.24 ± 0.08 (para) 0.31 ± 0.02 (perp)	N_3 fs-VMI	this work
193		0.3	Cl + N_3 TOF PTS$^{(b)}$	[30]

very important as it is recorded on a timescale shorter than the rotational period of the parent molecule and therefore, this drastic change cannot be explained by the rotation of the parent molecule. Taking the rotational temperature T_{rot} ~141 K deduced from the data at 268 nm and a dissociation time of 175 fs, we would expect a $\beta_2^{\parallel}$ = 1.8 and a $\beta_2^{\perp}$ = -0.9, which doesn't explain the isotropic distribution observed here. The fact that the anisotropy starts from higher values around 1 and goes during the dissociation time to around 0.3 suggest also a parallel transition $3^1A' \leftarrow X^1A'$ from the ground state to the fourth excited state of ClN_3. Nevertheless, there are two other possible explanations for this drastic change in the anisotropy:

- As there is a third excited state C^1A'' of ClN_3 with a perpendicular transition in this energy region, an evolvement of this state could lead to an anisotropy parameter of 0.3. Indeed if the $S_3(A'')$ and $S_4(A')$ states are both populated at t = 0, then the N_3 fragments will be populated in a superposition:

  $$\beta_2 \sim 0.3 \overbrace{=}^{?} (\beta_2 = 2)P_{3A'} + (\beta_2 = -1)P_{CA''} \tag{2.14}$$

  where P_{state} is the weight of the corresponding state involved. If these two states have different decay times the ratio will be time-dependent. However the rising times is clearly mono exponential.

- The isotropic anisotropy could also reflect the drastic change of the recoil vector of the center of mass of Cl-N_3 relative to the pump polarization, as the molecule has to bent drastically for a possible formation of cyclic N_3. This could be an experimental signature of the cyclic N_3 structure.

We will see that the first explanation is not compatible with the experimental observations presented in Section 2.5. But for this we have first to look at the behavior of the co-fragment chlorine which is presented in the next section.

Table 2.4 gives a summary and overview over the β_2 dependency with the dissociation wavelength from the literature in comparison to the values obtained in this work.

2.4.3 Energy and angular distribution of the Cl fragment

In general the second fragment from a dissociation, in this case chlorine, should show the same behavior as the two species are co-fragments. The chlorine TER as function of the pump-probe delay is shown in Figure 2.25. Scans were recorded as for N_3 at 268 and 201 nm in a parallel and perpendicular configuration of the polarizations of the pump and probe laser. The TER maps shown in Figure 2.25 are again interpolated for long delays as the data was not recorded with an equidistant time spacing. In the parallel configuration for intensities of the probe laser of around ∼200 µJ/p we were not able to collect data with a sufficient high signal to noise ratio to be able to make any conclusions. For instance, Figure 2.25 at 268 nm shows the energy distribution at $\Delta t = 400$ and 450 fs are plotted. At $\Delta t = 400$ fs a signal around 2 eV is observed as expected and at 450 fs the statistic is so bad, that this contribution is in the noise level. The ratio between the dissociative ionization contributions around 0 eV and the TER of chlorine as co-fragment of N_3, which is expected around 2 eV, is also not in favor of the co-fragment. This was the case for both pump laser wavelength, 268 and 201 nm. A multiphoton ionization process is, if no resonance is fulfilled (REMPI), quite inefficient. Moreover, the multiphoton ionization cross-section for atoms is much lower than for molecules. With these two drawbacks it is not surprising that the multiphoton ionization detection scheme using 800 nm is not suitable to detect the chlorine fragment efficiently.

Nevertheless, as seen already before, by rotating the 800 nm probe laser polarization perpendicular to the pump laser, it is easier to separate spatially the dissociative ionization signals from the rest of the signal. This gave, in the case of selecting the integrated ion signals from the TOF data and as well detecting the N_3 fragment, a better contrast and a better signal to noise ratio. We observe the same on the chlorine fragment. Using the perpendicular configuration the data is still noisy but a trend can be extracted as shown in Figure 2.25. The data could be fitted to extract the rising time of the chlorine fragment, in the same way as for the N_3 fragment shown in the section before. Figure 2.26 shows the area of the fit of the contribution around 2 eV for chlorine at 268 and 201 nm. Both parallel and perpendicular configuration are shown in blue and grey, respectively. The cross-correlation time is again shown as the blue shades areas. The dotted lines are only eye guidance, to show the huge fluctuations from one delay to another. The time transients are fitted by Eq. (2.6) introduced in Section 2.3. The dissociation times extracted in the perpendicular case of 276 ± 35 fs and 141 ± 66 fs for 268 and 201 nm, respectively, are quite similar to the ones observed on the N_3 fragment (∼260 fs at 268 nm, ∼170 fs at 201 nm), despite the huge fluctuations and difficulties to detect chlorine. The extracted FWHM of 0.47 ± 0.03 eV and the peak position of 2.00 ± 0.02 eV at 268 nm are also in agreement with the values found on the N_3 fragment using the same dissociation wavelength, as expected. The same is true at 201 nm, a FWHM of 1.05 ± 0.13 eV and a peak

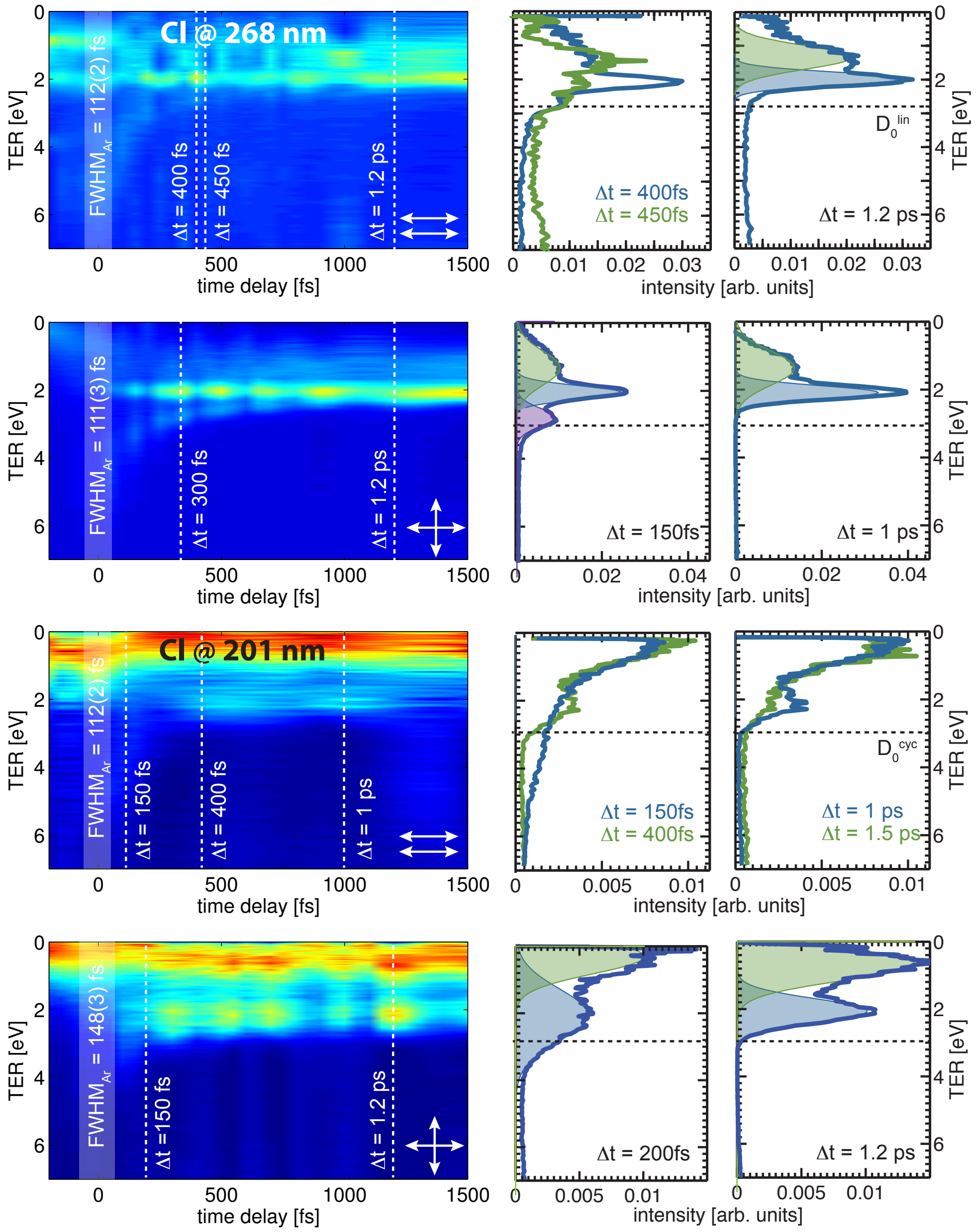

Figure 2.25: Translational energy release TER of the fragment Cl at 268 and 201 nm as function of the delay between the dissociation and ionizing laser for both, parallel and perpendicular configuration. Typical probe intensity is ∼200 μJ/p.

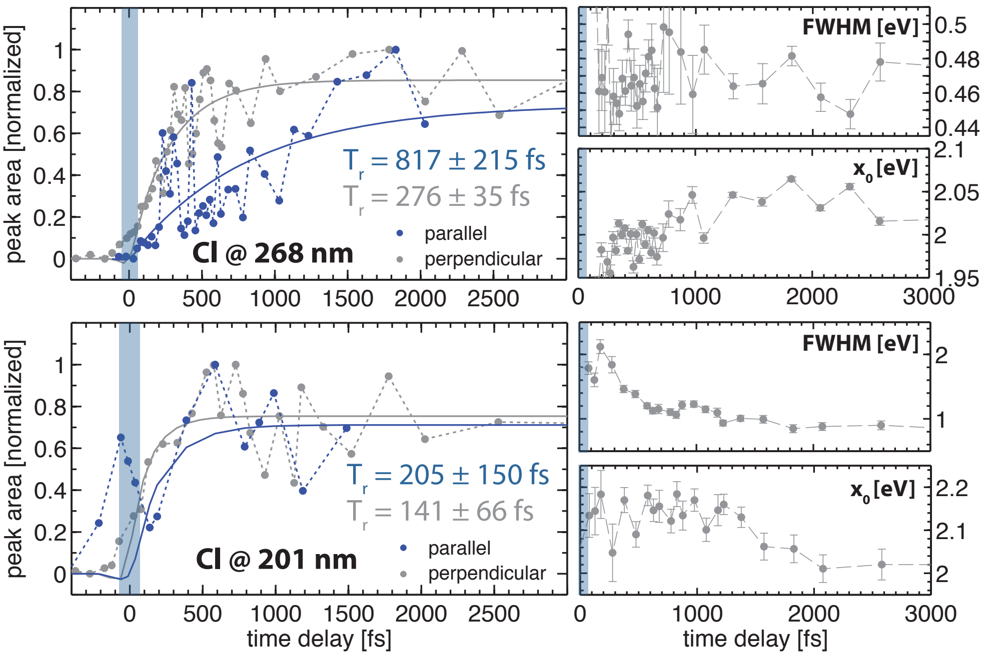

Figure 2.26: Time dependences of the Cl fragments at 268 and 201 nm recorded as well in two configurations, parallel and perpendicular. FWHM and peak position is only shown for perpendicular case.

position of 2.11 ± 0.06 eV is measured for a time window of Δt = 300 fs to 3 ps.

Extracting the angular distribution (β_2 parameter) as function of pump-probe delay obtained from the Abel inverted images of the chlorine fragment was not possible at this probe intensities, especially not for small pump-probe delays. At long pump-probe delays ($\Delta t > 1$ ps) a β_2 of 1.74 ± 0.08 and 0.30 ± 0.03 was obtained at 268 and 201 nm, respectively, for certain delays.

With in the last days of beam time for my Ph.D., the viewport of the VMI vacuum chamber through which both laser beams enter the VMI was changed due to a damage. This increased the transmission of UV pulse by a factor of two and allowed us to use up to 250 μJ/p in the 800 nm probe beam. Figure 2.27 shows the data recorded for the chlorine fragment in the parallel configuration in this new experimental conditions. The intensity of the 800 nm probe beam was probably too high, since we observe for small pump-probe delays a time-dependent energetic contribution. While the kinetic energy assignment of this peak is still a puzzling issue and has to be investigated as function of the pump and probe beam intensities, the angular distribution of this time-resolved scan could be extracted without any trouble for the large pump-probe delays where the peak is not energetically moving as can be seen in Figure 2.27. Clearly the β_2 at long delays is in agreement with the data recorded on N_3 which is shown in Figure 2.27 as grey stared points. This shows that in principle the chlorine fragments is behaving the same way as its counter part N_3 and its a question of efficiently detecting this chlorine fragment, where the multiphoton ionization with 800 nm shows to be not suitable without introducing artifacts due to the high intensities needed. Table 2.5 gives an overview over all measured values for the N_3 and Cl fragments at 268 and 201 nm.

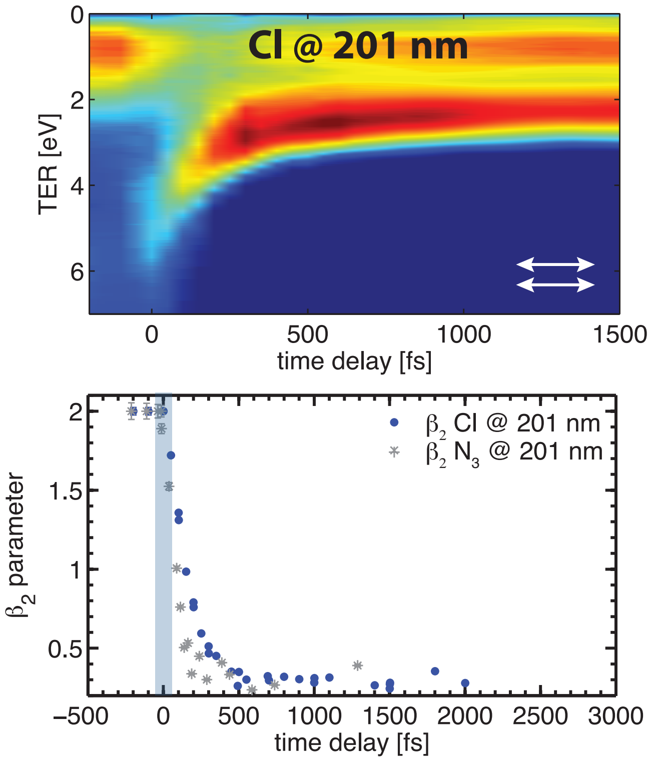

Figure 2.27: (A) Translational energy release TER of the fragment Cl at 201 nm as function of the delay between the dissociation and ionizing laser for parallel configuration with the new viewport and a probe intensity of ∼250 µJ/p. (B) Anisotropy parameter β_2 as function of the time delay 201 nm. Also shown in grey is the β_2 parameter of N_3 at 201 nm.

However, in the case of the photodissociation of ClN_3 at 268 nm in the perpendicular configuration we observed a second contribution in the translational energy release distribution of chlorine at higher energy as can be seen in Figure 2.25 second row (purple fit). This new component will be discussed in the following section.

Table 2.5: Comparison of the extracted experimental values between the two co-fragments N_3 and Cl. The values for N_3 are an average over the parallel and perpendicular configuration, whereas the values for Cl are only from the perpendicular configuration.

		dissociation time [fs]	FWHM [eV]	peak position x_0 [eV]	β_2
268 nm	N_3	257 ± 34	0.437 ± 0.012	1.972 ± 0.014	1.64 ± 0.06
	Cl	276 ± 35	0.47 ± 0.03	2.00 ± 0.02	1.74 ± 0.08
201 nm	N_3	175 ± 18	1.14 ± 0.14	2.10 ± 0.04	0.27 ± 0.05
	Cl	141 ± 66	1.05 ± 0.13	2.11 ± 0.06	0.30 ± 0.03

2.5 Chlorine abnormality at 268 nm

As mentioned before by turning the polarization of the 803 nm ionization probe pulse from parallel to perpendicular to the pump pulse polarization, we found out that not only the detection of chlorine is easier but we were producing at a dissociation wavelength of 268 nm

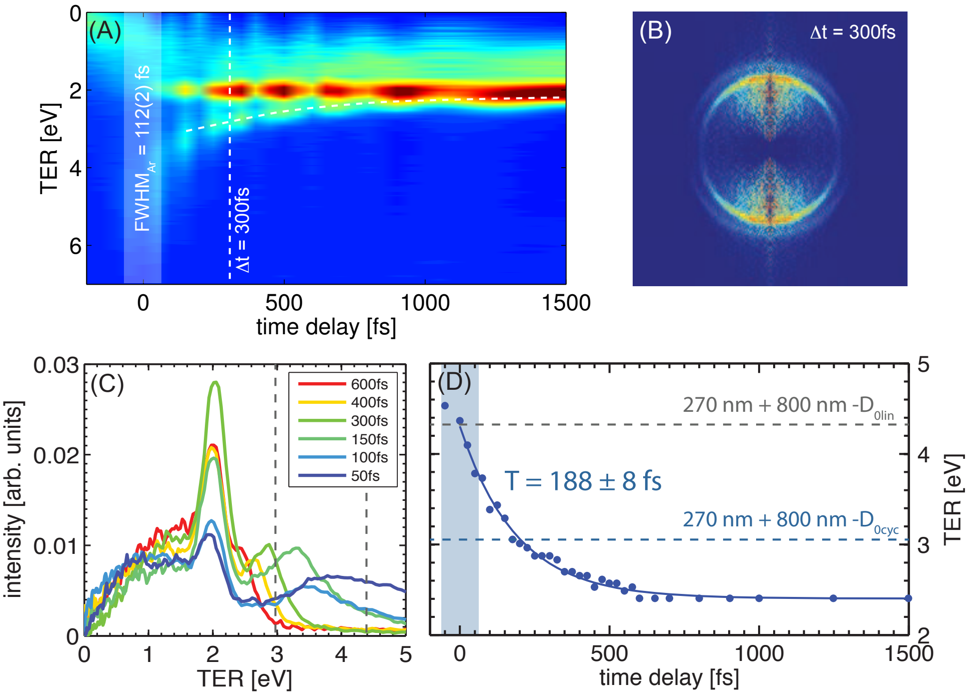

Figure 2.28: Abnormality of the chlorine fragment at 268 nm with an perpendicular 803 nm probe pulse. (A) the TER of the chlorine fragment as function of the time delay in a contour plot. The time axis is stretched and compressed as the data point are not equidistance. (B) Abel inversted image of chorine at a time delay of 300 fs. (C) TER of six delays from 50 to 600 fs in 50 fs steps. The dotted lines are the dissociation limits in the case of the production of linear N_3 at 268 nm (grey) and absorbing an extra 803 nm photon (blue). (D) The translational energy of the extra component as function of the time delay. The dotted lines are the dissociation limits D_L = (268 nm + 803 nm - D_0) using a dissociation energy D_0 for N_3 linear (grey) and cyclic blue, respectively.

an additional component at higher kinetic energy. The contour map of Figure 2.25 second row is again shown in Figure 2.28 (A) with increased contrast. Figure 2.28 (B) shows an Abel-inverted image of chlorine at the dissociation with 268 nm and a perpendicular 803 nm probe pulse at a pump-probe delay of Δt = 300 fs. We can clearly identify this second higher energetic component as a second ring. This new component as shown in the contour plot of Figure 2.28 A where the TER of chlorine is plotted against the pump-probe time delay is changing in kinetic energy and merging with the main contribution over time. Figure 2.28 C shows six cuts through this contour plot at pump-probe delays of 50 fs up to 600 fs. We see that this component is formed above the dissociation threshold for linear N_3 at a dissociation with 268 nm. Figure 2.28 (D) shows the kinetic energy of this component as function of the time delay. The exponential fit gives a time constant of 188 ± 8 fs. This is well below the dissociation time of around 268 fs determined on the N_3 fragment seen in the previous section (Figure 2.21). The blue area shows the cross-correlation time of 111 ± 3 fs of the two pulses. The kinetic energy of this component outside the cross-correlation seems to have exactly 1.55 eV more kinetic energy than the main contribution with is around 2 eV. This suggests that an extra 803 nm photon was absorbed. The dotted grey and blue lines in Figure 2.28 (D) show the dissociation limits for this case (D_L = 268 nm + 803 nm - D_0) using a dissociation energy D_0 for N_3 linear and cyclic, respectively. For the first 200 fs the energy balance shown in Fig-

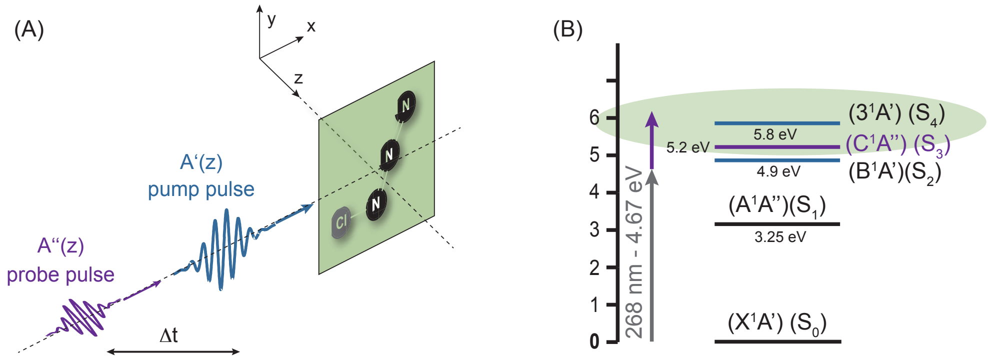

Figure 2.29: (A) pump pulse configuration in the case of an perpendicular 803 nm probe pulse in respect to the molecular plane of ClN_3 selected by the first 268 nm pump pulse. (B) electronic excitation states of ClN_3 reachable with 268 + 803 nm.

ure 2.28 (D) seems in agreement with the production of linear N_3 even though with 268 + 803 nm the excitation energy in total is the same as in the case of 201 nm excitation. Figure 2.29 B shows again the excitation levels of ClN_3. One can recognize the two states accessible in this energy region, the S_3 state with an A'' transition symmetry and the S_4 state with an A' transition symmetry. However, the electronic transition rules allow us to claim that the S_3 state is the main state populated since the polarizations of the 268 and 803 nm beam are crossed. The 268 nm transition to the $S_2(A')$ state at Δt = 0 selects molecular planes containing the pump polarization. This means that in the perpendicular configuration, the probe polarization will be mostly perpendicular to the molecular plane (see Figure 2.29 A). Consequently in the 268 + 803 nm excitation scheme, the second transition from $S_2(A')$ state can be only a perpendicular transition, namely only the $S_3(A'')$ state can be populated. Since the molecular plane is selected by the first transition $S_2(A') \leftarrow S_0(A')$, dissociation taking place from S_3 will still have a anisotropy of $\beta_2 > 0$, even taking into account the perpendicular character of the $S_3(A'') \leftarrow S_2(A')$ transition.

The fact that we can see the contribution from this $S_3(A'')$ state can let us conclude that the dissociation time of this electronic state has to be much faster than the duration of the probe laser. Indeed, if the dissociation from S_3 would be longer than 60 fs we wouldn't be able to absorb all the extra 803 nm photons to ionize the produced N_3 fragment at the same time (9 more photons are needed for ionization). Note that in a parallel configuration of the pump and probe laser beams at 268 + 201 nm, we should access the $S_4(A')$ state like in the 201 nm excitation scheme. On the data recorded in parallel configuration, there is however no obvious contribution observed. This is in agreement with the long lifetime (178 ± 22 fs) recorded for the S_4 state, populated at 201 nm (see Figure 2.21).

To explain the changing in kinetic energy of this component over time we have to look at the contributing energy balance. The translational energy release of this component as function of time can be written as follows:

$$TER(t) = S_3\left(R_{N-Cl}(t)\right) + E_{N-Cl}\left(R_{N-Cl}(t)\right) - D_0^{lin} \tag{2.15}$$

where $S_3\left(R_{N-Cl}(t)\right)$ is the potential energy surface of the C^1A'' state as function of the in-

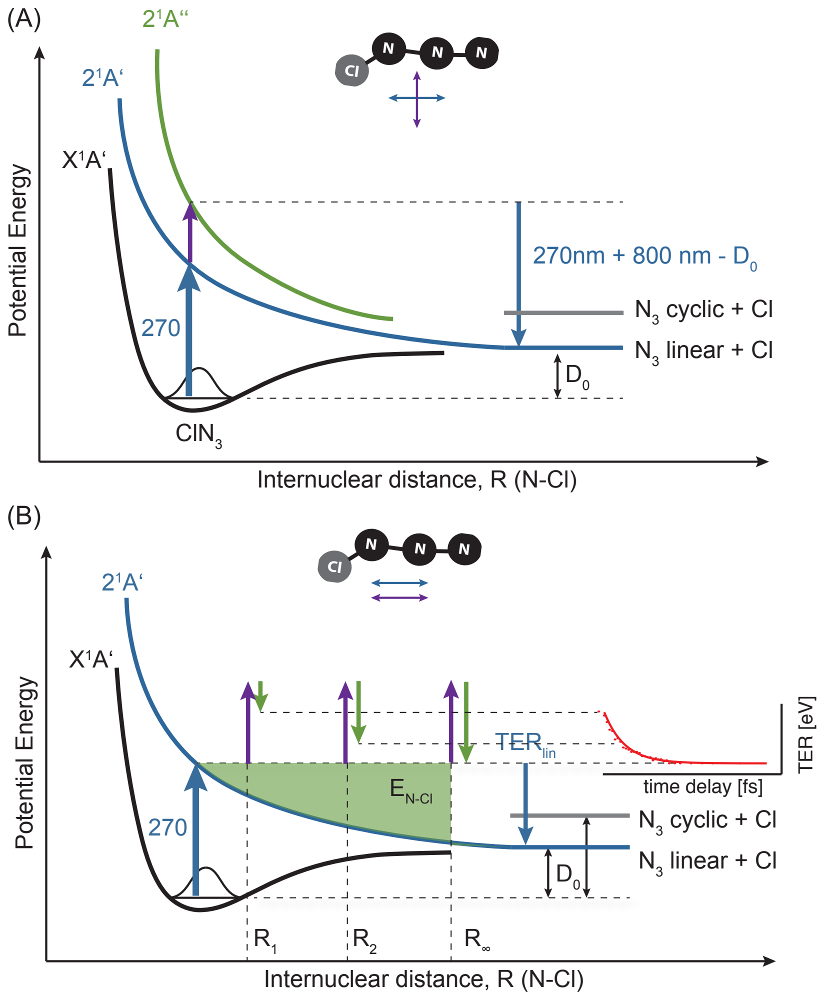

Figure 2.30: (A) schematic potential energy surface diagram for the $2^1A'$ and $2^1A''$ states. (B) showing the increasing energy E_{N-Cl} put into the N–Cl bond with the first 268 nm photon.

ternuclear distance R_{N-Cl} between N and Cl as shown in Figure 2.30, E_{N-Cl} the energy put into the N–Cl bond with the first 268 nm photon and D_0 the dissociation energy of ClN_3 for a linear N_3 production. Indeed, the smooth exponential pattern shown in Figure 2.28 D and taking into account the energy balance before $\Delta t < 200$ fs, D_0^{lin} is the most obvious limit to consider. Taking into account that the $S_3(A'') \leftarrow S_2(A')$ transition takes place on a femtosecond timescale, E_{N-Cl} does not change during this second transition and can be written as the difference between the 268 nm photon energy and the potential energy surface of the $S_2(^2A')$ state:

$$E_{N-Cl}(t) = E_{268\text{ nm}} - S_2\left(R_{N-Cl}(t)\right) \tag{2.16}$$

This energy will increase as a function of the dissociation process taking place along the S_2 potential. Putting Eq. (2.16) into Eq. (2.15) we can write the translational energy release of this component as

$$TER(t) = E_{268\text{ nm}} - D_0^{lin} + [S_3(2^1A'') - S_2(2^1A')]\,(R_{N-Cl}(t)) \tag{2.17}$$

The two first parts are constant and the third one depends on the difference between the two

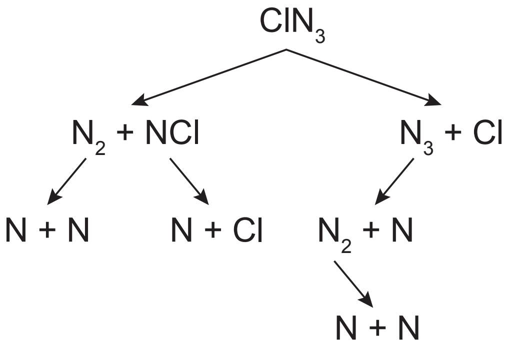

Figure 2.31: Secondary dissociation pathways of ClN_3.

potential energy surfaces (S_3 - S_2). If the surfaces are not parallel to each other this term will produce a time dependent factor which we are observing in the experiment. Looking at the N_3 fragment at the dissociation with 268 nm and a perpendicular 803 nm probe we can't identify this dissociation channel. Which lets us conclude that this channel produces N_3 which is highly excited and dissociated immediately into N_2 + N.

β_2 time dependancy at 201 nm

This observation is quite important if we now consider the β_2 time dependancy observed on the N_3 fragment at 201 nm shown in Figure 2.24. The first explanation was based on the excitation of both S_3 and S_4 states by the 201 nm pump pulse. The short lifetime required to rationalize the excitation at 268 + 803 nm and the absence of the N_3 co-fragment in this excitation scheme lead us conclude that the S_3 state, although being able to be populated, cannot participate in producing an $\beta_2(N_3, \Delta t > 200 \text{ fs}) = 0.3$. The β_2 time dependency at the 201 nm excitation is only due to a dissociation taking place from the $S_4(A')$ state with a huge drastic change of the Cl-N_3 center of mass such that the N_3 photo fragment is produced almost isotropically relative to the pump polarization. This observation is together with the energy balance the second experimental proof of the possible creation of N_3 in its cyclic form.

2.6 The other fragments N, N_2, NCl

Of course a complete picture of the dissociation of ClN_3 would include the other dissociation pathways and a time-resolved analysis of the fragments N, N_2 and NCl. However, this is beyond the scope of this presentation here. We tried to detect also all fragments, which was rather hard to do and we were not able to make a full time-resolved analysis. In Figure 2.32 the Abel inverted images of N, N_2 and NCl are shown at a pump-probe delay of 1 ps for completeness. The kinetic energy release (KER) is also shown. Even if we would have been able to detect these fragments with a better signal to noise ratio it questionable how easy any interpretation will be as these fragments not only come from the primary dissociation pathways but also from secondary dissociation pathways as shown in Figure 2.31.

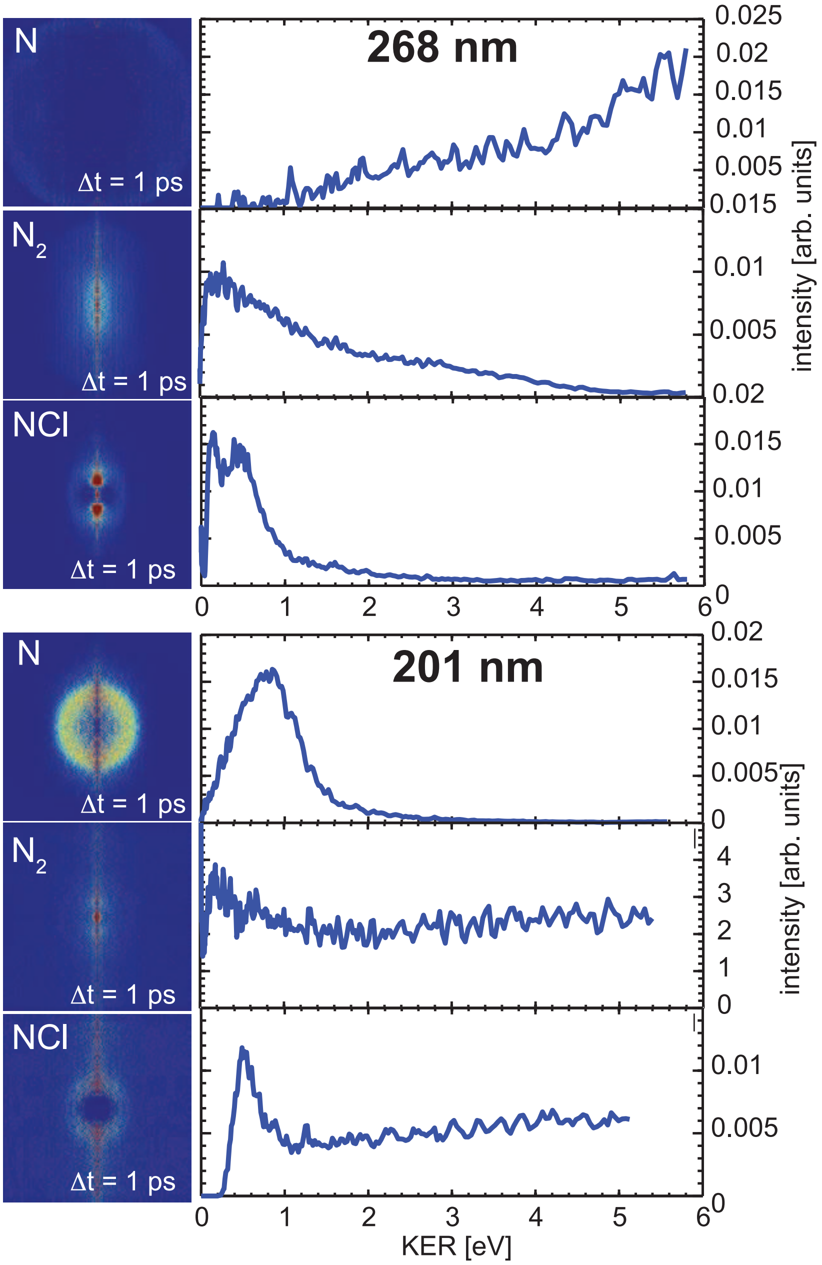

Figure 2.32: Abel inverted VMI images and kinetic energy distributions (KER) of N, N_2 and NCl at 268 and 201 nm for a pump-probe delay of 1 ps.

2.7 Conclusion

The femtosecond time-resolved photodissociation study of ClN_3 was able to detect for the first time the fragments N_3 directly using a velocity-map imaging spectrometer. This enabled us to measure not only the dissociation time but also a time-resolved angular distribution in two major energy regions, using a dissociation energy of 4.67 eV (268 nm), where linear N_3 is produced and 6.13 (201 nm), where cyclic N_3 is produced. The dissociation time was determined to be 262 ± 38 fs and 178 ± 22 fs for linear and cyclic N_3, respectively. Both dissociation times are more than twice longer as the time observed on the full integrated signal detecting the TOF directly. From this we can conclude that in the case of detecting the integrated signal as function of the pump-probe delay, the measurement is filtered in intensity and we are not able to detect the small amount of fragments that are produced. The smooth decay reveals that the dissociation is not a direct dissociation as suggested before [17]. A direct dissociation would occur roughly on half of the Cl-N_3 stretching period which is only 30 fs ($\nu_{stretch}$ = 545 cm^{-1} = 61 fs). The fact that the relaxation dynamics can be followed whatever the electronic state encountered, means that dissociative ionization is not sensitive to the electronic character, but simply depending on the amount of excited parent molecules. Maybe an ionization experiment, recording the fragments and the photo-electrons in coincidence could reveal properly the electronic states encountered.

The angular distribution measured from the N_3 velocity-map image revealed at long delays a β_2 parameter of 1.64 ± 0.06 and 0.27 ± 0.05 for linear and cyclic N_3, respectively. These values are in agreement with previous measurements done in the ns-time regime detecting only the Cl fragment via a REMPI transition. In addition, the time-resolved data shows in addition that these value are not reached immediately. It takes 170 ± 45 fs and 136 ± 7 fs for the linear and cyclic N_3 fragment, respectively, to reach the long delay limits. Unfortunately, the multiphoton ionization detection was not suitable to detect the chlorine fragment with a good signal-to-noise ratio at short pump-probe delays and no in depth time-resolved analysis has been possible so far. However, at long pump-probe delays the β_2 parameter obtained from the chlorine images is in good agreement with the values obtained from the N_3 images. Using a probe pulse with a polarization perpendicular to the dissociation laser delivered a better signal-to-noise ratio and allowed a dissociation time to be determined from the chlorine images, which is comparable, within the error bars, to the dissociation time obtained from the N_3 fragment.

Instead of a multiphoton ionization detection process, it would be ideal to employ a XUV photoionization detection, especially for detecting the chlorine fragment. The next experiment to confirm the formation of cyclic N_3 would be to generate a VUV pulse, such that only N_3 cyclic would be photoionized (VUV tuned to the ionization potential of N_3 cyclic) and to realize a Coulomb explosion with a 10 fs IR laser pulse to detect in coincidence the relative positions of the N fragments, along the lines of the study performed by Hasegawa et al. on CS_2 for instance [50].

References

[1] Griess, P. Proc. R. Soc. **13**: 375–384 (1864) (cited p. 50).

[2] Raschig, F. Chem. Ber. **41**: 4194 (1908) (cited p. 50).

[3] Samartzis, PC and Wodtke, AM. *Casting a new light on azide photochemistry: photolytic production of cyclic-N_3*. Phys. Chem. Chem. Phys. **9**:24 3054 (2007) (cited p. 50).

[4] Tornieporth-oetting, I and Klapötke, T. *Recent Developments in the Chemistry of Binary Nitrogen-Halogen Species*. Comments on Inorg. Chem. **15**:3 137–169 (1994) (cited p. 50).

[5] Ray, AJ and Coombe, RD. *An I* laser pumped by NCl($a^1\Delta$)*. J. Phys. Chem. **99**:20 7849–7852 (1995) (cited p. 50).

[6] Pritt, AT. *Decay kinetics of NCl($b^1\Sigma^+, v'$)*. J. Chem. Phys. **75**:12 5720–5727 (1981) (cited p. 50).

[7] Coombe, RD. *Photodissociation of ClN_3 at 193 and 249 nm*. J. Chem. Phys. **75**:5 2177–2190 (1981) (cited p. 50, 51).

[8] Coombe, RD and Van Benthem, MH. *Radiative rates of singlet–triplet transitions in nitrogen halide diatomics*. J. Chem. Phys. **81**:7 2984 (1984) (cited p. 50).

[9] Benard, DJ, Chowdhury, MA, Winker, BK, Seder, TA, and Michels, HH. *Production of NCl(a) by thermal decomposition of chlorine azide*. J. Phys. Chem. **94**:19 7507–7514 (1990) (cited p. 50).

[10] Ray, AJ and Coombe, RD. *Collisional Quenching of NCl($a^1\Delta, v = 0$) and the Chain Decomposition of ClN_3*. J. Phys. Chem. **98**:36 8940–8945 (1994) (cited p. 50).

[11] Henshaw, TL, Herrera, SD, Haggquist, GW, and Schlie, L. *Kinetics of NCl($a^1\Delta$) via photodissociation of ClN_3*. J. Phys. Chem. A **101**:22 4048–4056 (1997) (cited p. 50).

[12] Jensen, RH, Mann, A, and Coombe, RD. *Energy Transfer from $N_2(v)$ to ClN_3 and a Kinetic Model for the Chain Decomposition of Chlorine Azide*. J. Phys. Chem. A **104**:28 6573–6579 (2000) (cited p. 50).

[13] Komissarov, AV, Manke II, GC, Davis, SJ, and Heaven, MC. *Kinetic spectroscopy of NCl*. Proc. SPIE 3931 **138**: pages (2000) (cited p. 50).

[14] Komissarov, AV, Manke, GC, Davis, SJ, and Heaven, MC. *Rate constants for quenching and self-annihilation of NCl($a^1\Delta$)*. J. Phys. Chem. A **106**:36 8427–8434 (2002) (cited p. 50, 51).

[15] Wodtke, AM, Hansen, N, Robinson, JC, Sveum, NE, Goncher, SJ, and Neumark, DM. *The Cl to NCl branching ratio in 248-nm photolysis of chlorine azide*. Chem. Phys. Lett. **391**:4-6 334–337 (2004) (cited p. 50, 52).

[16] Hansen, N, Wodtke, AM, Goncher, SJ, Robinson, JC, Sveum, NE, and Neumark, DM. *Photofragment translation spectroscopy of ClN_3 at 248 nm: Determination of the primary and secondary dissociation pathways*. J. Chem. Phys. **123**:10 104305 (2005) (cited p. 50, 52, 54, 55, 81).

[17] Hansen, N and Wodtke, AM. *Velocity Map Ion Imaging of Chlorine Azide Photolysis: Evidence for Photolytic Production of Cyclic-N_3^+*. J. Phys. Chem. A **107**:49 10608–10614 (2003) (cited p. 50–52, 54, 78, 81, 91).

[18] Friedmann, A, Soliva, AM, Nizkorodov, SA, Bieske, EJ, and Maier, JP. *A $^3\Pi_u \leftarrow X^3\Sigma_g^-$ Electronic Spectrum of N_3^+*. J. Phys. Chem. **98**:36 8896–8902 (1994) (cited p. 50).

[19] Bittererová, M, Östmark, H, and Brinck, T. *A theoretical study of the azide (N_3) doublet states. A new route to tetraazatetrahedrane (N_4): $N+N_3 \rightarrow N_4$*. J. Chem. Phys. **116**:22 9740–9748 (2002) (cited p. 50, 52, 53, 73).

[20] Bodi, A, Johnson, M, Gerber, T, Gengeliczki, Z, Sztáray, B, and Baer, T. *Imaging photoelectron photoion coincidence spectroscopy with velocity focusing electron optics*. Rev. Sci. Instr. **80**:3 (2009) (cited p. 50).

[21] Mayer, PM, Staedter, D, Blanchet, V, Hemberger, P, and Bodi, A. *Comparing Femtosecond Multiphoton Dissociative Ionization of Tetrathiafulvene with Imaging Photoelectron Photoion Coincidence Spectroscopy*. J. Phys. Chem. A **117**:13 2753–2759 (2013) (cited p. 50).

[22] Quinto-Hernandez, A, Lee, YY, Huang, TP, Pan, WC, Lin, JJM, Bobadova-Parvanova, P, Morokuma, K, Samartzis, PC, and Wodtke, AM. *Dissociative photoionization of* ClN_3 *using high-resolution synchrotron radiation: The N-Cl bond energy in* ClN_3. Int. J. Mass Spec. **265**:2-3 261–266 (2007) (cited p. 50, 52, 54, 56, 66, 73).

[23] Coombe, RD, St, D, Henshaw, TL, and May, DJ. *Generation and quenching of* N_2 $(A^3\sigma + u)$ *in the photodissociation of* ClN_3. Chem. Phys. Lett. **120**:4-5 433–436 (1985) (cited p. 50, 51).

[24] Curtius, T. *Ueber Stickstoffwasserstoffsäure (Azoimid)* N_3H. Chem. Ber. **23**:2 3023–3033 (1890) (cited p. 51).

[25] Douglas, AE and Jones, WJ. *The 2 700 Angstrom bands of the* N_3 *molecule*. Can. J. Phys. **43**:12 2216–2221 (1965) (cited p. 51).

[26] Dyke, JM, Jonathan, NBH, Lewis, AE, and Morris, A. *Vacuum ultraviolet photoelectron spectroscopy of transient species*. Mol. Phys. **47**:5 1231–1240 (1982) (cited p. 51, 55).

[27] Beaman, RA, Nelson, T, Richards, DS, and Setser, DW. *Observation of azido radical by laser-induced fluorescence*. J. Phys. Chem. **91**:24 6090–6092 (1987) (cited p. 51).

[28] Tian, R, Facelli, JC, and Michl, J. *Vibrational and electronic spectra of matrix-isolated nitrogen trimer radical and azide*. J. Phys. Chem. **92**:14 4073–4079 (1988) (cited p. 51).

[29] Lewis, GN. *The Atom and the Molecule*. J. Am. Chem. Soc. **38**:4 762–785 (1916) (cited p. 52).

[30] Goncher, SJ, Sveum, NE, Moore, DT, Bartlett, ND, and Neumark, DM. *Photodissociation dynamics of* ClN_3 *at 193 nm*. J. Chem. Phys. **125**:22 224304 (2006) (cited p. 52, 54, 81).

[31] Samartzis, PC, Hansen, N, and Wodtke, AM. *Imaging* ClN_3 *photodissociation from 234 to 280 nm*. Phys. Chem. Chem. Phys. **8**:25 2958 (2006) (cited p. 52, 53, 79, 81).

[32] Samartzis, PC, Lin, JJM, Ching, TT, Chaudhuri, C, Lee, SH, and Wodtke, AM. *The simplest all-nitrogen ring: Photolytically filling the cyclic-*N_3 *well*. J. Chem. Phys. **126**:4 041101 (2007) (cited p. 52).

[33] Samartzis, PC, Lin, J, Ching, TT, Chaudhuri, C, Lee, YT, Lee, SH, and Wodtke, AM. *Two photoionization thresholds of* N_3 *produced by* ClN_3 *photodissociation at 248 nm: Further evidence for cyclic* N_3. J. Chem. Phys. **123**:5 051101 (2005) (cited p. 53).

[34] Tarroni, R and Tosi, P. *Cyclic and bent electronic states of the* N_3^+ *ion*. Chem. Phys. Lett. **389**:4-6 274–278 (2004) (cited p. 53).

[35] Pahnke, R, Ashworth, SH, and Brown, JM. *Detection of the* N_3 *free radical by laser magnetic resonance at 6.08* μm. Chem. Phys. Lett. (1988) (cited p. 53).

[36] Chambaud, G and Rosmus, P. *Rovibronic spectrum of the* N_3 *radical in the* $X^2\Pi_g$ *state*. J. Chem. Phys. **96**:1 77 (1992) (cited p. 53).

[37] Cook, RL. *Microwave Spectrum and Structure of Chlorine Azide*. J. Chem. Phys. **53**:6 2525–2528 (1970) (cited p. 53).

[38] Quinto-Hernandez, A. *Spectroscopic Studies of Azide compounds: Thermochemistry, Chemical Kinetics and Photodissociation Dynamics*. PhD thesis. University of California, 2012 (cited p. 54, 55).

[39] Hansen, N, Wodtke, AM, Komissarov, AV, Morokuma, K, and Heaven, MC. *Ion dissociation dynamics of the chlorine azide cation (ClN_3^+) investigated by velocity map imaging*. J. Chem. Phys. **118**:23 10485–10493 (2003) (cited p. 55, 66).

[40] Kerkines, ISK, Wang, Z, Zhang, P, and Morokuma, K. *Photodissociation of ClN_3 at 157 nm: Theory suggests a pathway leading to cyclic N_3*. J. Chem. Phys. **129**:17 pages (2008) (cited p. 54, 56).

[41] Zhang, P, Morokuma, K, and Wodtke, AM. *High-level ab initio studies of unimolecular dissociation of the ground-state N_3 radical*. J. Chem. Phys. **122**: 014106 (2005) (cited p. 53, 54, 56).

[42] Schulz, A, Tornieporth-Oetting, IC, and Klapoetke, TM. *Experimental and Theoretical Vibrational Studies of Covalent X-N_3 Azides (X=H, F, Cl, Br, I) - Application of the Density-Functional Theory and Comparison with Ab-Initio Results*. Inorg. Chem. **34**:17 4343–4346 (1995) (cited p. 63).

[43] Maguire, LP, Szilagyi, S, and Scholten, RE. *High performance laser shutter using a hard disk drive voice-coil actuator*. Rev. Sci. Instr. **75**:9 3077 (2004) (cited p. 65).

[44] Scholten, RE. *Enhanced laser shutter using a hard disk drive rotary voice-coil actuator*. Rev. Sci. Instr. **78**:2 026101 (2007) (cited p. 65).

[45] Peng, J, Puskas, N, Corkum, PB, Rayner, DM, and Loboda, AV. *High-Pressure Gas Phase Femtosecond Laser Ionization Mass Spectrometry*. Anal. Chem. **84**:13 5633–5640 (2012) (cited p. 66).

[46] Blanchet, V and Stolow, A. *Nonadiabatic dynamics in polyatomic systems studied by femtosecond time-resolved photoelectron spectroscopy*. J. Chem. Phys. **108**:11 4371–4374 (1998) (cited p. 69).

[47] Gessner, O. *Femtosecond Multidimensional Imaging of a Molecular Dissociation*. Science **311**:5758 219–222 (2006) (cited p. 69).

[48] Thiré, N, Cireasa, R, Staedter, D, Blanchet, V, and Pratt, ST. *Time-resolved predissociation of the vibrationless level of the B state of CH_3I*. Phys. Chem. Chem. Phys. **13**:41 18485–18496 (2011) (cited p. 70, 72).

[49] Gougousi, T, Samartzis, PC, and Kitsopoulos, TN. *Photodissociation study of CH_3Br in the first continuum*. J. Chem. Phys. **108**:14 5742–5746 (1998) (cited p. 79).

[50] Hasegawa, H, Hishikawa, A, and Yamanouchi, K. *Coincidence imaging of Coulomb explosion of CS_2 in intense laser fields*. Chem. Phys. Lett. **349**:1-2 57–63 (2001) (cited p. 91).

3

Relaxation and dissociation dynamics in tetrathiafulvalene (TTF)

Contents

Abstract

Tetrathiafulvalene (TTF, $C_6H_4S_4$) electronic relaxation is studied, while scanning the electronic excitation around 4 eV, by time resolved mass spectrometry and photoelectron spectroscopy. To enhance the sensitivity, the photoionization is achieved at different probe wavelengths (266 nm, 400 nm and 800 nm). With an intense 800 nm pulse the above threshold ionization (ATI) of TTF is studied. Within the internal energy achieved a variety of dissociation channels of the ion are accessible. In order to disentangle the complex ionic dissociation, we utilized the imaging photoelectron photoion coincidence (iPEPICO) technique. Above the dissociation threshold, iPEPICO results show that the molecular ion (m/z = 204) dissociates into seven product ions, six of which compete in a 1.0 eV internal energy window. The chapter starts with an introduction to TTF and its spectroscopy in Section 3.1. Section 3.2 covers the femtosecond electronic relaxation dynamics at various pump and probe wavelength. Section 3.3 presents the VUV dissociation results from the iPEPICO experiment.

Keywords: tetrathiafulvalene, electronic relaxation, iPEPICO, appearance energies, RRKM

3.1 Introduction

3.1.1 Tetrathiafulvalen, an organic conductor

Since discovering the first organic conductors based on tetrathiafulvalene (TTF) in 1972 [1], and metal TTF TCNQ in 1973 [2] tetrathiafulvalene has been among the most studied heterocyclic systems. TTF or $C_6S_4H_4$ and its derivatives are known as efficient π electron-donors [3]. The huge amount of research activity in the 1970s and 1980s was directed toward achieving metallic conductivity and superconductivity in TTF derivatives, although no industrially important TTF-based materials have ever been created. However, new functional TTF derivatives, appealing as photoactive materials designed for rapid intramolecular electron-transfer complexing abilities [4], are being synthesized as component of a variety of molecular devices with new functionalities [5–9] including for example dendrimers [10], molecular wires [11] and conducting microcrystals [12].

An ultrafast, photoinduced phase transition from the insulator phase to the metal phase has been observed in organic salts involving TTF [13]. The challenge in designing molecular systems for photoinduced charge-separation is to minimize undesirable competing side reactions since energy transfer occurs on a short time-scale. This issue is partly clarified by femtosecond-resolved spectroscopy done both on the donor-acceptor system and on the donor alone [14]. Electron diffraction experiments and density functional calculations showed that while TTF^+ and TTF^{2+} have a planar D_{2h} symmetry, neutral TTF has a boatlike equilibrium structure with a C_{2v} symmetry [15–18] as shown in Figure 3.1. However, because of the small difference between planar and boatlike conformations, TTF is very flexible and can appear in various conformations depending on the donor-donor and donor-acceptor interactions in the crystals. The isomerization barrier into the planar conformation of the neutral TTF is only ca 40 cm^{-1} [18]. The coupling between the electron removal and the 'boat' deformation is suggested to play a role in the mechanism of superconductivity with a metallic behavior depending on the intermolecular S-S contacts [17].

One of the fundamental steps in designing molecular systems for photoinduced charge separation is to investigate the primary photophysical relaxation. Spectral studies of fullerenes functionalized by TTF derivatives have been reported in the ultraviolet (UV) range [19], as well as picosecond-resolved absorption spectra [4, 20]. Femtosecond-resolved spectroscopy has been done both on the donor-acceptor system and on the donor alone [14] in liquid phase. For many of these photoactive compounds, made by Van der Waals polarization interactions, the electrons are mostly localized in the highest occupied molecular orbital (HOMO) of TTF [20, 21]. Whilst photoexcitation in the visible range induces in general a charge transfer from TTF to the acceptor functional group (moiety), in the UV range this is slightly different. Indeed, there the electronic relaxation of the TTF moiety alone can compete efficiently with the charge transfer. Nevertheless, in each of the UV studies [4, 19], electronic excitations are reported relative to the excitation of the fullerene moiety, despite the intense oscillator strength in the UV range characterizing the electronic spectrum of TTF molecules [22].

As shown in Figure 3.1 when TTF is ionized, it changes it geometry, and therefore it's sym-

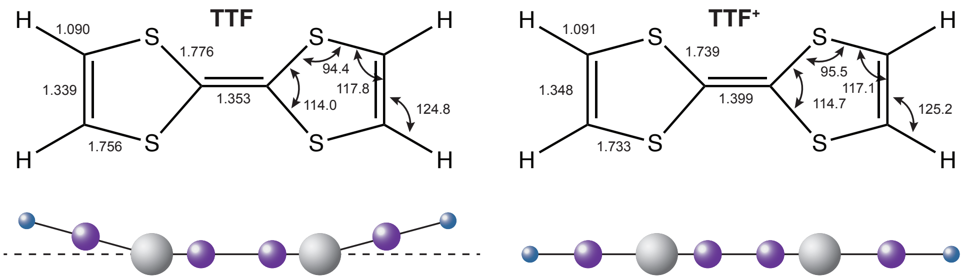

Figure 3.1: Structure of TTF and TTF$^+$ with structural parameters optimized at the B3P86/cc-pVDZ level. Bond distances are given in Å and angles in degrees. TTF shows a boatlike configuration while TTF$^+$ has a planar shape. Adapted from [23].

metry changes as well. Ionized TTF is a planar molecule and belongs to the D_{2h} point group, whereas neutral TTF has a boatlike configuration and therefore is not as symmetric as the planar molecule and belongs to a subgroup of the D_{2h} point group, the C_{2v} point group. The character tables for both point groups are shown in Appendix E. Calculations reveal the change in bond length on ionization, with the central C=C bond, which is lengthened significantly, being the most strong affected [15]. The highest occupied molecular orbital (HOMO) of the TTF molecule [24, 25] is π-antibonding with respect to the C–S bonds and π-bonding with respect to the C=C bonds, thus, in contrast to the C=C bond length increasing, the C-S bond distance decreases.

3.1.2 Absorption spectrum and photo-electron spectrum of TTF

TTF is well-known to be light sensitive with an absorption spectrum exhibiting two close-lying intense peaks at 317 (3.91 eV) and 303 nm (4.09 eV), as shown in Figure 3.2 (A) [22, 26–28]. This has significant effects on the absorption spectra of molecules coupled with TTF, for instance, the two main bands of C_{60} centered at 264 nm and 340 nm are significantly blue-shifted and broadened once coupled to TTF [19]. This pump-probe study of TTF in the gas-phase has employed photolysis wavelengths within this region of TTF's absorption band.

The photoelectron spectrum of TTF has been recorded by several groups reporting a vertical ionization energy I_p of 6.7 ± 0.02 eV and a first excited cation state at 8.58±0.02 eV [24, 29–31]. The dissociative ion continuum has been studied recently up to 13 eV [32]. This which will be presented in Section 3.3. The lowest energy transitions in both TTF and TTF$^+$ have been calculated by CASSCF and CASPT2 methods [33] and time-dependent density functional theory (TD-DFT) [23, 34, 35]. Looking closer at the photo-electron spectrum of TTF one can see that there are several ionization bands close to each other. The first two, as shown in Figure 3.2, are at 6.7 eV and 8.58 eV with a transition symmetry of 1^2B_{2u} and 1^2B_{2g}, respectively [24, 30] as shown in Figure 3.2 (B). Three more excited states were experimentally observed at 9.71 eV (1^2A_u), 10.09 eV (2^2B_{1g}) et 10.51 eV (2^2B_{3u}) [24, 33]. The ground state electronic configuration of TTF is given by [33]:

$$\ldots(2b_{3u})^2(2b_{2g})^2(3b_{3u})^2(2b1g)^2(2a_u)^2(3b_{2g})^2(4b_{3u})^2 \tag{3.1}$$

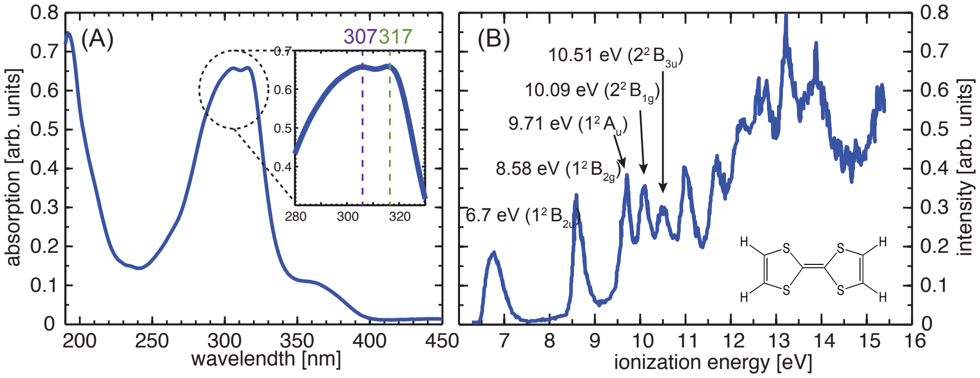

Figure 3.2: (A) Absorption spectrum of TTF in acetonitrile at ambient temperature with a concentration of 5×10^{-4} mol/l. (B) photo-electron spectrum of TTF. Adapted from [24].

The assignment of the two different, but close lying, absorption bands, has never been clear throughout the literature on TTF. Table 3.1 gives an overview of the proposed transitions involved at this wavelength range. Among the four computation results which are included in this table, the only common ground is the identification of the transition to be $\pi \rightarrow \pi^*$. Following the IUPAC convention, in the C_{2v} geometry, the (x,y) axis defines the C_2S_4 plane with the y-axis parallel to the central bond C-C. On the contrary in the D_{2h} geometry, the molecular plane is now the (y,z)-plane with the z-axis defined by the double central bond C-C. By TD-DFT converging to a C_{2v} boat geometry, Fabian assigned the weak absorption band around 368 nm to a $A_1 \rightarrow B_1$ transition (along x) and found only one state lying in the intense double structure at 303 and 317 nm, corresponding to $A_1 \rightarrow B_2$ transition (along y) [33, 34]. The oscillator strengths found at 368 nm and sim307 nm are similar, which goes strongly against the experimental observations. Andreu et al., as well by TD-DFT calculations from a C$_{2v}$ geometry, assigned the two most intense excitations around 303 and 317 nm from the HOMO to the LUMO+5(b$_1$) and LUMO+6(b$_2$), labelled as $^1B_1$ and $^1B_2$ states, respectively [35]. These later calculations match the experimental oscillator strengths as well as the polarization. The calculations use different symmetries which comes from the fact that gas-phase electron diffraction measurements suggested nonplanar C_{2v} 'boatlike' geometry for neutral TTF as seen above, however, theoretical calculations have indicated that TTF is ex-

Table 3.1: Summary of the assignments of the excited states of TTF at 303 and 317 nm

Publication	λ [nm]	assigned transition	symmetry	# states
Fabian [36]	317		C_{2v}	1
TD-DFRT	303	$A_1 \rightarrow B_1(\pi\pi^*)$		
Pou-Amérigo et al. [33]	317	$1^1A_g(4b_{2u}) \rightarrow 1^1B_{1u}(4b_{2g})(\pi\pi^*)$	D_{2h}	1
MS-CASPT2	303	$1^1A_g(4b_{2u}) \rightarrow 1^1B^*_{1u}(4b_{2g})(\pi\pi^*)$		
Batsanov et al. [37]	317	$3b_{3u} \rightarrow 3b_{1g}$ $(\pi\pi^*)$	D_{2h}	2
DFT	303	$3b_{3u} \rightarrow 3b_{2g}$ $(\pi\pi^*)$		
Andreu et al. [35]	317	$1^1A_1(a_1) \rightarrow 1^1B_2(b_2)$ $(\pi\pi^*)$	C_{2v}	2
TD-DFT	303	$1^1A_1(a_1) \rightarrow 2^1B_1(b_1)$ $(\pi\pi^*)$		

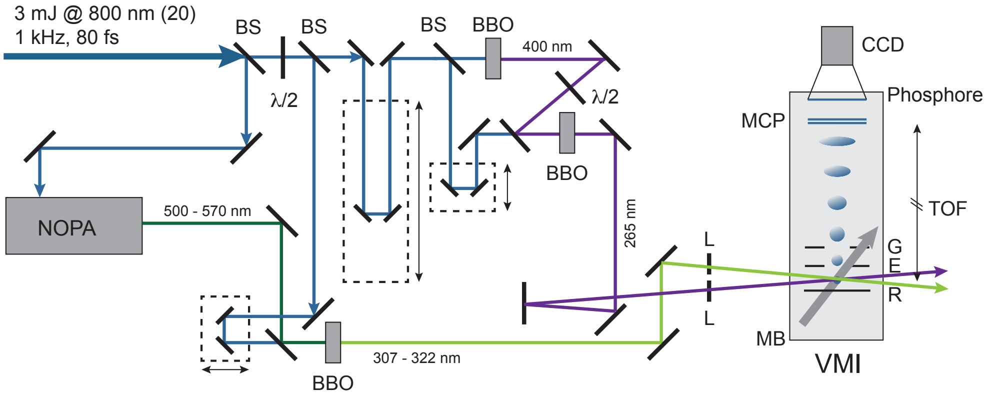

Figure 3.3: Schematic pump-probe fs-UV-VIS VMI setup used for the TTF relaxation experiment. The desired pump wavelengths of 303 to 322 nm are produced by a NOPA and frequency mixing. The probe wavelength is either the fundamental, SHG or THG achieved in BBO crystals. (BS: beamsplitter, BBO: Beta-Barium Borate, P: polarizer, L: lens, $\lambda/2$: half-wave plate).

tremely floppy due to a practically negligible C_{2v} to D_{2h} inversion barrier. Furthermore, in solid state a D_{2h} structure has been proposed by x-ray crystallography [38, 39]. Since the effect of the chosen geometrical structure on the theoretical absorption spectrum has been found to be insignificant. Both symmetries can be found as a basis set in these calculations. Finally, Pou-Armengo et al. did a multistate extension of a multiconfigurational second-order perturbation method (MAS-CAPSPT2) calculation [33] and a TD-DFT calculation [23] with an optimized geometry in the D_{2h}. They validate this geometry by the weak isomerization barrier with C_{2v}. They found with both calculations that the UV spectrum corresponds to $\pi \rightarrow \pi^*$ one-electron excitation from the HOMO. Around 382 nm, they predict a short-axis ($x \rightarrow y$ in the D_{2h}) polarized weak transition $1^1A_g \rightarrow 1^1B_{2u}$ and around 290 nm, an intense one, polarized along the long axis ($y \rightarrow z$ in the D_{2h}) to the 2^1B_{1u} state. The double structure at 303 and 317 nm is either explained by the presence of a Rydberg state [23, 33] or a vibrational structure in the 2^1B_{1u} band [40]. In addition, the vibrational mode suggested by Kerkines et al. is a strengthing mode on the C=C axis and has an energy of around 200 mV [15, 41], which is in good agreement with the experimental energy difference of the two absorption features.

3.2 Time-resolved electron relaxation dynamics in TTF

3.2.1 The fs-UV-VIS-VMI setup

The experimental setup for TTF is shown in Figure 3.3. The setup is basically the same as used for the dissociation of ClN_3 and described in Section 2.2.2. The difference are the used wavelength and how they are produced. Before the experiment the laser is again split into two beams to generate the pump and probe pulses which are now in comparison to before inverted. The probe beam is going though a long translation stage enabling time resolved measurements by varying the time delay between the two pulses.

The relaxation dynamics of TTF will be initiated between 303 up to 322 nm (4.09 eV - 3.85 eV). To create these wavelength a 400 nm-pumped non-collinear optical parametric amplifier

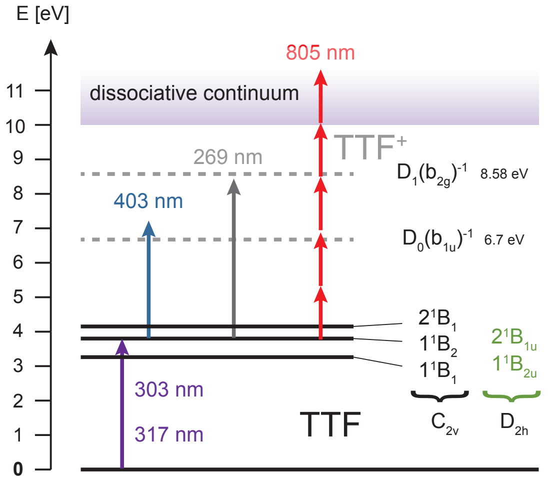

Figure 3.4: Different experimental pump-probe excitation schemes used for TTF. Electrons states of neutral TTF are shown in black and electronic states of the ion are displayed in grey.

(NOPA), with three-steps of amplification provides a 30 μJ/p pulse, tunable between between 500 and 700 nm, is used. A fused-silica pair of prisms in double path is used to for compression. The duration is measured to $\approx$ 80 fs by autocorrelation via a 50 µm BBO crystal. The UV pump pulse is produced by a subsequent sum frequency mixing (FM) or second harmonic (SHG), allowing a tuneability of the pump pulse from 370 to 300 nm. This is achieved through a 200 µm BBO crystal by focusing gently a 50 µJ part of the fundamental beam with about 15-18 µJ/p visible pulse, resulting in around 5-7 µJ/p UV pulse. The typical pulse bandwidth in the UV range is of 150 cm^{-1} ($\simeq$2 nm), that would correspond to FWHM $\sim$70 fs. However no prism compression is used to pre-compensate the chirp introduced by the different optics crossed by the UV pump pulse (mostly the vacuum chamber viewport and the BBO crystal). The probe pulse is either the fundamental pulse, its second harmonic (SHG- 40 µJ/p) or third harmonic (THG- 6 µJ/pulse). The Fourier-limited durations expected for these pump and probe pulses from their bandwidths are of 65 fs. The pump and the probe are focused on the molecular beam by 250 mm and 500 mm focal lengths, respectively, and combined with an angle of 7 ° between them.

The TTF molecules (Aldrich, 97% without further purification) are sublimed continuously at 380K with 200 Torr of Argon and then expanded through a 250 µm nozzle at 450 K to avoid cork formation. In most of the experiments presented here the polarizations are parallel to each other and parallel to the detector. For each pump-probe delay, an average over 210k laser pulses is done over 5 scans.

In the present experiment, the wavelength of the pump is varied from 322 nm to 307 nm as mentioned before. The idea is to reveal the possible change of the electronic character via a change in the measured decay time. As expected from the electron donor propriety of this compound, the two first vertical ionizations from the ground electronic state lie quite low at 6.7$\pm$0.02 eV and 8.58$\pm$0.02 eV [24]. They are as ssen before, assigned mainly to the departure of an electron from the highest occupied molecular orbital $b_{1u}(\pi)$ (HOMO) and the second highest occupied molecular orbital $b_{3g}(\pi)$, respectively. The excitation scheme is summarized

Table 3.2: The maximum kinetic energies possibly for the photoelectron kinetic energies for a pump wavelength centered at 317 nm and an IP_1 = 6.7 eV and IP_2 = 8.58 eV.

Probe wavelength [nm]	Excitation scheme	IP_1 [eV]	IP_2 [eV]
267	(1+1')	1.85	0
398	(1+1')	0.32	not reached
398	(1+2')	3.44	1.56
317	2	1.12	not reached
267	2'	2.58	0.71
398	3'	2.58	0.71
800	5'	1.0495	not reached

on Figure 3.4. One THG photon at 266 nm is enough to probe the wave packet dynamics onto the ground state of the ion or on the threshold of the first excited state. On the contrary, when photoionization takes place with a SHG probe (400 nm), only the ground state of the cation is reached at one photon and with an 800 nm probe pulse, multiphoton ionization is required. The excitation scheme used is shown in Figure 3.4. Table 3.2 summarizes the maximum kinetic energies we can expect for the photoelectron kinetic energy with the different probe pulses used. In pump-probe, the configuration encountered with the 800 nm probe pulse will be a combination of the 398 nm and 267 nm. Note that any energy above 2.2 eV, the maximum kinetic energy allowed by the detector size, won't be detected.

3.2.2 A probe centered at 266 nm

Figure 3.5 shows the TTF^+ ion signal as a function of the pump-probe delay after an excitation with wavelengths from 307 to 322 nm. In this excitation scheme, the mass spectra shows only one contribution that is the parent cation. Figure 3.5 (B) shows the typical $C_6S_4H_4^+$ ion signal recorded with a pump pulse of 317 nm and as well the DMA^+ signal through which the time overlap is determined. The transient parent ion signals are fit by assuming two components, a non-resonant contribution for the cross-correlation and a resonant decay component, comparable to what has been used in Chapter 2 Eq. (2.3), such that:

$$S_{fragment}(t) = y_0 + \Psi_{cc}(t) + \Psi_d(t) \tag{3.2}$$

where Ψ_{cc} is the cross-correlation function to take into account the cross-correlation time T_{cc} defined like in Eq. (2.4) (see Figure 3.5 (B) blue dotted line). The crosscorrelation time is determined by a step function fitted to the N,N-Dimethylaniline reference (Figure 3.5 (B) grey curve). The decay part is given by an exponential function corrected by an error function like Eq. (2.5), shown in Figure 3.5 (B) on the TTF^+ transient at 317 nm as dashed blue line.The cross-correlation between the pump and the THG probe is recorded through (1'+1) photon ionization of N,N-Dimethylaniline (DMA) resonant at 265 nm with a low 3s Rydberg state [42, 43]. Indeed, the difference between the ionization potential and the onset of the band is around 2.8 eV, a gap easily exceeded by the THG pulse. This ion transient allows to determine precisely the time-overlap between the pump and probe pulses. The cross-correlation time

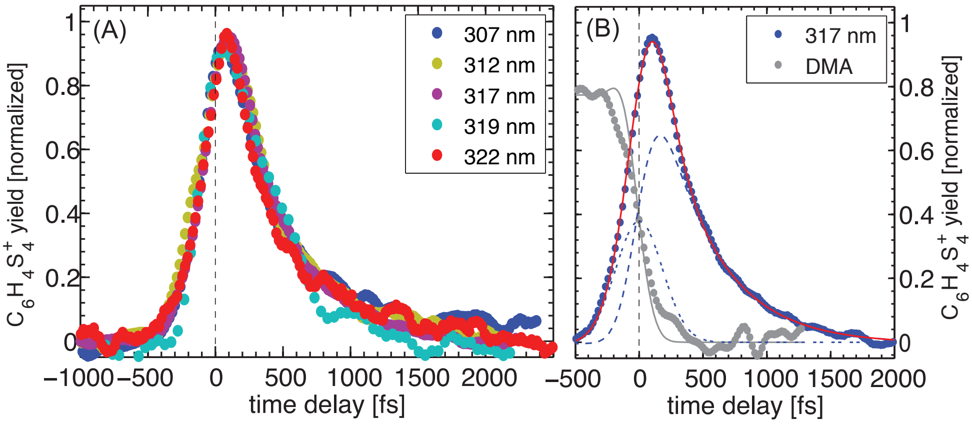

Figure 3.5: (A) Femtosecond time-resolved transients of TTF^+ as function of the pump pulse wavelength with a probe pulse centered at 266 nm. (B) The time overlap (Δ t = 0 fs) and the cross-correlation time of this UV-UV pump-probe excitation are both extracted from 3s-Rydberg excitation of the N,N-dimethylaniline at 266 nm that produces a long lifetime transient (triangle grey curve). Also shown is the TTF^+ time transient at 317 nm and the fit curve from Eq. (3.2) (red curve), cross-correlation component (green) and decay component (blue).

extracted by fitting the step function of the DMA cation is 320 ± 20 fs. This reveals the strong positive chirp expected for the UV pump pulse, as well as the UV probe pulse. The cross-correlation time between the pump and the SHG might be deduced from the TTF signal itself, as discussed further, while the ones between with the fundamental pulse is measured through the TTF_2^+ signal. Typical cross-correlation times with these two probe pulses are slightly less than 300 fs.

From Figure 3.5 (B) we see that the decay time is not depending on the pump wavelength in the energy region invstigated. The decay time measured is 437 ± 7 fs and corresponds to electronic coupling onto lower electronic states. The photoelectron distribution displayed on Figure 3.6 reveals that photoionization occurs to both cation states with a drastic vibrational limitation for the first excited cation state since ionization can take place only at threshold. In the one color two-photon ionizations from the ground electronic state of TTF, cations are produced in both cation states with the same probability, as can be seen in the photoelectron distribution at 267 nm shown(see the distribution recorded at 267 nm) and with all the possible binding energy available as clearly seen in the 317 nm ionization. On the contrary by comparing the two delays 100 fs and 400 fs, once the resonance has taken place, clearly the binding energy of the cation in its ground electronic state is produced mainly with 1.7 eV of vibrational energy that decreases to 1 eV with an increasing delay. Clearly the experiment is limited by the detector dimension ($E_{kin} \leqslant 2.2$ eV) At the time of the data aquisition the detector was only 40 mm in diameter, and not 75 mm, which was used for the ClN_3 experiment after the experimental vacuum chamber update. Nothing indicates in this photoelectron distribution that two different electronic state are populated at τ=0. The angular distribution of the photoelectron is quite peculiar since it is almost totally isotropic for all the excitation energies investigated here. Note that if a 3p Rydberg state would be populated here, as suggested by Pou-Armengo et al. [33], a clear p-wave with a well-defined energy should be observed since ionization is

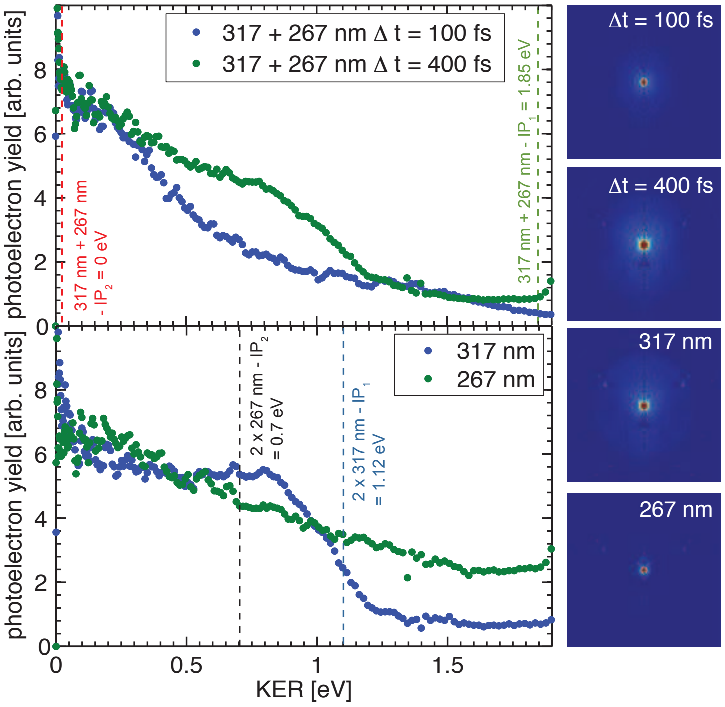

Figure 3.6: Photoelectron kinetic energy distribution of TTF^+ at 317 + 267 nm as a function of the pump-probe delay or (b) the pump and the probe alone. The images on right are the Abel inverted VMI images, 10^5 laser shot acquisitions and background free. The reference lines are respectively : 317 nm + 267 nm - IP_1 (green), 317 nm + 267 nm - IP_2 (red), 2×317 nm - IP_1 (blue) and 2×267 nm - IP_2 (black).

ruled by the conservation of the vibrational energy.

The invariance of the decay time as a function of the pump wavelength shown on the cation transient (Figure 3.5), suggests that only one electronic state is defining the absorption band around 4 eV. The long lifetime measured is quite unexpected taking into account the large bandwidth characterizing this absorption band. Indeed, within the assumption of a homogeneous broadening due to electronic relaxation, the 437 fs lifetime would correspond to a bandwidth of around 12 cm^{-1}, namely hundred times narrower than the bandwidths observed on Figure 3.2 (A). This indicates that at this excitation energy, the internal conversion rate depends on the difference in entropy between the initial and the final electronic states [44]. When the entropy in the prepared initial state increases at the same rate that the entropy in the final state, the internal conversion rate reaches a converging limit and won't vary anymore as function of the excitation energy as observed over the ∼200 meV investigated in Figure 3.5 [44]. Indeed, the entropy of the initial state has to be taken into account to reflect the dissipative character of the intramolecular vibrational relaxation. This is confirmed by the photoelectron spectrum that shows a vibrational energy distribution that converges to the flat photoelectron distribution observed when photoionization takes place from the ground electronic state of TTF. Knowing the adiabatic energies of the initial and final states and as well the density of states, the coupling parameter between the initial and final states could be deduced for such configuration [44]. The remaining question is what is the final electronic state involved. There are eight singlet states including the only one optically allowed at 370 nm (1^1B_{2u}) and the ground state

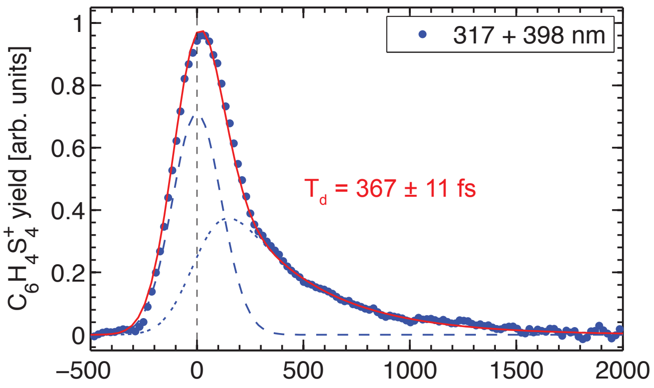

Figure 3.7: Femtosecond time-resolved transient of TTF^+ at 317 + 398 nm.

[33]. The two following investigations probe dynamics at two different probe wavelengths to confirm the long lifetime measurement as well as to enlighten the final state involved. The pump wavelength will be kept around 317 nm with a typical energy of 5 μJ/p.

3.2.3 A probe centered at 398 nm

The TTF^+ transient for a probe tuned to 398 nm is shown in Figure 3.7, and is as well fitted by Eq. (3.2). The dominant cross-correlation signal does not require as for the previous probe an independent determination of the time overlap $\Delta t = 0$. The decay time extracted is 10% lower than the previous one, that confirms the conclusion of a long internal conversion in TTF for this intense UV band. The photoelectron spectra as a function of the pump-probe delays as well as the background images are shown onFigure 3.8. Pump probe photoelectron images, once background substracted are too weak to achieve a relevant Abel transformation above a pump-probe delay of 300 fs. These photoelectron spectra reveal, that photoionization takes place both at one probe photon with a (1+1') energy of 7 eV and at two probe photon at a (1+2') energy of 10.13 eV. This corresponds just to the threshold of dissociative ionization. In the (1+1') channel, the photoelectron distribution appears with a kinetic energy of ~200 meV during the first 300 fs before to get a smooth energy distribution. Meanwhile, in the (1+2')-IP_2 channel, the photoelectron energy distribution spreads over the entire 1.5 eV window with a higher probability to the small kinetic energies. This is in contrast to the large kinetic energy as already observed for the (1+1') channel IP_1 transition at 267 nm. Only the amplitude of the distribution depends on the delay. This would confirm that a huge geometry distribution characterized the wave packet before its photoionization, as expected for a statistical description of the internal conversion. The one color photoelectron distribution recorded at 398 nm is quite similar to the one recorded at 267 nm. This is expected since the total energy is the same (2×267 nm $\approx 3\times398$nm). The angular distribution is still totally isotropic.

3.2.4 A probe centered at 800 nm

Investigations by tuning the probe wavelength to 800 nm with a typical intensity of 50 μJ/p reveals a relaxation taking place on longer timescale. Ionization threshold is reached by two

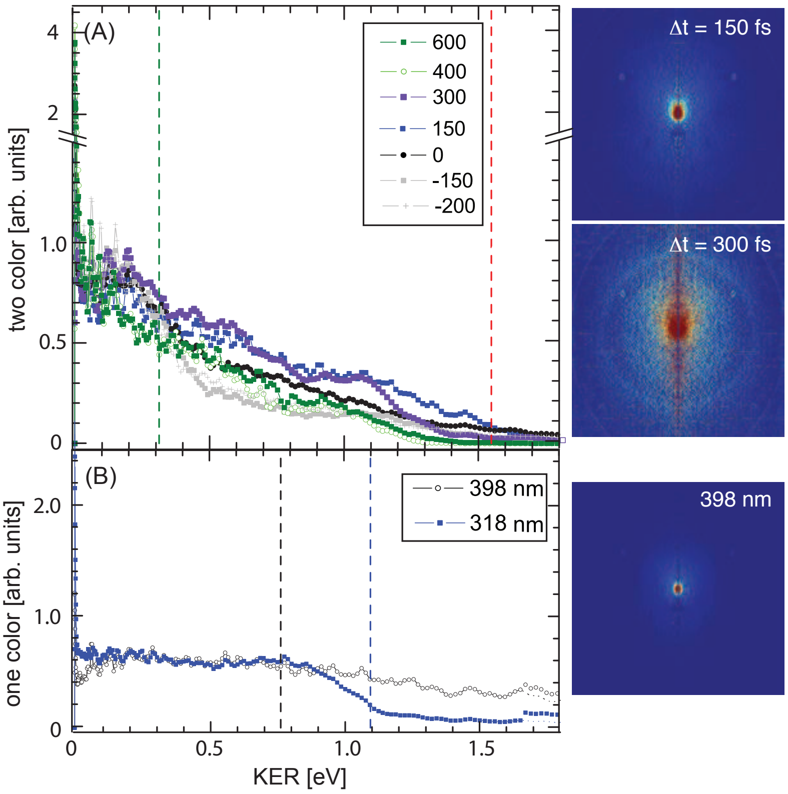

Figure 3.8: (A) Photoelectron kinetic energy distribution of TTF^+ at 318 + 398 nm as a function of the pump-probe delay and (B) the pump and the probe pulse alone. The inserted images are 10^5 laser shot acquisitions and background free. The reference lines are respectively : 318 nm + 398 nm - IP_1 (green), 318 nm + 2×398 nm - IP_2 (red), 2× 318 nm - IP_1 (blue) and 3×398 nm - IP_2 (black).

photon ionization with a small excess energy of ∼300 meV. Figure 3.9 shows the mass spectra recorded at negative and positive pump-probe delays as well as the ion image recorded at time overlap (Δt = 0 fs). Clearly dissociative ionization dominates these mass spectra leading as well to the formation of sulfur cations. The ion image shown in Figure 3.9 reveals not only the main dissociation contributions of TTF but as well the carrier gaz and the dimer of TTF. There is no spectroscopic data published on this dimer. This demonstrates that even with a continuous molecular beam, dimers of TTF can be produced. However, as shown by a depleted background at positive delay, the amount of dimers formed is not important. The time transients of the main components, the dimer TTT_2^+, TTF^+, $C_3H_2S_2^+$, $C_2H_2S_2^+$ and S^+ are shown in Figure 3.10. The cross-correlation time as well as the time overlap is determined by fitting the TTF_2^+ transient at negative pump-probe delay with a cross-correlation function and determined to 295 ± 7 fs. Indeed, clearly the time dependency of TTF_2^+ shows a shoulder at positive pump-probe delay as a signature of a resonance at 318 nm. The decay time extracted from this resonant transient is 134 ± 20 fs. Even without corrected cross-correlation time the lifetime of the excited state is rather short. To our knowledge, this state is unknown and no calculations on the dimer of TTF have been performed so far and all experimental studies did not result in the production of $(TTF)_2$. This could mean that the experimental conditions which allow the production of this dimer, are not easily reproducible. It can be a contamination with a reagent, special conditions of annealing, or the composition used in this experiment from

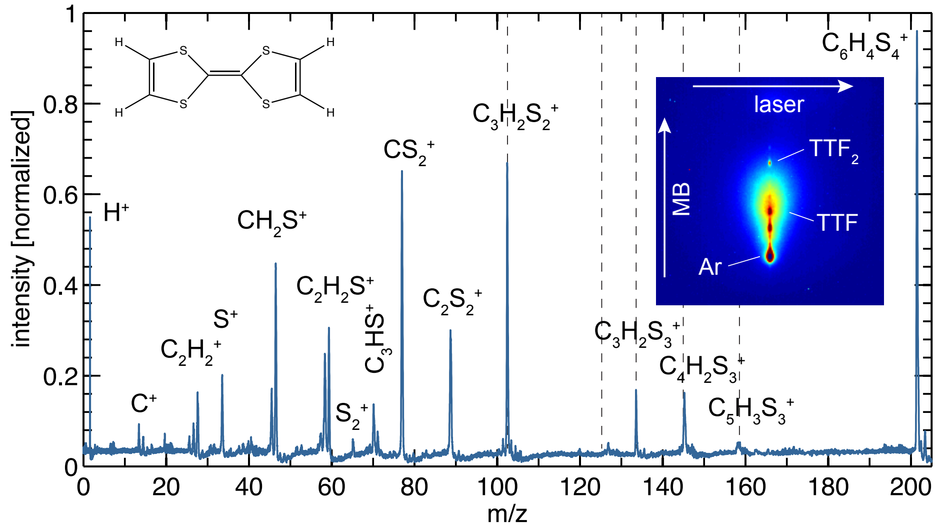

Figure 3.9: Mass spectrum of TTF produced by multiphoton ionization with 100 fs long 40 µJ femtosecond pulse focused with a 300 mm lens at an intensity of $\sim 0.3 \times 10^{13}$. No fragments are observed above *m/z* = 160. The gray vertical lines are the ions detected in the iPEPICO experiments, discussed in Section 3.3.

Sigma-Aldrich did already contain the dimer.

The decay on TTF^+ signal is significantly shorter than the previous measurements, for instance 40% lower than the one measured with a probe centered at 268 nm. The linear pump power dependencies observed on $C_2H_2S_2^+$ and S^+ signals for $\Delta t = 4$ ps, show that these cation transients reflect dynamics initiated at 3.9 eV and not dissociation taking place by multiphoton absorption of the pump pulse. For the S^+ and $C_2H_2S_2^+$ signals, in order to take into account the rising contribution due to dissociative ionization, an independent rising component with typical time constant T_r is added to equation 3.2 as already seen in Eq. (2.6) on ClN_3. The fits converge systematically to $T_e = T_r$, revealing that the electronic relaxation from the 2^1B_{1u} state leads directly onto vibrationally excited molecules in the ground electronic state with a lower probability to dissociative ionization than the electronically excited molecule. The decay times of the fragments are $T_r = 615 \pm 21$ fs for $C_3H_2S_2^+$, $T_r = 576 \pm 9$ fs for $C_2H_2S_2^+$ and $T_r = 704 \pm 13$ fs for S^+. It is interesting to note that the smaller the fragment the larger is the decay time. In addition, the linear dependency of the signal of the fragments $C_2H_2S_2^+$ and S^+ with the the pump energy, shown in the insets in Figure 3.10, reveal an one photon excitation process. The decay times extracted are summarized in Table 3.3 and do not depend on the probe intensities, which were varied between 30 to 90 µJ/p. These observations are similar to the ones obtained in a dissociative ionization study on $Cr(CO)_6$ with an excitation at 267 nm [45]. Here as well the decay time increases as the mass fo the fragments is decreasing. The explanation given by Trushin et al. is that during the relaxation of this molecule via different intermediate electronic states, which are well identified, the dissociative ionization is different and independent of the probe pulse energy. The degree of fragmentation is lower at small pump-probe delays [46]. Indeed, when the molecule relaxes, the electronic energy is converted into vibrational energy, which upon ionization remains in the ion causing dissociative ionization. This applies if the energies of the ion bonds are weaker than the binding energies of the neutral molecule.

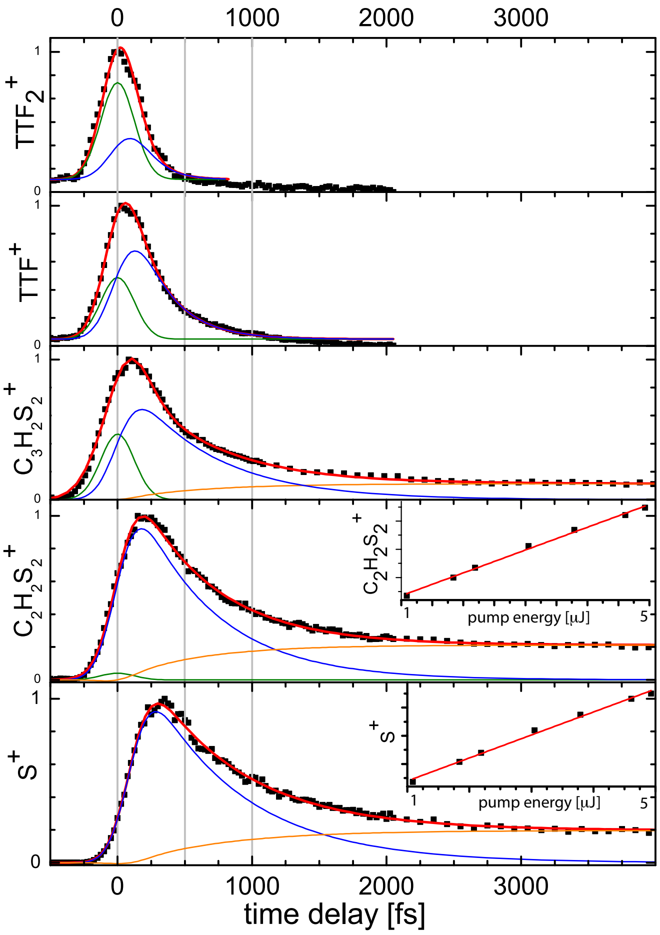

Figure 3.10: Time-resolved transients of different cations of TTF generated by 317 nm and detected with a probe pulse centered at 800 nm. The insert graphs show the pump power dependency of the fragments at a pump-probe delay of 4 ps.

The more this vibrational energy is important, following the transfer of population to the energetically lowest electronic states (for instance more vibrationally excited), the more ionized fragments with lower masses will be produced by dissociative ionization. This hypothesis is supported by the fact that the maximum fragment signal is also more shifted to positive values the smaller the mass (compare Figure 3.10). Indeed, observing the transients, we note that the maximum signal is shifted toward positive delays by t = 240 fs for $C_3H_2S_2^+$, t = 240 fs for

Table 3.3: Summary of the different decay times T_d and crosscorrelations times T_{cc} measured on the parent molecule and the fragments of TTF for the different probe wavelength

ion	λ probe [nm]	T_d [fs]	T_{cc} [fs]
$C_6H_4S_4^+$	266	437 ± 7	304 ± 2
	398	397 ± 11	272 ± 3
	800	259 ± 7	295 ± 7
$C_3H_2S_2^+$	800	615 ± 21	
$C_2H_2S_2^+$	800	576 ± 9	
S^+	800	704 ± 13 (with a delay 95 ± 7)	

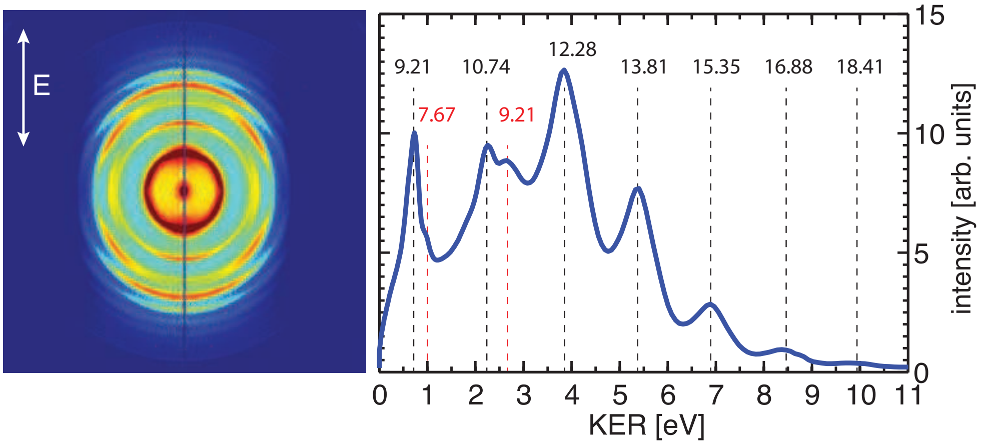

Figure 3.11: Photoelectron image of TTF (saturated) recorded with an intense fs 808 nm pulse. The white arrow indicates the laser polarization. The photoelectron kinetic energy distribution obtained from this image is shown on the right. The series of numbers indicate the energies reached in the ion continuum to produce each photoelectron component from the ground electronic state of the ion (red) or from the first electronic state (blue).

$C_2H_2S_2^+$ and t = 325 fs for S^+. We recall, that the assumption that the fragments are coming from the dissociation of neutral molecules, is not involved in this process.

3.2.5 Photoelectron spectrum of TTF with an intense 800 nm

The photoelectron spectrum and its angular distribution are shown in Figure 3.11. The photoelectron spectrum is characterized by regular peaks typically separated by 1.53 eV, the photon energy at 800 nm. Multiphoton ionization is thus the dominant ionization process. Up to 11 photons have been absorbed to produce the photoelectron spectrum, reaching up a total energy of 16.9 eV or an internal energy for the ion of 10.6 eV. These photoelectron components emerge from the ground state ionization (red series with IP_1 = 6.3 eV, HOMO) and the first cation state (blue series, IP_2 = 8.4 eV, HOMO-1).[24, 29–31]. Surprisingly, the spectrum is dominated by the first electronically excited cation state that lies at 8.4 eV, instead of the ground state. This can be rationalized by analyzing the angular distribution of the photoelectrons: while the first excited state of the cation ionizes preferentially along the laser polarization, the angular distribution from the ground state shows alternating photo- electron partial wave l values at each extra photon absorbed. This is due to a Rydberg resonance encountered at four photons. When these two photoionization channels merge, namely around 3.6 - 4 eV, the interferences lead to an atypical and quite unexpected angular distribution with minimum intensities at the poles and equators, yielding a plot with 4-fold symmetry. The femtosecond photoionization mass spectrum, as shown in Figure 3.9, displays a moderate degree of fragmentation with the parent ion still being the dominant peak. This mass spectrum is quite similar to the helium collision-induced dissociation mass spectrum of TTF^+ [47]. Resonances are encountered at four photons (large absorption band starting at 200 nm), and the ion continuum is reached with the fifth photon. This mass spectrum, as well as its time dependence once TTF is electronically excited around 4 eV by a pump pulse discussed in the previous sections, has motivated the iPEPICO experiment which will be presented in Section 3.3. Indeed fragments such as S_2^+ show that strong rearrangement processes are at play in the ion continuum. The intensity of 10^{13} Wcm^{-2} corresponds to an electric field of about 1 V/Å. At this intensity, field ionization may compete with multiphoton ionization, i.e., n photons coupled simultaneously into the molecule [48]. The pulse duration is too short, and the size of the system too small, for thermal ionization to play a role [49]. The ionization regime can be roughly estimated by calculating the Keldysh parameter γ as introduces in Section 1.3 (γ is the ratio between the laser and the tunnel frequency, here around 2) and by experimentally collecting the photoelectron spectrum [50]. Multiphoton ionization can produce photoelectron spectra characterized by discrete peaks regularly spaced by the photon energy (here 1.53 eV) attributed to above-threshold ionization, while field ionization produces a broad distribution extending far beyond the average quivering energy of the electron in the laser field, namely the ponderomotive energy, $U_p = IP/2\gamma^2$. In our case U_p reaches a maximum of around 1.2 eV.

3.3 The iPEPICO breakdown diagrams and the dissociation model

3.3.1 iPEPICO setup

In order to disentangle the complex ionic dissociation of TTF, the imaging photoelectron photoion coincidence (iPEPICO) technique is utilized to study the appearance energies of the TTF fragments. The iPEPICO experiment was carried out on the VUV beamline at the Swiss Light Source (Paul Scherrer Institute, Villigen, Switzerland). The apparatus and the measurement details have been described in detail elsewhere [51–53], and only a short introduction is given here. iPEPICO threshold ionization mass spectra were obtained by selecting ions detected in coincidence with threshold electrons (initially zero kinetic energy), arriving in the centre of an imaging multichannel plate (MCP) detector. 'Hot' electron contamination (the contribution to the mass spectra of coincidence events resulting from non-threshold electrons that happen to hit the same central spot on the MCP, was corrected by subtracting the mass spectrum obtained for electrons arriving in a narrow ring around the central spot [54]. Data were acquired as a function of photon energy from 10.0 eV to 12.6 eV, in steps of 0.2 eV. TTF was introduced via a 'probe' fitting, heated up to 74°C. Ions are accelerated first in 5 cm long region at the same low field as is used in velocity-map imaging photoelectrons, namely 40 – 120 Vcm^{-1}. If the TTF ions dissociate in a 100 ns up to a few µs time window, i.e. during the flight time in the first acceleration region, they will arrive at the detector at a time larger than the daughter ion time-of-flight (TOF). The resulting asymmetric peak shapes are a measure of the dissociation rate constant and can be used to extract experimental rates. The fractional parent and daughter ion abundances are also evaluated based on the TOF distributions, and plotted as a function of the photon energy in the breakdown diagram.

3.3.2 Computational procedures

Density functional theory calculations of molecular structure and vibrational frequencies were performed by P. Mayer at the B3-LYP/6-31+G(d) level of theory using the Gaussian 03 suite programs [55]. The harmonic vibrational frequencies and rotational constants of the neutral TTF molecule were used to calculate the internal energy distribution of the molecule at 74° Celsius. The vibrational frequencies and rotational constants of the ion were used in the calculation of the RRKM[1] rate constant for each channel using the standard expression [56, 57]:

$$k(E) = \frac{\sigma N(E - E_0)}{h\rho(E)} \tag{3.3}$$

where ρ(E) and $N(E - E_0)$ are the density and sum of states, respectively, at an ion internal energy E and transition state energy $E - E_0$ above the activation energy E_0. Sums and densities were calculated according to the direct count algorithm of Beyer and Swinehart [58]. The transition states of the reactions were approximated by using the frequencies of the parent ion, removing the normal mode that best corresponds to the reaction coordinate, and scaling the transitional modes to adjust the entropy of activation, which was calculated from the standard statistical mechanics equation. Possible isomer fragment ion structures were calculated with the G3B3 composite method [59], and their energies were compared with the experimental onsets. With the exception of the parent ion breaking in half to yield the *m/z* = 102 fragment, all dissociative photoionization reactions involve rearrangement or concerted bond-breaking steps, which are typically associated with reverse barriers. Therefore, we were searching for fragmentation pathways below the observed onset energies, and we propose product ion structures for five fragmentation channels. Direct dynamics calculations can be used to explore the potential energy surface [60] and have confirmed several unimolecular and bimolecular reaction pathways [61, 62]. Typical trajectory propagation times for comparable molecules are at most 3-6 ps [63] meaning that simulating the dissociation of the long-lived metastable TTF^+ ion close to threshold is intractable. In fact, only two of 20 B3LYP/6-31G(d) trajectories dissociated within 1.7 ps even at an internal energy of 12.25 eV: one by C_2H_2 loss and one by C_2H_2S loss. This mirrors two of the actually observed fragmentation channels in the low-energy regime. These calculations were done by A. Boedi. The breakdown diagrams were fitted using the MinimalPepico program developed by Sztaray, Boedi and Baer [64]. The program combines the RRKM dissociation rate curve, $k(E)$, with the internal energy distribution and instrument functions to model and fit the breakdown diagram and the experimental TOF distributions.

3.3.3 Results and Discussion

Figure 3.12 (A) contains the complete breakdown diagram for TTF ions over the photon energy range of 10.0 - 12.6 eV. Upon closer examination of the *m/z* = 133, 100, and 84 peaks, it is evident that these ions have relative intensities that are independent of the photon energy. Thus, they were assumed to be artifacts from impurities in the sample and were removed from Figure 3.12. Three significant observations from Figure 3.12 can be made:

(i) the *m/z* = 178, 171, 159, 146, 140, and 127 peaks all appear at approximately 10.0 eV.

---

[1] RRKM stands for Rice–Ramsperger–Kassel–Marcus theory. This method enables the computation of simple estimates of the unimolecular reaction rates from a few characteristics of the potential energy surface.

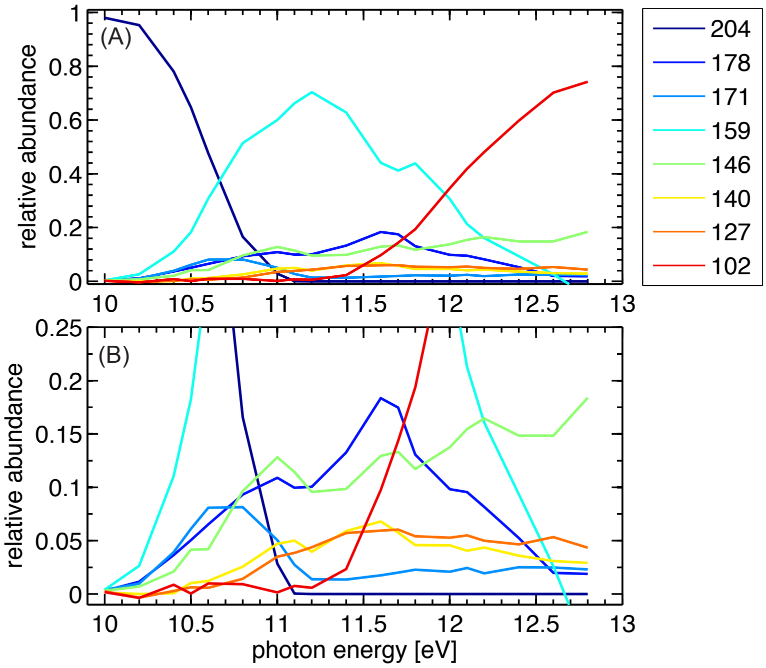

Figure 3.12: Breakdown diagram for the dissociation of ionized TTF as function of *m/z*. (A) Complete diagram. (B) expansion of the lower relative abundance fragments.

(ii) the *m/z* = 178, 171, 159, 140, and 127 breakdown curves have the same overall shape, appearing at 10.0 eV and disappearing by 12.6 eV.

(iii) the *m/z* = 102 and 146 signals both increase over the examined photon energy range.

Combining these observations leads to the conclusion that the product ions *m/z* = 178, 171, 159, 140, and 127 are formed over an isomerization barrier and the final product energies lie below this barrier. On the other hand, the fact that the *m/z* = 102 curve has a distinct appearance energy and that the relative abundances of *m/z* = 102 and 146 constantly increase over the photon energy range, means these two processes are independent. These observations lead to a three channel model for the dissociation of ionized TTF, illustrated in Figure 3.13. Onset energies derived from the appearance of each fragment ion channel are listed in Table 3.4. The stated uncertainties stem only from the step size chosen for the data acquisition. Notable in Figure 3.13 is the assumption of a reverse energy barrier for channel B.

On the basis of trajectory calculations starting out from parent ion structures as well as trial and error geometry optimizations, nine possible fragment ion minimum structures for five of the seven dissociative photoionization *m/z* channels have been found. The most stable fragment ions (at the G3B3 level of theory) are associated with C_2H_2 loss at 8.69 and 9.15 eV above the neutral TTF, but the profound change in the molecular structure and the associated barriers mean that these products are probably inaccessible by dissociative photoionization. Thus, the most stable fragment ion formed is probably the channel B product ion *m/z* = 146 at 9.27 eV, which is very low in energy relative to the onset energy listed in Table 3.4. The fact that this channel never dominates the breakdown diagram suggests that a tighter transition state at a higher energy is associated with it rather than with the channel C ions. The same level calculations for the highest lying channel A, the simple C=C bond rupture between the rings yielding

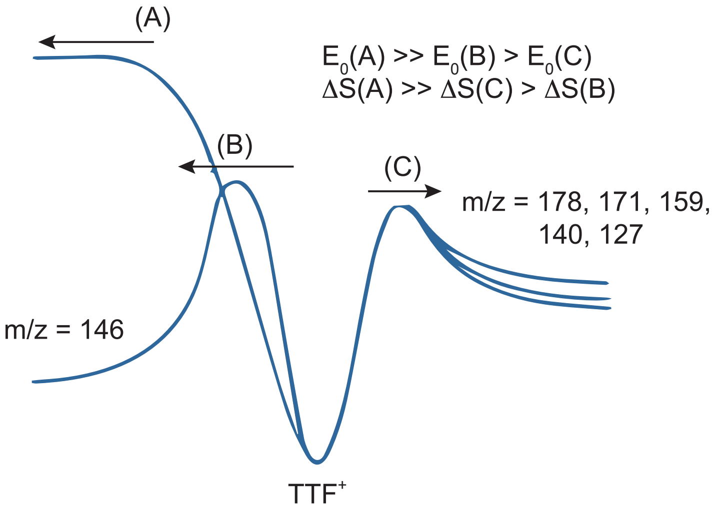

Figure 3.13: Simplified model for the dissociation of ionized TTF based on observations of the breakdown diagram.

the cyclic $C_3H_2S_2$ carbene (half of the TTF molecule) and its corresponding cation, indicate a conical intersection in the dissociation of the central C=C bond. At threshold, the dissociation is relatively slow and passing through the conical intersection will not affect the dissociation dynamics. Calculations also indicate no reverse barrier, which means a looser transition state than for channels B and C and efficient competition with them above the channel A onset at ≈11 eV.

The breakdown diagram in Figure 3.12 was modified by summing the relative abundances of all of the ions involved in channel C in Figure 3.13 (*m/z* = 178, 171, 159, 140 and 127). The adiabatic ionization energy is calculated at the B3LYP/6-311++G(2d,p)/B3-LYP/6-31+G(d) level of theory [47]. Any uncertainty in this value, which is 0.4 eV lower than the vertical IP_v = 6.7 eV [24] will translate into uncertainty in the derived dissociative photoionization onsets for the three channels in Figure 3.13 through the uncertainty in the density of states in the rate equation Eq. (3.3). In the experimental data, only peaks related to channels B and C exhibit asymmetric TOF distributions (an example of which is shown in Figure 8 for *m/z* = 159). It was not possible to model each peak since all of the ions resulting from channel C

Table 3.4: Appearance Energies, AE, for the fragment ions from TTF. S^+ (possibly O_2^+) is observed at the highest photon energy (12.6 eV), but not in the threshold spectrum. [a]Based on the observed signal onset in the breakdown diagram. [b]Based on the RRKM fitting, relative to the molecular ion.

m/z	ion	co-fragment	channel	AE^a [eV]	$E_0{}^b$ [eV]
102	$C_3H_2S_2$	$-C_3H_2S_2$	A	11.0 ± 0.2	3.65 ± 0.1
146	$C_4H_2S_3$	$-C_2H_2S$	B	10.0 ± 0.2	2.77 ± 0.1
178	$C_4H_2S_4$	$-C_2H_2$	C	10.0 ± 0.2	2.38 ± 0.1
171	$C_6H_3S_3$	-HS	C		
159	$C_5H_3S_3$	-CHS	C		
140	$C_6H_4S_2$	$-S_2$	C		
127	$C_5H_3S_2$	$-CHS_2$	C		

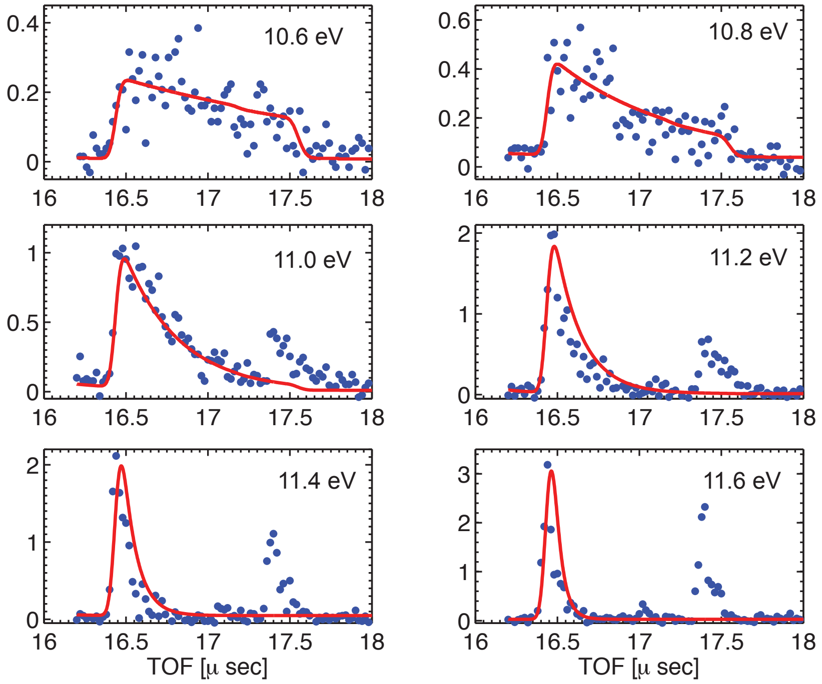

Figure 3.14: Threshold photoionization TOF distributions for the *m/z* = 159 peak as a function of photon energy. The solid line is the fitted curve to the normalized experimental data. The feature growing in at 17.5 μs is an impurity.

are formed over a common barrier and their relative abundances will be due to the dynamics of the system as it passes over the reaction barrier. Instead, we assume that the total observed rate constant, $k(E)$, can be calculated through the most abundant ion of channel C, namely *m/z* = 159. Figure 3.14 shows the threshold photoionization TOF distributions for the *m/z* = 159 peak as a function of photon energy. The fit shown in grey, was normalized to the experimental data.

The result of the fitting of the iPEPICO breakdown diagram using the three-channel model in Figure 3.13 is shown in Figure 3.15. The two lower energy dissociation channels, B and C, have E_0 values of 2.77 ± 0.10 eV and 2.38 ± 0.10 eV, respectively, and are characterized by an activation entropy $\Delta S^{\ddagger}_{600K}$ values of -9 ± 6 and 1 ± 6 J $\mathrm{K}^{-1}\mathrm{mol}^{-1}$, respectively, consistent with the qualitative argument presented above. Competing with them at higher internal energy is the cleavage of the central bond to form *m/z* = 102, with E_0 = 3.65 ± 0.10 eV, which corresponds to the C=C bond strength in the TTF ion at an activation entropy of $\Delta S^{\ddagger}_{600K}$ = 83 ± 10 $\mathrm{JK}^{-1}\mathrm{mol}^{-1}$. The uncertainties arise from the interplay of E_0 and $\Delta S^{\ddagger}$ in the fitting procedure. Nielsen et al. report a calculated (B3LYP/6-311++G(2d,p)/B3LYP/6- 31+G(d)) IP for the cyclic $C_3H_2S_2$ carbene of 8.66 eV, a neutral TTF C=C bond energy of 2.11 eV, and thus an ionic TTF C=C bond energy of 4.46 eV [47]. The latter value is 0.81 eV higher than the value measured here.

In relation to the femtosecond results, the iPEPICO data are characteristic of the lower internal energy ions generated by the 808 nm fs pulse. The fact that channel B and C ions are underrepresented in Figure 3.11 is due to the low $\Delta S^{\ddagger}$ associated with these processes. Since the femtosecond experiment results in ions with internal energies up to 12.1 eV, only high ΔS^{+}

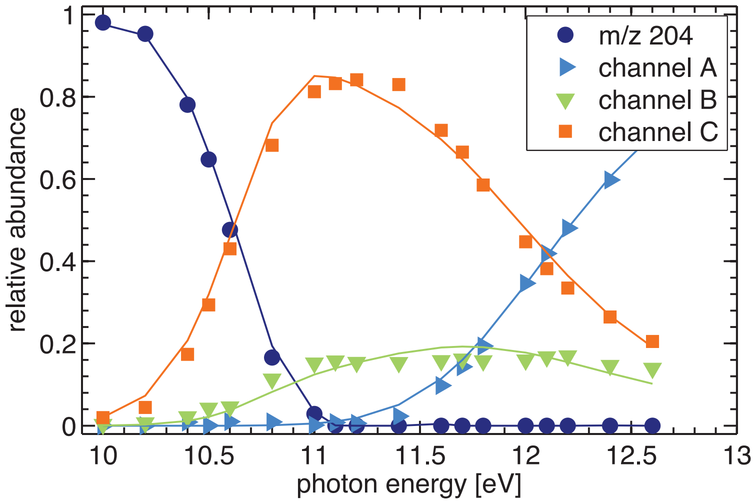

Figure 3.15: Modified breakdown diagram grouping together the relative abundance of all ions involved in channel C in Figure 3.13 as a function of photon energy (bottom axis) and TTF ion internal energy (top axis). Points are experimental data; the solid lines are the result of the RRKM fitting.

channels will be competitive, such as channel A, the breaking of the central C=C bond to form *m/z* = 102. Trajectory calculations at comparable internal energies on the ground electronic state surface (see above) yielded C_2H_2 and C_2H_2S loss reactions, which do not prominently feature in the femtosecond ionization mass spectra. A possible reason for this could be if the dissociation on the excited state surface were faster than internal conversion to the ground state, in which case the excited state dynamics would dictate the dissociation dynamics. On the other hand, we observed long-lived metastable parent ions in the iPEPICO experiment in the low-energy regime, which gives plenty of time for internal conversion to take place and indicates statistical behavior.

3.4 Conclusion

Femtosecond photoionization of TTF results in the absorption of up to twelve 808 nm photons and a subsequent ion internal energy of up to 12.1 eV. The photoelectron spectrum is consistent with this multiphoton ionization model as opposed to ionization by the intense laser field. The angular dependence of the ejected photoelectrons shows that this multiphoton process is more likely to occur from the first excited state of the ion. Within the range of these high internal energies, a variety of dissociation channels are accessible. Above the dissociation threshold, iPEPICO results show that the molecular ion (*m/z* = 204) dissociates into seven product ions, six of which compete in a 1.0 eV internal energy window and are formed with the same appearance energy. This shows that the loss of small neutral molecules from the TTF ion is governed by a relatively tight transition state leading to an unspecified reaction intermediate, which goes on to fragment in a number of ways. *Ab initio* calculations are reported on the possible fragment ion structures of five dissociation channels as well as trajectories showing the loss of C_2H_2 and C_2H_2S from high internal energy TTF cations. A three-channel dissociation model is used to fit the iPEPICO data in which two dissociation channels are treated as simple dissociations (one with a reverse barrier), while the rest involve a shared barrier. These channels cannot compete at higher internal energies with more entropically favorable pathways. The S^+ fragment in the VUV photoionization seems to appear at 12.6 eV from a secondary dissociation of S_2^+. This confirms that in the pump-probe studies of the second UV band of TTF a particular vibrational energy characterizes the S^+ production following dissociative ionization of TTF. This would explain why the time profile of the S^+ fragment has a 95 fs shift on its decay function.

References

[1] Wudl, F, Wobschall, D, and Hufnagel, EJ. *Electrical conductivity by the bis(1,3-dithiole)-bis(1,3-dithiolium) system*. J. Am. Chem. Soc. **94**:2 670–672 (1972) (cited p. 96).

[2] Ferraris, J, Cowan, DO, and Walatka, V. *Electron transfer in a new highly conducting donor-acceptor complex - Journal of the American Chemical Society (ACS Publications)*. Angew. Chem. Int. Ed. Engl. **40**:8 1372–1409 (2001) (cited p. 96).

[3] Segura, JL and Martin, N. *New Concepts in Tetrathiafulvalene Chemistry*. Angew. Chem. Int. Ed. Engl. **40**:8 1372–1409 (2001) (cited p. 96).

[4] Martin, C, Sánchez, L, Herranz, MA, and Guldi, DM. *Evidence for two separate one-electron transfer events in excited fulleropyrrolidine dyads containing tetrathiafulvalene (TTF)*. J. Phys. Chem. A **104**:19 4648–4657 (2000) (cited p. 96).

[5] Becher, J, Jeppesen, JO, and Nielsen, K. *Tetrathiafulvalenes: from heterocyclic chemistry to molecular devices*. Synthetic Metals **133-134**: 309–315 (2003) (cited p. 96).

[6] Sawano, F, Terasaki, I, Mori, H, Mori, T, Watanabe, M, Ikeda, N, Nogami, Y, and Noda, Y. *An organic thyristor*. Nature **437**:7058 522–524 (2005) (cited p. 96).

[7] Fang, CJ, Zhu, Z, Sun, W, Xu, CH, and Yan, CH. *New TTF derivatives: several molecular logic gates based on their switchable fluorescent emissions*. New Journal of Chemistry **31**:4 580 (2007) (cited p. 96).

[8] Canevet, D, Sallé, M, Zhang, G, and Zhang, D. *Tetrathiafulvalene (TTF) derivatives: key building-blocks for switchable processes*. Chem. Comm. (2009) (cited p. 96).

[9] Jia, C, Zhang, J, Bai, J, Zhang, L, Wan, Z, and Yao, X. *Synthesis, physical properties and self-assembly of conjugated donor–acceptor system based on tetrathiafulvalene and functionalized with binding sites*. Dyes and Pigments **94**:3 403–409 (2012) (cited p. 96).

[10] Wang, C, Bryce, MR, Batsanov, AS, Goldenberg, LM, and Howard, JAK. *Synthesis and electrochemistry of new tetrathiafulvalene (TTF) dendrimers:X-ray crystal structure of a tetrafunctionalised TTF core unit*. J. Mater. Chem. **7**:7 1189–1197 (1997) (cited p. 96).

[11] Sakai, M, Iizuka, M, Nakamura, M, and Kudo, K. *Fabrication and Electrical Characterization of Tetrathiafulvalene-tetracyanoquinodimethane Molecular Wires*. Jpn. J. Appl. Phys. **42**:Part 1, No. 4B 2488–2491 (2003) (cited p. 96).

[12] Mas-Torrent, M and Hadley, P. *Electrochemical Growth of Organic Conducting Microcrystals of Tetrathiafulvalene Bromide*. Small **1**:8-9 806–808 (2005) (cited p. 96).

[13] Chollet, M. *Gigantic Photoresponse in 1/4-Filled-Band Organic Salt* $(EDO\text{-}TTF)_2PF_6$. Science **307**:5706 86–89 (2005) (cited p. 96).

[14] Hal, PA van, Janssen, RAJ, Lanzani, G, Cerullo, G, Zavelani-Rossi, M, and De Silvestri, S. *Full temporal resolution of the two-step photoinduced energy-electron transfer in a fullerene-oligothiophene-fullerene triad using sub-10 fs pump-probe spectroscopy*. Chem. Phys. Lett. **345**:1-2 33–38 (2001) (cited p. 96).

[15] Katan, C. *First-Principles Study of the Structures and Vibrational Frequencies for Tetrathiafulvalene TTF and TTF-d_4 in Different Oxidation States*. J. Phys. Chem. A **103**:10 1407–1413 (1999) (cited p. 96, 97, 99).

[16] HARGITTAI, I, BRUNVOLL, J, KOLONITS, M, and KHODORKOVSKY, V. *Tetrathiafulvalene - Gas-Phase Molecular-Structure From Electron-Diffraction*. J. Mol. Struct. **317**:3 273–277 (1994) (cited p. 96).

[17] Demiralp, E and Goddard, WA. *Structures and Energetics Study of Tetrathiafulvalene-Based Donors of Organic Superconductors*. J. Phys. Chem. A **101**:43 8128–8131 (1997) (cited p. 96).

[18] Viruela, R, Viruela, PM, Pou-Amerigo, R, and Orti, E. *ScienceDirect.com - Synthetic Metals - Flexibility of TTF. a theoretical study*. Synthetic Metals **103**:1-3 1991–1992 (1999) (cited p. 96).

[19] Graja, A, Olejniczak, I, and Bogucki, A. *Spectral studies of the bis-linked tetrathiafulvalenes to [60]fullerene*. Journal of molecular structure (2002) (cited p. 96, 97).

[20] Kreher, D, Hudhomme, Pt, Gorgues, A, Luo, H, Araki, Y, and Ito, O. *Photoinduced electron transfer processes of a fused C_60-TTF-C_60 dumbbell triad*. Phys. Chem. Chem. Phys. **5**:20 4583–4592 (2003) (cited p. 96).

[21] Allard, E, Cousseau, J, Ord na, J, Garin, J, Luo, H, Araki, Y, and Ito, O. *Photoinduced electron-transfer processes in C_60-tetrathiafulvalene dyads containing a short or long flexible spacer*. Phys. Chem. Chem. Phys. **4**:24 5944–5951 (2002) (cited p. 96).

[22] Coffen, DL, Chambers, JQ, Williams, DR, Garrett, PE, and Canfield, ND. *Tetrathioethylenes*. J. Am. Chem. Soc. **93**:9 2258–2268 (1971) (cited p. 96, 97).

[23] Pou-Amerigo, R, Viruela, PM, Viruela, R, Rubio, M, and Orti, E. *Electronic spectra of tetrathiafulvalene and its radical cation: analysis of the performance of the time-dependent DFT approach*. Chem. Phys. Lett. **352**:5-6 491–498 (2002) (cited p. 97, 99).

[24] Lichtenberger, DL, Johnston, RL, Hinkelmann, K, Suzuki, T, and Wudl, F. *Relative electron donor strengths of tetrathiafulvene derivatives: effects of chemical substitutions and the molecular environment from a combined photoelectron and electrochemical study*. J. Am. Chem. Soc. **112**:9 3302–3307 (1990) (cited p. 97, 98, 100, 108, 112).

[25] Haddon, RC. *Quantum chemical studies in the design of organic metals. II. The equilibrium geometries and electronic structure of tetrathiofulvalene (ttf) andtetracyanoquinodimethane (tcnq) and their uni- and di-valent ions*. Aust. J. Chem. **28**:11 2333–2342 (1975) (cited p. 97).

[26] Wudl, F, Kruger, AA, Kaplan, ML, and Hutton, RS. *Unsymmetrical dimethyltetrathiafulvalene*. J. Org. Chem. **42**:4 768–770 (1977) (cited p. 97).

[27] Engler, EM, Scott, BA, Etemad, S, Penney, T, and Patel, VV. *Organic alloys: synthesis and properties of solid solutions of tetraselenafulvalene-tetracyano-p-quinodimethane (TSeF-TCNQ) and tetrathiafulvalene-tetracyano-p-quinodimethane (TTF-TCNQ)*. J. Am. Chem. Soc. **99**:18 5909–5916 (1977) (cited p. 97).

[28] Sandman, DJ, Holmes, TJ, and Warner, DE. *" One-pot" construction of the bithiopyran ring system from an acyclic precursor*. J. Org. Chem **44**:5 880–882 (1979) (cited p. 97).

[29] Gleiter, R, Schmidt, E, Cowan, DO, and Ferraris, JP. *The electronic structure of tetrathiofulvalene*. J. Electron Spec. and Relat. Phen. **2**:2 207–210 (1973) (cited p. 97, 108).

[30] Berlinsky, AJ, Carolan, JF, and Weiler, L. *Photoelectron Spectrum and Electronic Structure of Tetrathiofulvalene (TTF)*. Can. J. Chem. **52**:19 3373–3377 (1974) (cited p. 97, 108).

[31] Sato, N, Saito, G, and Inokuchi, H. *Ionization potentials and polarization energies of tetraselenafulvalene (TSF) derivatives determined from ultraviolet photoelectron spectroscopy*. Chem. Phys. **76**:1 79–88 (1983) (cited p. 97, 108).

[32] Mayer, PM, Staedter, D, Blanchet, V, Hemberger, P, and Bodi, A. *Comparing Femtosecond Multiphoton Dissociative Ionization of Tetrathiafulvene with Imaging Photoelectron Photoion Coincidence Spectroscopy*. J. Phys. Chem. A **117**:13 2753–2759 (2013) (cited p. 97).

[33] Pou-Amérigo, R, Orti, E, Merchan, M, Rubio, M, and Viruela, PM. *Electronic Transitions in Tetrathiafulvalene and Its Radical Cation: A Theoretical Contribution*. J. Phys. Chem. A **106**:4 631–640 (2002) (cited p. 97–99, 102, 104).

[34] Fabian, J, Diaza, LA, Seifert, G, and Niehaus, T. *Calculation of excitation energies of organic chromophores: a critical evaluation*. J. Mol. Struct. **594**:1-2 41–53 (2002) (cited p. 97, 98).

[35] Andreu, R, Garin, J, and Orduna, J. *Electronic absorption spectra of closed and open-shell tetrathiafulvalenes: the firste time-dependent density-functional study*. Tetrahedron **57**:37 7883–7892 (2001) (cited p. 97, 98).

[36] Fabian, J. *Electronic excitation of sulfur-organic compounds–performance of time-dependent density functional theory*. Theor Chem Acc **106**:3 199–217 (2001) (cited p. 98).

[37] Batsanov, AS, Bryce, MR, Heaton, JN, Moore, AJ, Skabara, PJ, Howard, JAK, Orti, E, Viruela, PM, and Viruela, R. *New functionalized tetrathiafulvalenes: X-ray crystal structures and physico-chemical properties of TTF–C (O) NMe_2 and TTF–C (O)–O–C_4H_9: a joint experimental and theoretical study*. J. Mater. Chem. **5**:10 1689–1696 (1995) (cited p. 98).

[38] Yakushi, K, Nishimura, S, Sugano, T, Kuroda, H, and Ikemoto, I. *The structure of tetrathiafulvalenium perchlorate, $TTF^+.ClO_4^-$*. Acta Cryst. **36**:2 358–363 (1980) (cited p. 99).

[39] Kistenmacher, TJ, Rossi, M, Chiang, CC, Van Duyne, RP, and Siedle, AR. *Crystal and molecular structure of an unusual salt formed from the radical cation of tetrathiafulvalene (TTF) and the trichloromercurate anion ($HgCl_3$), (TTF)($HgCl_3$)*. Inorg. Chem. **19**:12 3604–3608 (1980) (cited p. 99).

[40] Kerkines, ISK, Petsalakis, ID, Theodorakopoulos, G, and Klopper, W. *Low-lying absorption and emission spectra of pyrene, 1,6-dithiapyrene, and tetrathiafulvalene: A comparison between ab initio and time-dependent density functional methods*. J. Chem. Phys. **131**:22 pages (2009) (cited p. 99).

[41] Tugsuz, T. *DFT Study on the Standard Electrode Potentials of Imidazole, Tetrathiafulvalene, and Tetrathiafulvalene-Imidazole*. J. Phys. Chem. **114**:51 17092–17101 (2010) (cited p. 99).

[42] Tsubomura, H and Sakata, T. *A new electronic transition found for the aniline derivatives*. Chem. Phys. Lett. **21**:3 511–512 (1973) (cited p. 101).

[43] Fuke, K and Nagakura, S. *Rydberg transitions of aniline and N,N-diethylaniline*. J. Mol. Spec. **64**:1 139–146 (1977) (cited p. 101).

[44] Blanchet, V, Raffael, K, Turri, G, and Chatel, B. *Time-dependent photoionization of azulene: Competition between ionization and relaxation in highly excited states — Issue 16 - Journal of Chemical Physics*. The Journal of chemical … (2008) (cited p. 103).

[45] Trushin, SA, Fuss, W, Schmid, WE, and Kompa, KL. *Femtosecond Dynamics and Vibrational Coherence in Gas-Phase Ultraviolet Photodecomposition of Cr(CO) 6*. J. Phys. Chem. A **102**:23 4129–4137 (1998) (cited p. 106).

[46] Fuss, W, Kosmidis, C, Schmid, WE, and Trushin, SA. *The lifetime of the perpendicular minimum of cis-stilbene observed by dissociative intense-laser field ionization*. Chem. Phys. Lett. **385**: 423–430 (2004) (cited p. 106).

[47] Nielsen, SB, Nielsen, MB, and Jensen, HJA. *The tetrathiafulvalene dication in the gas phase: its formation and stability*. Phys. Chem. Chem. Phys. **5**:7 1376–1380 (2003) (cited p. 108, 112, 113).

[48] DeWitt, MJ and Levis, RJ. *Concerning the ionization of large polyatomic molecules with intense ultrafast lasers*. J. Chem. Phys. **110**:23 11368 (1999) (cited p. 109).

[49] Kjellberg, M, Bulgakov, AV, and Goto, M. *Femtosecond electron spectroscopy of coronene, benzo[GHI]perylene, and anthracene — Browse - Journal of Chemical Physics*. The Journal of chemical … (2010) (cited p. 109).

[50] DeWitt, M and Levis, R. *Observing the Transition from a Multiphoton-Dominated to a Field-Mediated Ionization Process for Polyatomic Molecules in Intense Laser Fields*. Phys. Rev. Lett. **81**:23 5101–5104 (1998) (cited p. 109).

[51] Bodi, A, Sztáray, B, Baer, T, Johnson, M, and Gerber, T. *Data acquisition schemes for continuous two-particle time-of-flight coincidence experiments*. Rev. Sci. Instr. **78**:8 084102 (2007) (cited p. 109).

[52] Bodi, A, Johnson, M, Gerber, T, Gengeliczki, Z, Sztáray, B, and Baer, T. *Imaging photoelectron photoion coincidence spectroscopy with velocity focusing electron optics*. Rev. Sci. Instr. **80**:3 (2009) (cited p. 109).

[53] Johnson, M, Bodi, A, Schulz, L, and Gerber, T. *Vacuum ultraviolet beamline at the Swiss Light Source for chemical dynamics studies*. Nuclear Instruments and Methods in Physics Research Section A: Accelerators, Spectrometers, Detectors and Associated Equipment **610**:2 597–603 (2009) (cited p. 109).

[54] Sztáray, B and Baer, T. *Suppression of hot electrons in threshold photoelectron photoion coincidence spectroscopy using velocity focusing optics*. Rev. Sci. Instr. **74**:8 3763–3768 (2003) (cited p. 109).

[55] Frisch, MJ, Trucks, GW, Schlegel, HB, Scuseria, GE, Robb, MA, Cheeseman, JR, Scalmani, G, Barone, V, Mennucci, B, Petersson, GA, Nakatsuji, H, Caricato, M, Li, X, Hratchian, HP, Izmaylov, AF, Bloino, J, Zheng, G, Sonnenberg, JL, Hada, M, Ehara, M, Toyota, K, Fukuda, R, Hasegawa, J, Ishida, M, Nakajima, T, Honda, Y, Kitao, O, Nakai, H, Vreven, T, Montgomery, Jr, A, J, Peralta, JE, Ogliaro, F, Bearpark, M, Heyd, JJ, Brothers, E, Kudin, KN, Staroverov, VN, Kobayashi, R, Normand, J, Raghavachari, K, Rendell, A, Burant, JC, Iyengar, SS, Tomasi, J, Cossi, M, Rega, N, Millam, JM, Klene, M, Knox, JE, Cross, JB, Bakken, V, Adamo, C, Jaramillo, J, Gomperts, R, Stratmann, RE, Yazyev, O, Austin, AJ, Cammi, R, Pomelli, C, Ochterski, JW, Martin, RL, Morokuma, K, Zakrzewski, VG, Voth, GA, Salvador, P, Dannenberg, JJ, Dapprich, S, Daniels, AD, Farkas, Ö, Foresman, JB, Ortiz, JV, Cioslowski, J, and Fox, DJ. *Gaussian 09, Revision A.1*. Gaussian, Inc., Wallingford CT (2009) (cited p. 110).

[56] Baer, T and Hase, WL. *Unimolecular reaction dynamics: Theory and experiments*. Oxford University Press: New York, 1996 (cited p. 110).

[57] Baer, T and Mayerfn, PM. *Statistical Rice-Ramsperger-Kassel-Marcus quasiequilibrium theory calculations in mass spectrometry*. J. Am. Soc. Mass. Spectrom. **8**:2 103–115 (1997) (cited p. 110).

[58] Beyer, T and Swinehart, DF. *Algorithm 448: number of multiply-restricted partitions*. Communications of the ACM **16**:6 379 (1973) (cited p. 110).

[59] Baboul, AG, Curtiss, LA, Redfern, PC, and Raghavachari, K. *Gaussian-3 theory using density functional geometries and zero-point energies*. J. Chem. Phys. **110**:16 7650–7657 (1999) (cited p. 110).

[60] Schlegel, HB. *Exploring potential energy surfaces for chemical reactions: An overview of some practical methods*. J. Comput. Chem. **24**:12 1514–1527 (2003) (cited p. 110).

[61] Spezia, R, Salpin, JY, Gaigeot, MP, Hase, WL, and Song, K. *Protonated Urea Collision-Induced Dissociation. Comparison of Experiments and Chemical Dynamics Simulations*. J. Phys. Chem. A **113**:50 13853–13862 (2009) (cited p. 110).

[62] Sekiguchi, O, Letzel, MC, Kuck, D, and Uggerud, E. *The unimolecular dissociation of protonated glyoxylic acid: Structure and dynamics of a step-by-step process*. Int. J. Mass Spec. **255**: 177–184 (2006) (cited p. 110).

[63] Tian, SX and Yang, J. *Ab initio photoionization dynamics of β-alanine*. J. Chem. Phys. **126**:14 141103 (2007) (cited p. 110).

[64] Sztáray, B, Bodi, A, and Baer, T. *Modeling unimolecular reactions in photoelectron photoion coincidence experiments*. J. Mass Spec. **45**:11 1233–1245 (2010) (cited p. 110).

4

Quantum beats in sulfur hexafluoride (SF_6)

Contents

Abstract

The diffracted XUV spectrum generated by high-order harmonic generation in vibrationally excited SF_6 is studied in two phase sensitive high-order harmonic spectroscopy (HHS) setups. By changing the geometry in the ground state of SF_6 through a vibrational excited state prepared by a Raman transition, we aim to shed light into the process of high-order harmonic generation in SF_6. Two sophisticated experimental set-ups, both based on an heterodyne detection are implemented to not only measure the amplitude but also the phase of the high-order harmonic emission. One setup uses two pump pulses to create a grating of vibrational excitation in the gas jet through which the probe pulse generates high-order harmonics. The second experiment uses two spatially separated probe pulses, both generating a XUV beam which interfere spatially in far field. Section 4.1 gives an overview over the extraordinary characteristics of SF_6, the vibrational spectrum and the early high-order harmonic generation experiments in SF_6. The following two sections describe each the experimental phase sensitive HHG spectroscopy technique used and their results, in Section 4.2 the transient grating and in Section 4.3 the two HHG source experiment. The chapter is closed in Section 4.4 with a conclusion.

Keywords: sulfur hexafluoride, shape resonance, Raman excited vibrational spectroscopy, two HHG source interferometry, strong field transient grating spectroscopy, heterodyne detection

4.1 Introduction

4.1.1 SF_6, a man-made molecule

Sulfur hexafluoride (SF_6) is a species of growing importance in the field of chemistry. This can be attributed to its 'fascinating characteristics' which include it being gaseous even at low temperature, chemically inert, non-flammable, non-toxic, non-corrosive. It shows a high dielectric strength through fluorine's high electronegativity, a high molar heat capacity, low viscosity and good heat transfer capabilities [1–3]. Due to its excellent dielectric properties it is heavily used for high voltage gas insulated systems where it is utilized above atmospheric pressure to circumvent electrical discharge [4]. It is also used in semiconductor manufacturing, and other sophisticated applications as thermoacoustic insulator and inert solvent for supercritical fluid chemical reactions [5, 6]. Furthermore, it is used in the medical field [7], e.g as inert gas in ophthalmologic surgeries [8] or as contrast agent in ultrasonography [9]. Its concentration in the Earths atmosphere is increasing at a rate of about 7 % per year due to industrial emissions and its extremely long lifetime in the atmosphere (~3200 years), and became a subject of interest in the field of atmospheric physics as a pollutant that can contribute to the greenhouse effect (GHE) [10]. Even though per molecule it is one of the strongest greenhouse gases known in its ambient mixing ratio of less than four parts per trillion (ppt, 10^{-12} moles per mole in dry air), it does not yet cause any significant climate change [11]. Nevertheless SF_6 is one of six chemical compounds to control since 2005 within in the Kyoto protocol [12]. Due to its relatively long lifetime it can be used as a trace gas in the evolvement of the greenhouse effect and its concentration has been reduced by 30-40% (depending on the country) between 1990 and 2004 [13].

The spectroscopy of this molecule, which is essential for quantitative measurements in the atmosphere and an understanding of the role of SF_6 in there, is still insufficiently known [14–18]. The structure of SF_6 was already determined by electron diffraction studies as early as 1933 [19] and showed a highly symmetrical molecule with the six fluorine atoms occupying the corners of a regular octahedron with the sulfur atom at the center. Today SF_6 is known as a textbook example of a spherical-top molecule which belongs to the highly symmetric O_h point group with three C_4 axes, four C_3 axes, six C_2 axes, three σ_h planes, six σ_d planes and a center of inversion i. Its structure is shown in Figure 4.1. The character and product tables for the O_h point group are shown in Appendix E in Table E.6.

4.1.2 HHG spectroscopy on SF_6

As seen in Section 1.3 high-order harmonic generation in molecules is an attractive tool in spectroscopy. From the harmonic emission, photochemical processes induced by a pump pulse can be revealed, with an analysis strongly based on molecular orbitals from and to which the electron is emitted and recombined [20]. Moreover attosecond hole dynamics induced by the probe laser field can eventually be extracted [21, 22]. All these aspects make high-order harmonic spectroscopy (HHS) a very appealing technique to complement conventional ultrafast spectroscopy.

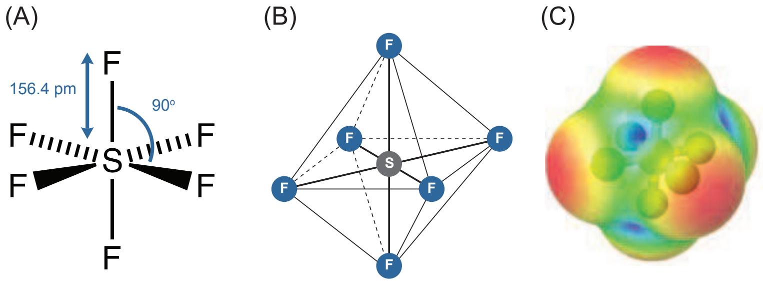

Figure 4.1: The structure of sulfur hexafluoride SF_6. A) B) octahedron structure C) surface simulation of SF_6. Surface view shows the electrostatic potential of the structure mapped onto the solvent excluded surface, based on a probe of radius 1.4 Å. Regions of negative potential mainly localized on the flour atoms are shown in red, positive in blue.

As early as 1996 Lynga *et al.* observed that SF_6 shows an anomaly in the HHG spectrum [23]. They measured the intensity of HHG in molecular gases and draw a comparison of the HHG spectra of Ar, N_2 and SF_6 which is shown in Figure 4.2 (A). N_2 and Ar exhibit a very similar behavior and show a typical HHG spectrum with perturbative regime (up to H11), plateau (up to H17) and cutoff (up to H29). SF_6 does not have the characteristic plateau behavior. Instead, the intensity plot of the harmonics shows a clear minimum around the 17th harmonic [23]. They postulated, that SF_6 dissociates at low intensities, during the rising time of the laser pulse, and that the minimum could come from harmonics produced from neutral fragments of SF_5 that is defined by an extra I_p of 9.6 eV. If two fragments, with different I_p generate harmonics it could lead to two plateaus of different heights and widths. However SF_5^+ appears as soon as the ionization threshold of SF_6 is reached [24]. This leads to a dissociation threshold of SF_5 neutral to around 5.8 eV. Moreover, the SF_5 produced by dissociation will have initially a square pyramidal geometry. But the equilibrium structure of SF_5 is a trigonal bipyramidal (D_{3h}), which means extensive rearrangement must occur during the dissociation process, leading to a dissociation time certainly longer than the short pulse duration observed in HHG (< 35 fs). Clearly in the excitation scheme proposed by Lynga et al., the differences in the I_p between SF_6 and SF_5 and the strong nuclear rearrangement required can not explain the spectrum they observed. However, this dissociative ionization of SF_6^+ as soon as the HOMO electron is removed should have a strong effect on HHG and consequently dynamics of the cation should take place in the HHG process.

Around 16 years after this discovery there is still no answer to this anomaly in the plateau of SF_6 around harmonic 17. As the technology and knowledge advances we are not restricted anymore to just a measurement of the intensity of the HHG spectrum. The CELIA group undertook a complex investigation of the HHG spectrum of SF_6 in various experimental setups which is summarized in Figure 4.2 B and will be discussed here shortly as it is the initiation of the pump-probe investigations described in this chapter. This advanced optical characterization of high-order harmonic emission from SF_6 was done by measuring not only the high-order harmonic spectrum, but also its dependence to the driving laser ellipticity, the direction of polarization of the harmonics from short and long trajectories, and the degree of ellipticity of the

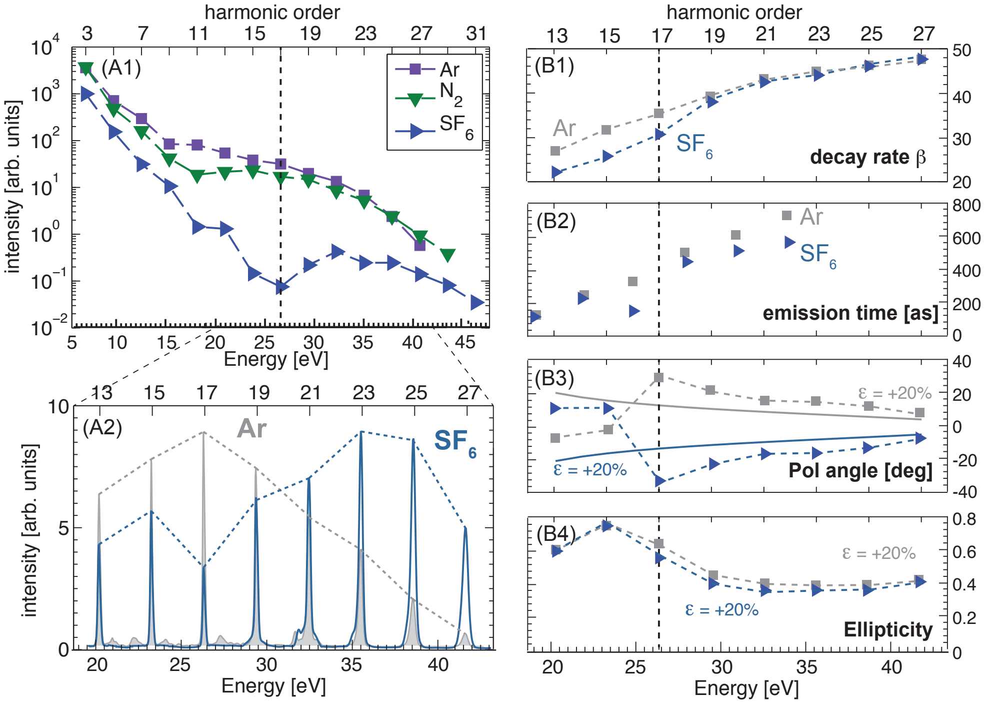

Figure 4.2: Summary of high-oder harmonic spectroscopy experiments on SF_6. (A1) Harmonic spectra from a rare gas (Ar), a diatomic molecule (N_2) and the polyatomic molecule (SF_6) measured by Lynga *et al.* [23]. (A2) Harmonic spectra of Ar and SF_6 measured in Bordeaux. (B1) decay rate with ellipticity (short trajectories), (B2) emission times of the high harmonics generated in Ar (grey and SF_6 (blue) at $I \approx 1.3 \times 10^{14}$ W/cm^2. (B3) Theoretical recollision angle of the electrons (solid) and measured harmonic polarization direction (measured) for high harmonics generated by a laser pulse with an ellipticity of $\varepsilon \pm 0.2$. (B4) measured harmonic ellipticity for short trajectories as a function of harmonic order. (data A2 to B4 are not yet published).

harmonic radiation. In addition they implemented RABBITT[1] measurements [25] to measure the emission times of the harmonics on the attosecond timescale and draw always a comparison to argon.

Intensity of the HHG spectrum The high-harmonic intensity spectra produced in argon and SF_6 under the same laser conditions are shown in Figure 4.2 (A2). The SF_6 spectrum shows, as in the measurements done by Lynga *et al.* in 1996, a pronounced minimum at harmonic 17. The laser intensity does not modify the position of this minimum. This minimum can be a structural minimum (like a Cooper minimum [26]) or either interferences between two channels of HHG with a similar I_p [27]. Indeed the phase difference acquired by the two cation states during the time the electron travels in the continuum can be written as $\varphi \propto \tau_e \times \Delta I_p$, with τ_e the traveling time of the electron (as pictured in Figure 1.15) that depends strongly on the laser intensity and with ΔI_p the ionization energy difference between the two cation states. If ΔI_p is small ($\sim$1 eV), then the variation of phase φ as a function of the laser intensity would

---

[1] RABBITT stands for reconstruction of attosecond beating by interference of two-photon transitions and is a technique to characterize an attosecond pulse in the XUV range [25]

not be drastic, leading to an invariance of the minima at H17 as a function of the laser intensity. The comparison with argon is done as the I_p's are quite close: 15.32 eV for SF_6 and 15.76 eV for argon. Consequently the cutoff energy, given by measured from these two systems should be similar. By taking a cutoff energy around harmonic 27 on argon ($\sim$ 42 eV) and by using Eq. (1.28), the ponderomotive energy is 8.23 eV for a laser intensity of 1.38×10^{14} W/cm^2. For SF_6 this should lead to a cutoff energy of around 41.5 eV. Clearly on Figure 4.2 (A2), the cut-off energy is larger than harmonic 27. By fixing a cutoff energy around harmonic 29 (45 eV), the effective I_p in SF_6 would be around 19 eV. Already on this spectrum only, two features are already intriguing: the minimum and the extension of the cut-off.

Ellipticity dependance of the HHG spectrum Using elliptical polarized light to generate high-order harmonics, the efficiency of HHG normally drops drastically with increasing ellipticity ε, where the largest efficiency for the harmonic emission is certainly reached for linear polarisation ($\varepsilon = 0$), except in chiral system [28] and aligned molecules [29]. This effect can be less drastic in molecules compared to atoms because of the extension of the molecular orbital [30]. For small ellipticities the decaying harmonic intensity can be fitted by an gaussian function, $I_q(\varepsilon) = I_q^0 e^{-\beta_q \varepsilon^2}$, where q is the harmonic order and β_q the decay rate with ellipticity. A lower β means a better acceptance to a lateral drift of the electron trajectory. This type of measurement has been shown to be sensitive to molecular structure like demonstrated on different chloromethane molecules [30]. Figure 4.2 B1 shows the decay rate β_q of the harmonic signal as function of the harmonic order for Ar and SF_6. For harmonic 19 to 27, above the minimum in the harmonic spectrum, the decay with ellipticity are remarkably similar, whereas below harmonic 17 the signal is less sensitive to ellipticity in SF_6 than in Ar. This means that the extension of the wavefunction is larger for the lowest harmonics, since the overlap between the returning electron with a lateral kick and the initial wavefunction is larger. This observation is coherent with a change in the polarization angle for harmonics smaller than H17 (Figure 4.2 (B3)). Also the emission time measured in a RABBITT setup shows a difference between harmonic 15 and 17 (Figure 4.2 (B2)).

HHG polarimetry The harmonic polarimetry measurements were performed by recording the harmonic spectrum as a function of the polarization direction of the 800 nm driving laser beam. The resulting signal follows an oscillatory law (Malus' law[1]) as a function of the waveplate orientation used to change the polarization direction. The phase and contrast of the oscillations (extracted from a Fourier transformation) provide respectively the polarization angle and the degree of ellipticity of the radiation, assuming a fully polarized state[2] [34]. The harmonic polarization angles as function of the harmonic order are shown in Figure 4.2 (B3). If the ground state wavefunction is fully symmetric (s orbital), the polarization direction of

---

[1] The classical Malus law predicts an attenuation of a polarized light beam through a linear polarizer which depends on the relative angle θ, between the polarization direction of the incoming wave and the orientation of the polarizer and is simply given by $I = I_0 \cos^2 \theta$ [31, 32].

[2] the polarization state of an electromagnetic wave is characterized by the so called Stokes parameters. The Stokes vector spans the space of unpolarized, partially polarized, and fully polarized light [33].

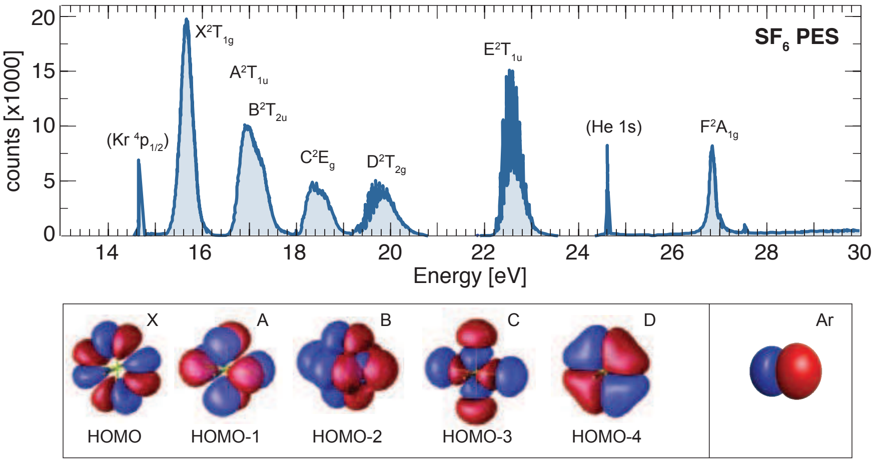

Figure 4.3: HeII ($\hbar\omega$ = 40.8 eV) photo-electron spectrum of SF$_6$ reported in binding energy between 15 and 30 eV. adapted from [38]. Calculated molecular orbitals of SF$_6$ from the HOMO to the HOMO-4.

the harmonics is expected to be equal to the recollision angle. Deviations from this situation reflect the influence of the orbital structure and symmetry [35]. One can again observe a drastic change in the harmonic polarization around H17. The ellipticity of the harmonic emission for short trajectories, assuming the light is fully polarized, is shown in Figure 4.2 (B4). It reaches almost 80% for harmonic 15 and drops to 40% above harmonic 17. This result is the most puzzling one. Indeed, in argon with an incident laser ellipticity of $\varepsilon\pm0.2$, the maximum ellipticity observed is 2% [36]. The significant polarization jump between H15 and H17 does not depend on the incident intensity.

Clearly these observations converge to a HHG process involving more than one molecular orbital. In the next section I will summarize the peculiar features encountered in the ion continuum of SF$_6$.

4.1.3 Tunnel-ionization and molecular orbitals of SF$_6$

To understand the the observations of HHG in SF$_6$ and the results shown here one has to look a bit closer to the special characteristics of SF$_6$ due to its highly symmetric structure and see which molecular orbitals are responsible for HHG in SF$_6$. Due to its highly symmetric shape and the encountered Jahn-Teller effect, the theoretical modeling of HHG in SF$_6$ is a complex task. The chemical bounds of SF$_6$ are linked to the electrons of the sulfur in the 3M shell (four in the 3p and two in the 3s). However as soon as valence excitation is activated, the 3d electrons of the sulfur are involved. This is the case for the $\rightarrow \varepsilon t_{2g}$ transition for the shape resonance [37]. Each of the 6 F atoms is missing a p electron to fill the 2L-p shell. Consequently the last occupied valence orbitals are closed in energies, making the photoelectron spectrum very dense near the I_p [38]. For the cation states investigated here, the emitted electrons are all from the 2p orbital of fluorine, only the atomic orbital of the sulfur changes. The d-orbitals might induce high mobility for the Sulfur electrons. To go a little bit further, the Hartree-Fock configuration for the ground electronic state of SF$_6$ with ($16 + 9 \times 6 = 70$) electrons to distribute is [39]:

$$\begin{aligned}&\underbrace{(\ldots)^{22}}_{\text{core}}\ \underbrace{(4a_{1g})^2(3t_{1u})^6(2e_g)^4(5a_{1g})^2(4t_{1u})^6(1t_{2g})^6(3e_g)^4[(1t_{2u})(5t_{1u})]^6(1t_{1g})^6}_{\text{valence electrons}}\ {}^1A_{1g}\\ &\qquad\underbrace{(6a_{1g})^0(6t_{1u})^0(2t_{2g})^0(4e_g)^0}_{\text{unoccupied}}\end{aligned} \tag{4.1}$$

The four highest occupied molecular orbitals (HOMO) are lying within 3 eV. Figure 4.3 shows the photo-electron spectrum of SF_6 and the assignments of the features. In this molecule, there is a direct assignment between the electron removal from the molecular orbitals and the cation states. Underneath the calculated molecular orbitals for the ground state and the HOMO-1 to HOMO-3 are shown.

To understand the origin of the drastic change in the harmonic emission around harmonic 17, the CELIA group and Serguei Patchovskii developed a simple harmonic emission model, where the harmonic dipole moment is determined by the tunnel ionization probability, the propagation of the electron in the continuum, and the recombination cross section. The different channels corresponding to ionization from different molecular orbitals are considered as uncoupled. The harmonic intensity for each molecular channel j (= X, A, B, C, D) is given by:

$$I^j = \left| P^j_{TI} d^j_{rec} e^{i\varphi^j} \right|^2 \tag{4.2}$$

where P^j_{TI} is the tunnel-ionization probability, d^j_{rec} the recombination dipole moment which is assumed to be equal to the photoionization cross-section in the VUV range and $\varphi^j \propto \Delta I^j_p \tau_e$ is a phase term accounting for the accumulated phase by the molecule between ionization and recombination due to the propagation in the continuum. ΔI^j_p is the difference between the ionization potential of channel j and the X channel, and τ_e is the electron travel time in the continuum, which increases with harmonic order from 0.6 fs to 1.7 fs for short trajectories [40]. Because the cross-sections are very similar, this picture is still very complex. In general, one would expect that the HOMO is the main contributing orbital due to the exponential dependence of the tunnel ionization (see Eq. (1.20)). Figure 4.4 shows the tunnel ionization probability calculated by Serguei Patchovskii summed over the different directions between the molecular axis and the linear polarized electric field. A summary of the values is given in Table 4.1. The tunneling probability from the HOMO is significantly reduced by the presence of nodes in the orbital, such that deeper channels are favored. The resulting contributions for the tunnel ionization probability shows only a significant contribution for channel B (HOMO-2) and C (HOMO-3). Indeed the HOMO-2 is the first molecular orbital with a simple parity (a single nodal plane) and the HOMO-3 is the first contracted molecular orbital, not as diffuse as the HOMO and the HOMO-1. By taking into account the contracted nature of the C orbital along the S-F bonds as can be seen in Figure 4.4 for the first molecular orientation, we can expect that the outgoing electron will have an extended wavefunction compared to the B channel that is a more diffuse molecular orbital. This feature will explain why the β parameters are lower at low energy in Figure 4.2 (B1) where tunnel-ionization is assumed to take place from the C channel. Clearly the B (HOMO-2) and C (HOMO-3) channels are largely

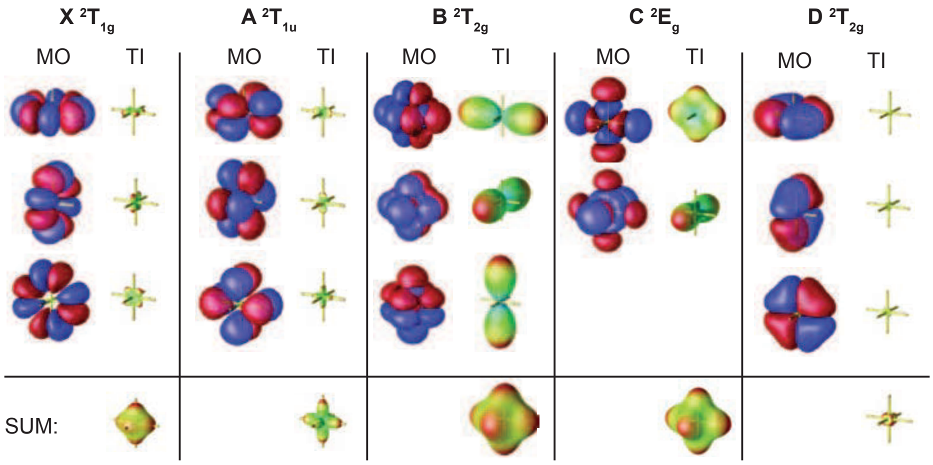

Figure 4.4: Graphical illustration of the calculated tunnel ionization probability shown for each molecular orbital and orientation. The lower line shows the summation over all orientations. Calculations by Sergei Patchkovskii, NRC Ottawa.

favored by tunnel ionization due to their symmetry and more localized character. Moreover these B and C channels are well known in photoabsorption spectroscopy to enhance the cross section around 23 eV (see Figure 4.6). Around that energy, an autoionization process (two electron operation) characterizes the photoionization onto the C channel, while a shape resonance process (one electron operation) characterizes the photoionization onto the B channel. The total harmonic intensity can be calculated by coherently summing the signals from the different channels with the recombination dipole moment d^j_{rec} equal to the XUV photoionization cross section (see Figure 4.5 (A)). In the present SF_6 harmonic emission calculations, the only parameters which take into account the shape resonance and autoionization enhancement are the ionization cross-sections. The result presented in Figure 4.5 (B) shows a minimum between harmonic 15 and 17 as observed in Figure 4.2 (A1/A2). The maxima for the dominant channels are related to resonances in the recombination/VUV ionization matrix elements: the autoionization resonance for channel C (a $5a_{1g} \rightarrow 6t_{1u}$ transition) and the shape resonance (a $1t_{2u} \rightarrow \varepsilon t_{2g}$ transition) for channel B. The HHG efficiency for these two channels overlap between 21.75 and 26.4 eV (HH15 = 23.5 eV and HH17 = 26.35), for which both get their highest photoabsorption cross-sections. The $5a_{1g} \rightarrow 6t_{1u}$ transition corresponds to an electron excitation on the sulfur that is 3s to 3p [42] while the $1t_{2u} \rightarrow \varepsilon t_{2g}$ is a 3p to 3d excitation. Note that these two electronic transitions are dipole allowed in the O_h symmetry group. The total photo-absorption cross-section form 13 to 30 eV is shown in Figure 4.6. Marked are as well

Table 4.1: Calculated tunnel ionization of the molecular orbitals of SF_6 summed up over all molecular orbital orientations

Molecular Orbital	X^2T_{1g}	A^2T_{1u}	B^2T_{2g}	C^2E_g	D^2T_{2g}
tunnel ionization probability [$\times 10^6$]	2.70	1.73	7.94	5.21	1.06
IP [eV]	14.743	15.918	16.369	17.373	18.506
$\langle d\|d\rangle$	0.912	0.909	0.918	0.928	0.907

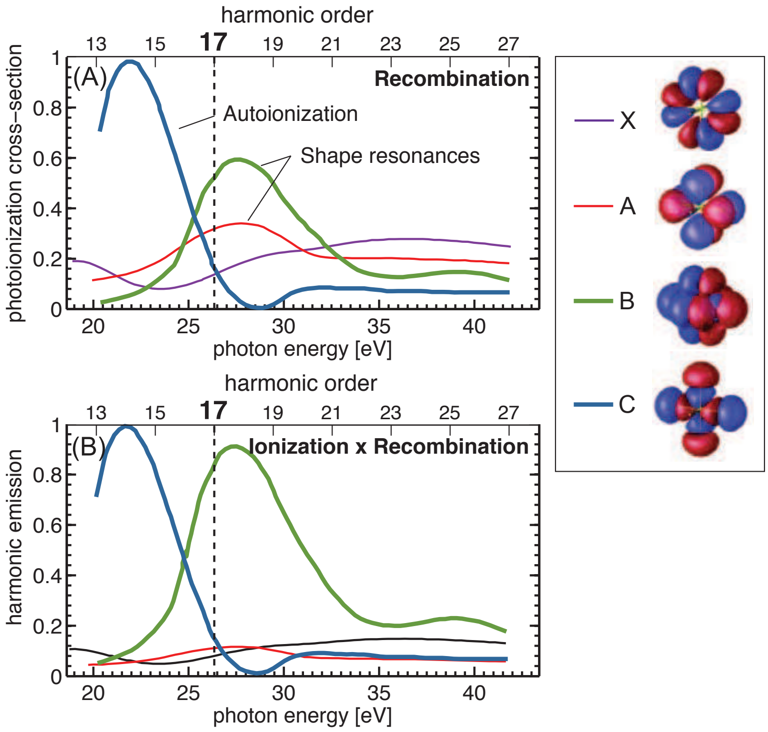

Figure 4.5: Simple theoretical study of the HHG emission from SF_6. (A) XUV photoionization cross sections from [41]. (B) Calculated harmonic emission (Tunnel-Ionization x Recombination).

the assignments of the corresponding electronic transitions [43].

There are four identified shape resonances encountered in SF_6: $2t_{2g}$, $4e_g$ above the I_p and $6a_{1g}$, $6t_{1u}$ near the I_p. Shape resonances in a simplified version are induced by dipole allowed transition (t_{1u} symmetry for O_h group), but vibronic coupling like the Jahn-Teller effect[1] that can take place from all cation states in SF_6 releases this condition. Resonances which lie above their parent I_p are called *shape resonances* or 'open-channel resonances' or 'Type II' [44]. They are quasi bound states where the potential forms a penetrable barrier which temporarily traps the incident particle (like electrons) near the target and through it may eventually tunnel and escape. Most of the barrier is formed by the angular momentum of the electron. Basically, the photoelectron before to become 'photo' (ionized) feels an extra energy barrier at long distance from the ion core, which is in the case of SF_6 along the S-F internuclear coordinate. Being quasi bound inside the potential barrier on the perimeter of the molecule, these resonances are localized, have enhanced electron density resulting in larger oscillator strength and are uncoupled from the external environment of the molecule [45]. The trapping might lead to a slowing down of the emission and introduce a phase effect on the recombination step in the HHG process. The concept of shape resonance in SF_6 can be illustrated in terms of a two-well potential model, introduced by Dehmer in 1972 [46] where 'inner-well' and 'outer-well' states result from an effective potential barrier located along the S-F bonds. Figure 4.7

---

[1] Jahn-Teller effect is a vibronic coupling induced by a geometrical distortion of molecules that is associated with certain electronic configurations.

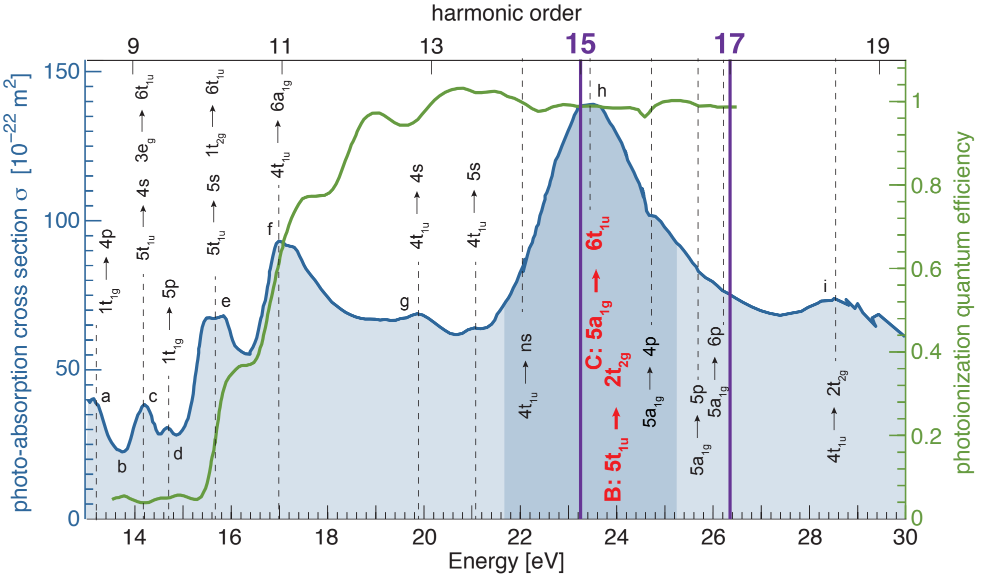

Figure 4.6: The absolute photoioniation cross section σ_{pi} (blue) and the photoionization quantum efficiency (green) of SF_6 with assignments. The two vertical purple lines indicate the energy of harmonic 15 (23.25 eV, 53.3 nm) and 17 (26.3 eV, 47.14 nm) using an 800 nm driving laser pulse. Adapted from [43].

shows a schematic diagram of this two-well potential [24]. In the case of SF_6, the fluorine atom traps the d-electron from the sulfur that wants to leave the core, due to the strong electronegativity of the fluorine[1] [42]. The inner well corresponds to valence orbitals. One can see from Figure 4.7, that four electronic levels seem to be supported by the barrier, assigned to the unoccupied molecular orbitals: $6a_{1g}$ and $6t_{1u}$ near the vacuum level/ionization threshold and $2t_{2g}$ and $4e_g$ lying in the electron continuum but within the effective barrier. Calculations by Stener et al. puts the $6a_{1g}$ also above the I_p [42]. Any electronic transition to these states will give an enhancement in the absorption cross section. This enhancement is called shape resonances. The outer-well corresponds to Rydberg orbitals. Since the overlap between the Rydberg orbitals and the initial electronic wavefunction is expected to be poor along the S-F distance, Rydberg transitions are in general weaker when shaped resonances characterize the molecular ionic potential. Due to the well defined position of the fluorine atoms, it is as well expected to get a really anisotropic molecular field, which is encoded in the photoelectron angular distribution ($\beta = 0$) [47–49]. The shape resonance/auto-ionization feature observed by Holland et al.[43] is 4 eV large and centered at 23.6 eV (see dark blue area in Figure 4.6). Table 4.2 summarizes the assignments of the photo-electron bands by removal of one electron of a molecular orbital. Also shown are the observed corresponding resonances in the absorption spectrum. This shape resonance appears as well very clearly on dissociative ionization onto SF_5^+ + F [50]. Since the shape resonance of the B channel is a photoelectron which is trapped for a few hundred attoseconds due to the electronegativity of the fluorine atoms, the arising question is how this effect will change as a function of S-F internuclear distance. Indeed, it is expected that the electronic barrier to the ionization might vary as a function of the

---

[1] Electronegativity of fluorine is 3.98 and of sulfur only 2.58 in Pauling units

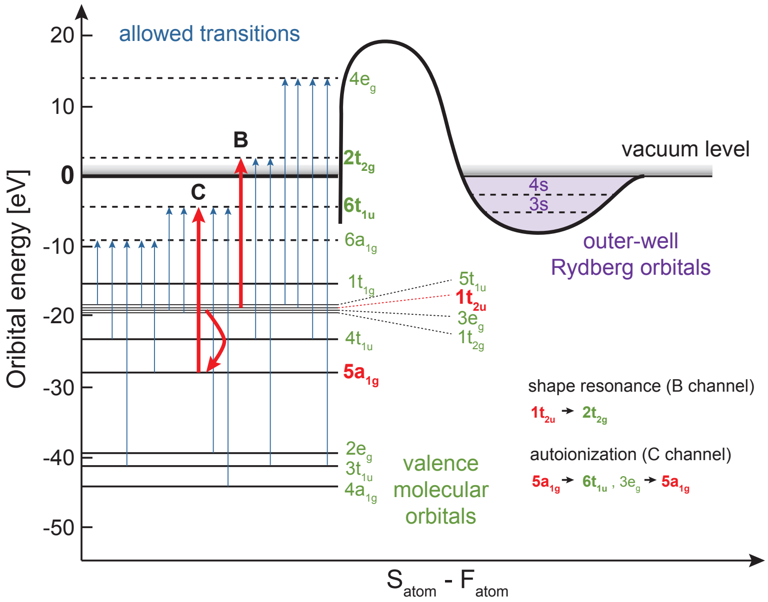

Figure 4.7: Schematic diagram of the two-well potential of SF_6 acting on the outgoing electrons in the photoabsorption process. Dashed lines are vacant orbital levels and full lines indicate occupied valence orbital levels. The arrows show the allowed transitions by the electric dipole moment for the O_h symmetry group. Marked in red are the autoionization resonance (C channel) and the shape resonance (B channel). Adapted from [24].

S-F distance [37]. The equilibrium S-F distance is known to be 1.556 Å for the molecular ground state [51]. By varying this distance, it is expected that the position, the intensity and the line shape of the $2t_{2g}$-shape resonance will vary. Changing the intermolecular distance can be achieved by vibrational excitation of the molecule. In the pump-probe experiments shown here, the goal was to determine the phase variation of the high harmonic emission as a function of the geometry of SF_6. The geometry variation is a vibrational wave packet oscillating in the ground electronic state and created at $\Delta t = 0$ by a Raman pump pulse. Two HHG techniques have been used in this thesis, one based on two non-colinear pump pulses (transient grating setup) and the second one based on two spatially separated probe pulses. The two setups will be described in the experimental section. But first we have to take a look at the vibrational spectrum of SF_6.

4.1.4 The vibrational spectrum of SF_6

The vibrational spectrum can be investigated by two types of spectroscopy, Raman and Infrared (IR) spectroscopy. When light (a photon) interacts with a molecule, it can either be elastically or inelastically scattered. In the first case, the absorbed photon has the same wavelength as the emitted one (Rayleigh scattering), but in the second case, the photon has lost or gained an amount of energy related to the vibrational energy spacing in the molecule. This amount corresponds to the wavelength of the so called Stokes and anti-Stokes lines which are equally displaced from the Rayleigh lines in the Raman spectrum. Infra-red spectroscopy also measures the vibrational energies of molecules. The absorption of light in the infrared region of the electromagnetic spectrum, gives a spectrum that corresponds to specific vibrational modes

Table 4.2: Summary of the photoelectron band assignments in SF_6 by removal of one electron from a molecular orbital. Also shown are the observed corresponding resonances in the absorption spectrum.

Cation electronic state	Energy [eV]	Electron removed from MO	Resonance at [eV]		Comments
			εt_{2g}	εe_g	
X^2T_{1g}	15.32 15.7 15.5	$1t_{1g}$	20.7	30.9	$\beta = 0$, branching ratio (> 17 eV) ~20%
A^2T_{1u} B^2T_{2u}	17 16.7	$5t_{1u}$ $1t_{2u}$	21.9	32.1	$\beta = 0$ branching ratio > 40% 2/3 is due to 1t2u
C^2E_g	18.6 18	e_g	23.2	33.4	$\beta = 0$ branching ratio energy dependent
D^2T_{2g}	19.7 19.245	t_{2g}	24.5	34.7	$\beta = 0$ branching ratio < 20%
	22.5 22.7		27.9	38.1	
	26.8		32	42.2	

and is unique to each molecular structure examined. In principle, Raman spectra are due to the scattering light by the vibrating molecules and IR spectra are the result of absorption of light by vibrating molecule.

Molecules in general have 3N degrees of freedom, where N is the number of atoms in the molecule. Taking translation (3) and rotations (3 for nonlinear and 2 for linear) into account one obtains 3N-6 (3N-5 for linear molecules) potential vibrational degrees of freedom. For SF_6 this means 15 potential vibrational modes. Due to the symmetry of the molecule some of these modes will be degenerated. Two symmetrically equivalent vibrations having the same wavenumber are called degenerated. SF_6 with a regular octahedron form belonging to the point group O_h shows only six fundamental vibrations, the so called normal modes [52]. One vibration is non-degenerated (class A_{1g}, υ_1), one is doubly degenerated (class E_g,cυ_2) and four are triply degenerated (two in class T_{1u}, υ_3 and υ_4, and one each in classes T_{2g},υ_5, and T_{2u}, υ_6) [52, 53]. Of these vibrations, υ_1, υ_2 and υ_5 are Raman-active, υ_3 and υ_4 are infra-red-active and υ_6 is inactive. A graphical interpretation of the normal vibrational modes of SF_6 is shown in Figure 4.8. If a vibration is active and if it is Raman- or IR-active is determined by the symmetry and the selection rules. In general for a vibration to be infrared-active, the vibrational motion must cause a nonzero dipole derivative at the equilibrium position. For a vibration to be Raman-active, it must have a non-zero derivative of the polarizability. The Raman spectrum of SF_6 was first studied by Yost el al [54] in 1934 who found three vibrational modes around 776(10), 642(2) and 522(2) cm^{-1}. The infrared spectrum as well has been studied by several groups which shows two modes around 615, and 948 cm^{-1} [53, 55–57]. These spectroscopic results confirmed the earlier conclusion that the SF_6 molecule has the

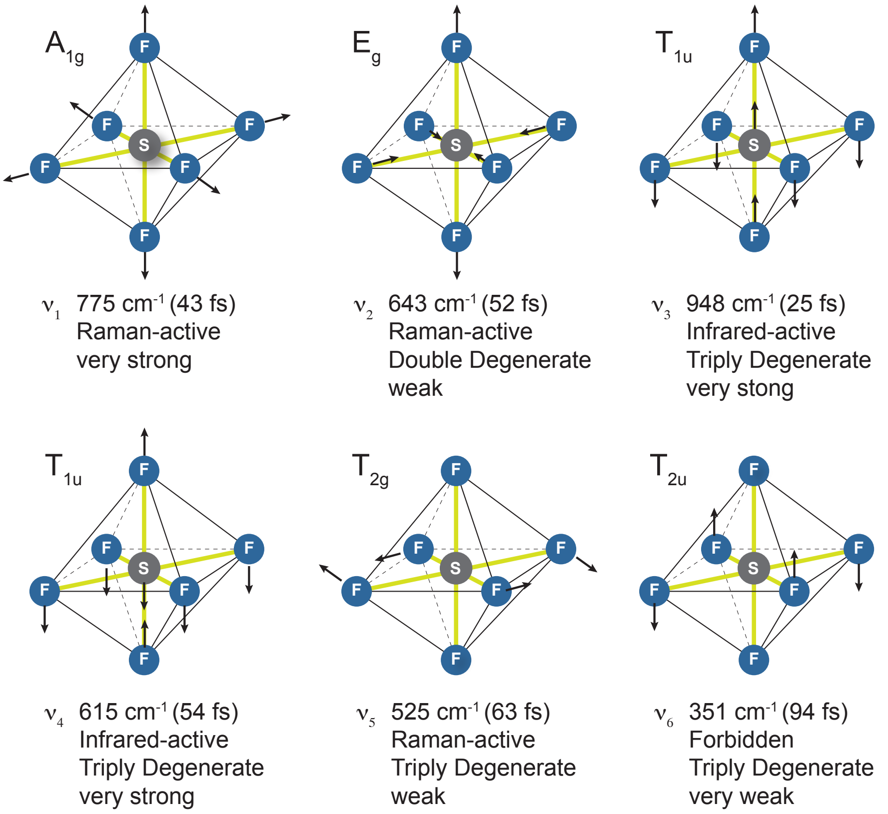

ν_1 775 cm^{-1} (43 fs)
Raman-active
very strong

ν_2 643 cm^{-1} (52 fs)
Raman-active
Double Degenerate
weak

ν_3 948 cm^{-1} (25 fs)
Infrared-active
Triply Degenerate
very stong

ν_4 615 cm^{-1} (54 fs)
Infrared-active
Triply Degenerate
very strong

ν_5 525 cm^{-1} (63 fs)
Raman-active
Triply Degenerate
weak

ν_6 351 cm^{-1} (94 fs)
Forbidden
Triply Degenerate
very weak

Figure 4.8: Normal modes of the vibration of SF_6. The wavenumber, period, degeneracy, and activity of each mode is shown. Of these 6 normal mode vibrations, υ_1, υ_2 and υ_5 are Raman-active, υ_3 and υ_4 are IR-active and υ_6 is inactive. Adapted from [52, 58].

octahedral symmetry O_h given by electron diffraction measurements.

Femtosecond laser pulses have shown to be able to excite vibrational wave packets in molecules, by Raman transitions [59–62]. One of the hot topics in HHG is to investigate the capacities of high-order harmonic spectroscopy to reveal nuclear dynamics. Measurements using HHG as time resolved signal in SF_6 have shown that the HHG emission is sensitive to the excited vibrational modes [58]. The high-order harmonic yield is observed to oscillate, at frequencies corresponding to all of the Raman-active modes of SF_6. These observations collectively demonstrate that monitoring HHG from vibrationally excited molecules yields useful data on intramolecular dynamics that can be directly interpreted independent of complex models or tomographic deconvolution techniques. Since the shape resonance which seems to play an important role in the minimum of the harmonic emission in SF_6 is strongly linked to S–F distance, they have a tendency to be smeared out by nuclear motion. By vibrational exciting the molecule we might therefore affect the shape resonance and the process of HHG in SF_6. In [58], a single pump and a single probe were used in a colinear geometry. This type of measurement leads only to the access of amplitude information without the phase information. In this work, the three Raman active modes that are 525 cm^{-1}, 643 cm^{-1} and 775 cm^{-1} appear with a branching ratio of 48%/9.6%/42%, respectively. These experimental results have been tentatively reproduced by calculations giving 5.6%/7%/87% branching ratio for 525/643/775 cm^{-1} vibrational modes, respectively [63]. This calculation however does not reproduce the experimental data. Moreover, they assume that tunnel ionization takes place only from the ground cation state X and not from the B and C channels. However, these are the most developed calculations so far to reproduce this type of experiment, since they take into account the Jahn-Teller effect in the ion continua, the possibility of an extra Raman transition induced by the probe pulse and cross-terms of ionization and recombination between vibrational levels of the cation state.

The goal here is to observe the vibrational dynamics as function of the harmonic order through a phase sensitive pump-probe measurement. The phase resolved dynamical measurements were performed in two different setups using a HHG interferometry setup (two probe pulses) and a transient grating setup (two pump pulses) at CELIA at the University of Bordeaux. The two setups will be described in the following sections. The Aurore laser system at CELIA[1] was used in both setups which delivers 7 mJ/p at a center wavelength of 800 nm and a repetition rate of 1 kHz with a pulse duration of 28 fs. The typival characteristics of the Aurore laser can be found in Appendix A.

4.2 Strong field transient grating spectroscopy

4.2.1 Experimental

The signal change after an excitation used in pump-probe experiments can be very weak leading to unfavorable S/N ratios. In case of electrical signals usually a Lock-In amplifier can be used to improve the S/N ratio. This electric filtering method cannot be applied for optical signals recorded via a CCD camera at 20 Hz. Therefore we choose an experimental setup that uses the well-known femtosecond degenerate four-wave mixing (DFWM) technique, also called femtosecond transient grating spectroscopy [64] which comes from the context of conventional perturbative nonlinear spectroscopy but was recently applied to nonperturbative nonlinear optics where it was used in high harmonic generation experiments [65]. Transient grating spectroscopy (TGS) is the method of choice for measuring femtosecond dynamics in solids, liquids, or gases whenever background suppression is important.

Two beams are used to create a grating of molecular excitation and a third beam is used to generate high-order harmonic radiation. The principle of a TGS setup is shown in Figure 4.9. Two synchronized non-collinear pump beams are crossed with an angle θ between them in the molecular beam to create an optical interference grating and thus the excitation of the sample is spatially modulated: a grating of molecular excitation is created. The fringe spacing a of the grating depends on the angle θ between the two pulses and is given by:

$$a = \frac{\lambda}{2\sin(\theta/2)} \tag{4.3}$$

In the present experiments the fringe spacing is 18 µm. The third probe beam is focused into the grating of excitation in the gas target to generate high-order harmonics. With a waist

---

[1] CELIA, Centre Lasers Intenses et Applications, Université Bordeaux 1

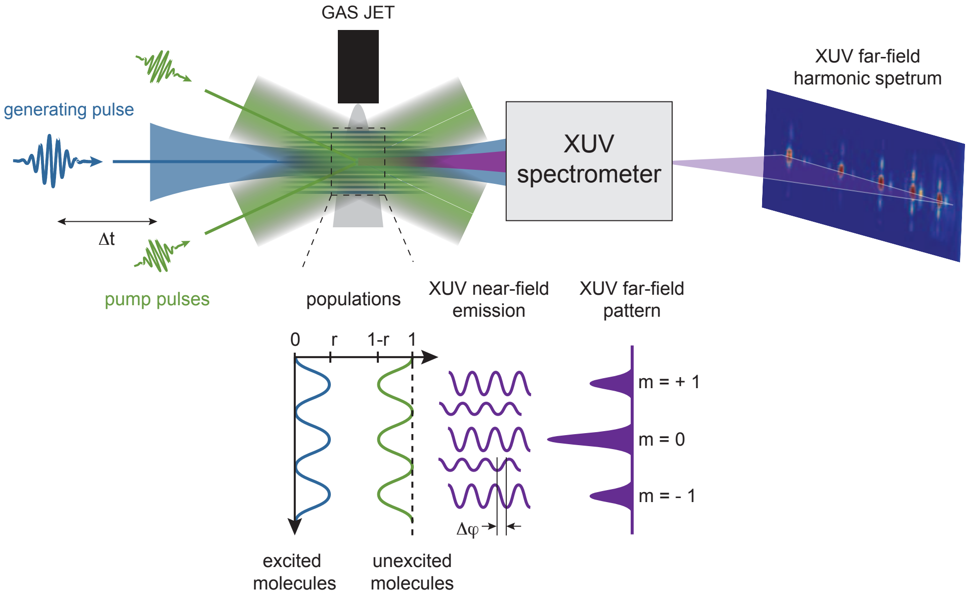

Figure 4.9: Principle of strong field transient grating spectroscopy. Two synchronized pump pulses set up a transient grating of excitation in the molecular beam. A delayed 800-nm pulse generates high-order harmonics from the grating. The periodic modulation of the high-harmonic amplitude and phase in the near field (in the laser focus) results, in the far field (at the detector), in an additional first-order diffraction (m = ± 1) signal.

size of 100 μm, the diffraction occurs through five fringes. At positions of low intensities, molecules remain unexcited and at high intensities they are excited. As amplitude and phase of the generated high harmonics are different for vibrational excited and unexcited molecules in the near field, the grating leads to a diffraction pattern in the far field. The geometry is chosen such that there is no light emitted in the diffraction direction if there is no grating (phase matching conditions such that HHG for long trajectories is not satisfied). Thus, the detected signal is zero when there is no excitation and the measurement is background free. The lower part of Figure 4.9 illustrates the spatially modulated fraction of excited molecules which has its maximum value r at constructive interference of the optical grating. The fraction of excited molecules is expressed as $r(z) = r(\cos(kz) + 1)$, where $k = 2\pi/a$ is defined by the fringe spacing a, in case of a single photon excitation process [66]. Consequently, the harmonic emission E across the transient grating at photon energy Ω in the near field is a superposition of the emission from molecules in the $\nu = 0$ state (E_g) and in the vibrationally excited state (E_e):

$$\begin{aligned} E(\Omega,z) &= E_g(\Omega,z) + E_e(\Omega,z) \\ &= (1 - r(z))A_g(\Omega)\, e^{i\phi_g} + r(z)A_e(\Omega)\, e^{i\phi_e} \end{aligned} \tag{4.4}$$

where A and ϕ are the amplitude and phase of the emission from the molecules in the $\nu = 0$ state (g = ground) and in a non-stationary vibrational state (e = excited) , called a vibrational wave packet. The signal in the far-field is the Fourier transform of this with the spatial fre-

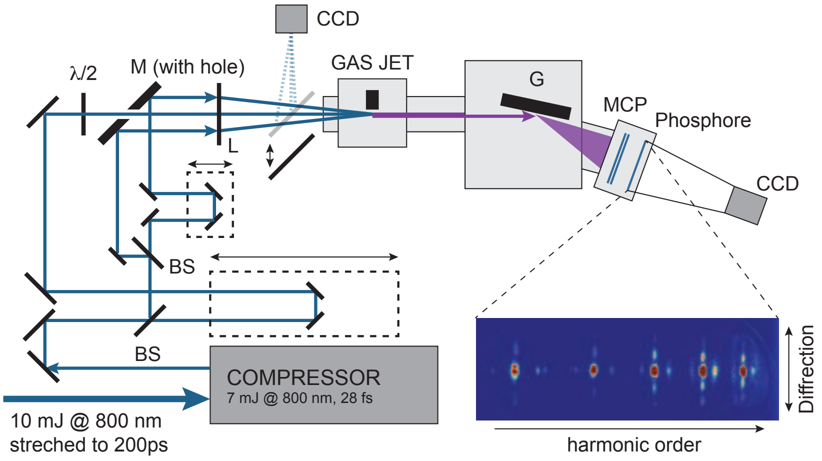

Figure 4.10: Schematic diagram of the TGS setup. The laser beam is split into a pump and probe beam. A π-phase plate (PP) in the probe arm is generating 2 vertical separated foci in the gas jet. The pump beam is overlapped with the lower focus via a hole mirror. All three beams are focused with a lens with a 500 mm focal length. The XUV spectrometer is a 1200 g/mm grazing incidence spherical grating with variable groove spacing that dispersed horizontally the HHG on a detector consisting of microchannel plates, a phosphor screen and a charge-coupled device camera.

quency ξ and given by [66]:

$$F(E) = \left((1-r)A_g\,e^{i\phi_g} + rA_e\,e^{i\phi_e}\right)\delta(\xi) + \frac{r}{2}\left(A_e\,e^{i\phi_e} - A_g\,e^{i\phi_g}\right)\left[\delta\left(\xi + \frac{k}{2\pi}) + \delta(\xi - \frac{k}{2\pi}\right)\right] \tag{4.5}$$

The observed intensity distribution in the far-field is the power spectrum of Eq. (4.5) and given for the undiffracted ($m = 0$) and the diffracted light ($m = \pm 1$):

$$I_{m=0}(\Omega) = \left|rA_e(\Omega)\,e^{i\phi_e} + (1-r)A_g(\Omega)\,e^{i\phi_g}\right|^2 \tag{4.6a}$$

$$I_{m\pm 1}(\Omega) = \frac{r^2}{4}\left|A_e(\Omega)\,e^{i\phi_e} - A_g(\Omega)\,e^{i\phi_g}\right|^2 \tag{4.6b}$$

These equations are only valid for small pump pulse intensities. Is the laser intensity too high a grating of free electrons (grating of ionization) is produced and the simple definition of $r(z) = r(\cos(kz) + 1)$ is not valid anymore. Indeed, ionization will start to flatten the high intensity part and the cosine intensity profile will be modified.

Figure 4.10 shows the schematic setup used for the transient grating spectroscopy in Bordeaux. The laser beam after the compressor is divided into two beams. The major part (probe) is sent through a computer-controlled delay stage towards the high-order harmonic generation chamber, while the minor part (pump) is sent through a 50:50 beam splitter to generate two equally intense 800 nm pulses. To get the shortest pulses possible for both, the pump and the probe, wedges are introduced to compensate the thick beam splitters. The two pump beams are aligned parallel to each other with a vertical offset of ~3 cm, and combined with the third probe beam via a mirror at 45° before the vacuum chamber. The probe beam passes through a hole in this mirror so that afterwards all three beams travel in the same vertical plane with an offset between them. The three beams are then focused via a 50 cm lens in a continuous

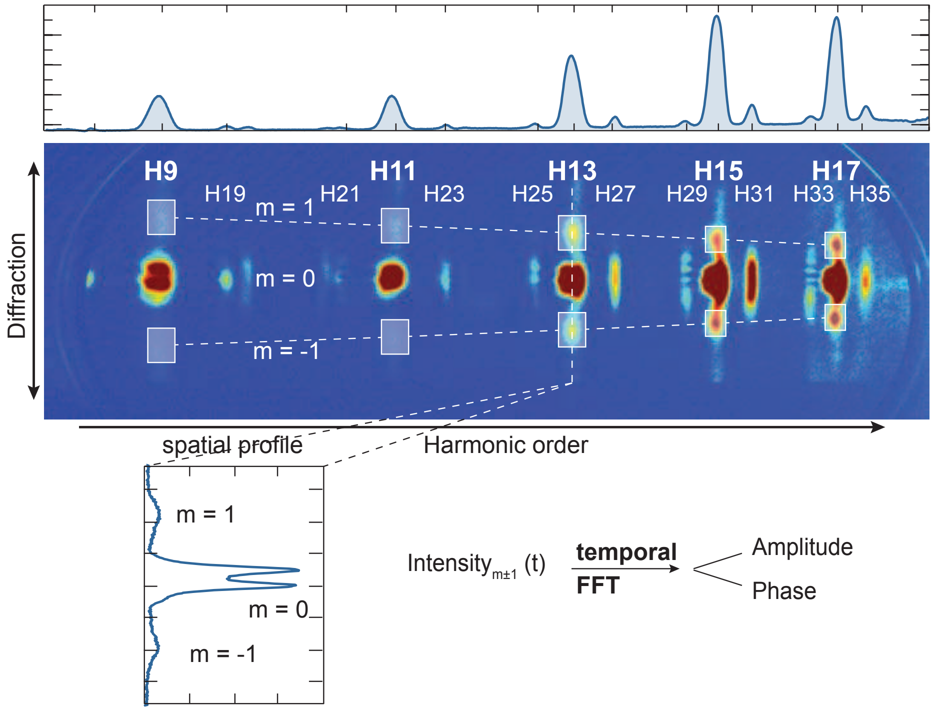

Figure 4.11: Transient grating image analysis. Shown is a recorded image at pump-probe delay of 1 ps. Harmonic 9 to 17 are visible in zero and first order diffraction ($m = \pm 1$). On top is shown the integrated signal over the spatial coordinate. Also visible are $m = 0$ of the second order diffraction from the XUV grating. The white areas show schematic the areas selected to extract the diffracted light for each harmonic. Shown is as well as example a spatial profile through harmonic 13. The depletion at the center of $m = 0$ is an artifact from a damage in the MCP.

molecular jet produced by a 60 µm nozzle (home-made) backed by a few hundreds of mbars of gas. Typically energies of $2\times$ 140 µJ/p and 320 µJ/p were used for the pump and probe pulse, respectively. The generated high-order harmonic spectrum is sent to a XUV spectrometer consisting of a grating with a groove spacing of 1200 mm^{-1} that images the XUV radiation onto a detector, which consists of a set of dual MCP's, a phosphor and a CCD camera. The pump pulse intensity had to be chosen carefully. Using to much intensity in the grating, one is able to produce harmonics with only the pump pulses alone or is able to create a grating of free electrons due to ionization (grating of ionization). To avoid such situation not only the pump intensity but as well the distance of the beams to the nozzle was varied. Indeed, with a larger beam size (a few mm away from the nozzle) the phase matching conditions for HHG by the pump pulse alone were not achieved anymore.

Alignment

The alignment procedure is tricky as three independent parameters (time delay, z- and y-direction) need to be well adjusted for a spatial and temporal overlap between all three beams. First the the spatial overlap is determined by imaging the overlap of the focii of the three beams on a CCD camera by introducing a mirror just after the lens. The temporal overlap of the two pump beams can be found as well on the camera by monitoring the interference pattern on the CCD. Afterwards one pump beam is blocked and the temporal overlap of the probe beam is adjusted as well by finding the interference pattern on the camera.

Image analysis

A typical image of an harmonic spectrum recorded with this setup is shown in Figure 4.11. Only HHG from short trajectories are observed. Harmonic 9 to 17 are clearly visible with the first order diffraction from the transient grating. The image is saturated in order to identify the first order diffraction from the transient grating. The first order diffraction is more visible for harmonic 17 and vanishes almost for harmonic 9. To extract the intensity oscillations from the zero order and first order diffraction of each harmonic we defined areas around each signal as shown in Figure 4.11 for the first order diffraction. These areas are then integrated separately for each delay to obtain the time-resolved signals. Also visible is the second order diffraction of the XUV grating showing H19 to H35. But here only $m = 0$ from the transient grating is visible. The time resolved signal is then analyzed by taking the Fourier transform to extract the amplitude and phase of the underlying frequencies of the intensity oscillations. The pump intensities are increased to the maximal value for which diffraction appears without HHG generation by the pump beams alone. Indeed Raman excitation at 800 nm is quite inefficient in SF_6.

4.2.2 Results from the transient grating setup

Figure 4.12 (A) shows the integrated signal of the first order diffraction from the transient grating ($m = \pm 1$) for harmonic 9 to 17 as function of the pump-probe delay up to 2 ps with a time resolution of 5 fs. For the higher harmonics, which are visible as second order diffraction from the grating, only $m = 0$ is visible. The polarizations of the pump and probe laser beams are parallel to each other. The signal from the first order diffraction as shown in Figure 4.12 (A) is a summation of $m = 1$ and $m = -1$ and normalized to the total harmonic signal ($S_{tot} = S_{m=1} + S_{m=-1} + S_{m=0}$) to give the efficiency of diffraction. The y-axis is arbitrary as the efficiency is normalized and an offset of 1 was added to be able to plot all five harmonic signals in one graph and to separate them. The total harmonic signal can be decomposed into the contribution of $\sim$80% in $m = 0$ and $\sim$20% in $m = \pm 1$ as can be seen in Table 4.3 which shows the harmonic yield in $m = 0$ ad $m = \pm 1$ and as well the modulation depth for each harmonic in relation to the total harmonic signal. Interesting to note is the aspect that we observe modulations of up to 15 - 30% in the high harmonic yield, which is an increase of around 30% compared to the experiment done by Wagner et al [58]. Note also that the undiffracted signal $S_{m=0}$ does not oscillate in contrary to Wagner *et al.*. This can be explained by the fact that the heterodyne detection acts as a filtering. As $m = 0$ is not oscillating, the division by S_{tot}, won't introduce a time dependency, but simply will smooth out the slow variation of the laser intensity. Indeed the time transients are averaged over 8 scans recorded over 3 hours.

To deduce which vibrational modes are detected, Figure 4.12 (B) shows a discrete temporal Fourier transform of the data shown in Figure 4.12 (A), for a time interval between 0.2 and 2 ps. Note that time duration of the pulse in the present experiment is $\sim$30 fs, while the vibrational

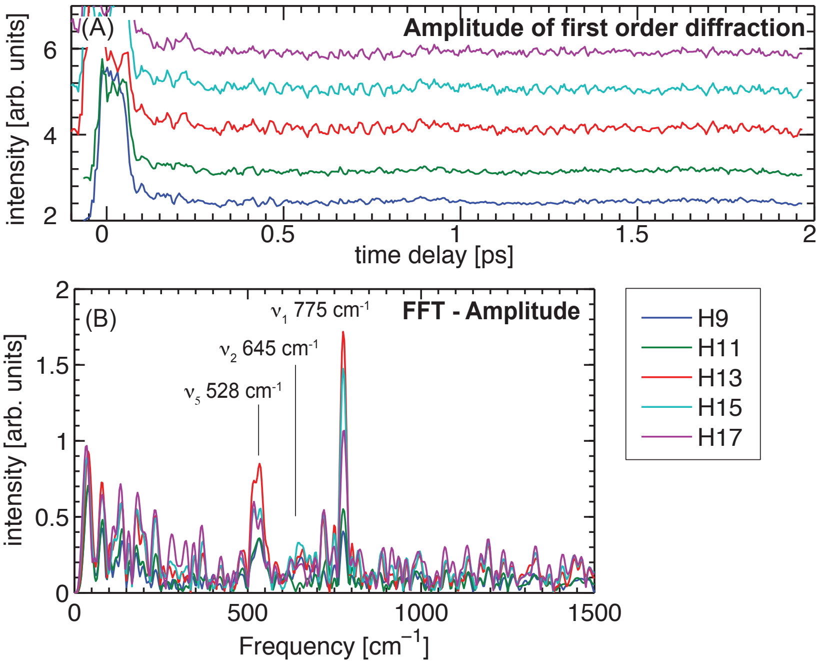

Figure 4.12: Integrated signal of the first order diffraction of the TG as function of the pump-probe time delay (A) and the amplitude of the temporal Fourier transform of this signal (B). To be able to distinguish between the harmonics an intensity offset was introduced in the time-resolved data. In the FFT the Raman active vibrational modes ν_1 at 775 cm^{-1} and ν_5 at 528 cm^{-1} can be observed. The third mode ν_2 at 645 cm^{-1} is almost not visible.

modes (775, 645, 525 cm^{-1}) are expected to oscillate at 43, 52 and 63 fs, respectively. This means that the molecule has time to almost do a full cycle of vibration during the probe pulse duration. Similar conditions are given for the pump beam, relative to Δt = 0. Two maybe all three Raman active vibrational modes can be identified on Figure 4.12 (B). The modes at 775 cm^1 (ν_1) and 528 cm^{-1} (ν_5) are clearly visible whereas the mode ν_2 at 645 cm^{-1} is basically in the noise level. In comparison to the data obtained previously by monitoring only the amplitude of the HHG in SF$_6$ in presence of only one Raman pump pulse by Wagner et al. [58] where they observed that the strongest signal was coming from the ν_5 (528 cm^{-1}) mode, we observe here that the mode ν_1 (775 cm^{-1}) is the strongest. Whatever the optical alignment was, this mode was always visible, whereas the other two modes where much more sensitive to the alignment and the laser beam intensities. The ν_1 vibrational mode being the

Table 4.3: Harmonic yield in the undiffracted ($m = 0$) and diffracted ($m = \pm 1$) signal in relation to the total yield in this harmonic. As well shown is the harmonic modulation depth and the ratio of harmonic q to the total harmonic intensity.

harmonic order	9	11	13	15	17
$I^q_{m=0}/I^q_{tot}$	.77	.82	.78	.80	.79
$I^q_{m=\pm1}/I^q_{tot}$	.23	.18	.22	.20	.21
I_{osc}/I_{bg}	.13	.14	.3	.28	.25
$I^q_{tot}/\sum_q I^q_{tot}$	.13	.12	.21	.28	.26

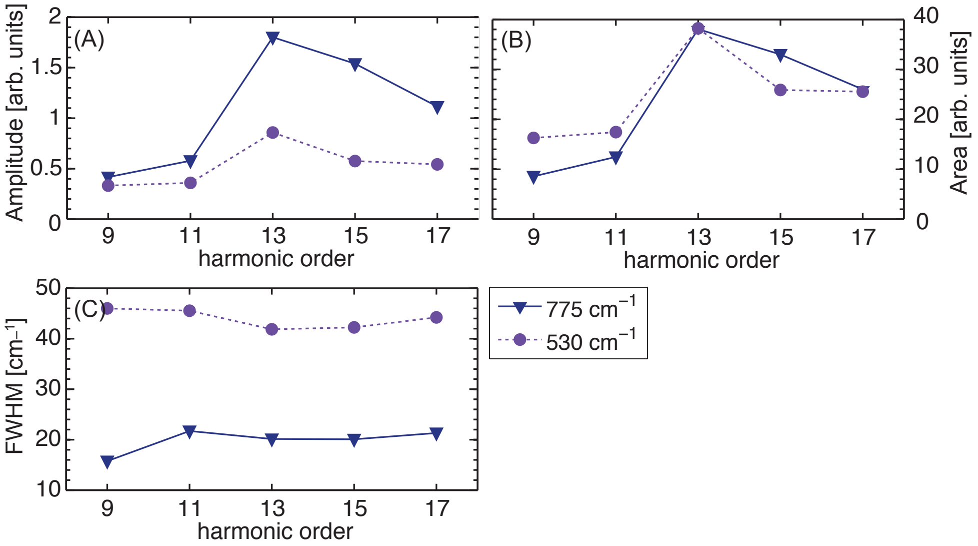

Figure 4.13: Amplitude (A), area (B), and bandwidth (C) of the vibrational modes in SF_6 observed in the TG setup (see Figure 4.12). As only mode ν_1 and ν_5 are clearly visible in Figure 4.12 (B) the data could only be extracted for these two modes.

strongest mode is not surprisingly as it is also the most often observed mode in traditional Raman spectroscopy and even the calculations done by Walters et al. give a branching ratio of 5.6%/7%/87% for 525/643/775 cm^{-1} vibrational modes, respectively, showing that ν_1 mode is the strongest [63]. Figure 4.13 shows the amplitude (A), the area under the peak (B) and the FWHM (C) of the vibrational mode observed in the temporal FFT from Figure 4.12 (B). To extract these, the FFT components were fitted by a gaussian function. The quality of the data was not good enough to apply the same analysis for the ν_2 (645 cm^{-1}) mode. For ν_1 and ν_5, we can see that for harmonic 9 and 11 the amplitudes are quite similar whereas for higher harmonic we observe a branching ratio (between the two visible modes) of 32%/68%, 27%/73% and 32%/68% for harmonic 13, 15 and 17, respectively. As the bandwidth for mode ν_5 with 45 cm^{-1} is almost double the bandwidth of mode ν_1 (see Figure 4.13 (C)) the areas under the peaks shown in Figure 4.13 (B) are quite similar for both modes. Clearly just on the branching ratio of the harmonics as a function of the vibrational modes nothing particular is observed around the resonance (H15 - H17). Walters *et al.* [63] in their theoretical investigation of the Raman process at 800 nm with a 25 fs pulse of 5×10^{13} W/cm^2, claimed that calculations show no appreciable population of the vibrational levels higher than $v = 1$. In the present experiment, the intensity of each pump pulse is twice larger. Although the wave packet in the JILA experiment (Wagner et al. [58]) was more or less a quantum beat between $v = 0$ and $\nu = 1$ for each vibrational mode, we can expect that in the present experiment a tiny bit more vibrational quanta in each mode are populated, leading to a slightly larger delocalisation of the nuclear wavefunction in SF_6. The branching ratio between the vibrational modes revealed by HHS in the calculations done by Walters *et al.* does not vary drastically with a larger coherent superposition of vibrational modes (their calculations include up to $v = 4$ in each mode), expecting still the 775cm^{-1}/ν_1 mode as the dominant one. This is exactly what we observe here in the grating of excitation experiment. Nevertheless, the detection implemented here is a heterodyne detection: it is only if the amplitude and the phase

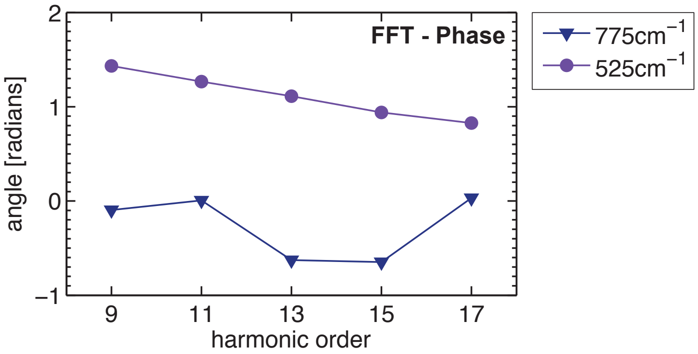

Figure 4.14: Phase of the temporal FFT of the time resolved oscillations in the TG setup presented in Figure 4.12 (A).

of XUV light emitted from vibrationally excited molecules is different from the one emitted from unexcited molecules, that a pump-probe signal with time-dependency will appear as a diffracted signal (see Eq. (4.6)). While Walter *et al.* calculated all the data required, they do not published the dipole of XUV emission. In these calculations, seen in one of there presentations, clearly the ν_1 mode is the dominant one in terms of dipole emission by one order of magnitude. The fact that we observe significantly the ν_5 mode could arise from a significant phase variation for the HHG produced from vibrational excited molecules in ν_5 compared to unexcited molecules. The S–F bond length variation is expected to be twice more important for the ν_1 vibrational mode than for the other modes. Already for one quantum populated by a Raman pulse, Walters *et al.* [67] reported a variation of 7.0 $\times$ 10^{-3} bohr, 8.4 $\times$ 10^{-3} bohr and 1.6 $\times$ 10^{-2} bohr for the 525, 643 and 775 cm^{-1} vibrational modes, respectively. This will correspond for the ν_1 to less than 1% variation of the S–F distance (1.6×10^{-2} $\times$ 2/2.94 bohr). These tiny variations in the collinear configuration, lead to oscillation amplitudes of 10 to 20% of the background, depending on the time delay [58]. In the present experiment, whatever the nuclear variation induced, nothing peculiar is observed on H15 and H17. In fact, although these harmonics are the most intense on the HHG spectrum (20% larger than H13 see Table 4.3), the contrast of the oscillations is slightly smaller. Indeed the percentage of the oscillations relative to the background is around 30% for H13, 28% for H15 and 25% for H17. This weaker contrast on H15 and H17 compared to H13 could be rationalized by a scrambling of the shape resonance in the photoabsorption leading to a lower sensitivity to vibrational dynamics.

The phase of the vibration as function of the harmonic order is shown in Figure 4.14. A Raman transitions will generate at t = 0 a wave packet localized at the equilibrium distance. The momentum of this vibrational wave packet depends only on the variation of polarizability $\delta\alpha$ as a function of the internuclear distance r. For a pump pulse much shorter than the vibrational period, note that this assumption is a tough one in our case, the overall momentum transfer to the vibrational mode is given by [68]:

$$p = \frac{1}{4}\frac{\delta\alpha}{\delta r}F_0^2\int f^2(t)\,dt \tag{4.7}$$

where F_0^2 is the peak amplitude of the electric field and $f(t)$ the carrier envelope[1].

At the moment, no calculation are undergoing to support the present experimental results. This means that in the data presented in Figure 4.12, we do not know if stretched or unstretched molecules enhanced the HHG emission. For instance in N_2O_4, HHG is fully optimized for a stretched geometry, generating a $T_0/4$ phase for the oscillation, where T_0 is the vibrational period [68]. A $T_0/4$ shift corresponds to 1.57 radians. In Figure 4.14 only H9 in the 525 cm^{-1} mode shows this phase dependency. This means that the geometry that favored H9 in the nuclear dimension visited by the 525 cm^{-1} vibrational mode, is the inner or the outer part of the potential. The probe duration is just short enough (28 fs) to resolve the vibrational periods (63, 52, 42 fs). The wave packet will have enough time to evolve significantly during the HHG process. Despite this limitation, the present data show a clear linear variation of the phase as a function of the harmonic order for the slowest vibrational mode ν_5. This phase change can not be explained by the natural chirp between the harmonics which is less than 1 fs as can be seen in Figure 1.15 (attochirp). Moreover, as the phase variation is vibrational mode dependent, it cannot be introduced by the temporal intensity profile of the probe pulse (like the negative chirp that defines the temporal profile of one harmonic (see end of Section 1.3.3). This means that the Raman wave packet is responsible for this phase variation. A 0.65 radian variation between H9 and H17 corresponds, for this vibrational period (63 fs), to a relative shift of 7 fs or 22% of of the maximum internuclear displacement[2]. In other words, harmonic 17 is enhanced before harmonic 9 at a geometrical configuration close to the equilibrium geometry (22%) for the 525 cm^{-1} mode. It is quite interesting to see that geometries that optimize the HHG emission is reached before the inner or outer potential well (not fully stretched or compressed molecules). On the contrary, the quickest vibrational mode ν_1 does not present any clear pattern. The zero phase observed on H9, H11 and H17 means that the SF_6 equilibrium geometry is favored for these HHG emissions. The 0.6 rad measured at H13 and H15 corresponds to an internuclear distance of 19% of the full intermolecular distance of the ν_1 mode. However it is quite important to note that the vibrational period of the ν_1 mode with T_0 = 43 fs, is only 1,5 times larger than the pump pulse duration (28 fs). A wave packet evolution within the pump pulse duration is not taken into account in this simple 1D analysis. Whatever the vibrational mode, the phase does not reveal any peculiar contribution around H15 and H17. But obviously, the first main critic for the present experiment is the small energy range investigated. It would have been more appropriate to record emissions up to H27 or larger. Second critic is the 28 fs pulse duration, which is not short enough to be neglected in the interpretation of the data.

The transient grating setup might not be the optimal setup to study the vibrational modes in SF_6. The Raman active modes are not very strong. A sufficient large pump beam intensity has to be used in order to excite them. But as we are using two pump beams to produce the

---

[1] Note that for a Gaussian pulse with FWHM of τ, the envelope integral is $\tau(\pi/ln16)^{1/2}$

[2] This percentage is given by $\delta R/\Delta R$, where ΔR is the maximum change in intermolecular distance S–F ($R_{max} - R_{min}$) and $\delta R = v\Delta t$ with Δt the phase variation in time for this period and v the speed of the oscillation given by $v = 2\Delta R/T_v$, where T_v is the period of this vibrational mode.

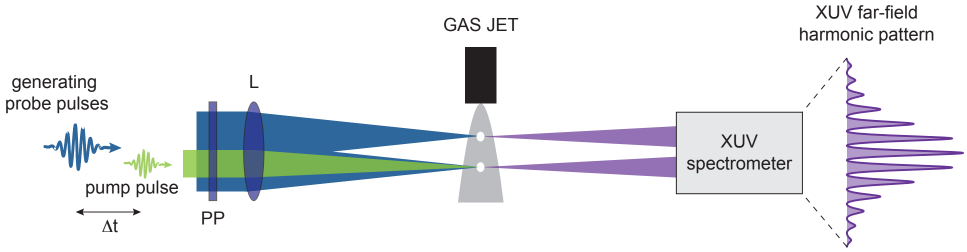

Figure 4.15: Principle of the two XUV source setup. Two harmonic sources are created by focusing two synchronized and phase locked laser beams (probe) in a gas jet which create an interference pattern in the far field on the detector. A third laser beam (pump) is superimposed on the lower source to Raman excite the molecules in one source only. The pump–probe delay Δt can be varied to observe the vibrational relaxation.

transient grating this can result in a large pump intensity. If the intensity of the grating is too large it can itself produce a high-order harmonic signal which adds to the background or even a grating of ionization, that will reduce the contrast of the vibrational grating. In order to improve this setup we decided to basically reduce the pump beam to one beam with no spatial interferences. In order to be still able to measure the phase of the harmonics we will use two HHG sources to produce an interference pattern, one which will be overlapped with a pump beam and one which will function as reference. These measurements will be relevant for the grating of excitation. Within the condition that the probe intensities are the same, in the unperturbed probe, the dipole moment of XUV emission in its phase and amplitude is the reference XUV emission that provides the heterodyne detection. In fact the two HHG sources set-up can be seen as a grating of excitation with only two fringes (one unexcited and one excited). We will see that with this setup we are also able to extract data for larger harmonic orders, up to H35.

4.3 Two HHG source interferometry

4.3.1 Experimental

The principle of the two HHG source setup is shown in Figure 4.15. Zerne et al. [69] demonstrated that if two pulses generate two harmonic sources in nearby positions in a gas jet and if the two sources are phase locked, they will interfere in the far field, producing a HHG fringe pattern similar to the one obtained by Young's double slit experiment. The phase evolution of a given harmonic can be investigated by inducing phase changes in one source while keeping the other as a reference. This has been shown to reveal the total dipole phase of an atom if one changes the intensity in one arm [70]. Are in one source the molecules aligned by a pump pulse, this allows the investigation of the angular phase variation with respect to the not aligned source [71, 72]. To measure not only the amplitude but also the phase of HHG, allows to determine both spectrally and angularly, the participation of multiple molecular orbitals and the underlying attosecond multi-electron dynamics in the process of HHG [27, 73].

If the two harmonic sources are separated by a distance d, the intensity of the total field at a

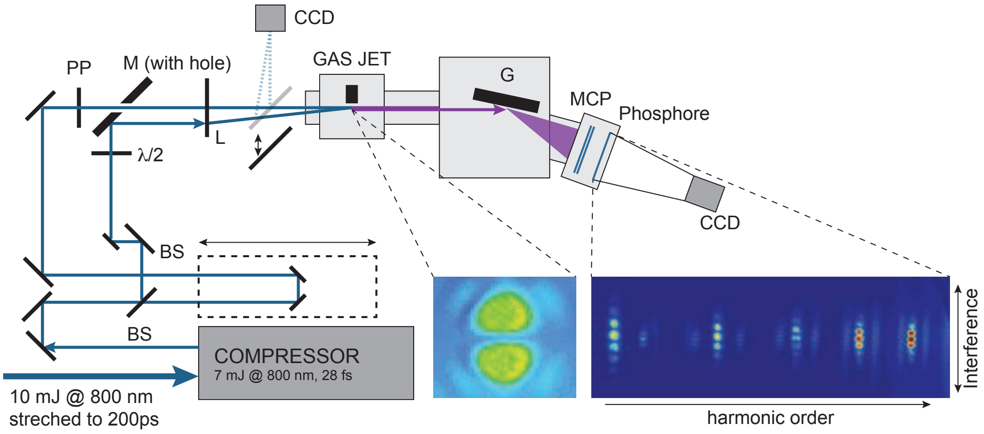

Figure 4.16: Schematic setup of the two HHG sources interferometry setup. The laser beam is split into a pump and probe beam. A π-phase plate (PP) in the probe arm is generating 2 vertical separated foci in the gas jet. The pump beam is overlapped with the lower focus via a hole mirror.

point X in an observation plane at distance L can be expressed by [69]:

$$I(t) = I_1 + I_2(t) + 2\sqrt{I_1 I_2(t)} \times \cos\left[2\pi \frac{dX}{\lambda_q L} + \varphi_1 - \varphi_2(t)\right] \tag{4.8}$$

where I_1 and $I_2(t)$ are the intensities of the two harmonic beams at the same point, λ_q the wavelength of the harmonic order q and φ_1, φ_2 are the phases of the generated fields at the observation point at time t. The pump pulse is superposed to I_2, making I_2 time-dependent in amplitude and phase. In the simple case, with no intensity-dependent phase and no chirp, the visibility or contrast of the fringes is given by:

$$V = \frac{I_{max} - I_{min}}{I_{max} + I_{min}} = \frac{2\sqrt{I_1/I_2}}{1 + (I_1/I_2)} \tag{4.9}$$

which is equal to 1 when both sources have the same intensity.

The setup is shown in Figure 4.16. The laser beam after the compressor is divided into two parts. The generating arm passes through a long translation stage to be able to vary the delay between the pump and probe laser pulse. A π-phase plate[1] is introduced to generate 2 spots at the focus in order to generate the two HHG sources. The π-phase plate is introducing a phase shift of π between the upper and lower part of the 800 nm laser beam, so that in the focus (far field) we observe two spots separated vertically due to the interference of the upper and lower beam as shown in Figure 4.16, recorded with a CCD camera put into the focus of the probe beam. High harmonics are generated by focusing the pulses with a f = 50 cm lens in a continuous jet produced by a 250 µm nozzle backed by a few hundreds of mbars of gas. Typically energies of 500 µJ/p and 300 µJ/p were used for the probe and pump pulse, respectively. The emitted radiation is analyzed by an extreme ultraviolet spectrometer the same way as with the previous experiment.

---

[1] The π phase is only a variation of the thickness of a fused silica plate by $\lambda/2 = 400$ nm

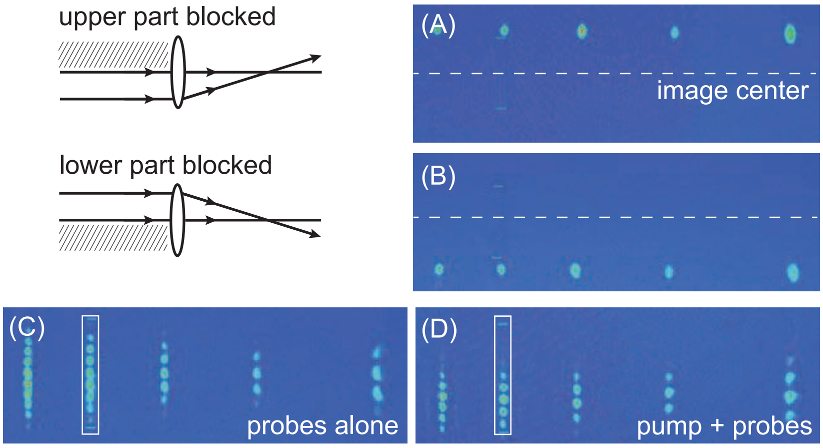

Figure 4.17: Two HHG source alignment. (A) and (B) shows the harmonic spectrum with the upper and lower part, respectively, of the beam blocked. (C) and (D) the interference pattern without and with the pump beam, respectively.

Alignment

To be sure that the pump beam is only overlapping with one of the two sources we observed the fringes at a long positive time delay with the highest available intensity of the pump beam. In theory if the pump beam is strong enough to ionize the molecules, the later arriving probe pulse is not able to generate HHG anymore in this volume. This should kill the fringes observed on the detector in the far field, leaving only the XUV light generated by the other HHG source visible. Figure 4.17 (A) and (B) shows what happens if half of the beam is blocked. The fringes are lost and the XUV beam in the far field is on the upper (A) or lower (B) part of the MCP when the upper or lower part is blocked, respectively. This can be explained as by blocking the upper or lower part of the beam, the beam is not going through the center of the lens which results in a kick upwards or downwards. Figure 4.17 (C) and (D) shows the HHG fringe pattern of the two sources without and with the pump pulse, repevely. We can clearly see that with the pump beam the fringe pattern is reduced and moved downwards indicating an overlap with the lower beam in the focus.

Image analysis

The HHG interference pattern was taken as a function of the pump-probe delay for a pump intensity of 300-330 µJ/p. A typical recorded interferometric HHG spectrum recorded in SF_6 at a pump-probe delay of 1 ps is shown in Figure 4.18. We are able to resolve harmonic 9 to 17 and as well visible is the second order of diffraction of the grating from harmonic 19 to 35. The data analysis is basically done in two steps. First the spatial Fourier transformation (sFFT) of the interference pattern for each harmonic is taken as a function of pump-probe delay. This first sFFT allows to extract an amplitude and phase of the spatial interferences for each pump-probe delay which we will call spatial amplitude (SA) and spatial phase (SP). The spatial phase of the interferogram gives us access to another observable. This spatial phase as function of the pump-probe delay will also have the oscillations encoded but does not depend on the laser intensities, which makes it less sensitive to any laser fluctuation. Afterwards in the second step the temporal FFT (tFFT) is produced from this amplitude and this new phase

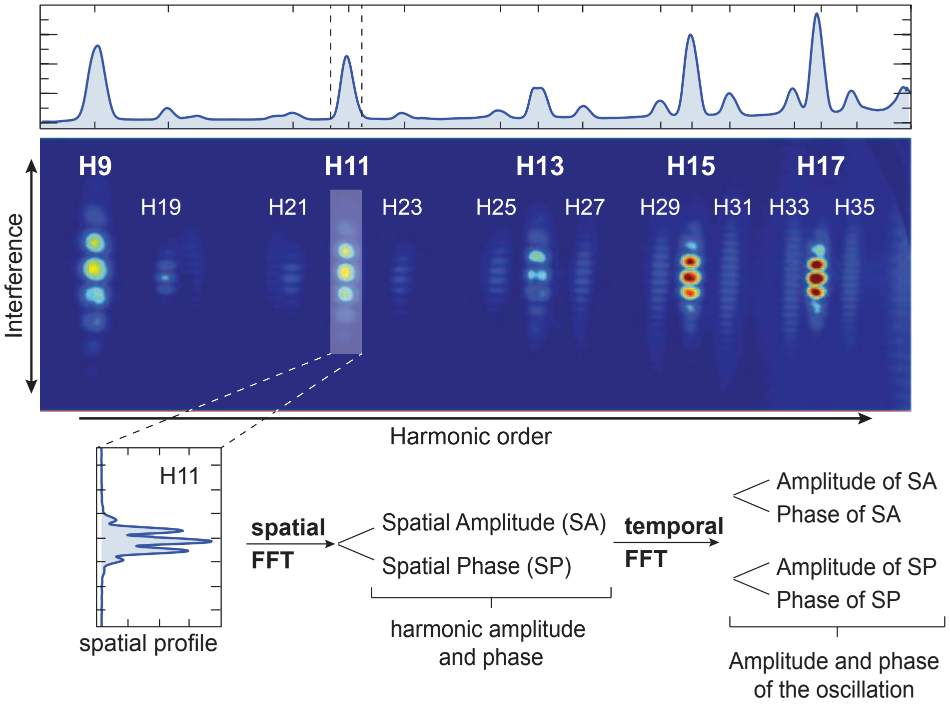

Figure 4.18: Two HHG source image analysis. Shown is atypical harmonic spectrum with the two sources. On top the signal is shown integrated over the interference coordinate. The harmonics are selected by defining an area around the harmonics as shown on H11. This area is then integrated over the frequency coordinate to optain the spatial profile as a function of the pump-probe delay. This data is then Fourier transformed first spatial and then temporal.

to extract the frequency components giving a second amplitude and phase which we will call amplitude and phase of SA and SP, respectively. In order to take the spatial FFT, the area of each harmonic is determined as shown in Figure 4.18 as example for harmonic 11. The top panel shows the integrated harmonic spectrum over the interference coordinate. The area is selected by the width of the corresponding harmonic and integrated over the interference coordinate to obtain the spatial interference profile of the each harmonic.

4.3.2 Results from the two HHG source setup

Figure 4.19 shows the result of the spatial Fourier-transform (sFFT) of the HHG fringe pattern as a function of pump-probe delay between the Raman pump and the two HHG source probe laser pulses for harmonic 9 (blue) to 35 (red) up to 1.1 ps. The intensity and phase is shown in arbitrary units as the mean of the signal was subtracted and an offset was added to be able to separate the harmonics in the y-axis for presentation purposes. Shown is the spatial amplitude (SA) in Figure 4.19 (A) and the spatial phase (SP) in (B) of the sFFT. We are able to observe an oscillatory behavior in both the amplitude and phase. The signal around 0.2 ps in the phase is an artifact which is not yet explained. Table 4.4 shows the harmonic modulation depth for SA and SP in percent. The oscillations in SA are only 5 - 10%, whereas in SP they are 25 - 40%, depending on the harmonic order.

To deduce which vibrational modes are detected, a discrete temporal Fourier transform (tFFT) of this data is taken for a time interval between 0.3 and 1.1 ps. Figure 4.20 shows the ampli-

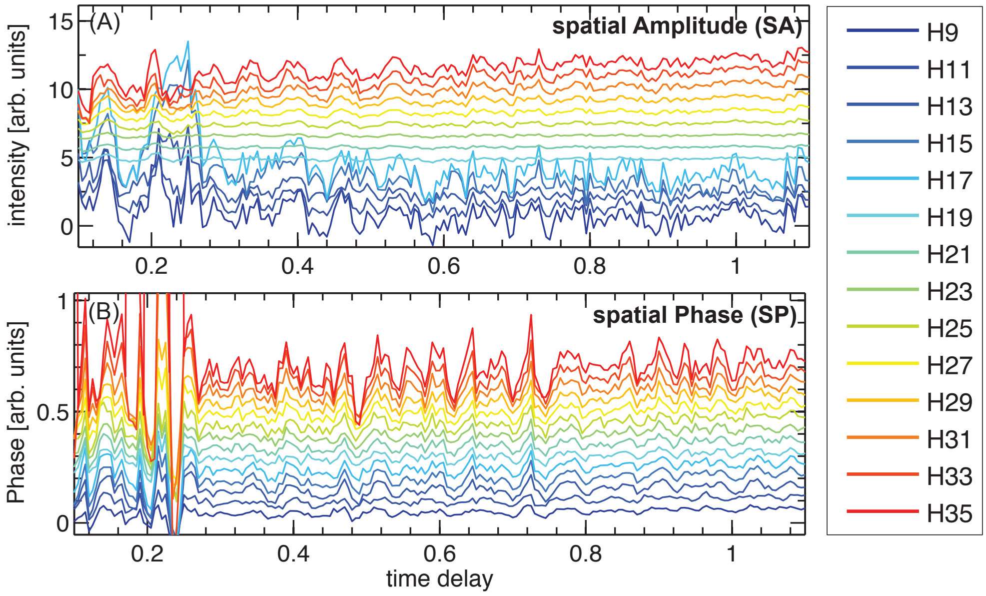

Figure 4.19: Spatial Fourier-transform (amplitude and phase) of the HHG fringe pattern as a function of pump-probe delay. The y-axis is arbitrary as the signal was normalized and an offset was added to separate the signal from each harmonic.

tude of the tFFT of the spectral amplitude and spectral phase from Figure 4.19. Three peaks are visible at 775, 638, and 528 cm^{-1}, corresponding to the three Raman active vibrational modes ν_1, ν_2 and ν_5 in SF_6, respectively. Clearly this setup is more sensitive to the vibrational dynamics induced in SF_6 than the transient grating setup. In the amplitude of SA (Figure 4.20 (A)) we observe almost the same as we did in the transient grating setup. The mode ν_1 and ν_5 are clearly visible whereas it is hard to identify the ν_2 mode. In contrary to the measurements before in the TGS setup here the mode ν_5 is the strongest as observed in the colinear pump-probe experiment done by Wagner *et al.* [58]. The ν_5 mode was less sensitive to the day to day alignment and to the fluctuations of the laser intensity compared to the other two modes. Undergoing analysis of the data collected in both setups takes the bandwidth of the each harmonic into account via a pixel by pixel study instead of integrating the harmonic area over the frequency coordinate. A first glance at this analysis shows that for instance for harmonic 15 the red and blue parts oscillate with opposite phase, so that that this modulation is cancelled out when integrating the harmonic over the frequency bandwidth. This effect seems to be stronger for the ν_1 mode than for the ν_5 mode where both sides of the harmonic bandwidth oscillate in phase. If the blue edge is maximized when the red edge is minimized, there is a spectral shift of the harmonic. This pixel by pixel analysis is still at the beginning no in-depth analysis has been performed so far to be able to present this here and wont be discussed any further. But this technique shows the potential to extract complementary information. Figure 4.20 (B)

Table 4.4: Harmonic modulation depths for SA and SP.

harmonic order		9	11	13	15	17	19	21	23	25	27	29	31	33	35
I_{osc}/I_{bg} %	SA	4.0	3.7	4.5	4.7	4.6	4.0	5.1	5.3	6.8	7.1	7.2	7.6	8.4	9.8
	SP	30	25	34	31	25	27	26	27	30	24	27	28	33	40

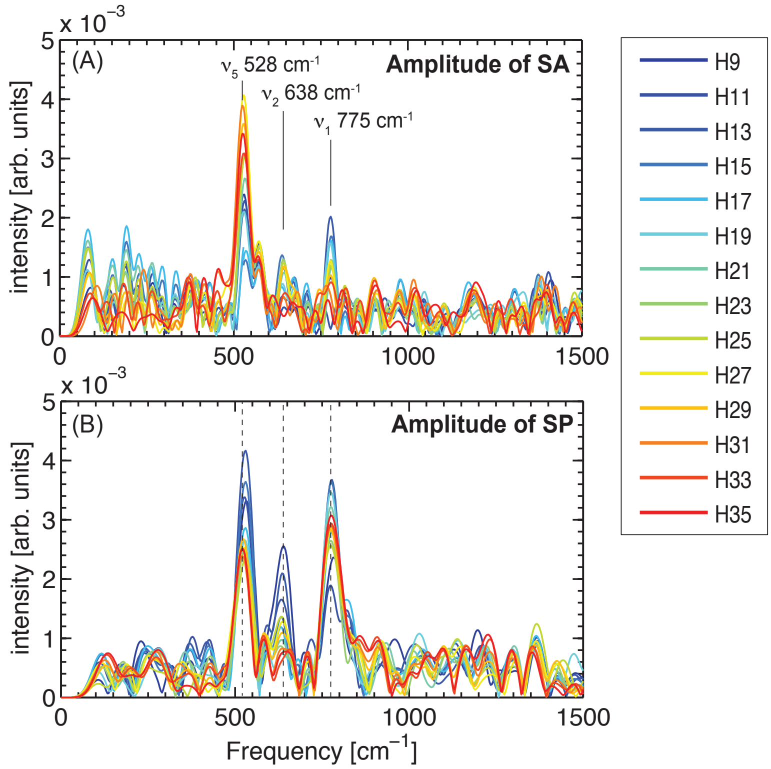

Figure 4.20: Amplitude of the tFFT of the spatial amplitude and phase. All three Raman active modes (528, 638 and 775 cm^{-1}) are visible.

shows the amplitude of the tFFT of the spatial phase. Whereas in the amplitude of SA we always observed the ν_5 mode and had difficulties to resolve the other two, in the amplitude of SP it was easier to observe the ν_1 mode. In general it was easier to observe the three vibrational modes in the spatial phase than in the spatial amplitude. Indeed the spatial phase corresponds to the determination where the maximum is in the interference pattern. Where the maximum is located is not sensitive to the fluctuations of the laser intensity, in contrary to the amplitude which is how many photons are produced. This is also reflected in the oscillation depth shown in Table 4.4 where there is almost a factor 10 between spatial amplitude and spatial phase. This makes the two source experiment due to the new observable of the spatial phase or harmonic phase, more sensitive as we are not limited like in the transient grating setup to measure only amplitudes.

It is evident that the branching ratios between the modes is changing with harmonic order. The peaks are fitted by a gaussian function to deduce not only the amplitude but also the area under the curve and the bandwidth at FWHM as function of the harmonic order as done before in the grating of excitation experiment. This is shown in Figure 4.21 on the left for the amplitude of SA and on the right for the amplitude of SP, where the amplitude was normalized to the total signal. For points in the amplitude that are close to 1×10^{-3} the area and the FWHM has to be regarded as noise, as these amplitudes are in the noise level. As we are looking for differences around harmonic 17, as observed in the static experiments (see Figure 4.2), H17 is marked by a dotted line. In the spatial amplitude we observe that the amplitude of the ν_5 (530

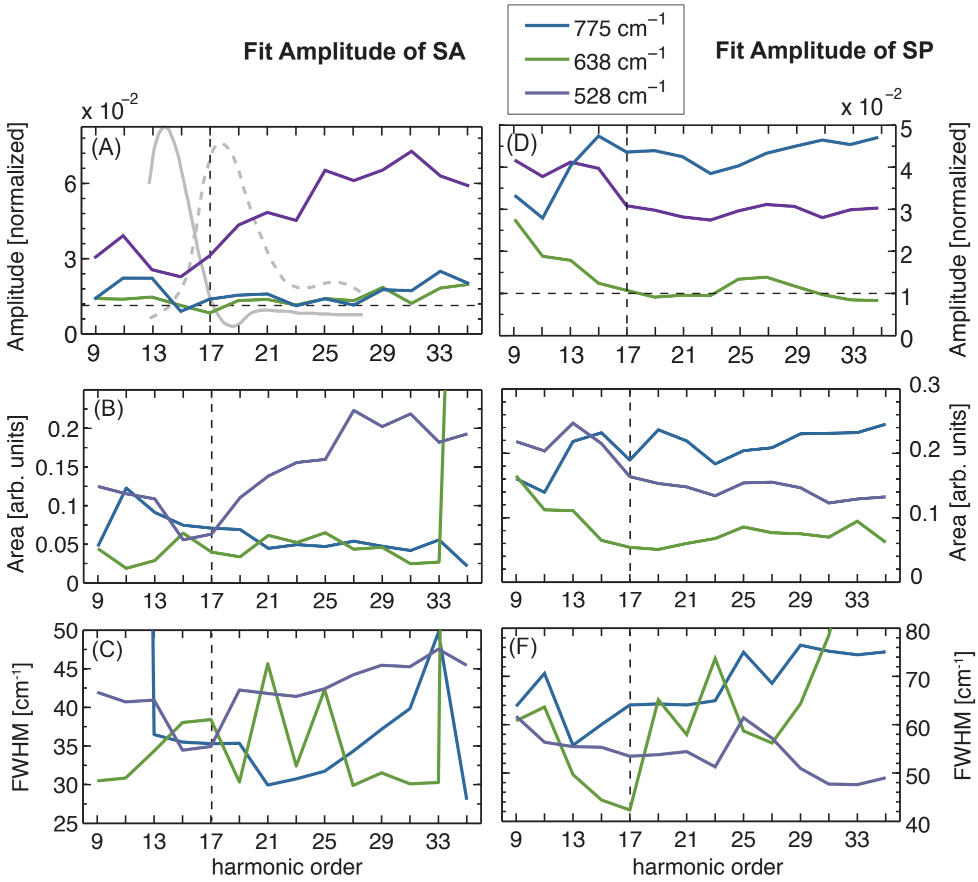

Figure 4.21: Amplitude, area, and bandwidth of the vibrational modes in SF$_6$ observed in the two HHG source setup (see Figure 4.20). (A)-(C) amplitude of SA, (D)-(F) amplitude of SP. The horizontal lines in (A) and (D) indicate the noise level. Shown as well in (A) in grey is the calculated HHG emission from Figure 4.5 (B) in comparision.

cm^{-1}) mode (Figure 4.21 (A) purple) shows a minimum at harmonic 15/17 and is increasing at higher harmonics. A minimum in the XUV spatial interferences, filtered at 525 cm^{-1} could mean that the phase between the two XUV beams around H15/17 are quite similar for this vibrational wave packet. This minimum cannot come from the overall harmonic emission minimum as it is the difference in amplitude of excited and non-excited molecules. This means that it is really an effect introduced by the vibrational wave packet, which corresponds exactly to the switching between the two molecular orbitals claimed to be involved in the HHG emission around this energy. This is the first experimental evidence that a particular high-order harmonic process in affected by a vibrational excited molecule, in SF$_6$ especially around harmonic 17. Mode ν_1 at 775 cm^{-1} is decreasing with harmonic order and the ν_2 mode at 645 cm^{-1} is basically constant. We also see that mode ν_2 is almost not visible and shows a bad signal-to-noise ratio as the amplitude is only slightly higher than the noise level which is around 1×10^{-3}, indicated by the horizontal dashed line. Mode ν_1 is vanishing with harmonic order. In contrary to the experiment with the transient grating the areas under the curves show exactly the same behavior as the amplitudes of the frequencies. In the spatial phase we can observe a switching in the amplitudes of ν_1 and ν_5 before an after H13/15. For lower harmonics than H13 the ν_5 mode is stronger than the ν_1 mode and after H15 it is the

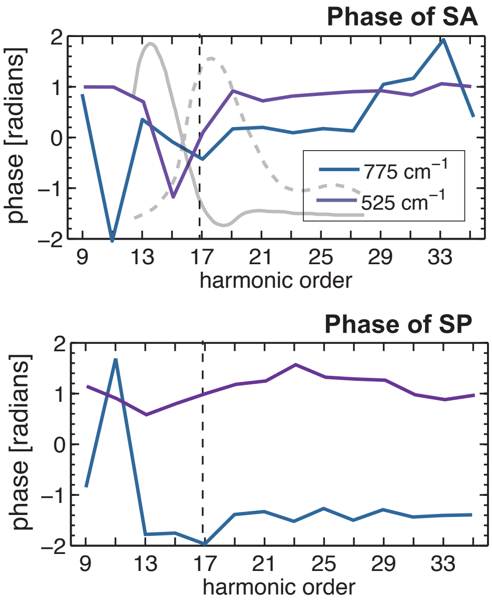

Figure 4.22: Phase of SA and SP as function of the harmonic order from the two HHG source setup for the the active Raman modes 775 and 528 cm^{-1}. Also shown in grey is the calculated HHG emission from Figure 4.5 (B) in comparision.

reverse. This could as well correspond to the switching in of the two molecular orbitals, as the two molecular orbitals have different structures and therefore will also react differently to different vibrational modes. The ν_2 mode vanishes almost totally after harmonic 17 and the amplitudes are lower than the noise level indicated by the horizontal dashed line. The areas show the same behavior. Nothing exceptional is going on around harmonic 17 in the FWHM plot.

Figure 4.22 shows the phase of the temporal FFT for the two vibrational modes ν_1 and ν_5 which show a nonzero amplitude (see Figure 4.21) as function of the harmonic order. In the phase of SA in contrary to the amplitude we observe a clear feature around harmonic 15 for the ν_1. This minimum for ν_1 around H17 is also visible in the phase of SP. Harmonic 11 shows a phase jump in the phase of SA in the ν_1 mode. In the phase of SP we observe as well a phase jump at harmonic 11. In the spatial amplitude, a phase jump around harmonic 15 for the ν_5 mode at 528 cm^{-1} is observed. Comparing these phase features with the absorption cross-section plot in Figure 4.6, we can identify all phase features with absorption peaks. The ones around H15/17 corresponds to the large absorption peak associated with the shape and autoionization resonance introduced in the introduction of this chapter and which seem to play a large role in the HHG emission of SF_6 around the energy of 25 eV. The phase feature at H11 as well corresponds to an absorption peak which is also associated with an autoionization resonance but which was not included in the theoretical model as no calculation is done at this low energy. Regarding the absolute values of the phase we observe that no harmonic is produced with a phase shift of $T_0/4$ which would correspond to 1.57 radians as expected for a Raman transition where the vibrational wave packet is created at the equilibrium distance of the S–F bond length. But this is not surprising and the absolute values have to be regarded with caution. As mentioned before our Raman pump pulse has a FWHM duration of around

30 fs and the vibrational periods of the encountered modes are all in this range, form 43, 52 and 63 fs for the ν_1, ν_2 and ν_5 mode, respectively. Nevertheless,for both vibrational modes (ν_1 and ν_5) in SA and SP the phase shift seems to be constant as function of harmonic order, only showing a change around harmonic 15 and 17. As mentioned before, this is the energy region where the autoionization resonance and the shape resonance play a role in the generation of high-order harmonics in SF_6 and maybe this change is a signature of these resonance.

4.4 Conclusion

Our goal was to observe, if the S–F distance in SF_6 is varied, whether the harmonic spectrum produced in SF_6 around H15 - H17 changes drastically compared to the HHG spectrum produced in static SF_6. To enhance the sensitivity, the experiments are done with interferometric techniques, based on a heterodyne detection in which the reference signal is always SF_6 in $\nu = 0$, namely at its equilibrium geometry. One setup uses two pump pulses to create a grating of vibrational excitation in the gas jet through which the probe pulse generates high-order harmonics. The second experiment uses two spatially separated probe pulses, both generating a XUV beam which interfere spatially in far field. Both setups showed that they are sensitive to the vibrational excitations in the generating medium. All three Raman active modes of SF_6, $\nu_1(775\ \mathrm{cm}^{-1})$, $\nu_2(638\ \mathrm{cm}^{-1})$, $\nu_5(528\ \mathrm{cm}^{-1})$, could be observed in the amplitude of the harmonic emission and as well in the phase.

For the transient grating setup it was possible to investigate harmonic 9 to 17 whereas in the two HHG source setup the harmonic spectrum from H9 up to H35 was analyzed. In both setups the main modes populated by this Raman excitation are the ν_1 and ν_5 modes as via traditional Raman spectroscopy. For the two HHG source setup the amplitude of the ν_5 mode shows a clear minimum around harmonic 17, whereas in the phase we observe a jump around harmonic 15. Mode ν_1 shows no clear pattern in the amplitude but in the phase we observe as well a minimum around harmonic 17. These minima cannot come from the previous observed minimum in the harmonic emission of SF_6, as we are in a heterodyne detection. This let us conclude that the features observed here are only introduced by the change of the S–F distance introduced by the vibrational wave packets. In addition, it seems that the harmonic emission is not optimized for fully stretched or compressed molecules as observed in similar experiments on N_2O_4. A full interpretation of these experimental results requires the development of a theoretical model to reproduce the amplitude and phase minima. Nevertheless, this is the first phase-resolved study of HHG, which provides a first step in understanding the origin of the modulation in the harmonic spectrum of SF_6.

As mentioned earlier, the recorded data is currently been analyzed to take the bandwidth of each harmonic into account, with a pixel by pixel analysis. A first glance at this showed that the intensity of the red and blue parts in the bandwidth of one harmonic is oscillating with a phase shift and sometimes even in opposite phase. Consequently, this modulation is cancelled out when integrating the one harmonic over the frequency coordinate as has been done in this analysis. Damages to the detector prevents an accurate pixel by pixel analysis. Ideally the data should be acquired again once an undamaged MCP is sourced. Furthermore, it would be interesting to use shorter pulse durations for the probe and pump pulse, as our ∼30 fs pulse duration is quite close to the vibrational periods. The Raman transitions as well could probably be enhanced by using a different pump wavelength. As well the polarization of the pump and probe laser in this experiment was fixed to a parallel configuration and should be changed to a crossed polarization configuration to investigate the polarization dependency of the incident laser beams. With an undamaged MCP both experiments, the transient grating and two sources could be realized in one integrated setup to measure both at the same time, under the same experimental conditions, namely an interference pattern from the two probe sources on the diffracted signals from the transient grating.

References

[1] Gianturco, FA. *Electronic Properties of Sulphur Hexafluoride. II. Molecular Orbital Interpretation of Its X-Ray Absorption Spectra*. J. Chem. Phys. **57**:2 840–846 (1972) (cited p. 122).

[2] Boggs, S. *Sulfur hexafluoride: Introduction to the material and dielectric*. IEEE Electr. Insul. Mag. **5**:5 18–21 (1989) (cited p. 122).

[3] EFCTC, EFTC. *About Sulphur hexafluoride (SF_6)*. http://www.fluorocarbons.org/chemical-families/sf6 () (cited p. 122).

[4] Christophorou, LG, Olthoff, JK, and Van Brunt, RJ. *Sulfur hexafluoride and the electric power industry*. IEEE Electr. Insul. Mag. **13**:5 20–24 (1997) (cited p. 122).

[5] Ihmels, EC and Gmehling, J. *Densities of sulfur hexafluoride and dinitrogen monoxide over a wide temperature and pressure range in the sub-and supercritical states*. International Journal of Thermophysics **23**:3 709–743 (2002) (cited p. 122).

[6] Olivet, A and Vega, LF. *Optimized molecular force field for sulfur hexafluoride simulations*. J. Chem. Phys. **126**:14 pages (2007) (cited p. 122).

[7] Maggon, KK. *Medical uses of sulfur hexafluoride*. Drugs of the Future **19**: 1101 (1994) (cited p. 122).

[8] RF, W and JT, T. *Prediction of the kinetics of disappearance of sulfur hexafluoride and perfluoropropane intraocular gas bubbles*. Ophthalmology **95**:5 609–613 (1988) (cited p. 122).

[9] Schneider, M. *SonoVue, a new ultrasound contrast agent*. Eur. Radiol. **9**:S3 S347–S348 (1999) (cited p. 122).

[10] Khalil, M. *Non-CO_2 greenhouse gases in the atmosphere*. Annual Review of Energy and the Environment **24**:1 645–661 (1999) (cited p. 122).

[11] Geller, LS, Elkins, JW, Lobert, JM, Clarke, AD, Hurst, DF, Butler, JH, and Myers, RC. *Tropospheric SF_6: Observed latitudinal distribution and trends, derived emissions and interhemispheric exchange time*. Geophys. Res. Lett. **24**:6 675–678 (1997) (cited p. 122).

[12] Reilly, J, Mayer, M, and Harnisch, J. *The Kyoto Protocol and non-CO_2 greenhouse gases and carbon sinks*. Environmental Modeling & Assessment **7**:4 217–229 (2002) (cited p. 122).

[13] Maiss, M, Steele, LP, Francey, RJ, Fraser, PJ, Langenfelds, RL, Trivett, NBA, and Levin, I. *Sulfur hexafluoride - A powerful new atmospheric tracer*. Atmos Environ **30**:10-11 1621–1629 (1996) (cited p. 122).

[14] Boudon, V and Pierre, G. *Rovibrational spectroscopy of sulfur hexafluoride: A review*. Recent Res. Devel. Mol. Spec. **1**: 25–55 (2002) (cited p. 122).

[15] Boudon, V, Hepp, M, Herman, M, Pak, I, and Pierre, G. *High-Resolution Jet-Cooled Spectroscopy of* SF_6*: The* $\nu_2 + \nu_6$ *Combination Band of* $^{32}SF_6$ *and the* ν_3 *Band of the Rare Isotopomers*. J. Mol. Spec. **192**:2 359–367 (1998) (cited p. 122).

[16] Bermejo, D, Martinez, RZ, Loubignac, E, Boudon, V, and Pierre, G. *Simultaneous Analysis of the* ν_2 *Raman and* $\nu_2 + \nu_6$ *Infrared Spectra of the* SF_6 *Molecule*. J. Mol. Spec. **201**:1 164–171 (2000) (cited p. 122).

[17] Boudon, V, Pierre, G, and Bürger, H. *High-Resolution Spectroscopy and Analysis of the* ν_4 *Bending Region of* SF_6 *near 615* cm^{-1}. J. Mol. Spec. **205**:2 304–311 (2001) (cited p. 122).

[18] Boudon, V and Bermejo, D. *First High-Resolution Raman Spectrum and Analysis of the* ν_5 *Bending Fundamental of* SF_6. J. Mol. Spec. **213**:2 139–144 (2002) (cited p. 122).

[19] L O Brockway, LP. *The Determination of the Structures of the Hexafluorides of Sulfur, Selenium and Tellurium by the Electron Diffraction Method*. Proc. Natl. Acad. Sci. **19**:1 68 (1933) (cited p. 122).

[20] Ruf, H, Handschin, C, Ferre, A, Thire, N, Bertrand, JB, Bonnet, L, Cireasa, R, Constant, E, Corkum, PB, Descamps, D, Fabre, B, Larregaray, P, Mevel, E, Petit, S, Pons, B, Staedter, D, Worner, HJ, Villeneuve, DM, Mairesse, Y, Halvick, P, and Blanchet, V. *High-harmonic transient grating spectroscopy of* NO_2 *electronic relaxation*. J. Chem. Phys. **137**: 224303 (2012) (cited p. 122).

[21] Smirnova, O, Patchkovskii, S, Mairesse, Y, Dudovich, N, and Ivanov, MY. *Strong-field control and spectroscopy of attosecond electron-hole dynamics in molecules*. Proc. Natl. Acad. Sci. **106**:39 16556–16561 (2009) (cited p. 122).

[22] Haessler, S, Caillat, J, Boutu, W, Giovanetti-Teixeira, C, Ruchon, T, Auguste, T, Diveki, Z, Breger, P, Maquet, A, 'e, BC, ieb, RT, and eres, PS. *Attosecond imaging of molecular electronic wavepackets*. Nature Phys. **6**: 200–206 (2010) (cited p. 122).

[23] Lynga, C, L'Huillier, A, and Wahlstrom, CG. *High-order harmonic generation in molecular gases*. J. Phys. B **29**:14 3293–3302 (1996) (cited p. 123, 124).

[24] Sasanuma, M, Ishiguro, E, Masuko, H, Morioka, Y, and Nakamura, M. *Absorption structures of SF6 in the VUV region*. Journal of Physics B: Atomic and Molecular Physics **11**:21 3655 (1978) (cited p. 123, 130, 131).

[25] Paul, PM, Toma, ES, Breger, P, Mullot, G, Balcou, P, Muller, HG, and Agostini, P. *Observation of a Train of Attosecond Pulses from High Harmonic Generation*. Science **292**:5522 1689–1692 (2001) (cited p. 124).

[26] Higuet, J, Ruf, H, Thiré, N, Cireasa, R, Constant, E, Cormier, E, Descamps, D, Mevel, E, Petit, S, Pons, B, Mairesse, Y, and Fabre, B. *High-order harmonic spectroscopy of the Cooper minimum in argon: Experimental and theoretical study*. Phys. Rev. A **83**:5 053401 (2011) (cited p. 124).

[27] Smirnova, O, Mairesse, Y, Patchkovskii, S, Dudovich, N, Villeneuve, D, Corkum, P, and Ivanov, MY. *High harmonic interferometry of multi-electron dynamics in molecules*. Nature **460**:7258 972–977 (2009) (cited p. 124, 143).

[28] Cireasa, R, Bhardwaj, R, Blanchet, V, Boguslavsky, A, Descamps, D, Fabre, B, Legare, F, Mairesse, Y, Patchkovskii, S, Pons, B, Ruf, H, Schmidt, B, Surarez, J, Thire, N, and Wong, M. *High-harmonic generation sensitive to chirality*. in preparation for Nature Physics (2013) (cited p. 125).

[29] Mairesse, Y, Dudovich, N, Levesque, J, Ivanov, MY, Corkum, PB, and Villeneuve, DM. *Electron wavepacket control with elliptically polarized laser light in high harmonic generation from aligned molecules*. New Jour. Phys. **10**: 025015 (2008) (cited p. 125).

[30] Wong, MCH, Brichta, JP, and Bhardwaj, VR. *Signatures of symmetry and electronic structure in high-order harmonic generation in polyatomic molecules*. Phys. Rev. A **81**:6 061402 (2010) (cited p. 125).

[31] Wodkiewicz, K. *Classical and quantum Malus laws*. Phys. Rev. A **51**:4 2785 (1995) (cited p. 125).

[32] Kahr, B and Claborn, K. *The Lives of Malus and His Bicentennial Law*. Chem. Phys. Chem. **9**:1 43–58 (2008) (cited p. 125).

[33] Collett, E. *Field guide to polarization*. Vol. FG05. SPIE PRESS BOOK, 2005 (cited p. 125).

[34] Antoine, P, Carré, B, L'Huillier, A, and Lewenstein, M. *Polarization of high-order harmonics*. Phys. Rev. A **55**:2 1314 (1997) (cited p. 125).

[35] Shafir, D, Mairesse, Y, Villeneuve, DM, Corkum, PB, and Dudovich, N. *Atomic wavefunctions probed through strong-field light-matter interaction*. Nature Phys. **5**:6 412–416 (2009) (cited p. 126).

[36] Shafir, D, Fabre, B, Higuet, J, Soifer, H, Dagan, M, Descamps, D, Mevel, E, Petit, S, Worner, HJ, Pons, B, Dudovich, N, and Mairesse, Y. *Role of the Ionic Potential in High Harmonic Generation*. Phys. Rev. Lett. **108**:20 203001 (2012) (cited p. 126).

[37] Pavlychev, AA, Brykalova, XO, Mistrov, DA, Flesch, R, and Rühl, E. *Position and line shape of the $2t_{2g}$-shape resonance in S 2p-excited sulfur hexafluoride clusters*. J. Electron Spec. and Relat. Phen. **166-167**: 45–52 (2008) (cited p. 126, 131).

[38] Holland, D, MacDonald, MA, Baltzer, P, Karlsson, L, Lundqvist, M, Wannberg, B, and Niessen, W von. *An experimental and theoretical study of the valence shell photoelectron spectrum of sulphur hexafluoride*. Chem. Phys. **192**:3 333–353 (1995) (cited p. 126).

[39] Christophorou, LG and Olthoff, JK. *Electron interactions with SF_6*. J. Phys. B **29**:3 267–330 (2000) (cited p. 127).

[40] Mairesse, Y. *Génération et caractérisation d'impulsions attosecondes*. PhD thesis. Université Paris X1 Orsay, 2005 (cited p. 127).

[41] Yang, L, Agren, H, Carravetta, V, Vahtras, O, Karlsson, L, Wannberg, B, Holland, D, and MacDonald, MA. *Energy-dependent valence photoelectron spectra of SF_6. Ab initio calculations and measurements*. J. Electron Spec. and Relat. Phen. **94**: 163–179 (1997) (cited p. 129).

[42] Stener, M, Toffoli, D, Fronzoni, G, and Decleva, P. *Time dependent density functional study of the photoionization dynamics of SF_6*. J. Chem. Phys. **124**:11 114306 (2006) (cited p. 128, 130).

[43] Holland, DMP, Shaw, DA, Hopkirk, A, MacDonald, MA, and McSweeney, SM. *A study of the absolute photoabsorption cross section and the photoionization quantum efficiency of sulphur hexafluoride from the ionization threshold to 420 Å*. J. Phys. B **25**:22 4823–4834 (1992) (cited p. 129, 130).

[44] Taylor, HS. *Qualitative Aspects of Resonances in Electron-Atom and Electron-Molecule Scattering, Excitation, and Reactions*. J. Chem. Phys. **45**:8 2872 (1966) (cited p. 129).

[45] Dehmer, JL, Parr, AC, and Southworth, SH. "Resonances in molecular photoionization". *Handbook on synchrotron radiation*. Ed. by Marr, GV. North Holland, 1987, 241–353 (cited p. 129).

[46] Dehmer, JL. *Evidence of Effective Potential Barriers in the X-Ray Absorption Spectra of Molecules*. J. Chem. Phys. **56**:9 4496 (1972) (cited p. 129).

[47] Dehmer, J, Parr, A, Wallace, S, and Dill, D. *Photoelectron branching ratios and angular distributions for the valence levels of SF_6 in the range $16 \leqslant \hbar\nu \leqslant 30$ eV*. Phys. Rev. A **26**:6 3283–3292 (1982) (cited p. 130).

[48] Holland, DMP, MacDonald, MA, Hayes, MA, Karlsson, L, Wannberg, B, and Baltzer, P. *A study of resonant behaviour in the photoelectron band of sulphur hexafluoride*. J. Phys. B **29**:3 487–498 (1999) (cited p. 130).

[49] Ono, M and Mitsuke, K. *Anisotropy of fragment ions from SF_6 by photoexcitation between 23 and 210 eV*. Chem. Phys. Lett. **366**:5-6 595–600 (2002) (cited p. 130).

[50] Peterka, DS, Ahmed, M, Ng, CY, and Suits, AG. *Dissociative photoionization dynamics of SF_6 by ion imaging with synchrotron undulator radiation*. Chem. Phys. Lett. **312**:2-4 108–114 (1999) (cited p. 130).

[51] Boudon, V, Doménech, JL, Bermejo, D, and Willner, H. *High-resolution Raman spectroscopy of the ν_1 region and Raman-Raman double resonance spectroscopy of the $2\nu_1 - \nu_1$ band of $^{32}SF_6$ and $^{34}SF_6$. Determination of the equilibrium bond length of sulfur hexafluoride*. J. Mol. Spec. **228**:2 392–400 (2004) (cited p. 131).

[52] Herzberg, G. *Molecular spectra and molecular structure. Vol.2: Infrared and Raman spectra of polyatomic molecules*. Vol. -1. Molecular spectra, molecular structure. Vol.2: Infrared, and Raman spectra of polyatomic molecules, by G. Herzberg. New York: Van Nostrand, Reinhold, 1945, 1945 (cited p. 132, 133).

[53] Gaunt, J. *The Infra-Red Spectra and Molecular Structure of Some Group-6 Hexafluorides*. Trans. Faraday Soc. **49**: 1122–1131 () (cited p. 132).

[54] Yost, DM, Steffens, CC, and Gross, ST. *The Raman Spectra and Molecular Constants of the Hexafluorides of Sulfur, Selenium and Tellurium*. J. Chem. Phys. **2**:6 311–316 (1934) (cited p. 132).

[55] Lagemann, RT and Jones, EA. *The Infrared Spectrum of Sulfur Hexafluoride*. J. Chem. Phys. **19**:5 534–536 (1951) (cited p. 132).

[56] Edelson, D and McAfee, KB. *Note on the Infrared Spectrum of Sulfur Hexafluoride*. J. Chem. Phys. **19**:10 1311 (1951) (cited p. 132).

[57] Lattre, A de. *Infrared Spectrum of SF_6 in the LiF Region*. J. Chem. Phys. **20**:3 520–522 (1952) (cited p. 132).

[58] Wagner, NL, Wüest, A, Christov, IP, Popmintchev, T, Zhou, X, Murnane, MM, and Kapteyn, HC. *Monitoring molecular dynamics using coherent electrons from high harmonic generation*. Proc. Natl. Acad. Sci. **103**:36 13279–13285 (2006) (cited p. 133, 138–141, 147).

[59] Weiner, AM, Leaird, DE, Wiederrecht, GP, and Nelson, KA. *Femtosecond pulse sequences used for optical manipulation of molecular motion*. Science **247**:4948 1317–1319 (1990) (cited p. 133).

[60] Wittmann, M, Nazarkin, A, and Korn, G. *fs-Pulse Synthesis Using Phase Modulation by Impulsively Excited Molecular Vibrations*. Phys. Rev. Lett. **84**:24 5508–5511 (2000) (cited p. 133).

[61] Weinacht, TC, Bartels, R, Backus, S, Bucksbaum, PH, Pearson, B, Geremia, JM, Rabitz, H, Kapteyn, HC, and Murnane, MM. *Coherent learning control of vibrational motion in room temperature molecular gases*. Chem. Phys. Lett. **344**:3 333–338 (2001) (cited p. 133).

[62] Bartels, R, Weinacht, T, Leone, S, Kapteyn, H, and Murnane, M. *Nonresonant Control of Multimode Molecular Wave Packets at Room Temperature*. Phys. Rev. Lett. **88**:3 033001 (2002) (cited p. 133).

[63] Walters, ZB, Tonzani, S, and Greene, CH. *Vibrational interference of Raman and high harmonic generation pathways*. Chem. Phys. **366**:1-3 103–114 (2009) (cited p. 133, 140).

[64] Brown, EJ, Zhang, Q, and Dantus, M. *Femtosecond transient-grating techniques: Population and coherence dynamics involving ground and excited states*. J. Chem. Phys. **110**: 5772 (1999) (cited p. 134).

[65] Mairesse, Y, Zeidler, D, Dudovich, N, Spanner, M, Levesque, J, Villeneuve, DM, Corkum, and B, P. *High-Order Harmonic Transient Grating Spectroscopy in a Molecular Jet*. Phys. Rev. Lett. **100**:14 143903 (2008) (cited p. 134).

[66] Woerner, HJ, Bertrand, JB, Kartashov, DV, Corkum, PB, and Villeneuve, DM. *Following a chemical reaction using high-harmonic interferometry*. Nature **466**:7306 604–607 (2010) (cited p. 135, 136).

[67] Walters, ZB, Tonzani, S, and Greene, CH. *High harmonic generation in SF_6: Raman-excited vibrational quantum beats*. J. Phys. B **40**:18 F277–F283 (2007) (cited p. 141).

[68] Spanner, M, Mikosch, J, Boguslavskiy, AE, Murnane, MM, Stolow, A, and Patchkovskii, S. *Strong-field ionization and high-order-harmonic generation during polyatomic molecular dynamics of N_2O_4*. Phys. Rev. A **85**:3 033426 (2012) (cited p. 141, 142).

[69] Zerne, R, Altucci, C, Bellini, M, Gaarde, M, Hänsch, T, L'Huillier, A, Lyngå, C, and Wahlstrom, CG. *Phase-Locked High-Order Harmonic Sources*. Phys. Rev. Lett. **79**:6 1006–1009 (1997) (cited p. 143, 144).

[70] Corsi, C, Pirri, A, Sali, E, Tortora, A, and Bellini, M. *Direct Interferometric Measurement of the Atomic Dipole Phase in High-Order Harmonic Generation*. Phys. Rev. Lett. **97**:2 023901 (2006) (cited p. 143).

[71] Zhou, X, Lock, R, Li, W, Wagner, N, Murnane, MM, and Kapteyn, HC. *Molecular recollision interferometry in high harmonic generation*. Phys. Rev. Lett. **100**:7 73902 (2008) (cited p. 143).

[72] Lock, RM, Zhou, X, Li, W, Murnane, MM, and Kapteyn, HC. *Measuring the intensity and phase of high-order harmonic emission from aligned molecules*. Chem. Phys. **366**:1-3 22–32 (2009) (cited p. 143).

[73] Bertrand, JB, Worner, HJ, Salieres, P, Villeneuve, DM, and Corkum, PB. *Linked attosecond phase interferometry for molecular frame measurements*. Nature Phys. **9**:3 174–178 (2013) (cited p. 143).

5

fs-VUV-VMI – HHG as a probe in the VMI

Contents

Abstract

This chapter makes a link between Chapter 2 and Chapter 4, since here the high-order harmonic emission is used as a secondary source lying in the VUV range to realize a universal detection scheme. For this a new VUV spectrometer was built and coupled to a velocity-map imaging spectrometer. The chapter is organized as follows, Section 5.1 gives an introduction to the need of direct ionization followed by the description of the new designed fs-VUV spectrometer in Bordeaux in Section 5.2. The first characterization using the fs-XUV spectrometer as a VUV source in the VMI analyzing the photoelectron spectra of argon is shown in Section 5.3. Section 5.4 describes the experimental results studying the photodissociation of acetylene at 9.3 eV using the VUV photon source as probe pulse in the VMI.

Keywords: fs-VUV VMI, fs-VUV spectrometer, spectral selection, direct ionization, VUV flux, side bands, acetylene

5.1 Introduction: the need for direct ionization

Apart from using HHG as an imaging tool for structural dynamics and electron dynamics on an attosecond timescale, HHG is also a new source of radiation giving easily access to the electromagnetic spectrum in the ultraviolet region (NUV/EUV) down to the soft X-ray regime, which is normally only accessible through synchrotrons and free-electron lasers (FEL). The use of coherent radiation in the EUV region for experiments in molecular dynamics and femtochemistry is demanding as methods are often based on the ionization of the reaction products.

However, in many situations, the ionization potentials exceed 7 electron volts. To reach such thresholds with conventional lasers necessarily involves multiphoton ionization and therefore the use of high laser intensities as we have seen in Chapter 2. These high intensities can cause disruptive effects related to the electric field (like the Stark effect), and thereby complicating the measurement and interpretation. Often the presence of resonances is important in the multiphoton regime, and used by techniques like REMPI. But resonances also introduce complications and lead to difficulties in the interpretation of the results [1].

In molecules, the situation is even more complicated as the states may consist of absorption bands rather than levels, like in atoms. Using photons with energies exceeding the ionization threshold conducting one-photon transitions or a direct ionization, can not only circumvent the problem of resonances, but also reduce the intensity of the laser light, and thus eliminate the disruptive effects of the electric field. For instance, the dynamic Stark effect with an $1/\omega^2$ dependency is found significantly reduced with the use of EUV radiation.

HHG can be used to construct Table-top tunable EUV sources. This EUV-region with wavelength of 200 nm down to 10 nm, thus photon energies of 6 eV up to 100 eV is therefore suitable for the implementation of direct (one photon) ionization processes. Indeed, the phenomenon is now sufficiently well known and mastered to be used routinely, with specific requirements for experimental setups (stability, repetition rate, spectral and temporal characterization of laser pulses [2]). The considerable advantage of high-order harmonic generation is undoubtedly that it fits on an optical table and is relatively cheap to operate, compared to other EUV sources as synchrotrons and free electron lasers which are large and expensive facilities with only short periods of availability. Moreover, the extremely short duration of the pulse train is also an attractive factor for the HHG source, which are of course on the order of a few femtoseconds depending on the driving laser duration. Indeed pulse duration provided by synchrotrons are more on the order of picoseconds. The new developed free electron laser facilities provide pulse durations on the order of 20 fs but with a serious jitter on the synchronization with another laser which is essential for pump-probe experiments.

5.2 The fs-VUV spectrometer

There are already different experimental schemes for HHG as a VUV light source using a grating monochromator for spectral selection. For instance, the grating monochromator at the Artemis facility uses four different gratings [3]. The overall monochromator transmission varies between 21% and 28% and pulses with 1.6×10^7 photons per pulse for harmonic 21

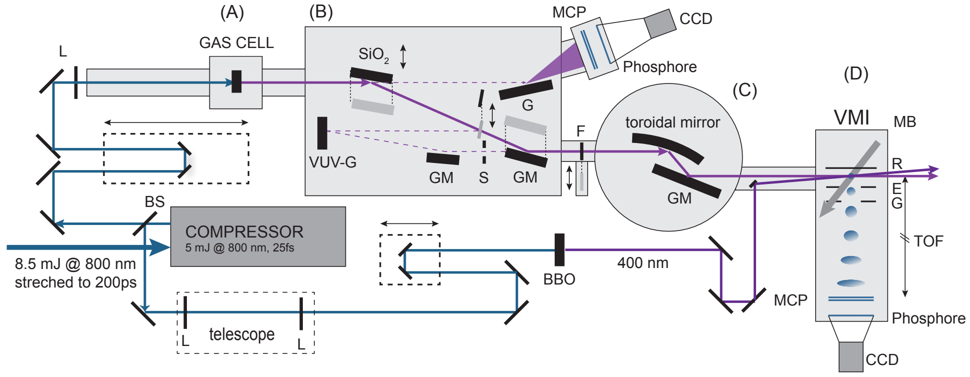

Figure 5.1: Schematic diagram of the fs-VUV HHG spectrometer. The setup consist of four different vacuum chamber, a generation chamber, a selection chamber, a directing and focusing chamber which is at the end coupled to the VMI chamber, labeled as A,B,C,D, respectively.

at 1 kHz and pulse durations around 30 fs were measured after the monochromator [4]. Another setup employing two toroidal gratings with a transmission of 2.6% is used in Japan [5] where 4.2×10^6 photons per pulse for harmonic 21 at 1 kHz with a pulse duration of 47 fs was measured after the monochromator. A setup with only one torroidal grating was implemented by Wernet and coworkers [6], leading to 10^7 photons per pulse at 1 kHz for harmonic 13 or harmonic 15, generated in Xenon. The tunability for the different setups varies between 8-9 harmonics, from harmonic 11 up to harmonic 29.

For the spectrometer in Bordeaux we applied a few constraints on the concept on construction:

- spectral selectivity between harmonic 9 and harmonic 17
- short time resolution
- low-budget
- a photon flux of 10^6 on target per pulse and harmonic
- easy switching with the ENLOS setup (extreme non-linear optical spectroscopy, see Chapter 4)

The developed spectrometer setup is shown in Figure 5.1. Basically it consists of a normal HHG spectrometer, which is modified to a selection chamber and a focusing chamber which is coupled to a VMI spectrometer, in order to use the VUV radiation in pump-probe experiments. The beam after the compressor can be split into two parts for pump-probe experiments. One arm is used to generate high-order harmonics and the other beam can be used as pump beam and is directly send to the VMI. On this arm of course BBO crystals can be used to double or triple the fundamental wavelength. The generating arm is send over a long translation stage to be able change the pump-probe delay between the two pulses. After that, the beam is focused in the generation chamber where HHG takes place either within a gas cell or in a gas jet using a pulsed valve (Even-Lavie valve). The generated VUV beam is then send to the new developed selection chamber. In this chamber we can select three different configurations shown in Figure 5.2:

- First we can send the beam directly onto a grating which sends the beam onto a detector to resolve the VUV radiation spectrally (see Figure 5.2 (A)). The detector consists of a dual MCP, a phosphor screen and a CCD camera. This setup is the general ENLOS setup as it was used in Chapter 4. Characterization of the harmonic spectrum is done using a variable pitch spherical EUV grating (1200 grooves per mm on average), placed on the axis of generation at almost grazing incidence (87°).
- In the second configuration (see Figure 5.2 (B)) the full VUV radiation is send into the VMI spectromter via a toroidal focusing mirror to use the the VUV radiation as probe or pump beam in the VMI. To send the whole VUV spectrum into the VMI the beam is sent onto a SiO_2 plate under an AOI of 70° which has an anti-reflective coating (AR coating) at 800 nm. Then the beam is reflected towards a plane gold mirror (AOI = 70°), a toroidal gold mirror and again on a plane gold mirror before being focussed into the VMI.
- The third configuration is similar to the second one with the aim of selecting only one specific harmonic which will be send to the VMI spectrometer and thus producing a monochromator (see Figure 5.2 (C)). In this configuration of the fs-VUV spectrometer a VUV-grating coupled to a slit is integrated in the beam path before focusing it with the toroidal mirror into the VMI setup.

In both configurations using the VMI, the focusing of the high-order harmonic radiation is done with a toroidal mirror. The main difference between the two last configurations is the transmission rate. Whatever the transmission rate for the full harmonic spectrum, using the monochromator with the VUV grating the transmission will be a factor 1000 less. The configuration and characteristics of the VUV spectrometer are discussed in further detail in the following sections.

5.2.1 Spectral selection

In the configuration where the whole spectrum is send into the VMI (Figure 5.2 (B)) metallic filters cut out the 800 nm and part of the VUV spectrum depending on the filter used. Selecting one single harmonic is done by sending the VUV radiation onto a grating which allows to separate the harmonics spatially (Figure 5.2 (C)), and in order to select only the desired harmonic a slit is placed after the grating, building together a VUV monochromator. The grating is placed on a motorized rotation stage, which allows to vary the angle of incidence of the EUV beam, so that only the harmonic of interest can pass through the slit after the grating. The principle is very simple, but it remains relatively complicated to implement in the field of VUV radiation, if one wants to keep both short pulses and a high photon flux. There are not many optical elements which work well in the VUV energy range. Conventional dielectric mirrors have a low reflectivity around 100 nm and are generally cost-intensive in the VUV range. Thus different solutions have to be applied in this wavelength regime. Indeed, because of the poor rate of reflection in this area, optics are usually used at grazing incidence to maximize the photon flux. However, illuminating a large portion of the grating brings along two important disadvantages: the VUV pulses are temporally broadened and the first order

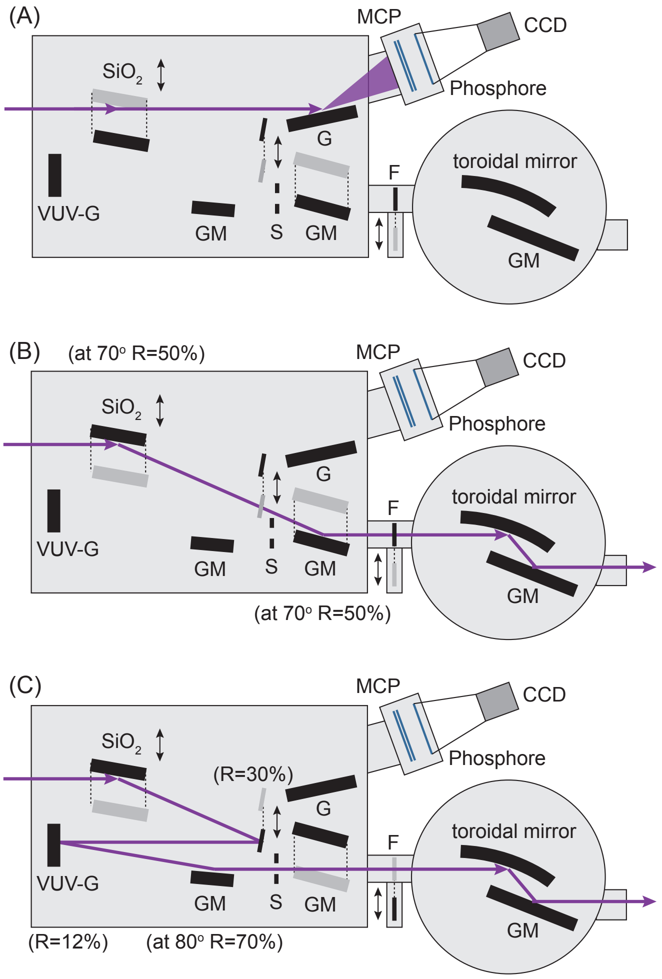

Figure 5.2: The different configurations of the HHG selection chamber. (A) basic ENLOS setup. (B) The whole VUV spectrum can be send to the VMI. (C) spectral selection of one harmonic which will be send to the VMI. For the optics used in configuration (B) and (C), the incident angles and the reflectivities are given.

diffraction efficiency is very low in terms of reflectivity. This effect is due to the different optical path introduced by each line of the grating. This path difference causes a delay per illuminated groove of $\Delta t = d\lambda/(gnc)$, with λ the wavelength of the the fundamental beam, n the harmonic order, g the groove spacing and c the speed of light in vacuum and makes it impossible to place the grating at grazing incidence. In addition, the harmonic beam dimension should be very small to illuminate only a small number of grooves. In order to achieve this, the harmonic beam is focused close to the grating, to keep the beam size small and thus the number of illuminated grooves as small as possible. The smallest laser spot size on the grating is limited by the damage threshold of the gold grating which is about 15 mJ/cm^2. This technique keeps a correct pulse duration (less than 20 fs enlargement see [7]) but sacrifices some of the harmonic flux. To avoid the introduction of aberrations, the focusing system consists of spherical mirror, a curved B_4C mirror. One further issue is the spatial separation of the harmonics on the slit, once the angle of the grating is adjusted for a certain harmonic. The slit size can be varied very precisely with a µm screw. It is placed 300 mm after the grating. The slit blocks the neighboring harmonics when choosing a slit size of 1.5 mm. By imaging the harmonics on a pair of MCPs the spatial selection of the slit up to harmonic 19 has been experimentally tested. As a matter of fact the spatial selection of the slit works even for second order diffracted harmonics. This type of monochromator is used to select the different harmonic spectrum with a resolution of about 0.5 nm in average (0.7 nm for harmonic 7 and 0.3 for harmonic 17) but with only a transmission rate between 0.5 and 1.5%, depending on the harmonic order. The characteristics are not among the best in the field but on the other hand, the cost of installation was very cheap (about 600 € for the monochromator grating against 10000-30000 € seen on the market or in other laboratories). A more detailed description of the device exists in the PhD thesis of H. Ruf, who designed and characterized the device of the monochromator during part of his thesis [7]. Unfortunately as we will see in Section 5.4 the monochromator has not been used to record pump-probe data in the VMI because of its poor transmission. We have indeed developed another strategy based on HHG at 400 nm and sideband detection to overcome the pour transmission of the monochromator.

5.2.2 VUV focusing

In order to maximize the laser illumination and to reduce the dimension of the interaction area in the VMI the VUV radiation has to be focused into the interaction chamber. The only focusing systems usable with EUV radiation are operated by optical reflection. Furthermore to minimize losses of VUV photons the focusing mirror must be positioned at grazing incidence as mentioned before. Such an procedure necessarily involves significant astigmatism at the harmonic focus, and focusing the radiation is not optimal (see [8]). One way around this problem is to use a toroidal mirror. In this case, astigmatism can be corrected by choosing wisely the radius of curvature R of the surface on which the incidence is high (tangential plane). The relationship between the focus position S' and the radi of curvature for a toroidal mirror is given by:

$$\frac{1}{S} + \frac{1}{S'_s} = \frac{2\cos\alpha}{R_s} = \frac{1}{f_s} \tag{5.1a}$$

$$\frac{1}{S} + \frac{1}{S'_t} = \frac{2}{R_t\cos\alpha} = \frac{1}{f_t} \tag{5.1b}$$

where α is the angle of incidence (to normal), S the object conjugate distance, S' the image conjugate distance and R the radius of curvature. The subscripts $_s$ and $_t$ are standing for the sagittal and tangential plane, respectively. R_s is also called the cylinder curve and R_t the base curve. The angle for which the object and image distance are equal is given by

$$\cos^2\alpha = \frac{R_s}{R_t} \rightarrow f_s = f_t \tag{5.2}$$

The radii of curvature that characterizes the mirror are ultimately determined by the desired focusing distance and the incident angle imposed which are given by the experimental setup. In our situation, the choice of the focusing distance is not trivial. It should be relatively short to allow the sharpest focus as possible, but should still leave enough room to insert the VMI spectrometer with its dimensions. An experimental compromise was made, setting this distance to 50 cm. With an incidence angle of 85°, the radii of curvature of the toroidal mirror are -11.474 m for the tangential radius and -8.7 cm for the sagittal radius. Toroidal mirrors have the advantage of being able to remove the astigmatism introduced by large angles of incidence, however, they are designed to operate at a particular angle of incidence. Unfortunately, if the angle of incidence of the beam deviates only slightly from the theoretical value, one introduces very fast a strong geometric aberration, distortion and astigmatism [8]. This sensitivity of the beam incidence makes the alignment of a toroidal mirror rather delicate. For optimum alignment of the mirror, it is mounted on a vertical micrometer translation stage for accurately positioning the laser beam on the mirror. Further, this translation stage itself is mounted on a rotation stage with seconds precision for fine tuning the angle of incidence according to the tangential plane. Finally, to facilitate the alignment of the VUV radiation into the VMI spectrometer we use a plane gold mirror placed at grazing incidence just after the toroidal mirror. The theoretical focus waist of the VUV beam was estimated to be around 60 µm [7]. One major drawback in the present setup is that the alignment of the toroidal mirror cannot be done under vacuum and that the spatial mode of the VUV light is not monitored. This is one of the updates that the team in Bordeaux wants to implement on this setup in the future.

5.2.3 VUV flux optimization

The observation of probably any pump-probe measurement with lasers involving molecular systems is a result of the interplay of different processes, involving the excitation of the system by the pump beam, the photodissociation following the excitation, the generation of the harmonic radiation if probed by an VUV radiation, ionization of the dissociation fragments via the VUV radiation, and the detection of these fragments or electrons produced by the interaction. Each of these steps can be connected to a yield, like the molecular excitation rate, the rate of dissociation after excitation, the efficiency of the HHG process, the ionization rate and the detection efficiency. The two main variables we can control is the HHG process using different gases to maximize the VUV photon flux and the molecular density to maximize the interaction by i.e. using a pulsed valve instead of a continous molecular beam like in Chapter 2.

For the new developed VUV spectrometer we therefore tried to optimize the VUV photon flux and to evaluate the number of events we can expect in the VMI using the VUV photon source as an universal detection (probe beam) in the pump-probe experiments planned. Figure 5.3 shows the harmonic spectra generated with a 800 nm driving laser pulse with an intensity of 800 µJ/p in krypton, argon and acetylene. A 1 cm long gas cell was used with an input and output hole generated by the laser itself to minimize the pressure in the source chamber. The gas pressures were optimized for each gas separately to 9, 20 and 6.5 mbar for krypton, argon and acetylene, respectively. At larger pressures the VUV radiation starts to be reabsobed. We can already see that by using krypton instead of argon we can increase the harmonic yield by a factor of two to three depending on the harmonic order. We also generated harmonics in acetylene where it can be seen that between harmonic 11 and 15 the HHG yield (purple line in Figure 5.3) lies somewhat between krypton and argon. Due to the relatively low ionization energy of 11.4 eV compared to argon and krypton with I_p's of 15.76 eV and

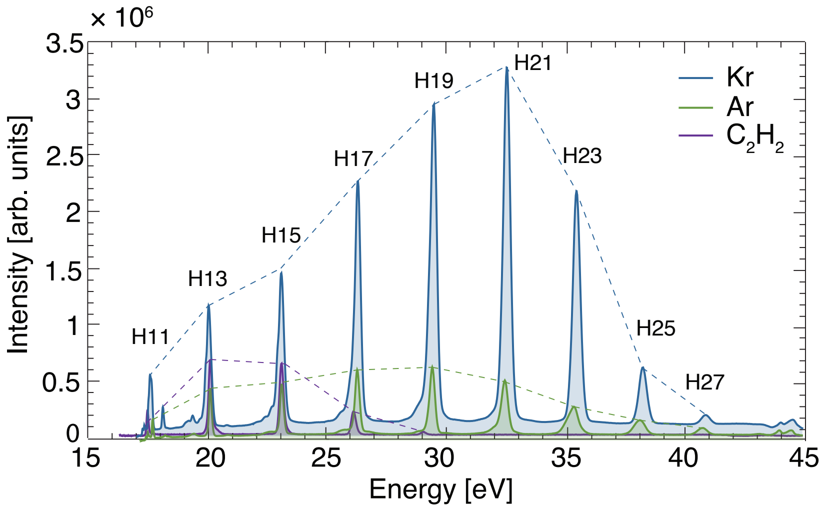

Figure 5.3: Harmonic spectra generated with an 800 nm driving laser with a lens with 1 m focal length in krypton, argon and acetylene at optimized pressures of 9, 20 and 6.5 mbar, respectively. The gas cell is 1cm long with an input and output hole created by the laser itself. Due to the diameter of the MCP (4 cm) only HHG > H11 are detected. A laser intensity of 800 µJ/p was used.

14.0 eV, respectively, the cutoff is obtained relatively fast. Here we have demonstrated that using acetylene gas for HHG, combined with a aluminium filter cutting energies higher than harmonic 11, allows already to produce a VUV radiation consisting only of a few harmonics by maintaining a reasonable high photon flux without using the monochromator and loosing a factor 1000.

Measurement of the number of VUV photons in the VMI

To be able to estimate the number of pump-probe events, we measured the total VUV photon flux with a VUV photodiode[1]. We used the calibration of the model to recover the number of photons per harmonic which is shown in Figure 5.4. Two aluminium filters are used to cut the 800 nm and a preamplifier with a factor of ×5 is employed to measure the signal of the photodiode with an oscilloscope. The number of VUV photons N_{VUV} is given by

$$N_{VUV} = \frac{N_e}{\eta} \tag{5.3}$$

where N_e is the amount of electrons supplied by the photodiode and η the internal quantum efficiency of the photodiode as shown in Figure 5.4. The amount of electrons N_e supplied by the photodiode in a time interval Δt is given by:

$$N_e = \frac{U\Delta t}{T_f R q_e} \tag{5.4}$$

---

[1] VUV-100 photodiode from OSI Optoelectronics

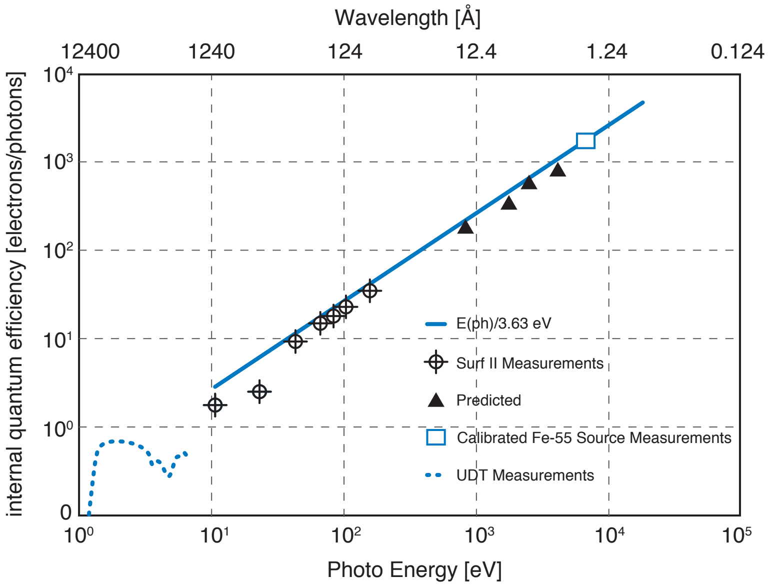

Figure 5.4: Internal quantum efficiency of the photodiode VUV-100 from OSI Optoelectronics. Adapted from the data sheet.

where U is the voltage measured by the oscilloscope, R the internal resistance of the oscilloscope (50 Ω), T_f the total transmission of the aluminium filters (10%, deduced from the CXRO databasis[1]) and q_e the elementary charge.

For the energies of interest (between 15 and 40 eV) the quantum efficiency of the photodiode is not very accurate as seen in Figure 5.4. The experimental points are not aligned with the calibration curve. The quantum efficiency also varies between 2 and 8 electrons per incident photon. For our calculation we took an average of 5 electrons per photon, which slightly underestimates the flux of photons for the low harmonics (H11, H13 and H15), and maximizes the flux for the higher harmonics (H23 - H27). By integrating the signal detected on the oscilloscope over Δt we obtain a total number of VUV photons of 3.5×10^8 photons per pulse. This measurement has been done in the configuration B in Figure 5.2 with the VUV photodiode inserted after the filter position (marked by F in Figure 5.2 (B)). If we consider the toroidal and plan gold mirror to send the beam into the VMI with a total reflectivity of 85% at grazing incidence for each mirror we obtain a photon flux of 2.5×10^8 photons per pulse in the VMI. In the HHG zone we obtain a photon flux of 14×10^8 photons per pulse by accounting for the two SiO_2 mirrors each one with a reflectivity of 50%. By taking the relative weight for each harmonic from Figure 5.3 we can give an estimate of the photon flux for each harmonic which is shown in Table 5.1.

Estimation of the pump-probe events in the VMI

With the photon number in the VUV we can now estimate the pump-probe event in the VMI. For this we consider a photodissociation experiment with a molecule AB dissociated (initiated) via a photon with $\lambda_i = \hbar\nu_i$ ($AB + \hbar\nu_i \rightarrow A + B$) and that one fragment, for instant A, is ionized

---

[1] Center for x-ray optics, filter transmissions: `http://henke.lbl.gov/optical_constants/filter2.html`

Table 5.1: Estimation of the number of VUV photon per pulse in the HHG generation zone and in the interaction region in the VMI. The relative weight is taken from Figure 5.3 for HHG in krypton with an 800 nm driving laser.

harmonic order energy [eV]	11 17.5	13 20.15	15 23.25	17 26.35	19 29.45	21 32.55	23 35.65	25 38.75	27 41.85
relative weight (% of total harmonic yield)	4.6	8.9	13.2	18.1	21.3	20.9	10.1	2.5	0.4
N_{ph} [$\times 10^8$] (generation zone)	0.6	1.2	1.8	2.6	3.0	3.0	1.4	0.4	0.06
N_{ph} [$\times 10^8$] (interaction zone)	0.1	0.2	0.3	0.45	0.5	0.5	0.25	0.06	0.01

(probed) via one photon in the VUV (A + $\hbar\nu_p$(= VUV) → A^+ + e^-). The number of pump-probe events N_{pp} for the detection the fragment A can be written as:

$$N_{pp} = \frac{N_A}{V}\sigma_A^{VUV} L N_{VUV} \tag{5.5}$$

where N_A is the number of fragments A produced after the dissociation with λ_i, V the interaction volume, σ_A^{VUV} the ionization cross section of fragment A in the VUV, L the interaction length and N_{VUV} the number of VUV photons per pulse determined in the section above. The number of fragments A, N_A, produced after the dissociation with 266 nm can be estimated as:

$$N_A = \rho_{AB}\sigma_{AB}^{\lambda_i}\eta_{AB} L N_{\lambda_i} \tag{5.6}$$

where ρ_{AB} is the molecular density of the molecule AB, $\sigma_{AB}^{\lambda_i}$ the absorption cross section of AB at λ_i, η_{AB} the dissociation probability and N_{λ_i} the numbers of photons at λ_i.

To evaluate this expression with some numbers we have to make some simplifications and assumptions. For the absorption and ionization cross sections we choose cross sections in the order of 1 Mb[1] for the considered photon energies. This value is on the lower limit of what can be found in experiments. The absorption cross section for argon for instance in the 25 eV energy region is about 30 Mb [9], for hydrogen the photoionization cross section between 14 and 20 eV is only a few Mb (6-2) [10] and for CH_3I for instance at 266 nm only 1 Mb [11], whereas acetylene has an absorption cross section around 9 eV of ~400 Mb [12]. So we decided to calculate this on the example of CH_3I at 266 nm to estimate a lower limit. The number of photons at 266 nm was determined to 1.3×10^{13} photons per pulse using 10 µJ per pulse. The molecular beam is produced by a pulsed valve, a Evan-Lavie valve, which produces a molecular density of 7.2×10^{23} atoms/cm^3 behind a 200 µ nozzle with a 40° opening angle and 12 bar of backing pressure [13]. This density is reduced to $\sim 7.2\times10^{21}$ #/cm^3 at the entrance of the skimmer placed 20 cm down stream from the nozzle to avoid turbulences at the skimmer walls. This longneck skimmer with a entrance diameter of 1 mm leading to a

---

[1] 1Mb = 1 mega barn = 10^{-18} cm^2. A barn (symbol *b*) is a unit of area and an expression for the cross sections of any scattering process

transmission factor of 0.03 and a length of 4.5 cm [13] will leading to density of 2.6×10^{19} #/cm^3. The beam leaving the skimmer is still expanding radially by 0.1 steradian reducing the beam density 8 cm away from the skimmer in the interaction region (fixed by the μ-metal diamter) by a factor 6.4 to 4×10^{18} #/cm^3. Consequently, if we assume a 1% mixture of CH_3I in the molecular beam (to avoid cluster formation), we will achieve a molecular density of $\sim\times10^{16}$ #/cm^3. The interaction volume and the interaction length is determined by the waist of the laser pulse and the diameter of the molecular beam. The interaction length is fixed to 3 mm, which corresponds to the molecular beam diameter 8 cm after the skimmer. The laser beam waist was determined to be 85 μm for the 266 nm using a lens with 50 cm focal length. If we consider that all molecules in the interaction region in the molecular beam are dissociated ($\eta_{AB} = 1$) we get a number of fragments N_A of 4×10^{10} per pulse which means 43000 pump-probe events per laser shot. Considering the detection efficiency of the MCP, the phosphor and the CCD which we assume to be around 25% we detect around 10000 events per laser shot. With a laser repetition rate of 1 kHz, the number of detected events should be quite suitable to obtain usable images after integration over a couple of minutes. In conclusion we can say that experiments using VUV light generated by HHG as a probe with femtosecond time resolution is possible and feasible. But in fact as we will see in Section 5.4, we did not observe any pump-probe signal with a VUV pulse as a probe beam.

5.3 fs-VUV VMI characterization

For testing the new VMI - VUV spectrometer combination we choose argon as target gas, which has two main advantages for the experiment apart from that it is a well known system. Firstly it has a relatively high absorption cross section of about 25 to 35 Mb between 15 and 30 eV. On the other hand, as argon is an atom we are not bothered by secondary processes (like for instance dissociation), which gives us a larger molecular density in the interaction volume. We undertook three different experiments to test the fs-VUV spectrometer. In the first experiment we detected the photoelectron spectrum of argon using the full VUV spectrum produced with a 800 nm driving laser (see Figure 5.3). For the second experiment we used the VUV monochromator in the spectral selection configuration to select only one harmonic (harmonic 11 and 13) to ionize argon. In the third experiment we recorded the photoelectron spectrum of argon in pump-probe configuration using the VUV radiation generated at 400 nm plus an additional 400 nm pulse. In the following three sections the results of these test experiments are presented.

5.3.1 Photoelectron detection of argon using a VUV spectrum

The HHG spectrum is produced by focusing ∼800 μmJ/p of the 800 nm driving laser, spatially filtered by a diaphragm, with a 1 m focal length lens into a 1 cm long gas cell, filled with krypton at 10 mbar. In addition an aluminium filter with a thickness of 150 nm is used which cuts all photons with photon energies lower than 15 eV and therefor also the remaining 800 nm. The setup is actually shown in Figure 5.1 without using the second arm to produce the

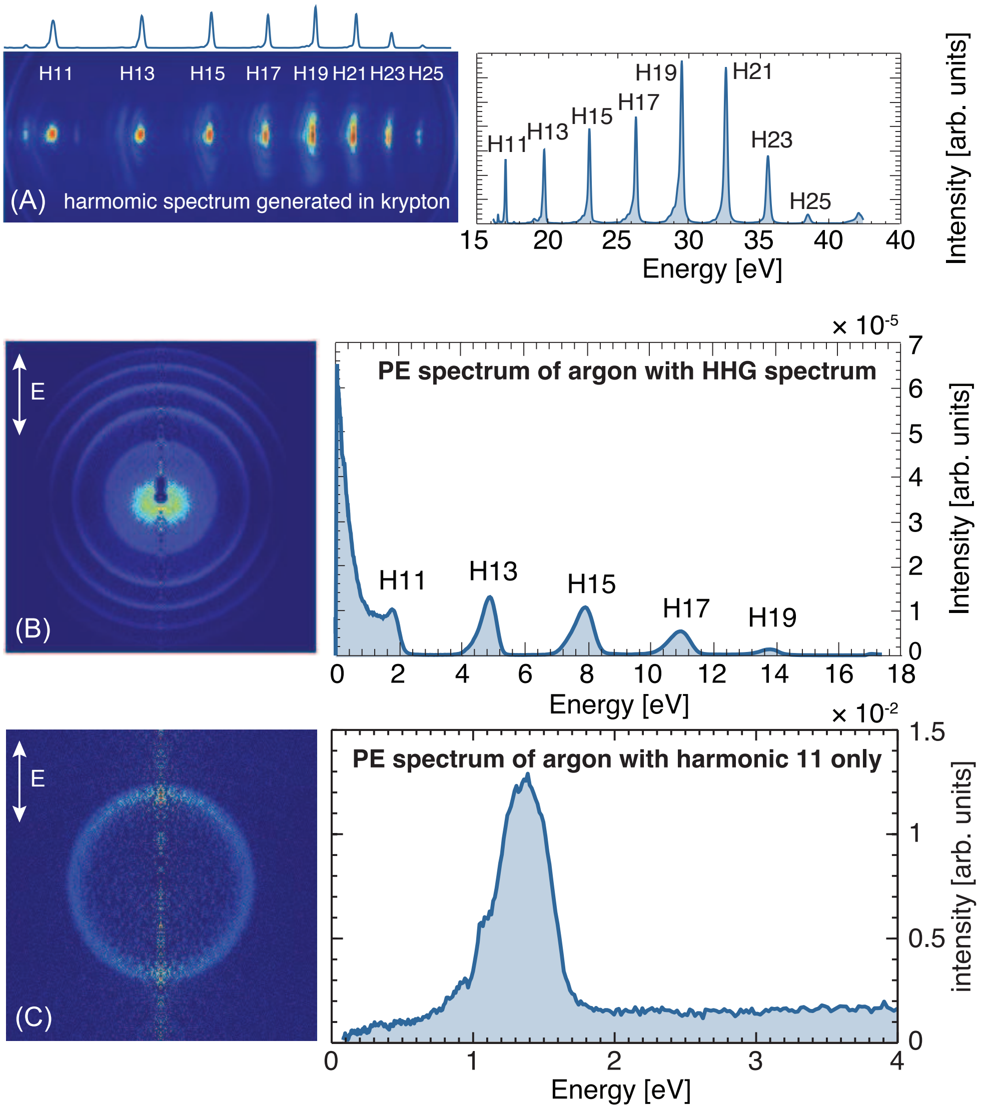

Figure 5.5: (A) high harmonic spectrum generated with an 800 nm driving laser pulse in krypton. On the left the calibrated spectrum in eV. (B) photoelectron spectrum of argon obtained with the harmonic spectrum above. (C) photoelectron spectrum with harmonic 11 only in the monochromator configuration.

400 nm. The molecular beam of argon in the VMI is produced by the Evan-Lavie pulsed valve with a backing pressure of 15 bar. Figure 5.5 shows the harmonic spectrum observed on the MCP. On the left the calibrated spectrum is presented. We observe harmonic 11 (17.05 eV) to harmonic 25 (38.7 eV). The photoelectron (PE) spectrum of argon recorded with the VMI using the VUV spectrum produced in krypton is shown underneath. The repeller and extractor voltages used were -5.5 kV and -4.17 kV, receptively. The image on the left is the Abel inverted PE image and on the right the kinetic energy release is shown after an integration of the PE image over the angle. The energy axis is calibrated using the VUV spectrum from Figure 5.5 (A) in krypton and the ionization potential of argon at 15.76 eV. The first harmonic which is able to ionize argon is harmonic 11 with an energy of 17.05 eV and we observe photoelectrons up to 14 eV (H19). The signal in the center is probably due to argon clusters or either from high kinetic energy scattering electrons which are ionizing the high density molecular beam.

5.3.2 Argon ionization with only one harmonic: spectral selection

Using the VUV spectrometer in the monochromator configuration (see Figure 5.2 C) we are able to select a specific harmonic. An Abel-inverted image of the photoelectrons obtained in the VMI with only harmonic 11 is shown in Figure 5.5 (C). We observe one component corresponding to the ionization of argon with only the harmonic 11. The main drawback of this configuration is its low intensity.

5.3.3 VUV plus 400 nm: The lifetime of a Rydberg state in argon

To test the pump-probe technique between the VUV radiation and a pump pulse we utilize a technique of generating so called *side bands* (SB), which is also used in the characterization of attosecond pulses using the RABBITT technique to experimentally determine an average pulse duration in the train of attosecond pulses [14, 15]. This technique makes use of the two-color ionization of a target atom with the VUV field and a time-delayed IR-field. A scheme of the RABBITT-method is depicted in Figure 5.6. For suitable IR-intensities, the atoms in the target region are not only ionized by the VUV-field alone, but can also be ionized by absorption of a harmonic photon and an IR-photon or by absorption of a harmonic photon and emission of an IR-photon. The electrons coming from these two-photon processes will peak at even multiples of the fundamental photon energy in the photoelectron spectra of the target gas. They will thus form sidebands to the photoelectrons coming from the ionization by the VUV field alone. Both processes, absorption of an VUV- and an IR-photon and absorption of an VUV-photon and emission of an IR-photon, are coherent and lead to the same electron energy. As a consequence, a modulation on the electron count rate of these sidebands in the electron spectrum with delay between IR and VUV field is to be expected. An analysis of these modulations then allows the extraction of the relative phase of two consecutive harmonics in the spectrum. But we can also use this to determine the cross-correlation time between the two pulses as this process depends on the temporal overlap of the two beams. As we will use 400 nm as a pump beam later for the study on acetylene we decided to generate harmonics also with 400 nm to be able to use this technique of side bands to characterize the temporal overlap and the cross-correlation of the two beams. As the sidebands are produced by absorption and emission of an extra photon of the second beam, the photon energy must be the same as used for generating the harmonics. Using 400 nm as driving laser wavelength will give a separation of the harmonics of $2\omega \approx 6$ eV. Using a second 400 nm pulse and controlling the delay between the VUV pulse and this 400 nm pulse we can analyze the photoelectron spectrum as a function of the pump-probe delay. The fifth harmonic in this case has an energy of 15.5 eV and is therefore just below the ionization potential of Argon of 15.76 eV, and in resonance with Rydberg states in argon of s or d symmetry (electronic configuration of argon is [Ne]$3s^2 3p^6$). This allows us to trace the lifetime of these excited Rydberg states which should be encoded in the side bands produced by harmonic 5 and 7 as shown in Figure 5.6 (C).

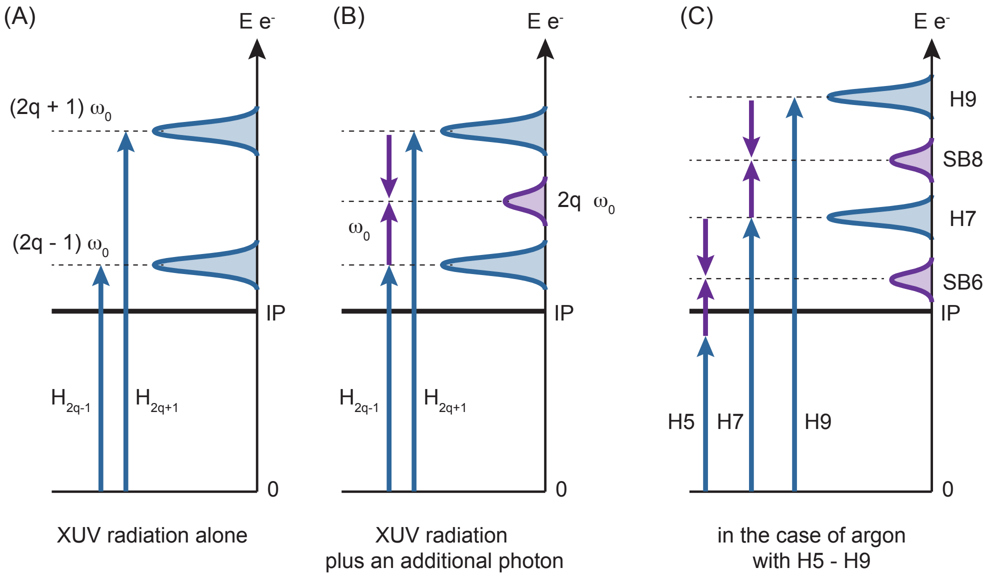

Figure 5.6: Scheme of the electron spectra generated with the RABBITT-technique. Two-photon processes lead to the occurrence of so called sidebands (purple) in the presence of an extra laser field at the same wavelength as the driving laser. (A) photoelectron spectrum with VUV radiation alone. (B) photoelectron spectrum with VUV plus an additional photon. (C) photoelectron spectrum in the case of argon with harmonic 5 - 9 produced with 400 nm, where H5 is with 15.5 eV just below the ionization potential of argon (15.76 eV).

Experimental

The setup for this experiment is similar to the one already shown in Figure 5.1. The beam is divided into two arms after the compressor. 20% is used to generate the 400 nm pulse and 80% is used for HHG. The relative delay is controlled by a long translation stage. In addition to what is shown in Figure 5.1 a second telescope on the harmonic arm is implemented to reduce the beam diameter for the conversion to 400 nm. The frequency doubling is done in a BBO crystal with a thickness of 200 µm. The thickness of the crystal was selected to not extend the pulse duration too much. In fact, in a recent experiment done on halo-uracil compounds, by reducing the thickness of the entrance window to the vacuum chamber from 3 mm to 1 mm, the HHG intensity has been increased by 50%. A spectral bandwidth of 14 nm centered at 402 nm was measured which should give a transform limited pulse duration of 24 fs. Two dichroic mirrors are used after the BBO crystal to remove the 800 nm beam. The beam of $\sim$1 mJ of 400 nm is then focused by a lens with a focal length of 50 cm into a 2 mm long cell filled with 15 mbar of Argon. The previously used 1 m lens had to be replaced by a shorter focal length because we discovered that the SiO_2 mirror after the generation chamber was damaged after some beam time. Using a shorter focal length reduced the HHG volume but did avoid the damage issue. At the beginning we also used a 10 mm cell which was replaced by a 2 mm because at 400 nm the absorption was to strong in a 10 mm cell. One parameter that can still be optimized is the length of this cell as 2 mm might not be the optimum for 400 nm. The obtained harmonic spectrum under these conditions is shown in Figure 5.7 (A). By comparing the harmonic intensity measurements for similar acquisition parameters to a generation using 800 nm (same MCP values, phosphor screen voltages and camera acquisition time), allows a rough estimate of the amount of harmonic signal at 400 nm. The intensity of the generated harmonic 7 with 400 nm in argon is on the same order of magnitude as of the 13th harmonic generated with the 800 nm using krypton. However, the amount of the total harmonic signal at 400 nm is less than the total harmonic signal at 800 nm (two times less harmonics and lower cutoff energy). The harmonic beam generated is then send to the VMI using the configuration B from Figure 5.2 to send the whole spectrum into the VMI. For the other arm the beam diameter is as well reduced by a telescope and then doubled in a BBO crystal with a thickness of 1 mm. The wavelength produced is centered at 401 nm with a bandwidth of FWHM = 7 nm. The maximum available pulse energy was measured to be 65 μJ. As well two dichroic mirrors are used to remove the 800 nm before the beam is focused into the VMI via a 60 cm focal length lens. The recombination of the two beam is done via a 45° mirror with a hole in the center in front of the VMI. The VUV radiation passes through this hole and the UV radiation is reflected by the mirror, so that the two beams enter the VMI in a collinear configuration. The spatial and temporal overlap is done in the VMI as described in Section 2.2.3 for the ClN_3 dissociation experiment with the exception that the overlap was not done using the VUV radiation. The HHG gas was switched off and the 400 nm which passes through the experiment was used instead (to get 400 + 400 nm). This was necessary as with the VUV light with energies higher than most of I_p's there is no multiphoton ionization and thus no contrast. Using two 400 nm pulses allows as well to get the time overlap ($\Delta t = 0$) through optical interferences monitored at the output of the VMI in the far field. The molecular beam of argon in the VMI is produced with the pulsed Evan-Lavie valve similar to the previous experiment.

Results

Figure 5.7 (B) shows the Abel inverted photoelectron image in pump-probe configuration at $\Delta t = 0$. On the right in blue the kinetic energy release in eV is shown. We observe harmonic 7 and 9 where harmonic 7 with 21 eV is the first harmonic to be able to ionize argon as harmonic 5 with 15.5 eV is just below the I_p. One can also notice the presence of the side bands, one produced by harmonic 5 and 7 (SB6) and one produced by harmonic 7 and 9 (SB8) by absorbing and emission of an extra 400 nm photon. The intensity of the 401 nm pulse was adjusted to 15 μJ/p to not saturate the signal with the 401 nm pulse alone by above threshold ionization (ATI). Figure 5.8 shows the integrated signal of SB6, SB8 and H7 as function of the time delay between the VUV pulse and the extra 401 nm pulse. In Figure 5.8 (A) the three signals are normalized to the highest signal which is harmonic 7. The percentage numbers shows the pump-probe yield at $\Delta t = 0$. Only around ∼15% contrast of pump-probe signal is achieved with a rather huge background signal on harmonic 7. Figure 5.8 (B-D) shows the the time-dependent pump-probe signal normalized to one for SB8, H7 and SB6, respectively. The blue and green data refer to the measurements taken without and with the aluminium filter in the VUV beam, meaning that harmonic 5 which is just below the I_p is used (without filter) or cut (with filter). SB8 which is produced by harmonic 7 and harmonic 9 which are both above the I_p of Argon shows a symmetric cross-correlation function as expected. In a typical situation where no resonance is involved, the magnitude of the sidebands as a function of the time delay between the two pulses is supposed to evolve according to a characteristic envelope

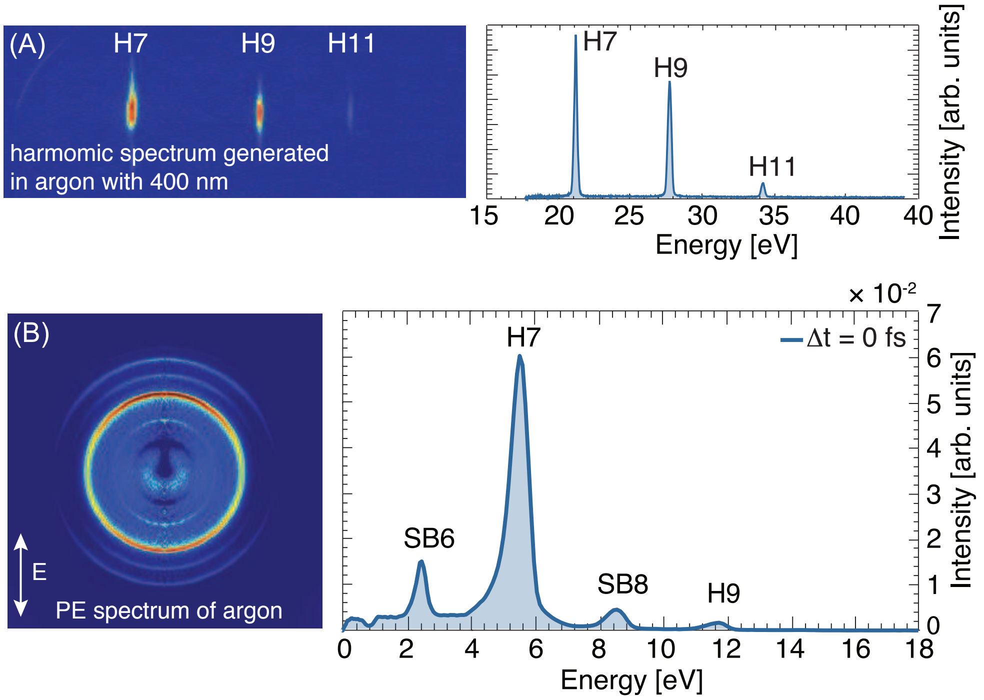

Figure 5.7: (A) high harmonic spectrum generated with a 400 nm driving laser pulse in argon, with 50 cm lens, a pressure of 15 mbar and 1 mJ/p. On the left the calibrated spectrum in eV at $\Delta t = 0$. (B) photoelectron spectrum of argon obtained with the harmonic spectrum above plus an extra 400 nm beam at $\Delta t = 0$, visible are harmonic 7 and 9 and as well the side bands produced by harmonic 5 and 7 (SB6) and SB8 produced by harmonic 7 and 9.

of the cross-correlation between the two pulses. This signal is maximum at $\Delta t = 0$ and the minimum outside of the temporal overlap. Similarly, the evolution of the photoabsorption of the harmonic peaks also has the symmetry of a cross-correlation function, with the difference that the signal is at its minimum at $\Delta t = 0$ and maximum outside of the temporal overlap. This is explained by the fact that a portion of harmonic photons are used at the time of the temporal overlap to participate in the creation of the sideband signals. The ionization by a simple harmonic transition is therefore less intense around zero delay. A gaussian fit to this temporal evolution gives us a typical pump-probe time resolution. On SB8 this is measured to be around 91 $\pm$ 2 fs at the FWHM. This mainly the duration of the 400 nm pulse, generated in the 1 mm thick BBO crystal. Indeed, the 7 nm bandwidth of this pulse gives an theoretical duration of 50 fs, which is unfortunately chirped in the 5 mm thick lens and the 3 mm thick vacuum window to $\sim$80 fs. For SB6 we observe, that if the filter is removed and harmonic 5 is used (blue data points), the intensity as function of the time delay shows not a symmetric cross-correlation function but a signal with a rather long decay time. Sideband 6 is not only created by harmonic 7 but also by harmonic 5 plus an extra 401 nm photon. The energy of H5 is 15.5 eV and is therefore just below the I_p of argon. However the density of states close to the I_p is rather high [16] and the spectral bandwidth of harmonic 5 with around 250 meV is therefore able to excite argon in several Rydberg states.

To estimate the lifetime of this excited state, the data is fitted with a similar function as seen

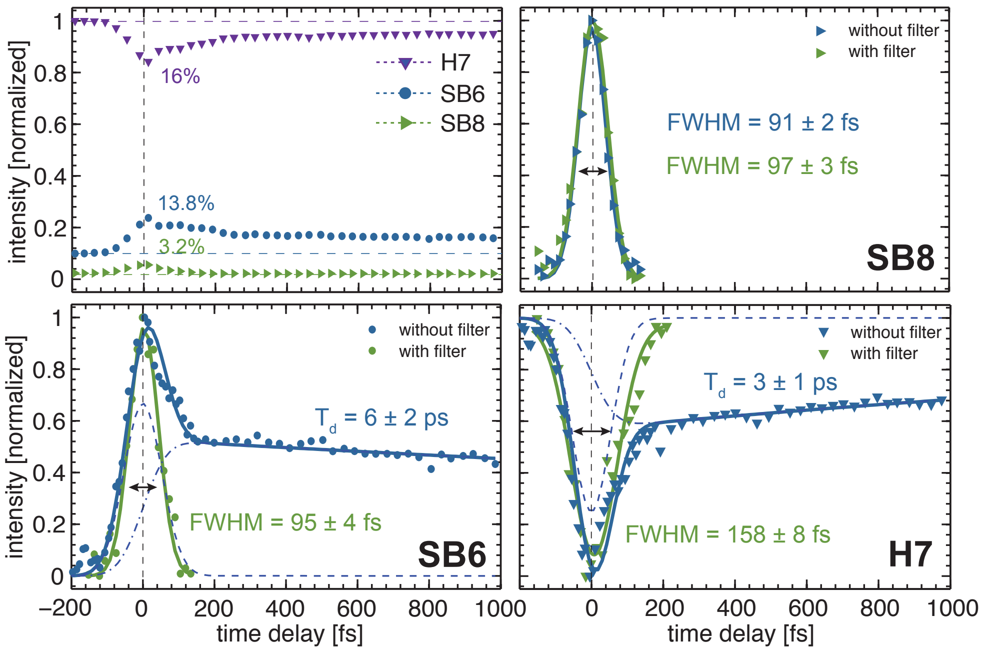

Figure 5.8: Integrated photoelectron signal of SB6, SB8 and H7 in argon as function of the time delay between the VUV pulse and the 401 nm pulse. (A) Yield SB6, H7, SB8 normalized to the largest signal (H7) with pump-probe contrast. The percentage numbers show that the pump-probe signal is rather tiny compared to the measured background. (B-D) shows the integrated yield of SB8, SB6 and H7, respectively, as function of the time delay without (blue) and with (green) filter in the VUV beam line.

in Section 2.3 Eq. (2.3):

$$I(t) = \psi_{cc}(t) + \psi_d(t) \tag{5.7}$$

where ψ_{cc} is a cross-correlation function defined as

$$\Psi_{cc}(t) = a_0\, e^{-\frac{1}{2}\left(\frac{\Delta t}{w}\right)^2} \tag{5.8}$$

with the width w determined on SB8 which only shows a cross-correlation function, and ψ_d is an exponential decay function as Eq. (2.5) from Section 2.3:

$$\Psi_d(t) = a_1\, e^{-\frac{\Delta t}{T_d}} \times [1 + erf\,(\phi(\Delta t, T_d))] \tag{5.9}$$

where T_d is the decay time and $\phi(\Delta t, T)$ the error function as defined in Eq. (2.7) which takes the cross-correlation time in account. The extracted decay time is 6 ± 2 ps. As we only measured up to a pump-probe delay of 1 ps this decay time is only an estimate. Indeed a Rydberg state can have easily a lifetime in the nanosecond regime. Using the filter to remove harmonic 5 from the VUV spectrum we observe on SB6, as on SB8, as well only a cross-correlation signal with a FWHM of 95 ± 4 fs, which is the same as measured on SB8. This test indicates clearly that a resonance is reached at 15.5 eV by H5. The time dependency measured on SB6 is expected and shows the possibility to use the VUV spectrum as tool to investigate dynamics. In contrary we also observe a time dependency on harmonic 7 which at first is not intuitive. Harmonic 7, if the filter is removed, shows a depletion in intensity which

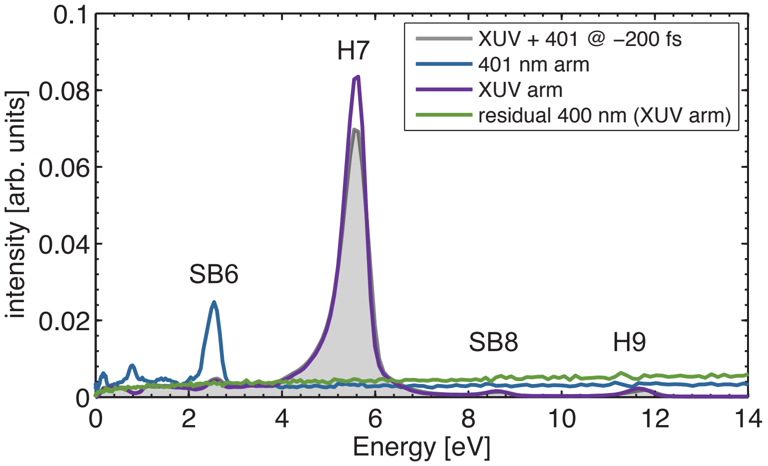

Figure 5.9: Photoelectron spectrum backgrounds of argon, showing the signals with the 401 nm probe alone (blue), the VUV beam alone (purple), and the residual 400 nm from the HHG arm (green) in comparison to the pump-probe signal at Δt = -200 fs (grey).

recovers on a timescale of 3 ± 1 ps. The data is fitted with the same function (Eq. (5.7)) as SB6. To explain this we will look first at the one laser background signal.

Figure 5.9 shows the photoelectron spectra of the one laser backgrounds, meaning for the 401 nm beam alone (blue curve), for the VUV beam alone (purple curve) and for the residual 400 nm from HHG driving pulse (green curve), when the gas is switched off, in comparison to a pump-probe signal at negative delays (grey curve). We see directly that the residual 400 nm in the HHG arm is not producing any background signal. For the 401 nm probe beam the main peak corresponds to SB6 with 6×401 nm. The two extra components at lower energies ($\sim$0.2 eV and $\sim$0.8 eV) are explained by two Freeman resonances encountered at two different intensities in the time and spatial profile of the 401 nm pulse. Basically because resonances are encountered at 5 photons, only 200 meV below the IP, not only the direction ionization is observed (SB6) but as well two resonances. However these resonances will be fulfilled at different laser intensities (time or spatial profile) and shifted in energy as well as in I_p. Important to notice here, is that the signal of SB6 at 401 nm is $\sim$40% larger than the signal of SB6 in pump-probe at time overlap (compare to Figure 5.7 (B)). This decrease of the SB6 pump-probe signal related to the SB6 signal from the 401 nm alone (ATI) indicates that the ground state is depleted by the VUV and thus a background subtraction is not possible. There is a background signal on SB6 with the VUV beam alone, which is coming from the VUV beam plus one photon from the residual 400 nm. For harmonic 7 we do not observe a background signal with the 401 nm alone coming from 7 photons which would be the second ATI peak. Again the background signal from the VUV alone is larger than the pump-probe signal at time zero and outside the cross-correlation. Here as well the background subtraction will not work because the 401 nm alone is depleting the ground state of argon.

The time profile of H7 is really intriguing and for the moment we don't have yet a clear explanation. Its picoseconds rising time at positive delay seems to indicate that a pump-probe path via the resonance reached at H5 is involved. Indeed, when the metallic filter is used and H5 is blocked, the expected cross-correlation profile is retrieved on H7. The obvious pump-

Table 5.2: Background signals for SB6 and H7 with one laser in comparison to the pump-probe signals at Δt = -200 fs and Δt = 0 fs

	SB6	H7
401 nm	2.5×10^{-2}	0
VUV	4.4×10^{-3}	8.3×10^{-2}
VUV + 401 nm Δt = -200 fs	4.8×10^{-3}	6.9×10^{-2}
VUV + 401 nm Δt = 0 fs	1.49×10^{-2}	5.9×10^{-2}
conclusions	S(401 nm)>S(Δt=0) → depletion of the ground state S(VUV)≈S(Δt=-200) → no dynamics from 400 nm	S(VUV)>S(Δt=-200) → depletion of the ground state by ATI at 401 nm

probe path on H7 would be H5 + 2×401 nm. However this quantum path will be present as soon as the Rydberg states are populated, meaning during the VUV pulse duration. This should result in a time behaviour for this path in the order of a few tenth of femtoseconds and not in a picoseconds rising profile. Obviously, the picosecond rising time reveals that the state(s) detected through the H7 transient is not the 'zeroth order state' populated by H5, but some other electronic state populated by the relaxation from this 'zeroth order state'. If this is the case and since this contribution appears on the photoelectron signal of H7, the energy E_n of this electronic state energy should satisfy the relation $E_n + p \times E_{401nm} = E_{H7}$, where p is an integer. Taking into account the density required for such a coupling, we will assume that the electronic coupling takes place without photon emission, namely at the energy of the 'zeroth order state'. The fact, that we do not observe a double exponential dependency on SB6 (only a long decay with a time constant of ~6 ps is observed), means that a one photon ionization is improbable and a two photons ionization onto the ground state of the cation will be highly probable. A doubly excited state, which will be the obvious electronic configuration, is however energetically not accessible since it starts at 273075 cm^{-1} (33.86 eV) with the 4s-4p excitation [17].

Taking into account the electronic ground state of argon [Ne]$3s^2 3p^6$, the populated Rydberg states must be of *s* or *d* symmetries. There are five allowed Rydberg series by electric dipole transitions: three series that converge to the first IP – $^2P_{3/2}$ at 127110 cm^{-1} : $ns(3/2)_1$, $nd(3/2)_1$, $nd(1/2)_1$ and two series that converge to the second IP – $^2P_{1/2}$ at 128542 cm^{-1} : $ns'(1/2)_1$, $nd'(3/2)_1$. Note that the VMI resolution combined with the large bandwidth of the H5 is not enough to resolved the spin-orbit splitting of Ar^+, that is only 177 meV. Yoshino et al. showed that these two types of Rydberg series are coupled to each other with the main coupled pair being the nd(1/2) and the nd′(3/2) [16]. Based on the spectroscopy done by Yoshino et al., the main Rydberg states that might be populated by our H5 at ~125000 cm^{-1} (~15.5 eV) with a FWHM of ~2000 cm^{-1} (~250 meV) are shown in Table 5.3. Clearly the dominant Rydberg character is expected to be nd(3/2). Two important questions remain: first, if the nd(x) Rydberg states relaxes to the nd′ series, why are these ones not observed by a one-

Table 5.3: Main Rydberg states in argon accessible with H5 at ∼125000 cm^{-1} (∼15.5 eV) with a FWHM of ∼2000 cm^{-1} (∼250 meV). extracted from [16]

$3p^5ns(3/2)_1 \leftarrow 3p^6\ ^1S_0$		
n	energy [cm^{-1}]	intensity[a]
8	123936	42
9	124782	41
10	125332	15
11	125715	30
12	125984	42
13	126181	28
14	126332	30
15	126447	60

$3p^5nd(3/2)_1 \leftarrow 3p^6\ ^1S_0$		
n	energy [cm^{-1}]	intensity
6	123997	67
7	124788	51
8	125377	53
9	125718	49
10	125979	42
11	126204	47
12	126334	42
13	126447	60

$3p^5nd(1/2)_1 \leftarrow 3p^6\ ^1S_0$		
n	energy [cm^{-1}]	intensity
7	124554	32
8	125136	36
9	125613	30
10	125898	27
11	126099	35
12	126293	30

$3p^5ns'(1/2)_1 \leftarrow 3p^6\ ^1S_0$		
n	energy [cm^{-1}]	intensity
7	123882	39
8	125353	38
9	126211	43

---

[a] Estimated relative intensity I measured from densitometer traces. I = 100 is the n = 3 line (not shown here) in the $3p^5nd(3/2)_1 \leftarrow 3p^6\ ^1S_0$ series, the strongest line in the region below 1000 Å[16]

photon ionization at 401 nm but by a two photons transition? Does this mean that a spin orbit coupling from nd(3/2)$_1$ to nx(5/2)$_2$ is undergoing? Indeed Yoshino et al. detected a np(5/2)$_2$ and a nf(5/2)$_2$ Rydberg series in the same energy range that are allowed only by quadrupole electric transitions. And secondly, why is the H7 depleted at positive pump-probe delays, like if some background signal will be missing? This last question is in fact the most puzzling one. Figure 5.9 shows that the level of signal of H7 for negative pump-probe delay is already smaller than the one expected from the VUV beam alone. So at positive delay, when the 401 nm interacts later, depletion of the ground state of argon is not effective and the level of H7 should be the purple plot in Figure 5.9. This means that the depletion observed on H7 at positive pump-probe delay, when the metallic filter does not cut H5, is in fact larger than it appears. In fact, the H7 transient experimentally observed would be understood if a resonance with a picosecond lifetime would be encountered at H7 (21.7 eV). However it is not so simple, because such transient is not observed with the metallic filter, so if a resonant state exists at 21.7 eV it won't be populated by H7 alone. Another possibility is that the 21.7 eV energy range is populated by H5 + 2×400 nm, where 400 nm is the residual beam from the HHG process, that will be cut by the aluminium filter. Such state could autoionize on a picosecond timescale and consequently, contribute to the background of H7. In the pump-probe configuration, this level would be depleted by absorption or emission of a 401 nm to produce SB8 or SB6, leading to the depletion observed on H7, until this state autoionizes by itself. The main problem is that there is no such state expected at that energy. However we could imagine that at that energy a Kramers–Henneberger (KH) potential can be created with a picoseconds lifetime. This hypothesis needs of course more experimental investigations, to be confirmed. A KH atom is mostly a theoretical concept, since it has been put in evidence experimentally only via one experiment [18]. A KH state is a stable state against ionization due to an effective binding potential created by the presence of a strong electric field (here the residual 400 nm) [19]. This is called a stabilization state. Definitively this first pump-probe experiment on a simple system like argon, requires more experimental investigations which was not expected.

5.3.4 Conclusion

The VUV pump 400 nm probe excitation of argon has shown that we were able to probe the relaxation dynamics of a Rydberg state via photoelectron sideband detection. For this we generated high-order harmonics using 400 nm, where the energy of the fifth harmonic is approximately 250 meV below the ionization threshold of argon and in resonance with a series of Rydberg states. These states are then probed by a one-photon transition with another 400 nm pulse, producing sideband 6. We observed as well, that the photoelectron peak connected to harmonic 7, shows also a relaxation dynamic. However, the transient observed on H7, and especially its depletion at positive delay, need further experimental investigation in order to be understood.

Although the main interest of this experiment was not probing Rydberg states in argon, given the extremely broad spectral bandwidth of our harmonic pulse compared to the energy levels of the spectroscopic excitation in this region, this experience has allowed us to verify the feasibility of such pump-probe experiments with the new fs-VUV-VMI spectrometer.

5.4 Photodissociation of acetylene, C_2H_2, using 9.3 eV

5.4.1 Motivation

After testing the new fs-VUV VMI spectrometer we looked for a molecular system with a scientific interest that wont ask for too many experimental constraints in order to use this technique. Acetylene seemed a good candidate because of the dissociation dynamics taking place in the far ultraviolet around 9.3 eV, and as well as mentioned before, because acetylene has numerous absorption bands, with a very large absorption cross-section ($\sim$ 400 Mb around 9.3 eV) [12]. Furthermore, acetylene may be used in gaseous form at very high pressures (tens of bars), which allows us to use a pulse molecular beam source (Even-Lavie valve) producing a molecular beam with higher densities. Acetylene is also not corrosive and does not present any particular health hazard.

The molecule acetylene (C_2H_2) was first synthesized in 1836 by Edmund Davy and the first experimental studies of the absorption spectroscopy of acetylene in ultraviolet date back as early as 1931 [20], followed by studies in the VUV range in 1935 [21]. The formation mechanism of amino acids and polyols in the extraterrestrial atmosphere is an important question in biology, planetary astrophysics, and cosmology. The existence of a variety of important species can be traced to interstellar photochemistry taking place in interstellar molecular clouds [22, 23]. The most abundant molecules in the interstellar medium include H_2, CO, and acetylene. Ultraviolet photolysis of these simple molecules is a fundamental process in understanding the steps leading to larger carbon-based systems, a challenge for interstellar chemistry. One of the main dissociation products is the C_2H radical which is in the models of interstellar chemistry one of the precursor to the formation of carbon chains. A detailed understanding of photoinduced reactions, including direct dissociation and predissociative mechanisms, is implicit to completing the photoreactive scenario behind the formation of larger molecules such as sugars and amino acids. In despite its relatively simple structure (H–C≡C–H), acetylene has an abundant spectroscopy, especially in the UV and VUV region and shows numerous vibrational modes and several types of geometries [24]. These different aspects have motivated the scientific community and this molecule has been the subject of numerous studies. Here I can only give a short introduction and summary to the spectroscopy of acetylene to show why we wanted to study this molecule using the fs-VUV-VMI setup.

5.4.2 Acetylene's electronic configuration, structure and Rydberg states

Acetylene is a linear molecule in its ground state ($\tilde{X}^1\Sigma_g^+$) and belongs to the symmetry group $D_{\infty h}$ (which has in addition to its linearity a center of inversion). The two central carbon atoms are connected by a triple bond. When the molecule is in its ground state, the 14 electrons are distributed as follows:

$$(1\sigma_g)^2(1\sigma_u)^2(2\sigma_g)^2(2\sigma_u)^2(3\sigma_g)^2(1\pi_u)^4(1\pi_g)^0 \tag{5.10}$$

The first two orbitals (1σ) contain the core electrons of the molecule. The following two orbitals (2σ) form the C–H bond. The triple bond C≡C is formed by the last two occupied orbitals: $3\sigma_g$ and $1\pi_u$. When the molecule is excited, the valence electrons are promoted to the first excited states of the molecule:

$$\begin{aligned} \ldots(3\sigma_g)^2(1\pi_u)^4 \quad &\rightarrow \quad (3\sigma_g)^2(1\pi_u)^3(1\pi_g)^1 \\ &\rightarrow \quad (3\sigma_g)^1(1\pi_u)^4(1\pi_g)^1 \\ &\rightarrow \quad (3\sigma_g)^2(1\pi_u)^2(1\pi_g)^2 \end{aligned}$$

The molecule then relaxes through different degrees freedom. During the relaxation, the molecule may change its geometry, from a linear $D_{\infty h}$ geometry to planar geometries of the type C_{2h} (also called *trans*) or C_{2v} (also called *cis*). Figure 5.10 shows the different vibrational modes of the molecule in the three types of geometries. The vibrational transitions are identified by the following notation: $\nu_{n_i}^{n_f}$ where ν represents the mode of vibration for a transition occurring from the initial state i to state final state f and n_i and n_f are the number of quanta excited during the transition [24]. These notations are regularly used to specify the

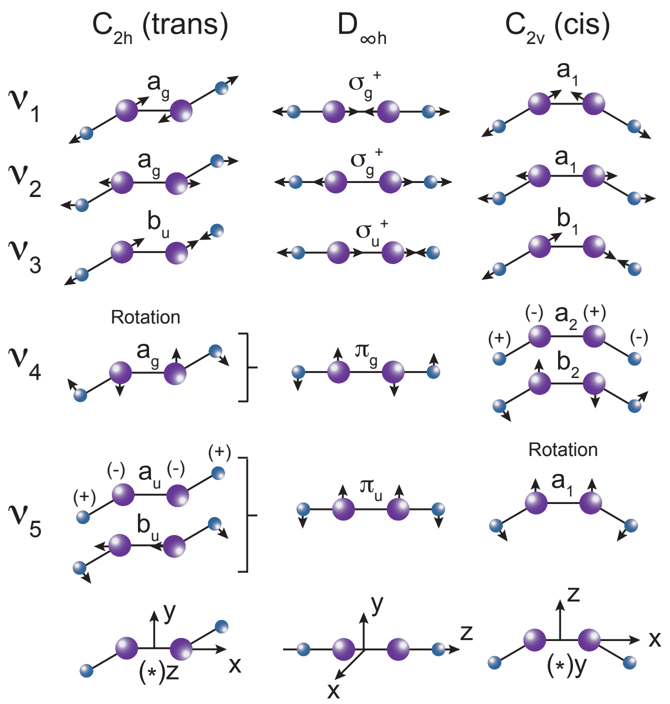

Figure 5.10: Representation of the vibrational modes of the molecule C_2H_2 in its three geometries (linear, trans and cis). Aadapted from [24].

excitations.

The excitation range investigated here is the 3d-4s Rydberg supercomplexe lying from 74500-76500 cm^{-1} (9.24-9.48 eV). Rydberg states correspond to the promotion of an electron from a valence orbital to a unbound very excited molecular orbital, labelled by an atomic character in analogy with the hydrogen Rydberg states. Since the electron is in a molecular orbital far away from the ionic core with only the Coulomb potential as an attractive strength, the Rydberg states in acetylene are built like:

$$(1\sigma_g)^2(1\sigma_u)^2(2\sigma_g)^2(2\sigma_u)^2(3\sigma_g)^2(1\pi_u)^3$$

with an extra atomic orbital (n,l,λ) where n is the main quantum number, l the angular momentum quantum number and λ the projection of the angular momentum along the C–C molecular axis. A Rydberg complex is the set of Rydberg states built from the (n,l) orbital with all the possible projection values λ $(0 \leqslant \lambda \leqslant l)$. With 10 valence electrons in C_2H_2, the corresponding atom is neon with its main quantum number of its last orbital $n_0 = 2$ and $l_0 = p$. The Rydberg electron has to be in a larger main quantum number, $n > n_0$ with $l = l + 1$ which means the first Rydberg states of C_2H_2 have the quantum number $n = 3, l = d$ and are labelled $3d - \sigma(\lambda = 0), 3d - \pi(\lambda = 1)$ and $3d - \delta(\lambda = 2)$. To take into account the scattering of this Rydberg electron at the ionic core, the quantum defect $\delta_{l,\lambda}$ is introduced and it corresponds to the change of phase of the electron wavefunction when the electron is close to the ionic core. This dephasing depends on λ. This leads to the energy for the Rydberg states given by:

$$T_{n,l,\lambda} = T_\infty - \frac{Z^2 R_y}{(n - \delta_{l,\lambda})^2} \tag{5.11}$$

where T_∞ is the converging limit for the Rydberg states, namely the ionization potential, Z the charge of the core ($Z = 1$ for a neutral molecule) and R_y the Rydberg unit of energy ($1R_y \approx 13.6$ eV, where $R_y = hcR_\infty$ with R_∞ the Rydberg constant given by $R_\infty = \frac{m_e e^4}{8\varepsilon_0^2 h^3 c}$ where m_e is the rest mass of the electron, e the elementary charge, ε_0 the permittivity of free space, h the Planck constant and c the speed of light in vacuum. Since the equilibrium geometry of $C_2H_2^+$ cation is linear and since the Rydberg electron is weakly coupled to the ionic core, the equilibrium geometry of the Rydberg states is as well linear. We will use the $D_{\infty h}$ linear geometry in the following. Taking into account a one-photon excitation (VUV excitation) or a 3-photons excitation ($3\times$ 400 nm), the electronic symmetry of the states populated by a dipolar transition from the ground electronic state has to be ungerade.

This 3d-4s supercomplexe around 9.3 eV is made of the 3d and 4s complexes that are very close energetically. It consists of the origin band vibrational excited levels of $\tilde{F}$ and $\tilde{D}$ Rydberg states with as well the $\tilde{E}$ valence state which is coupled to these Rydberg states. Both states relax mainly via predissociation [25]. The electronic transition from the ground electronic state $\tilde{X} - 1\Sigma_g^+$ to the Rydberg states are of type $3d\lambda_g \leftarrow (1\pi_u)$, with an untouched spin such that we get an electronic description of the Rydberg states as follows:

$$\begin{array}{ll} \ldots(3\sigma_g)^2(1\pi_u)^3(3d\sigma_g) : {}^1\Pi_u & \text{labelled R}''' \\ \ldots(3\sigma_g)^2(1\pi_u)^3(3d\pi_g) : {}^1\Sigma_u^+, {}^1\Sigma_u^-, {}^1\Delta_u^+ & \text{labelled R}' \\ \ldots(3\sigma_g)^2(1\pi_u)^3(3d\delta_g) : {}^1\Pi_u, {}^1\phi_u & \text{labelled R}'' \end{array}$$

The $\tilde{D}^1\Pi_u$ and $\tilde{F}^1\Sigma_u^+$ states are the first terms of the $3d\sigma_g$ and $3d\pi_g$ Rydberg series, respectively. These two Rydberg states have both a linear geometry as confirmed by Herman and Colin via the isotope comparison of the VUV spectra [24]. The $\tilde{E}$ valence state is known to be stabilized at lower energy into near bent geometry. Lundberg et al. have reported a non planar near *cis*-bent geometry for this state observed via rotational analysis of double-resonance spectra [26]. Table 5.4 gives the position and expected lifetime of the different possible populated levels. For Rydberg states, the photoelectron removed by photoionization would be produced in a wave with dominantly $l^+ = 1$ or 3, since it is a $3d$ atomic orbital Rydberg state.

Table 5.4: Lifetime of the states lying in the 3d-4s Rydberg supercomplex deduced from absorption or ionization spectra and by assuming homogeneous bandwidths. (a) [27] and (b) [28].

	state	lifetime	position (cm^{-1})
C_2H_2	$\tilde{X}$	∞	
	$\tilde{D}0_0^0$		74500
	$\tilde{E}0_0^0$		74623
	$\tilde{F}0_0^0$	90 fs (b)	74754
	$\tilde{F}4_0^2$		75578
	$\tilde{E}5_0^2$	150 fs (a)	75831
	$\tilde{E}4_0^2$	150 fs (a)	75870
	$\tilde{E}2_0^1$	120 fs (a)	76122
	$\tilde{D}2_0^1$	60 fs (a)	76279
	$\tilde{F}2_0^1$	100 fs (a)	76498

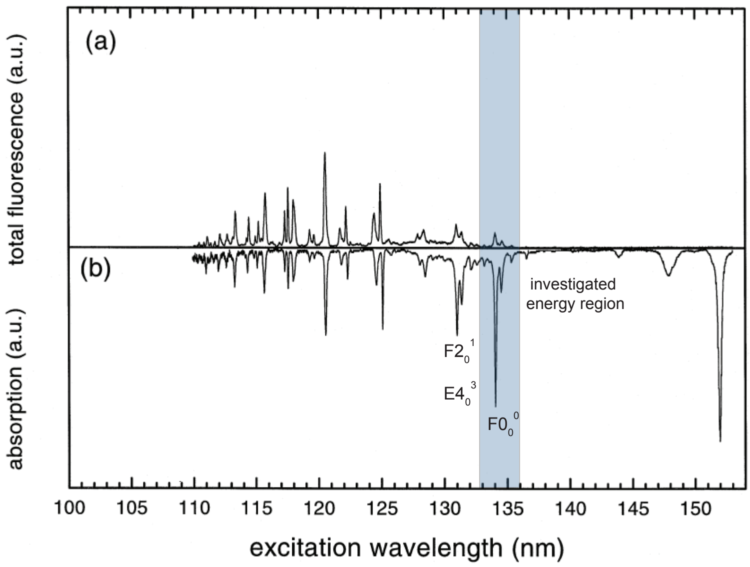

Figure 5.11: Fluorescence excitation (a) and absorption (b) spectra of acetylene in the 150 - 100 nm region, recorded at the synchrotron radiation. The blue shaded area shows the energy region investigates here. Adapted form[31].

5.4.3 The spectroscopy of acetylene

Photoabsorption of acetylene starts at 240 nm with the transition to the first excited state A_1A_u. As stated before the spectroscopy of acetylene is quite rich and different studies have revealed the presence of many absorption bands, ranging from 240 nm (5.17 eV) up to the ionization limit, located at 108.8 nm (11.4 eV) [12, 28, 29]. The excitation through the first bands usually leads to a equilibrium geometry of cis or trans while the excitation through the higher energy bands (excitation to Rydberg states) tends to involve the linear geometry. The different dissociation channels of acetylene and their energy occurrence levels are [27]:

$$\begin{aligned}
C_2H_2+\hbar\nu &\rightarrow H+C_2H(\tilde{X}^2\Sigma^+) && D_0=5.71\,\text{eV} && (5.12a)\\
&\rightarrow H+C_2H(\tilde{A}^2\Pi) && D_0=6.16\,\text{eV} && (5.12b)\\
&\rightarrow H_2+C_2(\tilde{X}^2\Sigma^+) && D_0=6.2\,\text{eV} && (5.12c)\\
&\rightarrow 2CH(\tilde{X}^2\Pi) && D_0=9.9\,\text{eV} && (5.12d)
\end{aligned}$$

It has been found that the channel 5.12a is the predominant process when the excitation takes place through the first absorption bands (between 240 nm and 190 nm) [30]. For higher energy excitation, it is observed that the probability of cleavage via the channel 5.12a is increased.

Figure 5.11 shows a panoramic absorption spectrum of C_2H_2 in the bottom panel and the corresponding excitation spectrum in the top panel between 153 and 102 nm [31]. The fluorescence signal in this excitation range is produced by fragment C_2H ($\tilde{A}^2\Pi$) and the spectrum shows the emerging channel 5.12b as function of the excitation energy. Except for a continuum signal arising in the 132 nm region, this spectral region exhibits the prominent s- and d-Rydberg series of acetylene converging to the first ionization potential, where the energy position of the

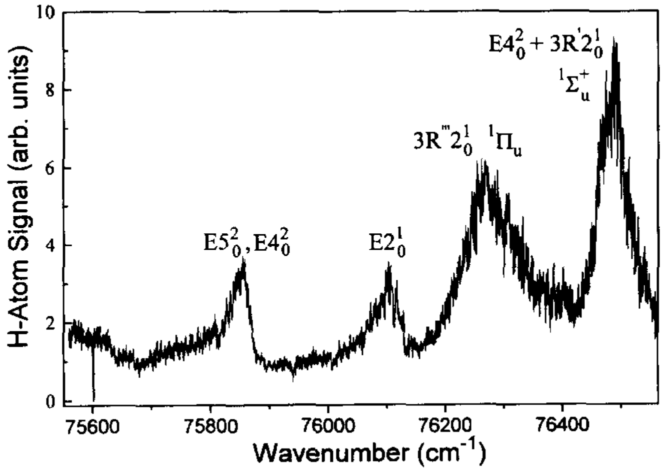

Figure 5.12: H atom fragment spectra from VUV photolysis of C_2H_2 in the energy region 75600 cm^{-1} (9.37 eV) to 76600 cm^{-1} (9.5 eV). Adopted from [27].

$v = 0$ $\tilde{X}^2\Pi_u$ ground state of the $C_2H_2^+$ ion is indicated by a dashed line.

However, despite all the studies on acetylene, some processes remain uncertain, in particularly in the VUV spectral region as the technical requirement to produce photons in this area are quite complicated. The ideal experiment would be a tunable VUV beam as pump pulse and an intense VUV beam as probe pulse to detect the fragments C_2H and H.One way around this problem is to use a multiphoton excitation scheme via the resonant states using the technique of REMPI. This approach has shown its success in studying the vibrational spectroscopy of acetylene [28], but keeps difficult for dynamic studies using the femtosecond pump-probe technique. Indeed the numerous resonances encountered can cause complications when probe photons come into resonance with a process of the pump or vice versa. Tunable wavelength sources (for instant like NOPA) may allow to choose the pump and probe wavelength wisely but this technique still has its limitations as the photon intensities achieved are small and most of the time not sufficient for multiphoton excitation.

There have been of course also some experiments in the field of VUV to investigate in more detail the different reaction pathways. Löffler et al. measured the absorption bandwidth of the first two channels for several vibrational excitation states, using a VUV excitation and collecting the amount of H fragments produced (see Figure 5.12) [27]. Their technique is based on the excitation between 121 and 132 nm where the production of the radiation is done by four-wave mixing in a cell of krypton and the detection of the photofragment H is also done with a VUV radiation. Using a similar technique, Zhang et al. were able to measure the translational energy distributions of the H fragments for two different excitations at 148.3 and 151.8 nm [32]. Measuring as well the anisotropy parameter for the two excitations they demonstrate that the dissociation is occurring on different timescales via two channels.

In the time domain, Zamith et al. have made a VUV pump UV probe study [33]. The excitation was done using one photon in a region between 134 and 131 nm, in which the Rydberg super-complex 4s–3d is located. This excitation region consists of several absorption bands of which some are connected to states which will eventually lead to dissociation (predisso-

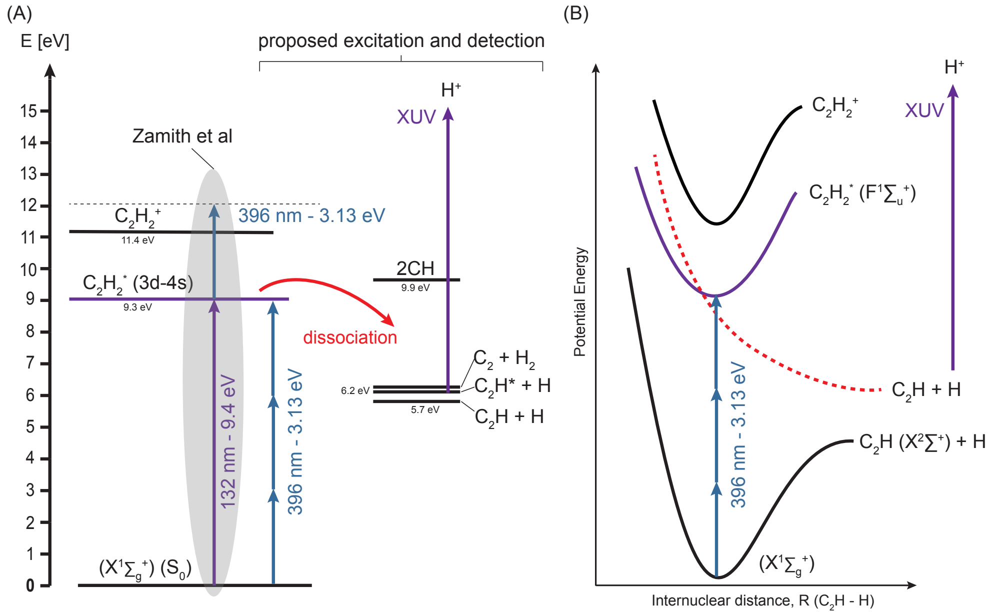

Figure 5.13: (A) C_2H_2 excitation scheme used in this work with comparison to the one Zamith et al. used before. (B) schematic potential energy diagram with the excitation form the ground state $\tilde{X}^1\Sigma_u^+$ to the Rydberg state $\tilde{F}^1\Sigma_u^+$ (purple) and the dissociative state which is coupled to the Rydberg state (dashed red line).

ciative states). To generate the pump beam at 9.4 eV (∼ 132 nm), the third harmonic of 400 nm was used via high-order harmonic generation in a gas jet. As probe beam to ionize the excited molecule, another 400 nm pulse is used. The dynamics of the excited state are analyzed through time-resolved photoelectron spectroscopy (PES) and ion spectrometry. There are only two dissociation channels open at the 9.4 eV pump energy [31]. Both lead to C_2H radical formation in the $A^2\Pi$ electronic state or the $X^2\Sigma$ ground state with 0.45 eV separation between the electronic origins [34]. However, the dynamics here are probed only through ionization of the parent molecule. Our goal here was to probe the dissociation dynamics of the fragments by directly ionizing the fragments H or C_2H. This would allow to measure the energy distributions of the different fragments, coming from the same excited state.

5.4.4 Experimental excitation scheme and experimental realization

For this we proposed a complementary study using the same excitation of acetylene to the complex 3d–4s with a time-resolved detection of the photofragments using the new fs-VUV-VMI spectrometer. The VUV radiation is not used to initiate the excitation but to ionize the fragments. The two different excitation schemes are shown in Figure 5.13. With only a single harmonic source, we attempted to populate the Rydberg complex through the band $\tilde{F}_0^0$ located at 133.8 nm using a selective three-photon transition with a 3 nm narrow bandwidth centered at 401.4 nm. This band has the advantage to be intense while remaining relatively isolated from other bands, allowing easy excitation and assuring excitation of only one state at a time (see Figure 5.17). According to Blanchet et al. this band has a spectral bandwidth at FWHM of 0.15 nm which corresponds to a lifetime of 90 fs (assuming a homogeneous spectral band) which is within our temporal resolution. As indicated before the nomenclature 0_0^0 means that

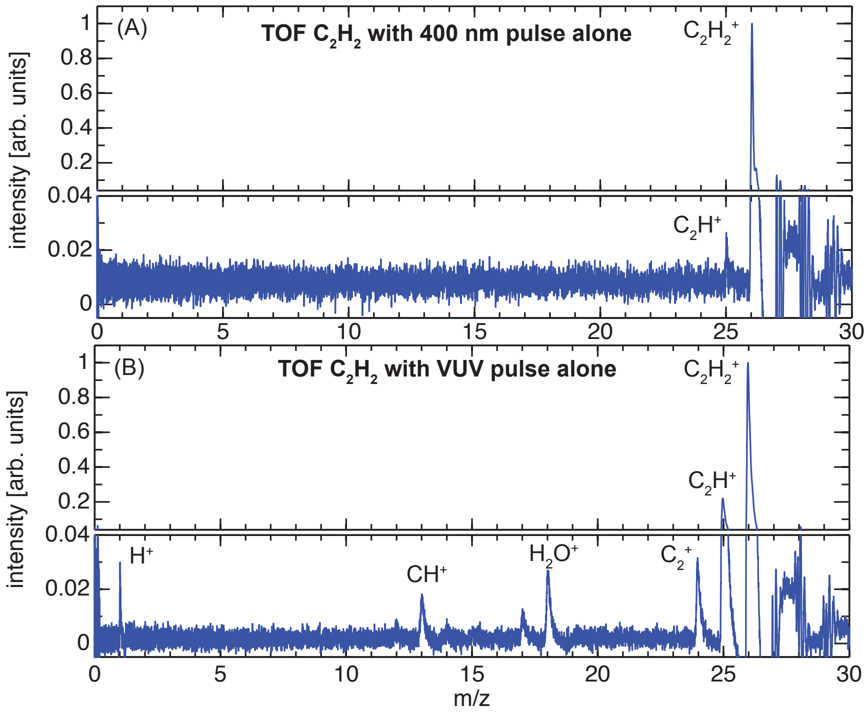

Figure 5.14: Time-of-flight mass spectrum of C_2H_2 recorded with fs-VUV-VMI spectrometer using 400 nm alone (A) and with the VUV pulse alone (B). The y-axis is normalized to $C_2H_2^+$ and broken into 2 parts with different scaling to visualize the small peaks besides $C_2H_2^+$ which are only around 2-4%.

no vibrational quanta is excited. In addition, the state $\tilde{F}$ is a binding state with a $^1\Sigma_u^+$ symmetry which corresponds to a linear equilibrium geometry $D_{\infty h}$. The dissociation evolved therefore by coupling with another potential surface. Considering the previous work and the excitation pattern, the potential energy curves may be represented as in Figure 5.13 (B). The energies of the states are represented qualitatively along the interatomic distance R between the hydrogen radical and C_2H fragment.

Experimental realization and encountered problems

The setup for this experiment is similar to the one already shown in Figure 5.1 and used in Section 5.3.3 for the argon photoelectron test to characterize the new setup. The experimental principle is as mentioned before based on a pump-probe study using a UV pump and a VUV probe pulse. After the three-photon excitation through the band $F0_0^0$, the molecule moves towards dissociation and the dissociation fragments are then ionized by the VUV pulse generated with high-order harmonic generation. The ions or photoelectrons are then detected using the VMI spectrometer at different pump-probe delays.

The experimental realization took place in two main phases, with regard of the generating of the VUV beam. In the first phase we generated harmonics using the fundamental wavelength at 800 nm. Unfortunately this experience was more difficult than anticipated. We were not able to detect any H fragments coming form the dissociation with three photons at 400 nm. Finding and adjusting the spatial overlap and the time overlap was only possible by switching off the HHG part and using the 800 nm which are transmitted through the experimental setup. After adjusting the 800 plus 400 nm beams we switched back to HHG. But even with this method we were not sure if the spatial overlap between the VUV and the 400 nm beam was correct as we had no possibility to detect a cross-correlation between the VUV and the 400 nm pulse. To be able to at least be sure that we have the right spatial overlap and the correct time overlap we decided to generate harmonics as well in 400 nm to be able to use the technique of the sidebands as introduced on argon in the section before. The big advantage of this generation scheme is the fact that at zero time delay, the photoelectron spectrum from the ionization of the patent molecule (C_2H_2) consists not only of the peaks from the harmonics, but also of the side-bands. With these sideband it is easier to find the time overlap and to adjust the spatial overlap between the VUV beam and the 400 nm beam directly on the signal. However, note that the third harmonic of 400 nm is resonant with the state $\tilde{F}^1\Sigma_u^+$, and that two excitation patterns are now possible. Even though we were certain now that we had a correct spatial overlap and a correct time overlap we still weren't able to detect an pump-probe signal on the H fragment. Note that as can be seen in the mass spectrum recorded on acetylene with a VUV beam and the 400 nm in Figure 5.14, we are able to detect the parent ion $C_2H_2^+$ with 400 nm alone and with the harmonic spectrum alone we are detecting $C_2H_2^+$, C_2H^+, C_2^+, CH^+ and H^+. But apart from C_2H^+ with 20% the other fragments are only 2-4%.

However, if the dissociation takes place, we should see the fragments H^+ and C_2H^+ appearing and observe the amount of $C_2H_2^+$ ions decrease over time. None of the three aspects mentioned were observed even not by switching off the harmonic source and using a 800 nm multiphoton ionization detection. We also tried to search the VMI images for any trace of ions having a non-zero kinetic energy. For this, we time gated the VMI by pulsing the detector at the time where we expect the H^+ or the C_2H^+ fragment as done in Chapter 2 for ClN_3. This way we could increase the MCP voltages without being saturated by the parent ion signal $C_2H_2^+$. However, once again, we did not observe any significant measurable fragment amounts with none-zero kinetic energy. We also tried different mixtures of acetylene, from pure acetylene over 15%, 6% and 4% of acetylene in neon to prevent the formation of clusters. We varied as well the pump intensity and the laser bandwidth to be sure that we are not populating the wrong state.

5.4.5 Time-resolved photoelectron spectrum of acetylene

Previous experiments did not yield any results concerning the dissociation of the molecule after excitation at 401 nm, and we decided to detect at least the photoelectrons of C_2H_2 with the sideband detection. The photoelectron spectrum of acetylene recorded with a harmonic spectrum generated at 401 nm plus an extra 401 nm pulse is shown in Figure 5.15, where (A) shows the Abel inverted image and (B) the energy distribution after integration over the angle. This spectrum is composed of three main components, corresponding to the peak of side-band SB4 with the absorption of the harmonic 3 (or 5) plus (emission of) a pump photon at 400 nm, the photoabsorption peak from the 5th harmonic and the photoabsorption peak of harmonic 7. Sideband SB6 is not visible. Of course the sideband signal can not only come from the interaction of the VUV pulse and the 401 nm but from the 400 nm alone via ATI. In this case

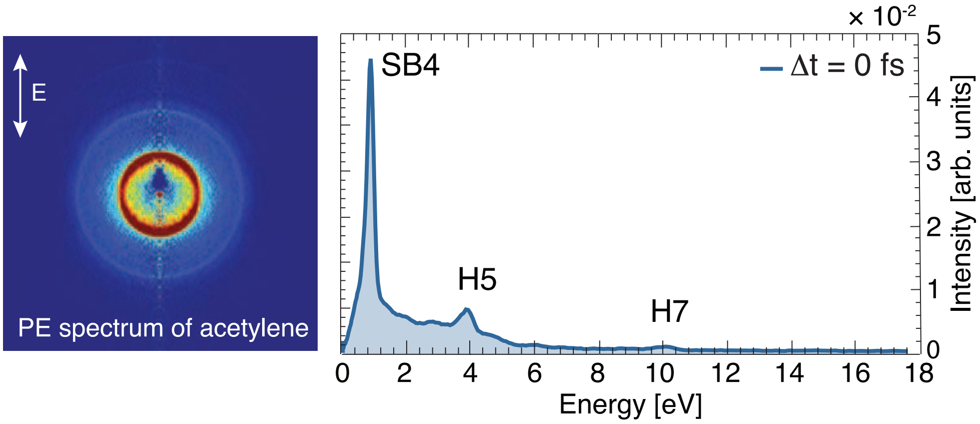

Figure 5.15: Photoelectron spectrum of acetylene obtained with the harmonic spectrum generated at 400 nm in argon plus an extra 400 nm beam, visible are harmonic 5 and 7 and as well the side bands produced by harmonic 3 and 5 (SB4).

we shouldn't observe any dynamics. Note that the peak at the position of the sideband 4 is particularly intense compared to the other peaks, which is probably due to the resonance at 9.3 eV for acetylene, namely 3 + 1 photoionization.

The time-resolved photoelectron dynamics in VUV pump 400 nm probe as function of the pump-probe delay is shown in Figure 5.16. The signals are normalized to the largest signal, which is SB4. The pump-probe signals we were able to measure are for SB4 12% and for H5 and H7 only 2.6% and 0.44%, respectively. One would normally expect, for the harmonic peaks in the photoabsorption spectra and as well for the sidebands, a cross-correlation signal between pump and probe pulses. However, similarly to the experiment in argon in the section before, a clear asymmetry with respect to time zero is observed on all measured signals as can be seen in Figure 5.16 (B). For SB4 it is clear, that the asymmetry is explained, as in the previous case on argon by the excitement of the Rydberg state with a certain lifetime. It is the 3rd harmonic (centered around 9.3 eV) which is directly resonant with the Rydberg state complex of acetylene around 9.3 eV. This means we are in a situation where harmonic 3 plays the role of the pump at 9.3 eV and the 401 nm beam takes the role of the probe pulse. This is exactly the excitation scheme used by Zamith et al. [33]. To estimate the lifetime of this state, the data is fitted as done on argon with a combination of a cross-correlation function and an exponential decay function like Eq. (5.7). The cross-correlation time is determined on SB8 of argon recorded on the same day in the same conditions as acetylene, to be 137 ± 4 fs at FWHM. This is slightly larger than the cross-correlation time shown in Figure 5.8 because of the change in BBO crystal. Indeed, the bandwidth has been reduced to 3 nm instead of 7 nm, in order to be more selective. The 3 nm corresponds to a theoretical duration of 85 fs. The emerging bump at positive delays around Δt = 120 fs is a signature of a third order dispersion (TOD measured in fs^3) in the crystal. The lifetime is extracted to be 195 ± 17 fs. To assign the excited states in resonance with harmonic 3, the photoabsorption spectrum of acetylene in Figure 5.17 is represented. We note that the spectrum of harmonic 3 spans over a series of absorption bands, including the $F0^0_0$, several bands of the E series and the $D0^0_0$. According to this figure, we can assume that the $F0^0_0$ is the main one populated by harmonic 3. In fact,

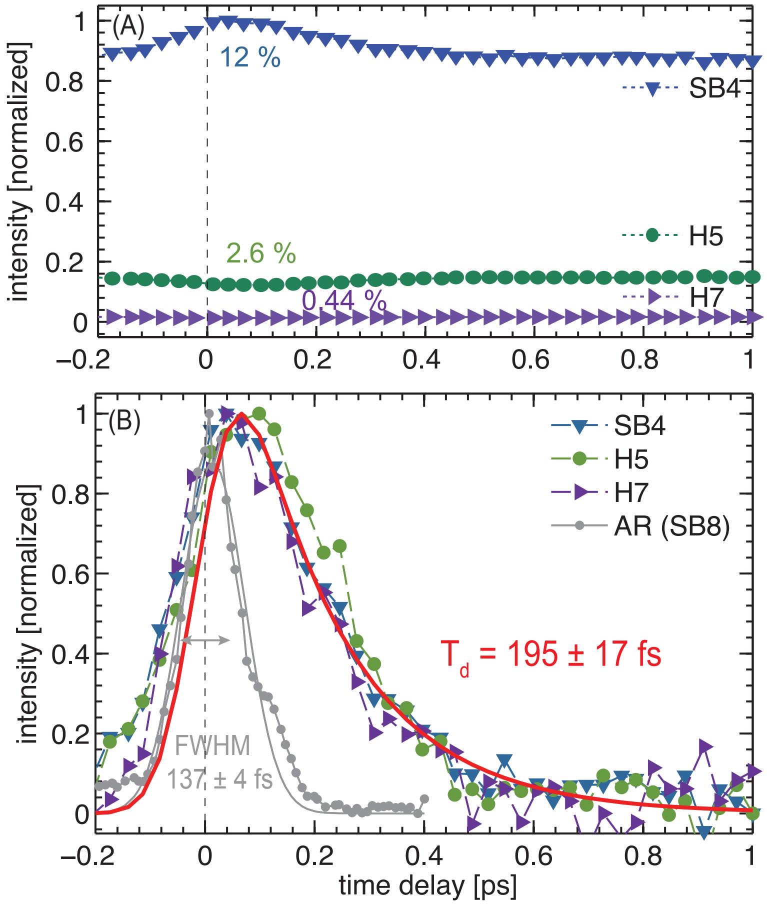

Figure 5.16: Integrated photoelectron signal of SB4, H5 and H7 in C_2H_2 as function of the pump-probe delay between the VUV pulse and the 401 nm pulse. (A) Yield of SB4, H5, H7 normalized to the largest signal (SB4) (The percentage numbers show the pump-probe signal is rather tiny compared to the measured backgrounds). (B) shows the integrated yield of SB4, H5 and H7 normalized to one in comparison to the signal obtained on SB8 in argon (grey line) under similar conditions. Note that the H5 and H7 profiles have been inverted.

this band not only has the largest absorption cross-section among the covered bands within the spectrum of harmonic 3, but it is also one of the bands on which the spectrum of harmonic 3 is more centered. The dynamics observed on the photoelectron peaks here corresponds probably to the lifetime of this excited state. However, the relaxation time is not measured in accordance with the one deduced by Blanchet et al. from the REMPI absorption spectrum which specified a relaxation time close to 90 fs [28]. Löffler et al. have reported by measuring the H fragment absorption spectrum a relaxation time around 150 fs for the bands $E4_0^2$ and $E5_0^2$ [35], which are closer to the lifetime we measured and which are covered by the bandwidth of our harmonic pulse. Zamith et al. measured by time-resolved photoion detection 219 ± 30 fs for the $F4_0^2$ and 171 ± 25 fs for the $E4-5_0^2$ [33]. So 195 ± 17 fs for the $F0_0^0$ is a relevant value and not totally out of range.

On the other hand, we recall that the dynamic we see through these photoelectron signals can not be linked to the dynamics of the dissociation, since we measure a signal from the parent molecules. In contrast to argon, harmonic 5 and 7 show exactly the same time dependency as SB6. Unfortunately, as it was the case in argon, there is so far no obvious explanation for the

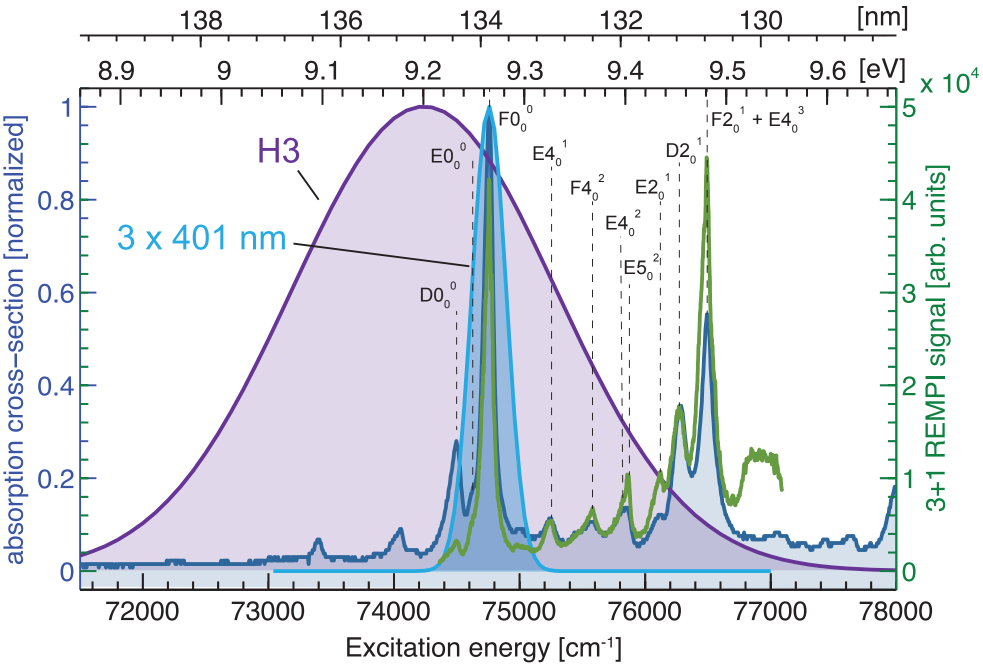

Figure 5.17: Spectrum of harmonic 3 (purple) overlapped with the absorption cross-section of acetylene (blue) obtained in the synchrotron in this energy region [12] and the 3+1 REMPI signal (green) [28]. Also shown is the spectrum of the 401 nm (3 photons at 401 nm) in light blue.

time dependency observed on the depletion of these harmonics. Similarly, if our interpretation of the dynamics observed in argon is valid, the time-resolved dynamic observed on H5 and H7 reflects the fact that the excited molecules relax to other electronic states with energies E_n that again have to fullfill the energy conservation given by $E_n + p \times E_{401nm} = E_{H5}/E_{H7}$. However, this means that the contribution from molecules moving towards dissociation is negligible. This consideration seems to be an argument for the fact that the excitement over the band $F0_0^0$ does lead to very low dissociation probability, and the relaxation evolves through vibrational excitation. This statement remains very suggestive and has to be considered with precaution. It would be interesting to verify whether the observed relaxation is due to the excitation via the band $F0_0^0$ by slightly moving the harmonic spectrum to lower energies, so that it no longer includes the E state series. This might be achieved by playing very lightly on the phase-matching angle of the doubling crystal, being careful not to lose too much doubling efficiency in order to maintain enough intensity for the HHG. This way one could also see if the transients observed on H5 and H7 depend on which states are involved in this broadband exciatation.

5.4.6 Conclusion

We have attempted to study the photodissociation of acetylene at 9.3 eV using the new the fs-VUV-VMI spectroscopy setup. Two different approaches were used. Initially, we employed a three-photon pump transition centered at 401.3 nm and a probe step using the harmonic spectrum to ionize the dissociation fragments. However, no dissociation fragments were detected with this method. It is still unclear as to why the experiment did not work. On one hand, it is possible that our harmonic photon flux is insufficient to probe the dissociation fragments with low absorption cross-sections, as is the case for the hydrogen fragments, which are moreover, the results from low efficiency processes (low dissociation efficiency). On the other hand, it does not exclude that we do not control the pump excitation step precise enough. Although we excite the molecule at an absorption band with a very high absorption cross-section (a three-photon resonance), it is possible that we do not leave any population in the excited state due to a single photon transition from this state to the ion continuum. The dissociation rate of $F0_0^0$ might not be sufficient to study the photodissociation via this state. The employed type of multiphoton excitation scheme is particularly problematic, especially when the resonant transition involves a relatively large number of photons compared to the transition leading to ionization. This illustrates the relevance of photon sources in the VUV range. Indeed, making a one-photon transition from the ground state to the state of interest brings the focus on the excitation without risking ionization of the molecule by a transition involving a second photon. This aspect we tried to develop in the second experimental approach, by exciting the molecule acetylene by a one-photon transition using the third harmonic generated at 400 nm. A second pulse at 400 nm was used to probe the dissociation of the molecule. Once again, no trace of ionized fragments was found. The analysis of the photoelectron spectra as a function of the pump-probe delay revealed, nevertheless, the femtosecond dynamics of the relaxation of the excited states brought into play. However, given the large spectral bandwidth of the 3rd harmonic, it is difficult to assign the states involved. This large spectral bandwidth is the major drawback of HHG as a source of VUV photons for atomic and molecular spectroscopy.

Recently, a novel scheme for HHG based on using two gas cells has been demonstrated [36]. This allows the production of fs-VUV pulses by HHG generation in the nJ/p regime. Such high energy pulses could overcome the issue of low photon flux and could prove to be the key to ion detection for the fs-VUV-VMI setup. The principle is based on using below-threshold harmonics, generated in a ‘seeding cell’, to boost the HHG process in a ‘generation cell’, placed further downstream in the focused laser beam. By modifying the fundamental driving field, these low-order harmonics alter the ionization step of the nonlinear HHG process and it has been shown that the HHG process is boosted by a factor of 7 in neon.

Furthermore, to increase the VUV photon flux in the monochromator configuration we could replace the gold grating by a aluminium grating which would increase the monochromator transmission by a factor of 10 from 1×10^{-3} to 1×10^{-2}. In addition, replacing the B_4C focussing mirror with an aluminium mirror would lead to monochromator transmission of about 3×10^{-2}. Howeber, using aluminium would mean we cut all harmonics above H10. A pricier alternative would be to invest in a new diffraction grating. To increase the HHG efficiency produced with 400 nm the plan is also to generate 400 nm under vacuum with a metallic focusing mirror to focus the 400 nm in a cell. This will result in a shorter transform-limited pulse at 400 nm and therefore increase the efficiency of the HHG process.

There are two key drawbacks on the present experimental setup, which should be implemented. The first one, the real duration of the VUV pulse cannot be measured. Indeed, it is currently assumed that the duration of the VUV pulse is around half of the duration of the fundamental pulse. This could mean for harmonics generated at 400 nm a VUV pulse with a duration of around 20 fs. However, to be able to measure this duration, an even shorter pulse is required. This could be achieved by first broadening an 800 nm pulse via a with neon filled capillary and afterwards recompressing it with chirped mirrors. Unfortunately, such equipment was not available and has not been implemented on the experimental apparatus. The second drawback is that it is not possible to investigate the quality of the VUV spatial mode. We examined only the 400 nm waist position, in order to place the center of the VMI directly at this position. Later on the VMI position was optimized at the multiphoton signal at 400 nm. As mentioned before, the impossibility to adjust the toroidal mirror under vacuum has to be overcome in order to adjust the VUV spatial mode directly. For this particular optomechnics are required to control the mirror positions from outside and to be able to adjust the VUV spatial mode based for instance on detecting the waist of the VUV pulse by the luminescence emitted by a crystal. With this, the pump-probe volume could be optimized, leading to a larger pump-probe contrast compared to the unsatisfactory 10% observed here.

Recently the fs-VUV-VMI facility has been used to study fenchone to investigate the circular dichroism of the photoelectons when the VUV light is produced in SF_6. For this experiment the source has been changed for a needle placed between the repeller and extractor plate. Compared to the previous experiments using a pulsed molecular beam source place 12 cm away from the VMI center, the signals were multiplied by 100. Pump-probe experiments with such source developments are ongoing.

References

[1] HIPPLER, M and PFAB, J. *Detection and Probing of Nitric-Oxide (No) by 2-Color Laser Photoionization (Rempi) Spectroscopy on the a[-X Transition*. Chem. Phys. Lett. **243**:5-6 500–505 (1995) (cited p. 158).

[2] Mairesse, Y, Gobert, O, Breger, P, Merdji, H, Meynadier, P, Monchicourt, P, Perdrix, M, eres, PS, and 'e, BC. *High Harmonic XUV Spectral Phase Interferometry for Direct Electric-Field Reconstruction*. Phys. Rev. Lett. **94**:17 173903 (2005) (cited p. 158).

[3] Frassetto, F, Bonora, S, VILLORESI, P, Poletto, L, Springate, E, Froud, CA, Turcu, ICE, Langley, AJ, Wolff, DS, Collier, JL, Dhesi, SS, and Cavalleri, A. *Design and characterization of the XUV monochromator for ultrashort pulses at the ARTEMIS facility*. Optical Engineering + Applications **7077**: pages (2008) (cited p. 158).

[4] Frassetto, F, Cacho, C, Froud, CA, Turcu, ICE, Villoresi, P, Bryan, WA, Springate, E, and Poletto, L. *Single-grating monochromator for extreme-ultraviolet ultrashort pulses*. Opt. Express **19**:20 19169 (2011) (cited p. 159).

[5] Ito, M, Kataoka, Y, Okamoto, T, Yamashita, M, and Sekikawa, T. *Spatiotemporal characterization of single-order high harmonic pulses from time-compensated toroidal-grating monochromator*. Opt. Express **18**:6 6071–6078 (2010) (cited p. 159).

[6] Wernet, P, Gaudin, Jm, Godehusen, K, Schwarzkopf, O, and Eberhardt, W. *Femtosecond time-resolved photoelectron spectroscopy with a vacuum-ultraviolet photon source based on laser high-order harmonic generation*. Rev. Sci. Instr. **82**:6 pages (2011) (cited p. 159).

[7] Ruf, H. *Dynamique moléculaire par imagerie attoseconde*. PhD thesis. Universite Bordeaux 1, 2012 (cited p. 161–163).

[8] Bourassin-Bouchet, C, Mang, MM, Delmotte, F, Chavel, P, and Rossi, S de. *How to focus an attosecond pulse*. Opt. Express **21**:2 2506–2520 (2013) (cited p. 162, 163).

[9] Chan, WF, Cooper, G, Guo, X, Burton, GR, and Brion, CE. *Absolute optical oscillator strengths for the electronic excitation of atoms at high resolution. III. The photoabsorption of argon, krypton, and xenon*. Phys. Rev. A **46**:1 149–171 (1992) (cited p. 166).

[10] Palenius, H, Kohl, J, and Parkinson, W. *Absolute measurement of the photoionization cross section of atomic hydrogen with a shock tube for the extreme ultraviolet*. Phys. Rev. A **13**:5 1805–1816 (1976) (cited p. 166).

[11] Jenkin, ME, Murrells, TP, Shalliker, SJ, and Hayman, GD. *Kinetics and product study of the self-reactions of allyl and allyl peroxy radicals at 296 K*. J. Chem. Soc. Fara. Trans. **89**:3 433 (1993) (cited p. 166).

[12] Suto, M and LEE, LC. *Quantitative photoexcitation and fluorescence studies of C2H2 in vacuum ultraviolet*. J. Chem. Phys. **80**:10 4824 (1984) (cited p. 166, 177, 181, 188).

[13] Luria, K, Christen, W, and Even, U. *Generation and Propagation of Intense Supersonic Beams*. J. Phys. Chem. A **115**:25 7362–7367 (2011) (cited p. 166, 167).

[14] Paul, PM, Toma, ES, Breger, P, Mullot, G, Balcou, P, Muller, HG, and Agostini, P. *Observation of a Train of Attosecond Pulses from High Harmonic Generation*. Science **292**:5522 1689–1692 (2001) (cited p. 169).

[15] Varjú, K, Johnsson, P, Lopez-Martens, R, Remetter, T, Gustafsson, E, Mauritsson, J, Gaarde, MB, Schafer, KJ, Erny, C, and Sola, I. *Experimental studies of attosecond pulse trains*. Laser Phys. **15**:6 888–898 (2005) (cited p. 169).

[16] YOSHINO, K. *Absorption Spectrum of the Argon Atom in the Vacuum-Ultraviolet Region*. J. Opt. Soc. Am. **60**:9 1220 (1970) (cited p. 172, 175, 176).

[17] Baig, M, Ahmad, S, Connerade, J, Dussa, W, and Hormes, J. *Overlapping sequence of doubly excited series in the vuv spectrum of argon*. Phys. Rev. A **45**:11 7963–7968 (1992) (cited p. 175).

[18] Eichmann, U, Nubbemeyer, T, Rottke, H, and Sandner, W. *Acceleration of neutral atoms in strong short-pulse laser fields*. Nature **461**:7268 1261–1264 (2009) (cited p. 177).

[19] Morales, F, Richter, M, Patchkovskii, S, and Smirnova, O. *From the Cover: Imaging the Kramers-Henneberger atom*. Proceedings of the National Academy of Sciences **108**:41 16906–16911 (2011) (cited p. 177).

[20] Kistiakowsky, G. *On the Ultraviolet Absorption Spectrum of Acetylene*. Phys. Rev. **37**:3 276–278 (1931) (cited p. 178).

[21] Price, W. *The Absorption Spectra of Acetylene, Ethylene and Ethane in the Far Ultraviolet*. Phys. Rev. **47**:6 444–452 (1935) (cited p. 178).

[22] Bernstein, MP, Dworkin, JP, Sandford, SA, and Cooper, GW. *Racemic amino acids from the ultraviolet photolysis of interstellar ice analogues*. Nature (2002) (cited p. 178).

[23] Caro, G, Meierhenrich, UJ, Schutte, WA, and Barbier, B. *Amino acids from ultraviolet irradiation of interstellar ice analogues*. Nature (2002) (cited p. 178).

[24] Herman, M and Colin, R. *The absorption spectra of C_2H_2, C_2D_2, and C_2HD in the region 1260 to 1370 Å*. J. Mol. Spec. **85**:2 449–461 (1981) (cited p. 178–180).

[25] Kono, M, Hoshina, K, and Yamanouchi, K. *Photofragment emission yield spectroscopy of acetylene in the $\tilde{D}^1\Pi_u$, $\tilde{E}^1A$, and $\tilde{F}^1\Sigma_u^+$ states by vacuum ultraviolet and infrared vacuum ultraviolet double-resonance laser excitations*. J. Chem. Phys. **117**:3 1040 (2002) (cited p. 180).

[26] Lundberg, JK, Jonas, DM, Rajaram, B, Chen, Y, and Field, RW. *Rotationally resolved ultraviolet–ultraviolet double resonance study of the nonplanar E state of acetylene*. J. Chem. Phys. **97**:10 7180–7196 (1992) (cited p. 180).

[27] Löffler, P, Lacombe, D, Ross, A, Wrede, E, Schnieder, L, and Welge, KH. *Photofragment action spectroscopy of the acetylene molecule in the vacuum ultraviolet*. Chem. Phys. Lett. **252**:5-6 304–310 (1996) (cited p. 180–182).

[28] Blanchet, V, Boyé, S, Zamith, S, Campos, A, Girard, B, Liévin, J, and Gauyacq, D. *(3+1)-resonantly enhanced multiphoton ionization-photoelectron spectroscopy of the (3d-4s) supercomplex of acetylene: The geometry of the E state revisited through experiment and theory*. J. Chem. Phys. **119**:7 3751 (2003) (cited p. 180–182, 187, 188).

[29] Van Craen, JC, Herman, M, Colin, R, and Watson, J. *The $\tilde{A}-\tilde{X}$ band system of acetylene: Analysis of medium-wavelength bands, and vibration-rotation constants for the levels $n\nu_3'$ (n = 4-6), ν_2' + $n\nu_3'$ (n = 3-5), and ν_1' + $n\nu_3'$ (n = 2,3)*. J. Mol. Spec. **111**:1 185–197 (1985) (cited p. 181).

[30] Wodtke, AM and Lee, YT. *Photodissociation of acetylene at 193.3 nm*. J. Phys. Chem. **89**:22 4744–4751 (1985) (cited p. 181).

[31] Campos, A, Boyé, S, Bréchignac, P, Douin, S, Fellows, C, Shafizadeh, N, and Gauyacq, D. *Vacuum–ultraviolet photodissociation of C2H2 via Rydberg states: a study of the fluorescent pathways*. Chem. Phys. Lett. **314**:1-2 91–100 (1999) (cited p. 181, 183).

[32] Zhang, Y, Yuan, K, Yu, S, Parker, DH, and Yang, X. *Photodissociation dynamics of acetylene via the $\tilde{C}\ ^1\Pi_u$ electronic state*. J. Chem. Phys. **133**:1 014307 (2010) (cited p. 182).

[33] Zamith, S, Blanchet, V, Girard, B, Andersson, J, Sorensen, SL, Hjelte, I, Björneholm, O, Gauyacq, D, Norin, J, Mauritsson, J, and L'Huillier, A. *The predissociation of highly excited states in acetylene by time-resolved photoelectron spectroscopy*. J. Chem. Phys. **119**:7 3763–3773 (2003) (cited p. 182, 186, 187).

[34] Hsu, YC, Chen, FT, Chou, LC, and Shiu, YJ. *193.3 nm photodissociation of acetylene: Nascent state distribution of CCH radical studied by laser-induced fluorescence*. J. Chem. Phys. **105**:20 9153 (1996) (cited p. 183).

[35] Löffler, P, Wrede, E, Schnieder, L, Halpern, JB, Jackson, WM, and Welge, KH. *Dissociation dynamics of acetylene Rydberg states as a function of excited state lifetime*. J. Chem. Phys. **109**:13 5231 (1998) (cited p. 187).

[36] Brizuela, F, Heyl, CM, Rudawski, P, Kroon, D, and Rading, L. *Efficient high-order harmonic generation boosted by below-threshold harmonics : Scientific Reports : Nature Publishing Group*. Scientific Reports (2013) (cited p. 189).

Conclusion and Perspectives

The femtosecond time-resolved molecular spectroscopy studies treated in this manuscript included the photodissociation of chlorine azide (ClN_3) in two excitation regimes using femtosecond velocity-map imaging (VMI), a phase resolved Raman pump high-order harmonic generation (HHG) probe study of sulfur hexafluoride (SF_6) and last but not least the development of of a new femtosecond XUV-VMI spectrometer to use high-order harmonic generation as a XUV photon source for pump-probe experiments.

The femtosecond time-resolved photodissociation study of ClN_3 using a velocity-map imaging spectrometer presented in Chapter 2, was able to detect for the first time the fragment N_3 directly in two major energy regions, using a dissociation energy of 4.67 eV (268 nm), to access the region where linear N_3 is produced and of 6.13 eV (201 nm), where cyclic N_3 is produced. The dissociation time was determined to be 262 ± 38 fs and 178 ± 22 fs for linear and cyclic N_3, respectively. The energy distribution balance confirms that at 6 eV, N_3 and Cl are produced in agreement with the cyclic N_3 energy threshold. The angular distribution revealed at large pump-probe delays a β_2 parameter of 1.64 ± 0.06 and 0.27 ± 0.05 for linear and cyclic N_3, respectively which are in agreement with previous measurements in the ns-time regime, detecting only the Cl fragment via a REMPI transition. In addition, the time-resolved data reveals that these values are not reached immediately. It takes 170 ± 45 fs and 136 ± 7 fs for the linear and cyclic N_3 fragment, respectively, to reach the long delay limits. The $\beta_2 \sim 0.3$ angular distribuiton obtained on a shorter timescale than the rotational period of the parent ion, lead us conclude that N_3 is indeed produced in its cyclic form and the isotropic angular distribution is a signature of a drastic rearrangement during the dissociation process with a huge change of the N_3–Cl center of mass.

Chapter 3 presented the tetrathiafulvalene (TTF, $C_6H_4S_4$) electronic relaxation study by time resolved mass and photoelectron spectroscopy. The pump wavelength has been varied from 322 nm to 307 nm to reveal a possible change of the electronic character via a change of in the decay measured time and we were able to show that the main absorption band of TTF is the excitation of the system in a single electronic state and not two as predicted by theory. Femtosecond photoionization of TTF at 800 nm results in the absorption of up to twelve photons leading to ion internal energies up to 12.1 eV as deduced from the photoelectron spectrum. Within this internal energy a variety of dissociation channels are accessible. In order to disentangle the complex ionic dissociation, we utilized the imaging photoelectron photoion coincidence (iPEPICO) technique. Above the dissociation threshold, iPEPICO results show that the molecular ion (m/z = 204) dissociates into seven product ions, six of which compete in a 1.0 eV internal energy window and are formed with the same appearance energy. Ab initio calculations are reported on the possible fragment ion structures of five dissociation channels as well as trajectories showing the loss of C_2H_2 and C_2H_2S from high internal energy TTF cations. A three-channel dissociation model is used to fit the iPEPICO data in which two dissociation channels are treated as simple dissociations (one with a reverse barrier), while the rest involve a shared barrier. The two lower energy dissociation channels, m/z = 146 and the channel leading to m/z = 178, 171, 159, 140, and 127, have E_0 values of 2.77 ± 0.10 and 2.38 ± 0.10 eV, respectively, and are characterized by $\Delta S^{\ddagger}_{600K}$ values of -9 ± 6 and 1 ± 6 $\mathrm{JK^{-1}mol^{-1}}$, respectively. Competing with them at higher internal energy is the cleavage of the central bond to form the m/z = 102 fragment ion, with an E_0 value of 3.65 ± 0.10 eV and $\Delta S^{\ddagger}_{600K} = 83 \pm 10\ \mathrm{JK^{-1}mol^{-1}}$.

In Chapter 4 the high-order harmonic generation in vibrational excited SF_6 was investigated with two phase sensitive interferometric techniques based on heterodyne detection (strong field transient grating spectroscopy and two HHG source interferometry). The transient grating setup uses two pump pulses to create a grating of vibrational excitation in the gas jet through which the probe pulse generates high-order harmonics. The second experiment uses two spatially separated probe pulses, both generating an XUV beam, which interfere spatially in far field. All three Raman active modes of SF_6, $\nu_1(775\ \mathrm{cm^{-1}})$, $\nu_2(638\ \mathrm{cm^{-1}})$, $\nu_5(528\ \mathrm{cm^{-1}})$, could be observed in the amplitude and phase of the harmonic emission. The amplitude of the ν_5 mode shows a clear minimum around harmonic 17, whereas in the phase we observe a jump around harmonic 15. Mode ν_1 shows no clear pattern in the amplitude but in the phase we observe a minimum around harmonic 17. These minima cannot result form the previously observed minimum in the harmonic emission of SF_6, due to the heterodyne detection used here. From this we are able to conclude that the features observed here are only due to the change of the S–F distance, introduced by the vibrational wave packet. In addition, it appears that the harmonic emission is not optimized for fully stretched or compressed molecules as it is the case in a similar experiments on N_2O_4. Moreover, we observe a frequency chirp on each harmonic that is vibrational dependent. In order to fully interpret the results, a theoretical model to reproduce the amplitude and phase minima has to be developed. Nevertheless, this is the first phase-resolved study of HHG, which provides a first step in understanding the origin of the modulation in the harmonic spectrum of SF_6. The recorded data is currently being analyzed to take the bandwidth of each harmonic into account, with a pixel by pixel analysis. A first glance at this showed that the intensity of the red and blue parts in the bandwidth of one harmonic are oscillating with a phase shift and sometimes even in opposite phase. Consequently, this modulation is cancelled out when integrating one harmonic over the frequency coordinate as has been done in this analysis. Several additional experimental properties could be modified to complete the picture, for instance employing a shorter pulse duration, as the currently 30 fs duration is quite close to the vibrational periods observed. Changing the parallel polarization configuration between the pump and probe laser to a crossed configuration could also bring further insights. The transient grating and two sources setup could be realized in one integrated setup to measure both at the same time, under the same experimental conditions, namely an interference pattern from the two probe sources on the diffracted signals from the transient grating.

The last chapter (Chapter 5) described the development of the femtosecond XUV spectrometer to use high-order harmonic generation as an XUV photon source for pump-probe studies in the VMI. We tested the new VMI spectrometer by recording the photoelectron spectra of argon with a HHG spectrum, with one single harmonic and in pump-probe configuration using an additional laser pulse at the same frequency as the HHG driving laser frequency, to detect sidebands. In particular, we were able to measure the lifetime of an initially excited Rydberg state in argon, which showed the potential of this setup. After these preliminary test of the experimental setup had been performed, the fs-XUV spectrometer was employed to study the photodissociation of acetylene (C_2H_2) around 9.3 eV. In the first experimental attempt, we tried to observe the dissociation into the co-fragments H and C_2H, following an excitation of 9.3 eV (133.8 nm). The excitation was realized by a three-photon transition using 401.4 nm and we used the XUV pulse to detect the dissociation fragments via a one photon ionization. However, we observed no measurable amount of the desired dissociation fragments. In second experimental attempt, the setup was modified to use a 400 nm pulse for the HHG process. This way the molecule would be excited by the third harmonic and then probed by the additional 400 nm pulse creating sidebands in the photoelectron spectrum. By studying these photoelectron spectra as a function of the delay between the two pulses, we are able to observe dynamics of the relaxation of the excited state. However, these dynamics are not the result of the dissociation, but rather reflect the relaxation of the excited parent molecule. In fact, the ionization cross-section of hydrogen in the XUV region is significantly smaller than for acetylene around 9.3 eV, which means the detection process does not have a high enough efficiency. There are already several concepts in place on how to increase the XUV photon flux or the density of the molecular beam. On the other hand, it is not excluded that the dissociation of the acetylene is not very efficient either for the absorption band we excite. In such a case, it is normal to have observed no dissociation fragments. One should, apart from improving the the harmonic flux, consider the study of other molecular systems, which might show a better dissociation efficiency.

For the studies discussed in both Chapter 2 and Chapter 4, strong field interaction has been used. However, only little is known on how to describe a molecular system dressed by a strong electromagnetic field. Indeed, to properly treat a molecule in a strong field, electronic states up to the cation states have to be calculated and then investigated under the influence of a strong electric field. For femtochemistry purposes, these types of calculations have to be performed not only at equilibrium geometries, but also for all the main geometries encountered. This is an excellent challenge to theory as a proper quantum description of the dynamics demands time-dependent computations of the field-distorted potential energy surfaces, including multiexcited states. We have seen in azulene [1] that these type of states can be accessed from any geometry whatever the vibrational energy (more than 2 eV investigated) and relaxes efficiently to Rydberg states. These are pure electronic state dynamics and it will be relevant to investigate how this description is maintained in a strong field approach. Another aspect is the adiabaticity in the electron dynamics in conventional femtochemistry experiments. This adiabaticity in HHG originates from the fact that, upon reaching the field strength required for tunneling, the electron has sufficient time to tunnel and recombine before there is any further increase in field strength. However, the notion of handling one electron at a time seems quite a rough approximation. For instance in tetrathiafulvalene (TTF), we have seen that the ATI photoelectron spectrum is mostly produced from the first excited state of the cation and not from the ground state of the ion [2]. However, this is not the most obvious example. The main one that I encountered during my Ph.D. is when HHG is produced on large polyatomic systems such as SF_6. We are still puzzled to understand for instance how the cation dynamics during the short $\sim$500 attosecond travel time of the electron in the continuum can produced a frequency chirp for each harmonic that is vibrational dependent.

These different experimental observations lead us to the conclusion that we need to investigate experimentally what it actually means if a large polyatomic molecule is dressed by a strong electromagnetic field. Most of the strong field experiments in the past, have been based on detecting the amount of ionized fragments produced as a function of either the electric field or the wavelength. [3–8]. But recently with the advances in coincidence detection with high efficiency (COLTRIMS) [9], in the carrier envelope phase (CEP) control [10, 11] and the merging of attosecond science with femtochemistry, one of the main question which arises is how important is the coherent interaction between different molecular orbitals [12–18]. Obviously, although strong field effects have been studied for a long time, to understand sequential ionization or the formation of new species [16, 19], there is a need to follow non-adiabaticity dynamics of electrons at the level of the electric field oscillations [20]. Two totally different techniques seem to emerge to investigate this issue, both based on a control of the CEP. The first one is coincidence experiments coupled to Coulomb explosion [21] or dissociative ionization. Coincidence set-ups allow the determination of the orientation of the molecular system [22, 23], which is exactly what we would like to achieve to confirm the isomerization of N_3 following the dissociation of ClN_3 at 6 eV). In addition, in the case of tunnel ionization, it allows the determination from which molecular orbital the electron is tunneling [13, 24], which is known as channel resolved above threshold ionization (CRATI). The channel observed here is in fact the cation state from which the ATI electrons are emitted. ATI kinetic energy spectra are recorded in covariance with the parent ion and the fragment ions. Once a direct strong field ionization to an electronically excited ion state takes place, the correlated ion fragments will exhibit an ATI comb shifted relative to the one related to the parent ion. In contrast, if the excited ion states were populated subsequently by post-ionization excitation, meaning that the continuum electron has departed before further excitation occurs, then the fragments would have the same ATI spectrum as the parent ion because post-ionization excitation can no longer influence the departed continuum electron. This CRATI measurement, that is strongly dependent on a well-known spectroscopy of the dissociative ionization, directly reveals the population of multiple electronic continua and the Stark shifts in the strong field ionization of polyatomic molecules [20]. CRATI measurements on SF_6 are ongoing in the moment. The most recent update of this technology is the use intense laser pulses defined by only a few optical cycles with CEP control [25]. This tremendous technological achievement allows, for instance, to disentangle bond softening, recollision excitation and sequential ionization by simply varying the CEP and recording the anisotropy of the fragments and the change in the kinetic energy distribution [26, 27]. The other technique is XUV absorption spectroscopy using a laser pulse with only a few optical cycles. In the moment, this emerging technique is mostly used on atomic systems and known as absorption transient attosecond spectroscopy (ATAS). ATAS combines an IR pulse and an attosecond XUV pulse, overlapping in time. The signal is the delay-dependent absorption spectrum of the XUV light. The first experiments were performed with attosecond pulse trains to reveal the interference of electron wave packets in atoms initiated by the individual pulses in the train [28, 29]. Recently, these experiments have been extended to single attosecond XUV pulses, giving access to the instantaneous response of the excited system both on femtosecond and attosecond timescales. It has allowed, for instance, to determine if coherence exists when photoionization of an atom takes place with a few optical cycle laser pulse [30]. To the best of our knowledge, no such studies have been performed experimentally on molecular systems. However, experiments employing sub-cycle field transients with CEP control, such as ATAS, open new prospects to reveal as well the non-adiabatic electron dynamics of outer valence electrons in molecular systems.

References

[1] Piecuch, P, Hansen, JA, Staedter, D, Faure, S, and Blanchet, V. *Communication: Existence of the doubly excited state that mediates the photoionization of azulene*. J. Chem. Phys. **138**:20 201102–4 (2013) (cited p. 195).

[2] Mayer, PM, Staedter, D, Blanchet, V, Hemberger, P, and Bodi, A. *Comparing Femtosecond Multiphoton Dissociative Ionization of Tetrathiafulvene with Imaging Photoelectron Photoion Coincidence Spectroscopy*. J. Phys. Chem. A **117**:13 2753–2759 (2013) (cited p. 196).

[3] Corkum, PB, Ivanov, MY, and Wright, JS. *Subfemtosecond processes in strong laser fields*. Ann. Rev. Phys. Chem. **48**:1 387–406 (1997) (cited p. 196).

[4] DeWitt, MJ and Levis, RJ. *Concerning the ionization of large polyatomic molecules with intense ultrafast lasers*. J. Chem. Phys. **110**:23 11368 (1999) (cited p. 196).

[5] Hankin, S, Villeneuve, D, Corkum, P, and Rayner, D. *Nonlinear Ionization of Organic Molecules in High Intensity Laser Fields*. Phys. Rev. Lett. **84**:22 5082–5085 (2000) (cited p. 196).

[6] Lezius, M, Blanchet, V, Ivanov, MY, and Stolow, A. *Polyatomic molecules in strong laser fields: Nonadiabatic multielectron dynamics*. J. Chem. Phys. **117**:4 1575–1588 (2002) (cited p. 196).

[7] Lezius, M, Blanchet, V, Rayner, DM, Villeneuve, DM, Stolow, A, and Ivanov, MY. *Nonadiabatic multielectron dynamics in strong field molecular ionization*. Phys. Rev. Lett. **86**:1 51–54 (2001) (cited p. 196).

[8] Harada, H, Tanaka, M, Murakami, M, Shimizu, S, Yatsuhashi, T, Nakashima, N, Sakabe, S, Izawa, Y, Tojo, S, and Majima, T. *Ionization and Fragmentation of Some Chlorinated Compounds and Dibenzo- p-dioxin with an Intense Femtosecond Laser Pulse at 800 nm*. J. Phys. Chem. A **107**:34 6580–6586 (2003) (cited p. 196).

[9] Ullrich, J, Moshammer, R, Dorn, A, Dörner, R, Schmidt, LPH, and Schmidt-Böcking, H. *Recoil-ion and electron momentum spectroscopy: reaction-microscopes*. Rep. Prog. Phys. **66**:9 1463–1545 (2003) (cited p. 196).

[10] Feng, X, Gilbertson, S, Mashiko, H, Wang, H, Khan, SD, Chini, M, Wu, Y, Zhao, K, and Chang, Z. *Generation of Isolated Attosecond Pulses with 20 to 28 Femtosecond Lasers*. Phys. Rev. Lett. **103**:18 183901 (2009) (cited p. 196).

[11] Kienberger, R, Goulielmakis, E, Uiberacker, M, Baltuska, A, Yakovlev, V, Bammer, F, Scrinzi, A, Westerwalbesloh, T, Kleineberg, U, Heinzmann, U, Drescher, M, and Krausz, F. *Atomic transient recorder*. Nature **427**:6977 817–821 (2004) (cited p. 196).

[12] Akagi, H, Otobe, T, Staudte, A, Shiner, A, Turner, F, Dörner, R, Villeneuve, DM, and Corkum, PB. *Laser Tunnel Ionization from Multiple Orbitals in HCl*. Science **325**:5946 1364–1367 (2009) (cited p. 196).

[13] Boguslavskiy, AE, Mikosch, J, Gijsbertsen, A, Spanner, M, Patchkovskii, S, Gador, N, Vrakking, MJJ, and Stolow, A. *The Multielectron Ionization Dynamics Underlying Attosecond Strong-Field Spectroscopies*. Science **335**:6074 1336–1340 (2012) (cited p. 196).

[14] Kelkensberg, F, Lefebvre, C, Siu, W, Ghafur, O, Nguyen-Dang, T, Atabek, O, Keller, A, Serov, V, Johnsson, P, Swoboda, M, Remetter, T, L'Huillier, A, Zherebtsov, S, Sansone, G, Benedetti, E, Ferrari, F, NISOLI, M, Lépine, F, Kling, M, and Vrakking, M. *Molecular Dissociative Ionization and Wave-Packet Dynamics Studied Using Two-Color XUV and IR Pump-Probe Spectroscopy*. Phys. Rev. Lett. **103**:12 123005 (2009) (cited p. 196).

[15] Znakovskaya, I, Hoff, P von den, Zherebtsov, S, Wirth, A, Herrwerth, O, Vrakking, M, Vivie-Riedle, R de, and Kling, M. *Attosecond Control of Electron Dynamics in Carbon Monoxide*. Phys. Rev. Lett. **103**:10 103002 (2009) (cited p. 196).

[16] Markevitch, A, Romanov, D, Smith, S, and Levis, R. *Coulomb Explosion of Large Polyatomic Molecules Assisted by Nonadiabatic Charge Localization*. Phys. Rev. Lett. **92**:6 063001 (2004) (cited p. 196).

[17] Patchkovskii, S, Zhao, Z, Brabec, T, and Villeneuve, D. *High Harmonic Generation and Molecular Orbital Tomography in Multielectron Systems: Beyond the Single Active Electron Approximation*. Phys. Rev. Lett. **97**:12 123003 (2006) (cited p. 196).

[18] Smirnova, O, Mairesse, Y, Patchkovskii, S, Dudovich, N, Villeneuve, D, Corkum, P, and Ivanov, MY. *High harmonic interferometry of multi-electron dynamics in molecules*. Nature **460**:7258 972–977 (2009) (cited p. 196).

[19] Furukawa, Y, Hoshina, K, Yamanouchi, K, and Nakano, H. *Ejection of triatomic hydrogen molecular ion from methanol in intense laser fields*. Chem. Phys. Lett. **414**:1-3 117–121 (2005) (cited p. 196).

[20] Spanner, M, Mikosch, J, Gijsbertsen, A, Boguslavskiy, AE, and Stolow, A. *Multielectron effects and nonadiabatic electronic dynamics in above threshold ionization and high-harmonic generation*. New Jour. Phys. **13**:9 093010 (2011) (cited p. 196).

[21] Eremina, E, Liu, X, Rottke, H, Sandner, W, Schätzel, M, Dreischuh, A, Paulus, G, Walther, H, Moshammer, R, and Ullrich, J. *Influence of Molecular Structure on Double Ionization of* N_2 *and* O_2 *by High Intensity Ultrashort Laser Pulses*. Phys. Rev. Lett. **92**:17 173001 (2004) (cited p. 196).

[22] Itakura, R, Yamanouchi, K, Yasuike, T, and Someda, K. *Formation of* $[C_5H_6(NH_3)_2]^+$ *and* $[NH_4(NH_3)_m]^+$ *(m=1–3) from size-selected aniline–ammonia cluster cations in intense laser fields*. Chem. Phys. Lett. **396**:1-3 208–212 (2004) (cited p. 196).

[23] Legare, F, Lee, K, Litvinyuk, I, Dooley, P, Wesolowski, S, Bunker, P, Dombi, P, Krausz, F, Bandrauk, A, Villeneuve, D, and Corkum, P. *Laser Coulomb-explosion imaging of small molecules*. Phys. Rev. A **71**:1 013415 (2005) (cited p. 196).

[24] Kotur, M, Weinacht, TC, Zhou, C, and Matsika, S. *Strong-Field Molecular Ionization from Multiple Orbitals*. Physical Review X **1**:2 021010 (2011) (cited p. 196).

[25] Kremer, M, Fischer, B, Feuerstein, B, Jesus, VLB de, Sharma, V, Hofrichter, C, Rudenko, A, Thumm, U, Schröter, CD, Moshammer, R, and Ullrich, J. *Electron Localization in Molecular Fragmentation of* H_2 *by Carrier-Envelope Phase Stabilized Laser Pulses*. Phys. Rev. Lett. **103**:21 213003 (2009) (cited p. 197).

[26] Kling, MF, Siedschlag, C, Verhoef, AJ, Khan, JI, Schultze, M, Uphues, T, Ni, Y, Uiberacker, M, Drescher, M, Krausz, F, and Vrakking, MJJ. *Control of Electron Localization in Molecular Dissociation*. Science **312**:5771 246–248 (2006) (cited p. 197).

[27] Xie, X, Doblhoff-Dier, K, Roither, S, Schöffler, MS, Kartashov, D, Xu, H, Rathje, T, Paulus, GG, Baltuška, A, Gräfe, S, and Kitzler, M. *Attosecond-Recollision-Controlled Selective Fragmentation of Polyatomic Molecules*. Phys. Rev. Lett. **109**:24 243001 (2012) (cited p. 197).

[28] Loh, ZH, Khalil, M, Correa, R, Santra, R, Buth, C, and Leone, S. *Quantum State-Resolved Probing of Strong-Field-Ionized Xenon Atoms Using Femtosecond High-Order Harmonic Transient Absorption Spectroscopy*. Phys. Rev. Lett. **98**:14 143601 (2007) (cited p. 197).

[29] Holler, M, Schapper, F, Gallmann, L, and Keller, U. *Attosecond Electron Wave-Packet Interference Observed by Transient Absorption*. Phys. Rev. Lett. **106**:12 123601 (2011) (cited p. 197).

[30] Goulielmakis, E, Loh, ZH, Wirth, A, Santra, R, Rohringer, N, Yakovlev, VS, Zherebtsov, S, Pfeifer, T, Azzeer, AM, Kling, MF, Leone, SR, and Krausz, F. *Real-time observation of valence electron motion*. Nature **466**:7307 739–743 (2010) (cited p. 197).

A

Femtosecond laser pulses

A.1 The femtosecond laser chain

To be able to investigate dynamic processes in molecular systems which are on the order of femtosecond (fs, 10^{-15} seconds) to picoseconds (ps, 10^{-12} seconds) one need pulsed laser systems and to be able to do nonlinear optics, like frequency conversion and HHG, one need high power and short pulses. Both laser systems in Toulouse and Bordeuax are bases on a Kerr-lens mode locked (KLM) Titanium-Sapphire (Ti:Sa) Oscillator in combination with a chirped pulse amplification (CPA) system [1]. In this amplifier short pulses of a few femtoseconds from the KLM laser are stretched in time to a few hundreds of picoseconds, before they are amplified in two stages, and at the end again re-compressed to a few femtoseconds. Two types of amplifiers are used in this system, a regenerative amplifier and a multipass amplifier. The KLM laser is pumped by a continues wave (cw) laser The CPA system delivers in both facilities pulses at a repetition rate of 1 kHz. The pulses can be controlled and shaped by a acousto-optical programmable filter called Dazzler from Fastlite[1]. This enables one to control the spectral amplitude and to correct the phase of the laser chain.

The femto-second laser system used in Toulouse is from Amplitude Systems[2] and chaired between two groups (Béatrice Chatel and Valérie Blanchet). It is currently maintained by Elsa Baynard. At the exit of the laser chain we have pulses of 60 fs FWHM duration at a central wavelength of 805 nm, with a typical bandwidth of 25 nm and an output power of 3 mJ per pulse. This is enough fluence (10^{11-13} W/cm^2) to be able to utilize nonlinear optics like frequency mixing in birefringent crystals (second, third and fourth harmonic generation) and/or nonlinear parametric amplifications (NOPA) to achieve wavelength tuneability in the range from 200 - 700 nm.

The laser system in Bordeaux is a high power laser system, called Aurore. It's basic concept is the same as the one in Toulouse except that the pump lasers are more powerful and that in the amplification stage of the multipass not one but four pump lasers are used. In addition to the

---

[1] www.fastlite.com

[2] www.amplitude-systems.com

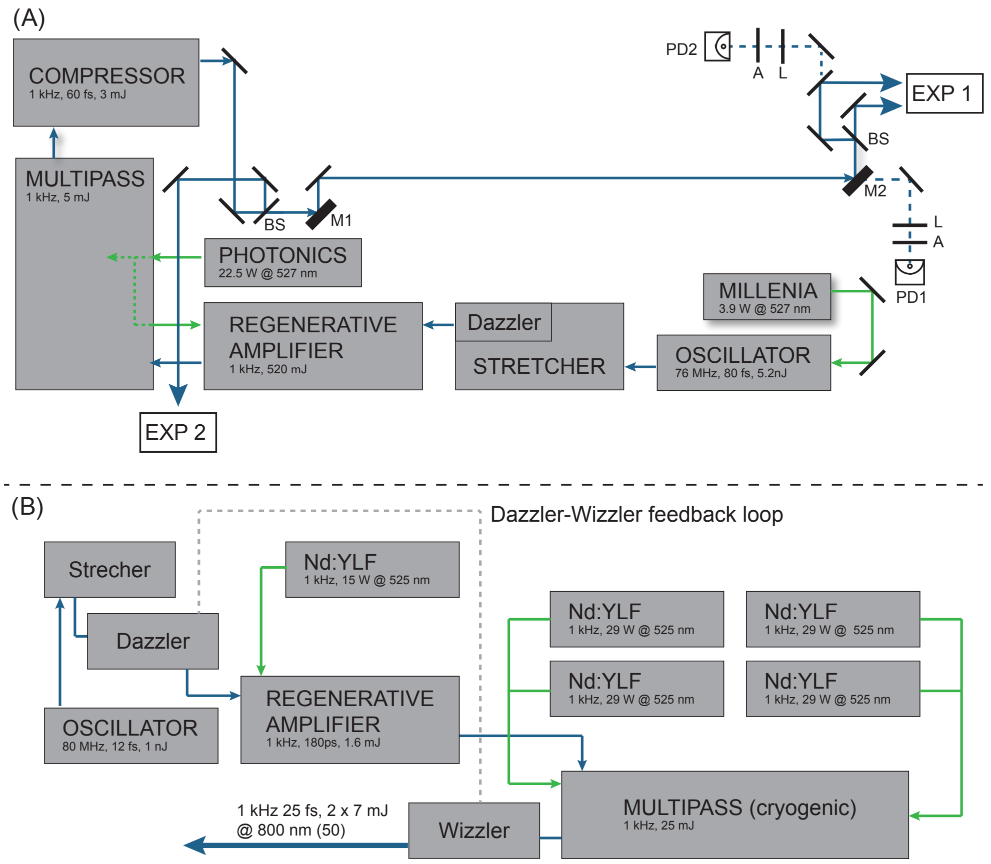

Figure A.1: (A) Setup of the femtosecond laser chain in Toulouse. BS = beam splitter, PD = photodiode, L = lens, A = attenuator. M1 and M2 are motorized mirrors which in combination with the two photodiodes and a labview program are implemented to stabilize the beam path. (B) Setup of the Aurore laser chain in Bordeaux.

Dazzler there is a Wizzler implemented which gives active realtime feedback to the Dazzler to compensate the nonlinear phases introduced by the propagation though the elements in the laser chain in real time. At the exit of the laser chain pulses with an energy of 7 mJ in the two arms, with a duration of 25 fs and a central wavelength of 800 nm at a repetition rate of 1 kHz are deliverd. Both laser setups are shown schematically in in Fig. A.1 and there characteristics are summarized in Tab. A.1.

Following the elements are briefly described and the main characteristics of short laser pulses are discussed as they are important for the experiments shown in this thesis. For more details about femtosecond laser system I refer to the standard literature like e.g. [2, 3].

Mode-locked Titanium-Sapphire Oscillator In standard femtosecond laser system the initial pulse is generated in a KLM Ti:Sa laser. The gain medium Ti:Sa, which is a saphire crystal doped by titanium is very suitable for generation and amplification of ultra short pulses, due to its very broad gain bandwidth of 235 nm around 800 nm [4]. The schematic structure and the necessary optics are shown in Figure A.2 (A). In this type of laser typically a plurality of spectral modes with frequencies $\nu = nc/2L$ where L the resonator length, c the velocity of light and n an integer, simultaneously oscillate in the resonator, but not at the same, and thus the elec-

Table A.1: Characteristics of the femtosecond laser chain in Toulouse and Bordeaux (Aurore).

	Properties	Oscillator	Regenerative Amplifier	Multipass	Chain Exit
Toulouse	repetition rate	76 MHz	1 kHz	1 kHz	1 kHz
	energy per pulse	5.2 nJ	520 μJ	5 mJ	3 mJ
	average power	400 mW	520 mW	5 W	3 W
	central wavelength	805 nm	805 nm	805 nm	805 nm
	spectral bandwidth	70 nm	35 nm	35 nm	35 nm
	pulse duration	25 fs	210 ps	210 ps	60 fs
Bordeaux	repetition rate	80 MHz	1 kHz	1 kHz	1 kHz
	energy per pulse	1 nJ	1.6 mJ	25 mJ	2×7 mJ
	average power	200 mW	1.6 W	25 W	14 W
	central wavelength	798 nm	798 nm	798 nm	798 nm
	spectral bandwidth	89 nm	50 nm	50 nm	50 nm
	pulse duration	12 fs	300 ps	300 ps	25 fs

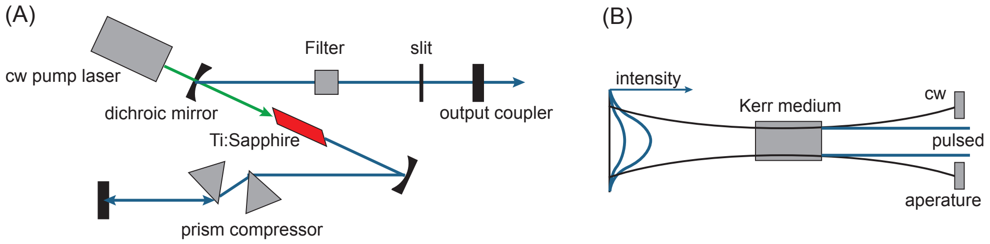

Figure A.2: (A) Typical cavity setup of a KLM Ti:sapphire laser, (B) Kerr-lens mode locking (KLM) principle

tric field is continuously as there is no phase relationship between these modes. The laser is running in cw operation (continuous wave). For a pulsed mode the different longitudinal laser modes must be coupled to each other so that they oscillate in phase with one another, which is called modelocking. The more modes are coupled, the higher the pulse intensity, and the smaller the pulse duration in accordance to the energy-time uncertainty principle. The principle can be used to determine the limiting value of the product of the spectral width $\Delta\nu$ and the time duration Δt, called the time-bandwidth product (TBWP). For a pulse with a Gaussian distribution (temporal and spectral) the minimum time-bandwidth product is

$$\Delta\nu\Delta t \leqslant \frac{4\ln 2}{2\pi} = 0.441. \qquad \text{(A.1)}$$

Modelocking in short pulsed lasers is achieved by a periodic modulation of the losses in the resonator. This can be be done by active optical shutters like EOM's or AOM (electro-optical or acousto-optic modulators) or passively by materials that are transparent for high intensities, so-called saturable absorbers. In femtosecond lasers typically a more elegant design of a passive shutter is used by implementing the optical Kerr effect within the medium [5, 6]. The optical Kerr effect is the change of the refractive index n of the material induced by a strong electric field and given by:

$$n = n_0 + n_2 I \qquad \text{(A.2)}$$

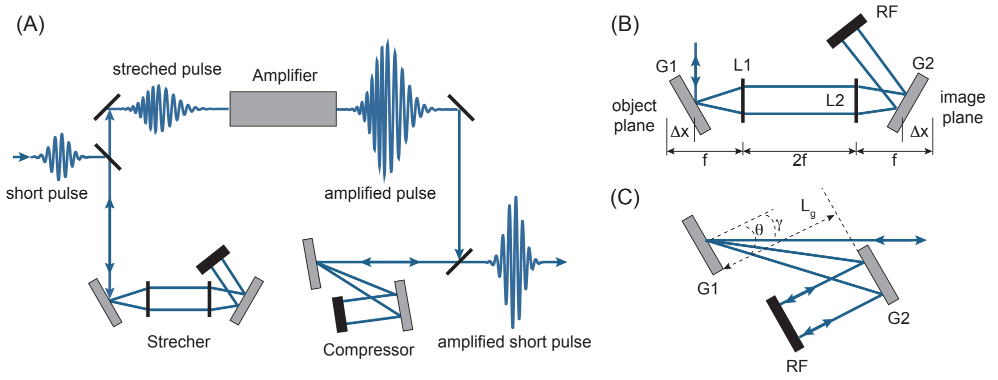

Figure A.3: (A) Principle setup of a chirped pulse amplification (CPA) system, (B) Strecher, (C) Compressor setup.

with n_0 the low intensity linear refractive index ($n_0 = 1.76$ at 800 nm in Ti:sapphire), and n_2 is the non-linear refractive index which changed as function of the light intensity I ($n_2 = 3.1 \times 10^{-16}\mathrm{cm}^2\mathrm{W}^{-1}$) [7]. At high intensities lensing effects will occur because the refractive index will be higher in the centre of the laser pulse, creating a gradient index lens in the material due to the spacial shape of the pulse which has a Gaussian profile. In combination with an additional slit in the beam path this allows to increase the losses of the CW beam. For this purpose, the slit is placed at a position at which the mode-locked beam has a smaller diameter than the CW beam. This Kerr-lens and the slit together form a saturable absorber and is graphically shown in Figure A.2 (B). This type of mode locking is successfully used for the generation of laser pulses with a duration down to 10 fs [6]. Each element in the beam path causes a chirp of the pulse due to dispersion, as the refractive index of the materials is in general wavelength dependent. When light travels through a dispersive medium like glass, the red spectral component will travel faster than the blue spectral components, in this manner the pulse will be stretched, as the spectral components arrive at different times at a detector after passing through a medium. This separation of spectral components in time is called chirp. The intensity-dependent self-focusing (Kerr effect) gives rise to a self-phase modulation. Because of the intensity dependent refractive index this leads to a spectral broadening inside the laser medium, and so actually to shorter pulses. Since the self-phase modulation in the Ti:sapphire crystal is not as strong as the dispersion of the elements in the laser chain, an additional element must be installed. In the KLM laser the material dispersion of one round trip in the laser is compensated by a prism pair placed within the resonator cavity. The length of the resonator dominates the repetition rate as: $\tau_{rep} = 1/T = c/(2L)$. A summary of the mechanisms in compact ultrfast lasers is given for instance in the review article by Ursula Keller [8]

Chirped pulse amplification (CPA) In this amplifier short pulses of a few femtoseconds from the KLM laser are stretched in time to a few hundreds of picoseconds, before they are amplified in mostly two stages before being re-compressed to a few femtoseconds at the end as illustrated in Figure A.3. Most high-power ultrafast laser systems use a high gain preamplifier stage, placed just after the pulse stretcher, which is designed to increase the energy of the nJ pulses from the laser oscillator to the 1-10 mJ level. The preamplifier is then followed by sev-

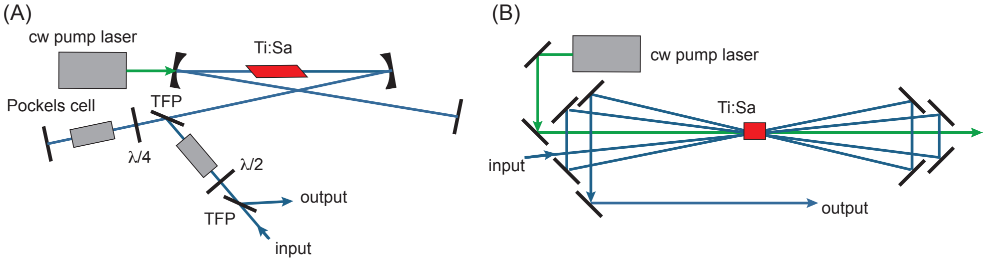

Figure A.4: Principle setup of an amplification system. (A) regenerative amplifier, (B) multipass amplifier.

eral power amplifiers designed to efficiently extract the stored energy in the amplifier and to increase the output pulse power even further. There are two basic preamplifier designs, regenerative [9, 10] and multipass [11] amplifiers. Both are illustrated in Figure A.4. Regenerative amplifiers are very similar to a laser cavity or resonator. The low-energy chirped pulse is injected into the cavity using a time-gated polarization device such as a Pockels cell and a thin film polarizer. The pulse then makes a couple of roundtrips through a relatively low gain medium, after that the high energy pulse is switched out by a second time-gated Pockels cell. A low gain configuration is typically used in this amplifier cavity to prevent amplified spontaneous emission (ASE). With high gain, ASE can build up quite rapidly in this configuration and deplete the gain before it can be extracted.

A multipass preamplifier configuration differs from the regenerative amplifier in that, as its name suggests, the beam passes through the gain medium multiple times without the use of a cavity. In a multipass amplifier, since the optical path is not a resonator, ASE can be suppressed to a greater degree than with a regenerative amplifier. Thus, multipass amplifiers typically have higher gain per pass, and fewer passes through the gain medium are needed. As a result, there is less high-order phase accumulation in multipass systems, and shorter pulses are easier to obtain upon recompression. Moreover, nonlinear phase accumulation due to the B-integral is also less in multipass amplifiers. We will come back to the B-integral in a moment. Multipass preamplifiers are not as efficient as regenerative amplifiers since the pump signal overlap must change on successive passes through the gain medium in order to extract the beam by separating it spatially.

A.2 General characteristics of femtosecond laser pulses

Light is described as an electromagnetic wave, a solution of the Maxwell equations, and can be written as

$$E(\vec{r},t) = E_0 e^{i(\vec{k}\vec{r}-\omega t)} \tag{A.3}$$

These solutions stand for the sinus waves traveling in vacuum at an angular frequency of ω and a wavenumber of k, where ω and k have a relation of $c = f\lambda = \omega/k$. E_0 is the amplitude of the waves and $\vec{k}\vec{r}-\omega t$ stands for the phase of the sinus wave. An optical pulse is formed through the coherent superposition of optical waves in a broadband frequency range. The electric fields in the temporal domain are described by adding the optical waves through the whole spectral domain (Fourier transform), and the electric fields in the frequency domain are described by the summation of the optical wave through the whole temporal domain (Inverse Fourier transform):

$$E(\vec{r},t) = \int_{-\infty}^{+\infty} E(\vec{r},\omega)e^{-i\omega t}\,d\omega \tag{A.4a}$$

$$E(\vec{r},\omega) = \frac{1}{2\pi}\int_{-\infty}^{+\infty} E(\vec{r},t)e^{-i\omega t}\,dt \tag{A.4b}$$

Since half-maximum quantities are experimentally easier to measure, the relationship between the duration and spectral bandwidth of the laser pulse can be written as

$$\Delta\nu\Delta t \leqslant K \tag{A.5}$$

where $\Delta\nu$ is the frequency bandwidth measured at full-width at half- maximum (FWHM) with $\omega = 2\pi\nu$ and Δt is the FWHM in time of the pulse. The number K will depends only on the pulse shape. In order to generate a laser pulse within femtosecond time domain one needs to use a broad spectral bandwidth. If the equality is reached one speaks about a Fourier-transform-limited pulse or simply a *transform limited* pulse. The minimum time duration of this transform limited pulse is given by

$$\Delta t = K\frac{\lambda_0^2}{\Delta\lambda c} \tag{A.6}$$

with $\Delta\lambda$ is the bandwidth in nm at FWHM and λ_0 the central wavelength.

A transform-limited pulse is obtained under the constant phase. In vacuum the optical pulse receives no modulation because the wave vector doesn't depend on the frequency. In a dispersive device however the wave vector becomes a function of the frequency so the electric field is rewritten as follows:

$$E(\vec{r},\omega) = E(0,\omega)e^{i\vec{k}(\omega)\vec{r}} = E(\omega)e^{i\phi(\omega)} \tag{A.7}$$

where $E(0,\omega) = E(\omega)$ is the spectral amplitude of the incident beam and $k(\omega)$ is the frequency-dependent wave-vector. The spectral phase $\phi(\omega) = k(\omega)r$ becomes a function of the angular frequency. The temporal electric field is then described as:

$$E(\vec{r},t) = \int_{-\infty}^{+\infty} E(\omega)e^{i\phi(\omega)}e^{-i\omega t}\,d\omega \tag{A.8}$$

If a transform limited pulse propagates through a dispersive medium, the spectral phase will be chirped as discussed earlier due to the wavelength dependent refractive index. Mathematically, if a spectral phase $\phi(\omega)$ varies slowly with the frequency ω, it can be expanded into a Taylor series around the carrier frequency ω_o as follows:

$$\phi(\omega) = \sum_{k=0}^{\infty} \frac{\phi^{(k)}(\omega_0)}{k!}(\omega-\omega_0)^k \tag{A.9}$$

with

$$\phi^k(\omega_0) = \left.\frac{\delta^k \phi(\omega)}{\delta \omega^k}\right|_{\omega=\omega_0} \tag{A.10}$$

The first term $\phi(\omega_0)$ describes the absolute phase of the pulse in the time domain. The first derivative $\phi' = T_g(\omega_0)$ is called the group delay (GD). The GD leads to a shift of the pulse envelope in the time domain. The second derivative $\phi'' = D_2(\omega_0)$ is the group delay dispersion (GDD) and $\phi''' = D_3(\omega_0)$ is the third-order dispersion (TOD) etc, respectively. Since these higher order derivatives (GDD and higher) describe the frequency dependence of the GD they are responsible for dispersive effects and changes in temporal structure of the pulse envelope. By analogy, the temporal phase $\phi(t)$ can be expanded into the Taylor series around time zero for small derivations:

$$\phi(t) = \sum_{k=0}^{\infty} \frac{\phi^{(k)}(0)}{k!} t^k \tag{A.11}$$

with

$$\phi^k(0) = \left.\frac{\delta^k \phi(t)}{\delta\, t^k}\right|_{t=0} \tag{A.12}$$

The time derivative of the temporal phase defines the instantaneous frequency

$$\omega(t) = \omega_0 - \frac{d\phi(t)}{dt} \tag{A.13}$$

The first term in the Taylor series $\phi(0)$ is the absolute phase of the pulse. and gives the temporal relation of the pulse envelope with respect to the underlying carrier oscillation. The first derivative ϕ' which is linear with time, describes a shift of the carrier frequency ω_0 and the term with ϕ'' corresponds to the linear motion of the instantaneous frequency and called linear chirp. The next terms are the quadratic, cubic, etc chirp. For example, the phase introduced by a material is given by $\phi_{mat} = L_{mat} n(\omega)\omega/c$, where n is the refractive index of the material, which can be decomposed as seen in Eq. (A.1) into a linear refractive index n_0 and a laser intensity dependent refractive index n_2. The value of the nonlinear phase contribution due to the nonlinear refractive index is given by [1]:

$$\phi_{nonlinear} = \frac{2\pi n_2}{\lambda} \int I(t,z)\, dz \tag{A.14}$$

The peak value of this expression is also known as the *B-integral* which gives a measure of of the nonlinear phase shift at peak intensity. The nonlinear group delay is approximately $d\phi/d\omega = B/\Delta\omega$, where $\Delta\omega$ is the half-width of the spectrum. A *B-integral* of 1 rad over a spectral half-width of 20 nm would add not only an additional delay variation of 17 fs but also introduce severe distortions as the phase varies across the beam. Thus, it is important if possible to maintain a value of the *B-integral* of less than 1.

A.3 Nonlinear optical effects - frequency mixing

In general for pump-probe experiments one would like to adjust the laser wavelength accordingly to the system or excited states of interest. The possibility of up- or down-converting the fundamental frequency of the laser (usually 800 nm form a Ti:sapphire laser) is the field of nonlinear optics. First discovered by Franken who focused light from a ruby laser into a quartz crystal and observed how a small amount of laser light was converted to the second harmonic [12]. However, the full impact and realization of nonlinear optics came only with an understanding of how a signal wave generated through a nonlinear optical polarization grows as it propagates through a nonlinear medium [13]. The beautiful and elegant perturbation treatment of nonlinear optics developed by Bloembergen and co-workers made it possible to develop both birefringent-phase-matching and quasi-phase- matching (QPM) techniques for efficiently converting laser light from one wavelength to another [14]. Optics is the study of the interaction of electromagnetic radiation and matter. Electromagnetic radiation is described by the Maxwell's equations and for the case here the Gauss's law given by:

$$\nabla\vec{D} = 4\pi\rho \tag{A.15}$$

is the most important one. The electric displacement field D is related to the electric field E through the polarization field P in a medium by:

$$\vec{D} = \vec{E} + 4\pi\vec{P} \tag{A.16}$$

In general the polarization field in the medium depends linearly on the incident electric field

$$\vec{P} = \varepsilon_0\chi^{(1)}\vec{E} \tag{A.17}$$

where ε_0 is the permittivity of the free space $\chi^{(1)} = n^2 - 1$ is the linear susceptibility of the medium with n the (complex) refractive index of the sample. In reality the polarization field is more complex and especially when dealing with higher field intensities such as in laser beams, the induced polarization is often not a linear function anymore. For small variations, the nonlinear polarization can be expanded in a Taylor series:

$$\vec{P} = \varepsilon_0\left(\chi^{(1)}\vec{E} + \chi^{(2)}\vec{E}^2 + \chi^{(3)}\vec{E}^3 + \dots\right) \tag{A.18}$$

where $\chi^{(n)}$ is the n^{th} order susceptibility. In general an n^{th} order will lead to $(n+1)^{th}$ wave mixing. As an example, if we consider only a second order nonlinearity (three-wave mixing), then the polarization $\vec{P}^{(2)}$, takes the form

$$\vec{P}^{(2)} = \varepsilon_0\chi^{(2)}\vec{E}^2(t) \tag{A.19}$$

Considering an electric field $\vec{E}(t)$, made up of two components at frequencies ω_1 and ω_2, given by $\vec{E}(t) = \vec{E}_1 e^{-i\omega_1 t} + \vec{E}_2 e^{-i\omega_2 t} + cc$ one can write the second-order polarization field with nonzero *chi*$^{(2)}$ for instance as

$$\begin{aligned}\vec{P}^{(2)}(t) &= \varepsilon_0\chi^{(2)}\vec{E}^2(t) = \varepsilon_0\chi^{(2)}\left[E_1\, e^{-i\omega_1 t} + E_2\, e^{-i\omega_2 t} + cc\right]^2 \\ &= \varepsilon_0\chi^{(2)}\left[|E_1|^2\, e^{-i2\omega_1 t} + |E_2|^2\, e^{-i2\omega_2 t}\right. \\ &+ 2E_1E_2\, e^{-i(\omega_1+\omega_2)t} \\ &+ 2E_1E_2^*\, e^{-i(\omega_1-\omega_2)t} \\ &\left.+2(|E_1| + |E_2|)e^0\right]\end{aligned} \tag{A.20}$$

The resulting polarization field contains components oscillating at various frequencies ($2\omega_1$, $2\omega_2$, $\omega_1 + \omega_1$, $\omega_1 - \omega_1$ and 0). The first two terms oscillating at 2ω are called second harmonic generation (SHG). The third and fourth term are known as sum frequency generation (SFG) and difference frequency generation (DFG). The last term does not oscillate in time and is known as optical rectification, a conversion of an oscillating electric field to a static DC field. The third-order susceptibility not discussed here would give rise to nonlinear effects known as the DC Kerr effect, the third harmonic generation and the optical Kerr effect. Of course these phenomena are not all automatically observed. The above representation ignores the position dependence of the electrical fields. Additional constrains apply, that both energy and momentum of the photons involved must be conserved. Considering an electric field $E_j(\vec{x},t) = e^{i(\vec{k}_j\vec{x}\omega_j t)}$ at position $\vec{x}$ with the wave vector $|\vec{k}| = n(\omega_j)\omega_j/c$, where $n(\omega_j)$ is the frequency dependent refractive index and c the speed of light, the second order polarization field at the angular frequency $\omega_3 = \omega_1 + \omega_2$ is given by:

$$\vec{P}^{(2)}(\vec{x},t) \propto E_1^2E_2^2\, e^{i[(\vec{k}_1+\vec{k}_2)\vec{x}-\omega_3 t]} \tag{A.21}$$

Energy conservation is given by $\hbar(\omega_3) = \hbar\omega_1 + \hbar\omega_2$. Constructive interference and a high intensity conversion will only occur if also the momentum is conserved given by $k_3 = k_1 + k_2$, which is known as the phase-matching condition. If this relationship is not maintained during the propagation in the medium, destructive interference will make the conversion process extremely inefficient. Thus for constructive interference the two waves have to be phase matched which means they have to travel with the same phase velocity. This can be achieved for instance for SHG, when the refractive index of the material is equal for the two frequencies ($n(\omega_3) = n(\omega_1)$). In general anisotropic crystals are used like β-barium borate (BBO), where the refractive index varies with the propagation direction. As the velocity in the medium is related to the refractive index by $v = c/n$ anisotropic crystals are often said to have a fast and slow axis of propagation. If the fundamental and the second harmonic wave are polarized at right angles to each other it is generally straightforward to find an angle of propagation through the crystal for which the refractive index and therefore the velocity for both beams are equal. Parametric amplification (OPA) optical parametric generation (OPG) are variations of difference frequency generation, where in general $\omega_1 \neq \omega_2$ and where the lower frequency of one of the two generating fields is much weaker (parametric amplification). This can be used as a laser light source that emits light of variable wavelengths.

Conversion efficiency, phase-matching bandwidth and time duration of SHG

The efficiency of the second-harmonic generation $\eta_{SHG} = I(2\omega)/I(\omega)$ is proportional to $L^2 I(\omega)$, where $I(\omega) = P/A$, with P the incident power and A the cross-sectional area of the interaction volume. Therefore, the SHG efficiency can be written as [15]

$$\eta_{SHG} = C^2 \frac{L^2}{A} P \qquad C^2 = 2\omega^2 \eta_0^2 \frac{d^2}{n^3} \tag{A.22}$$

where C^2 is a material constant depending on the second-order susceptibility $\chi^{(2)} = 2d$ and the refractive index n of the material. Apart from increasing P, to maximize the the efficiency, the ratio L^2/A has to maximum. Therefore, the beam must be focused and the interaction length L should be maximized. If the dimensions of the nonlinear crystal are not limiting factors, the maximum value of L for a given area A is limited by the beam diffraction. A Gaussian beam, focused to a beam width W_0 maintains a beam cross-sectional area $A = \pi W_0^2$ over a depth of focus $L = 2z_0$ with $z_0 = 2\pi W_0^2/\lambda$ the Rayleigh length, so that the ratio $L^2/A = 2L/\lambda = 4A/\lambda^2$

For a finite interaction length L, a phase mismatch $|\Delta k| \leqslant 2\pi/L$ is tolerated (equality would give the coherence length). If exact phase matching is achieved at a set of nominal frequencies of the mixed waves, then small frequency deviations from those values may be tolerated, as long as the condition $\omega_3 = \omega_1 + \omega_2$ is satisfied. For SHG we have two waves with frequencies $omega_1 = \omega$ and $\omega_3 = 2\omega$. The crystal is designed for exact phase matching at a nominal fundamental frequency ω_0, $\Delta k(\omega_0) = 0$. For phase-matching conditions with a bandwidth $\Delta\omega$: $|\Delta k(\omega_0 + \Delta\omega) = 2\pi/L|$. For small $\Delta\omega$ one can write this as $\Delta k(\omega_0 + \Delta\omega) = (d/d\omega)\Delta\omega$ at ω_0 and therefore

$$\Delta\omega = \frac{2\pi}{|\Delta k'|L} \qquad \text{or} \qquad \Delta\nu = \frac{1}{|\Delta k'|L} \tag{A.23}$$

As $\Delta k(\omega) = k_3(2\omega) - 2k_1(\omega)$ and $dk_i(\omega)/d\omega = 1/v_i$ with v_i the group velocity at of wave i, the spectral width can be written as:

$$\Delta\nu = \frac{1}{2L} \left| \frac{1}{v_3} - \frac{1}{v_1} \right|^{-1} \tag{A.24}$$

One can see, the thiner the crystal, the larger the bandwidth and the shorter the pulse duration.

References

[1] Backus, S, Durfee, CG, Murnane, MM, and Kapteyn, HC. *High power ultrafast lasers*. Rev. Sci. Instr. **69**:3 1207–1223 (1998) (cited p. 201, 207).

[2] Svelto, O. *Principles of Lasers*. Springer. 2010 (cited p. 202).

[3] Träger, F. *Springer handbook of lasers and optics*. Springer, 2007 (cited p. 202).

[4] MOULTON, PF. *Spectroscopic and Laser Characteristics of Ti-Al$_2$O$_3$*. J. Opt. Soc. Am. B **3**:1 125–133 (1986) (cited p. 202).

[5] Brabec, T, Spielmann, C, Curley, PF, and Krausz, F. *Optics InfoBase: Optics Letters - Kerr lens mode locking*. Optics letters (1992) (cited p. 203).

[6] Christov, IP, Stoev, VD, Murnane, MM, and Kapteyn, HC. *Optics InfoBase: Optics Letters - Sub-10-fs operation of Kerr-lens mode-locked lasers*. Optics letters (1996) (cited p. 203, 204).

[7] Brouard, M and Vallance, C. *Tutorials in molecular reaction dynamics*. Royal Society of Chemistry Cambridge, UK, 2010 (cited p. 204).

[8] Keller, U. *Recent developments in compact ultrafast lasers*. Nature (2003) (cited p. 204).

[9] Wynne, K, Reid, GD, and Hochstrasser, RM. *Optics InfoBase: Optics Letters - Regenerative amplification of 30-fs pulses in Ti:sapphire at 5 kHz*. Optics letters (1994) (cited p. 205).

[10] Barty, C, Korn, G, Raksi, F, and Rose-Petruck, C. *Optics InfoBase: Optics Letters - Regenerative pulse shaping and amplification of ultrabroadband optical pulses*. Optics ... (1996) (cited p. 205).

[11] Backus, S, Peatross, J, Huang, CP, and Murnane, MM. *Optics InfoBase: Optics Letters - Ti:sapphire amplifier producing millijoule-level, 21-fs pulses at 1 kHz*. Optics ... (1995) (cited p. 205).

[12] Franken, PA, Hill, AE, Peters, CW, and Weinreich, G. *Generation of Optical Harmonics*. Phys. Rev. Lett. **7**:4 118–119 (1961) (cited p. 208).

[13] Popmintchev, T, Chen, MC, Arpin, P, Murnane, MM, and Kapteyn, HC. *The attosecond nonlinear optics of bright coherent X-ray generation*. Nature Photonics **4**:12 822–832 (2010) (cited p. 208).

[14] Armstrong, J, Bloembergen, N, Ducuing, J, and Pershan, P. *Interactions between Light Waves in a Nonlinear Dielectric*. Phys. Rev. **127**:6 1918–1939 (1962) (cited p. 208).

[15] “Nonlinear Optics”. *Fundamentals of Photonics*. Ed. by Saleh, B. Wiley, 2013 (cited p. 210).

B

Reconstructing velocity-map images

Velocity-map images are 2D projections of the 3D velocity distribution as we have seen in Section 1.2. The physical information is lying only in the central slice of this 3D distribution. If one doesn't use slicing techniques but has an axis of cylindrical symmetry the 2D projection parallel to this axis contains enough information to reconstruct the full 3D distribution using a mathematical inversion method. The reconstruction method will be summarized here shortly and follows the description given in [1].

In the case of photodissociation experiments the polarization of the photolysis laser is usually put parallel to the detector plane so that the photofragments are ejected with cylindrical symmetry around this axis parallel to the detector. Under these circumstances the mathematical procedure known as inverse Abel transformation is able to recover the 3D distribution from its projection [2].

The velocity distribution of the photofragment ions in cartesian coordinates centred on the point of interaction can be written as $i(x,y,z)$, where z is the symmetry axis (in this case the laser polarization vector), and y the direction of the extraction field. Than the distribution on the detector can be written as:

$$I(x,y) = \int_{-\infty}^{+\infty} i(x,y,z)\,dy \tag{B.1}$$

If we consider just one row of the image taken along the x axis at some value of $z = z_0$ we have:

$$f(x) = I(x,z_0) = \int_{-\infty}^{+\infty} g(x,y)\,dy = 2\int_{0}^{+\infty} g(x,y)\,dy \tag{B.2}$$

where $g(x,y) = i(x,y;z_0)$ is a slice through the 3D distribution perpendicular to the symmetry axis taken at z_0. The function $f(x)$ is illustrated in Figure B.1 B. To reconstruct the original velocity distribution (illustrated in Figure B.1 C.) one has to recover $g(x,y)$ from the measured function $f(x)$. As the problem is cylindrical symmetric one can by a simple change of variables with

$$x^2 + y^2 = r^2 \rightarrow y = \sqrt{r^2 - x^2} \Rightarrow dy = \frac{rdr}{\sqrt{r^2 - x^2}} \tag{B.3}$$

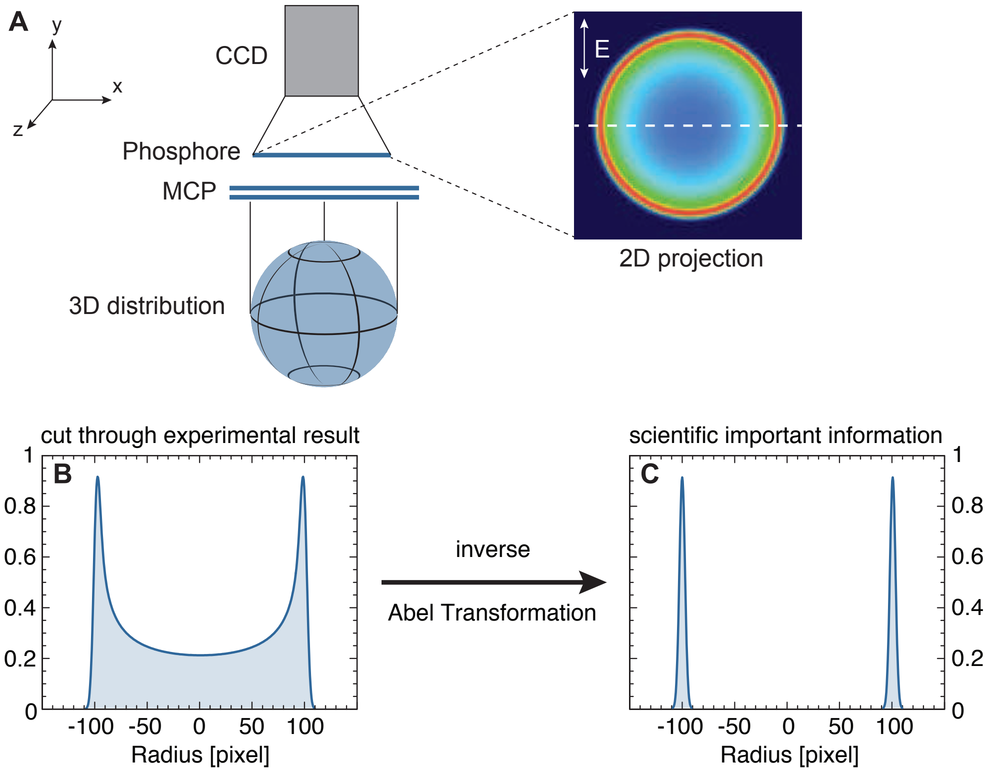

Figure B.1: Velocity-map images, experimental data vs scientific important information. (A) Principle experimental setup (2D projection). (B) Cut through the experimental result (function $f(x)$). (C) Scientific important information, cut through reconstructed data ($g(x)$).

express Eq. (B.2) in polar coordinates as

$$f(x) = 2\int_{x}^{+\infty} \frac{g(r)r}{\sqrt{r^2 - x^2}}\,dr \tag{B.4}$$

This is the Abel Transform [3], and its inverse will recover $g(r)$ from the measured $f(x)$. The inverse transform can be found by applying the Fourier transform convolution theorem and is given by [4]:

$$g(r) = -\frac{1}{\pi}\int_{r}^{+\infty} \frac{f'(x)}{\sqrt{x^2 - r^2}}dx \tag{B.5}$$

Solving this equation in practice is quite difficult because of the singularity at $r^2 = x^2$ and because the derivative in the integrand tends to magnify noise. Smith and Keefer [5] proposed a method to solve this problem. First one has to take the Fourier transform F of the function $f(x)$ from Eq. (B.2):

$$F[f(x)] = \int_{-\infty}^{+\infty}\int_{-\infty}^{+\infty} g(\sqrt{x^2+y^2})exp(-i2\pi xq)\,dxdy \tag{B.6}$$

This can be written in polar coordinates as:

$$F[f(x)] = 2\pi\int_{-\infty}^{+\infty} rg(r)J_0(2\pi rq)\,dr \tag{B.7}$$

where J_0 is the zero order Bessel-function with

$$J_0(y) = \frac{1}{2\pi}\int_0^{2\pi} exp(-iy\cos\theta)\,d\theta \tag{B.8}$$

The right hand side of Eq. (B.7) is the zero order Hankel transform H of $g(r)$. Since the Hankel transform is identical to its inverse, the original distribution $g(r)$ can be recovered by taking the Hankel transform of the Fourier transform of the projected intensity $f(x)$ as :

$$\begin{aligned} g(r) &= H[F[f(x)]] \\ &= 2\pi\int_0^{+\infty} qJ_0(2\pi qr)\left[\int_{-\infty}^{+\infty} f(x)exp(-2\pi xq)\,dx\right]dq \end{aligned} \tag{B.9}$$

Eq. (B.9) has several advantages over the Abel Trasnform given by Eq. (B.5) because it avoids the difficulty associated with the lower limit of integration and allows one to filter and smooth the data in the Fourier transform step. To evaluate equation Eq. (B.9) a fast Fourier transform algorithm (FFT) on each line of the image is performed and then the Bessel function is calculated by direct summation. This algorithm is implemented in the labview program written by Stephane Faure, engineer in our laboratory at LCAR, and was used to analyze the experimental results shown in this thesis.

References

[1] Whitaker, BJ. *Imaging in Molecular Dynamics: Technology and Applications*. Cambridge: Cambridge Univ. Press, 2003 (cited p. 213).

[2] Heck, AJR and Chandler, DW. *Imaging Techniques for the Study of Chemical Reaction Dynamics*. Ann. Rev. Phys. Chem. **46**:1 335–372 (1995) (cited p. 213).

[3] Dasch, CJ. *One-dimensional tomography: a comparison of Abel, onion-peeling, and filtered backprojection methods*. Appl. Opt. **31**:8 1146–1152 (1992) (cited p. 214).

[4] Bracewell, RN. *The Fourier transform and its applications*. McGraw-Hill, New York, 1978 (cited p. 214).

[5] Smith, LM and Keefer, DR. *Abel inversion using transform techniques*. J. Quant. Spectrosc. Radiat. Transfer (1988) (cited p. 214).

C

Angular distribution and the Legendre polynomials

$$\begin{aligned} I(\theta) &= \frac{1}{4\pi}\int_0^{2\pi} |\vec{\mu}\vec{\varepsilon}_p|^2\, d\Phi \\ &= \frac{(\mu\varepsilon_p)^2}{4\pi} \times \left[1+\sum_n \beta_{2n} P_{2n}(\cos\theta)\right] \end{aligned} \tag{C.1}$$

$$P_0(x) = 1 \tag{C.2}$$

$$P_2(x) = \frac{1}{2}(3x^2-1) \tag{C.3}$$

$$P_4(x) = \frac{1}{8}(35x^4-30x^2+3) \tag{C.4}$$

$$P_6(x) = \frac{1}{16}(231x^6-315x^4+105x^2-5) \tag{C.5}$$

$$P_8(x) = \frac{1}{128}(6435x^8-12012x^6+6930x^4-1260x^2+35) \tag{C.6}$$

$$P_{10}(x) = \frac{1}{256}(46189x^{10}-109395x^8+90090x^6-30030x^4+3465x^2-63) \tag{C.7}$$

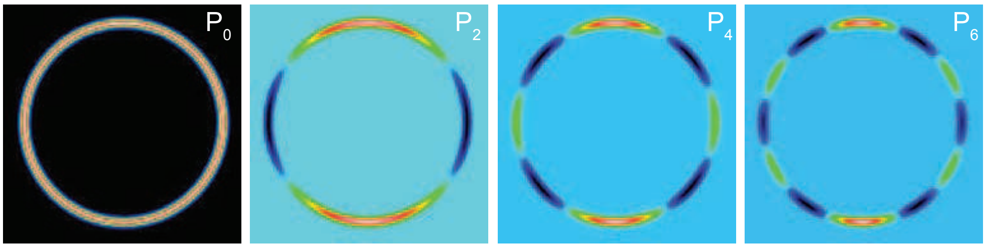

Figure C.1: Angular distribution of a Newton sphere on the VMI detector with higher orders of the Legendre polynomials, P_{2n} with n = 0, 1, 2, 3.

D

The Lewenstein model of high-order harmonic generation

To deal with the strong field response of atoms and molecules in general and HHG in particular in a quantum mechanical picture one has to solve the time-dependent Schrödinger equation (TDSE):

$$i\hbar\frac{\delta}{\delta t}\psi(\vec{r},t) = \hat{H}\psi(\vec{r},t) \tag{D.1}$$

where ψ is the wave function of the quantum system and $\hat{H}$ is the Hamiltonian operator, which characterizes the total energy of any given wave function. The Hamiltonian is given by:

$$\hat{H} = -\frac{\hbar^2}{2m}\nabla^2 + V(\vec{r},t) \tag{D.2}$$

where in this case the time-dependent potential $V(\vec{r},t)$ is the given by the sum of the atomic coulomb potential and the dipole interaction with the electric field as seen in the three step model. Although the TDSE can be solved numerically for the simplest case of an hydrogen atom, it requires considerable computational time. And to solve this equation for multielectron systems is almost impossible. Thus one has to consider approximations to derive an analytical solution. In the case of atoms in strong laser fields this has been done the first time in 1994 by Lewenstein and coworkers and is known as the strong field approximation (SFA) [1] which uses the single active electron approximation (SAE) developed by Keldysh in 1965 [2]. Within the scope of the SFA, the follwing assumptions are necessary:

- In order to ensure the horizontal ionization channel (tunnel ionization) $\gamma \ll 1$ is sufficient. This assumes a low frequency of the laser field and a strong laser field. Only the ground state of the atomic/molecular system is considered.

- The electron in the continuum is unaffected by the Coulomb potential and only the interaction with the laser field is taken into account. The electron is assumed to be free in the continuum $U_p \gg I_p$.

- Depletion of the ground state is neglected $I_0 \ll I_{sat}$.

These assumption are conflicting. On one side the field has to be strong but not too strong. This defines a small intensity regime for HHG. The theory of high harmonic generation can be divided into two parts: First, the single atom response is the dipole of a single atom in a strong optical field. Second, propagation deals with the phase-matching and absorption in the medium and effectively adds up the contributions for all of the atoms generating harmonics. The goal of this model is to calculate the dipole responsible for the emission of high harmonics for an arbitrary optical pulse. The nonlinear dipole is calculated as a function of time in the fundamental field. This dipole is then twice differentiated to get the electric field of the emitted harmonics. A Fourier transform then gives the high harmonic spectrum. The time-dependant dipole moment can be written as:

$$\vec{\mu}(t) = \langle \psi(\vec{r},t)| - \vec{r} |\psi(\vec{r},t)\rangle \tag{D.3}$$

from which we can then extract the harmonic spectrum by Fourier transformation. The time-dependent electron wavefunction (where only one electron is considered to be responsible for harmonic generation ‘single-active electron approximation’ (SAE) can be written in terms of the bound electron ground state of the atom and the continuum states $|\vec{v}\rangle$ where v stands for the kinetic momentum as:

$$|\psi(\vec{r},t)\rangle = e^{iI_p t}\left(a(t)|0\rangle + \int b(\vec{v},t)|\vec{v}\rangle d^3\vec{v}\right) \tag{D.4}$$

with time-dependent ground-state $a(t)$, and continuum-state amplitudes, $b(\vec{v},t)$. By doing so, we do not take into account excited bound states of the electron. Since the continuum states are defined to be solutions to the free electron Schrödinger equation $E_{kin}|\vec{v}\rangle = -1/2\,\nabla^2|\vec{v}\rangle$, the potential of the nucleus is neglected as soon as the electron is ionized. Using the definition of the time-dependent electron wavefunction in equation Eq. (D.4), the time-dependent dipole moment can be calculated to be:

$$\vec{\mu}(t) = i\int_0^t dt_i \int d^3\vec{p}\,E\cos(\omega t_i) \times \underbrace{\vec{d}(\vec{v}(t_i))}_{(a)} \times \underbrace{\exp(-iS(\vec{p},t,t_i))}_{(b)} \times \underbrace{\vec{d}^*(\vec{v}(t_i))}_{(c)} + c.c. \tag{D.5}$$

where $\vec{v}(t)$ is given by the vector potential of the laser field $\vec{A}(t)$ and the canonical momentum $\vec{p}$ by $\vec{v}(t) = \vec{p} - \vec{A}(t)$. S is the so-called quasi-classical action and given by

$$S(\vec{p},t,t_i) = -\int_{t_i}^{t_r} dt' \left(\frac{(\vec{p}+\vec{A}(t'))^2}{2} + I_p\right) \tag{D.6}$$

The expression $\vec{d}(\vec{v})$ in Eq. (D.5) stands for the transition probability from the bound electronic state $|0\rangle$ to a continuum state $\langle\vec{v}|$ (describing ionization), where the complex conjugate describes the inverse process, i.e. recombination of the free electron to the ground state:

$$\vec{d}(\vec{v}) = \langle \vec{v} | \vec{r} | 0 \rangle \tag{D.7a}$$

$$\vec{d}^*(\vec{v}) = \langle 0 | \vec{r} | \vec{v} \rangle \tag{D.7b}$$

With this we can identify the different parts of the formula Eq. (D.5) as follows:

(a) ionization of the ground state at time t_i,

(b) propagation in the continuum in the time interval $t_r - t_i$

(c) recombination to the ground state at time t_r.

Thus, the classical three-step model discussed before is contained in the quantum- mechanical description as well. By Fourier transforming the time-dependent dipole moment, the harmonic spectra can be calculated:

$$\vec{\mu}(\omega_q) = \int_{-\infty}^{+\infty} dt_r \, \vec{\mu}(t_r) e^{i\omega_q t_r} = \int_{-\infty}^{+\infty} dt_r \int_0^{t_r} dt_i \int d^3\vec{p} \, \vec{B}(\vec{p}, t_r, t_i) e^{i\varphi(\vec{p}, t_r, t_i)} \tag{D.8}$$

where $\vec{B}$ is the amplitude of the integrant in the integral from Eq. (D.5) and the dipole phase φ defined as:

$$\varphi(\vec{p}, t_r, t_i) = \omega_q t_r - S(\vec{p}, t_r, t_i) \tag{D.9}$$

Sattle-point approximation

Eq. (D.8) can be interpreted with the help of the Feynman path integrals [3]. To calculate $\vec{\mu}(t)$ we do not need to calculate the integral over all possible paths $\vec{p}$. We only need to consider the pathways $\vec{p}$ for which the action becomes stationary:

$$\vec{\nabla}_p S(\vec{p}, t_r, t_i) = 0 \tag{D.10}$$

According to Hamilton's principle the trajectory which is fulfilling this condition corresponds exactly to the classical path and the relation can again be interpreted in terms of the classical three-step model and the following statements have to be fulfilled (sattle point equations):

$$\frac{(\vec{p} - \vec{A}(t_i))^2}{2} + I_p = 0 \tag{D.11a}$$

$$\int_{t_i}^{t_r} dt \, \vec{p} + \vec{A}(t))^2 = 0 \tag{D.11b}$$

$$\frac{(\vec{p} - \vec{A}(t_r))^2}{2} + I_p = \omega_q \tag{D.11c}$$

Eq. (D.11a) states that the sum of the kinetic energy and the ionization potential is zero at the time of ionization t_i. This results in a negative kinetic energy of the electron which can be justified by tunnel ionization when allowing complex values. Eq. (D.11b) shows that we only need to account for those electron trajectories that return at time t_r to the same point they left at time t_i, where they were ionized. In other words its trajectory is closed. Eq. (D.11b)

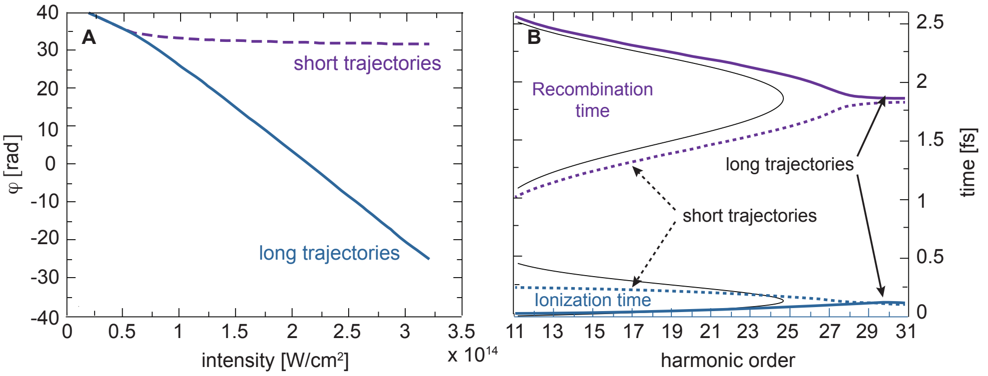

Figure D.1: (A) Dipole phase of harmonic 19 geherated Argon calculated for short (purple dashed line) and long trajectories (solid blue line). (B) Calculated variation of the dipole phase with intensity, for long (solid line) and short trajectories (dashed line) according to the ionization and recombination times. Black lines represent the classical trajectories (adapted from [6, 7].

implies conservation of energy. The energy of the emitted photon is exactly equal to the energy released by the recolliding electron.

According to the formula for the dipole moment Eq. (D.5), different electron trajectories contained in the integral acquire different phases $\varphi = S(p, t_r, t_i)$ during their propagation in the continuum. The shape of the electronic wave-packet at the moment of recombination will be governed by the interference between these separate quantum paths. In particular, different trajectories leading to the same photon energy (having the same kinetic energy at the time of recombination) will interfere with each other. Therefore, there are two electron trajectories which are most important for the generation of a particular photon energy. Since one of them spends a longer time in the continuum, it is called the 'long trajectory' (the one ionizing at a smaller phase of the electric field), the other one is called the 'short trajectory'. Only one of the two trajectories (the long trajectory) exhibits a phase that is linearly proportional to the laser intensity I, while the other (short) one is almost constant [4, 5]

$$\frac{d\varphi_l}{dI} = a, \qquad \frac{d\varphi_s}{dI} \approx 0 \tag{D.12}$$

where φ_l and φ_s are the atomic dipole phases of the long and the short trajectory, respectively, and α is a constant on the order of 26×10^{14} cm^2/W. The calculated dipole phase of both trajectories for the harmonic 19 generated in Argon is shown in Figure D.1 A.

Quantum mechanical cut-off law

Most importantly, the quantum-mechanical treatment also yields the classical cut-off law equation up to a small correction. The cut-off photon energy can be found to be

$$(\hbar\nu)_{max} = 3.17\,U_p + f\left(\frac{I_p}{U_p}\right) I_p \tag{D.13}$$

where $f(x)$ is a slowly varying function on the order of 1, which assumes the values $f(0) \approx 1.32$ at $x = 0$ ($U_p \gg I_p$) and $f(3) \approx 1.25$. The physical origin of this correction lies in purely quantum mechanical effects such as tunneling and the spreading of the electron wave-packet in the continuum that have not been included in the purely classical treatment. These effects enable the electron to collect more energy on its trajectory than the amount predicted by the classical equations of motion.

References

[1] Lewenstein, M, Balcou, P, Ivanov, MY, L'Huillier, A, and Corkum, PB. *Theory of High-Harmonic Generation by Low-Frequency Laser Fields*. Phys. Rev. A **49**:3 2117–2132 (1994) (cited p. 219).

[2] Keldysh, LV. *Ionization in the field of a strong electromagnetic wave*. Sov. Phys. JETP **20**:5 1307–1314 (1965) (cited p. 219).

[3] Salières, P, Carre, B, Le Deroff, L, Grasbon, F, Paulus, GG, Walther, H, Kopold, R, Becker, W, Milosevic, DB, and Sanpera, A. *Feynman's path-integral approach for intense-laser-atom interactions*. Science **292**:5518 902–905 (2001) (cited p. 221).

[4] Gaarde, MB, Salin, F, Constant, E, Balcou, P, Schafer, KJ, Kulander, KC, and L'Huillier, A. *Spatiotemporal separation of high harmonic radiation into two quantum path components*. Phys. Rev. A **59**:2 1367–1373 (1999) (cited p. 222).

[5] Balcou, P, Dederichs, AS, Gaarde, MB, and L'Huillier, A. *Quantum-path analysis and phase-matching of high-order harmonic generation and high-order frequency mixing processes in strong laser fields*. J. Phys. B **32**: 2973 (1999) (cited p. 222).

[6] Varju, K, Mairesse, Y, 'e, BC, Gaarde, MB, Johnsson, P, Kazamias, S, Lopez-Martens, R, Mauritsson, J, Schafer, KJ, Balcou, P, L'Huillier, A, and eres, PS. *Frequency chirp of harmonic and attosecond pulses*. J. Mod. Opt. **52**:2-3 379–394 (2005) (cited p. 222).

[7] Mairesse, Y. *Génération et caractérisation d'impulsions attosecondes*. PhD thesis. Université Paris X1 Orsay, 2005 (cited p. 222).

E

Molecular symmetry: point group character and product tables

Table E.1: C_s point group character and product table (e.g. ClN_3).

	E	σ_h	linear rotations	quadratic
A′	1	1	x, y, R_z	x^2, y^2, z^2, xy
A″	1	-1	z, R_x, R_y	yz, xz

	A′	**A″**
A′	A′	A″
A″	A″	A′

Table E.2: C_{2v} point group character and product table (e.g. C_2H_2 cis).

	E	C_2(z)	σ_v(xz)	σ_v(yz)	linear rotations	quadratic
A_1	1	1	1	1	z	x^2, y^2, z^2
A_2	1	1	-1	-1	R_z	xy
B_1	1	-1	1	-1	x, R_y	xz
B_2	1	-1	-1	1	y, R_x	yz

	A_1	**A_2**	**B_1**	**B_2**
A_1	A_1	A_2	B_1	B_2
A_2	A_2	A_1	B_2	B_1
B_1	B_1	B_2	A_1	A_2
B_2	B_2	B_1	A_2	A_1

Table E.3: C_{2h} point group character and product table (e.g. C_2H_2 trans).

	E	C_2(z)	i	σ_h	linear rotations	quadratic
A_g	1	1	1	1	R_z	x^2, y^2, z^2, xy
B_g	1	-1	1	-1	R_x, R_y	xz, yz
A_u	1	1	-1	-1	z	
B_u	1	-1	-1	1	x, y	

	A_g	**B_g**	**A_u**	**B_u**
A_g	A_g	B_g	A_u	B_u
B_g	B_g	A_g	B_u	A_u
A_u	A_u	B_u	A_g	B_g
B_u	B_u	A_u	B_g	A_g

Table E.4: D_{3h} point group character and product table (e.g. N_3).

	E	$2C_3$	$3C_2'$	σ_h	$2S_3$	$3\sigma_v$	linear rotations	quadratic
$\mathbf{A}_1'$	1	1	1	1	1	1		x^2, y^2, z^2
$\mathbf{A}_2'$	1	1	-1	1	1	-1	R_z	
$\mathbf{E}'$	2	-1	0	2	-1	0	(x,y)	(x^2-y^2, xy)
$\mathbf{A}_1''$	1	1	1	-1	-1	-1		
$\mathbf{A}_2''$	1	1	-1	-1	-1	1	z	
$\mathbf{E}''$	2	-1	0	-2	1	0	(R_x, R_y)	(xz, yz)

	$\mathbf{A}_1'$	$\mathbf{A}_2'$	$\mathbf{E}'$	$\mathbf{A}_1''$	$\mathbf{A}_2''$	$\mathbf{E}''$
$\mathbf{A}_1'$	A_1'	A_2'	E'	A_1''	A_2''	E''
$\mathbf{A}_2'$	A_2'	A_1'	E'	A_2''	A_1''	E''
$\mathbf{E}'$	E'	E'	$A_1'+A_2'+E'$	E''	E''	$A_1''+A_2''+E''$
$\mathbf{A}_1''$	A_1''	A_2''	E''	A_1'	A_2'	E'
$\mathbf{A}_2''$	A_2''	A_2''	E''	A_2'	A_2'	E'
$\mathbf{E}''$	E''	E''	$A_1''+A_2''+E''$	E'	E'	$A_1'+A_2'+E'$

Table E.5: D_{3h} point group character and product table (e.g. C_2H_2).

	E	$2C_\infty$	…	$\infty\sigma_v$	i	$2S_\infty$	…	$\infty C_2'$	linear rotations	quadratic
$\mathbf{A}_{1g}=\Sigma_g^+$	1	1	…	1	1	1	…	1		x^2, y^2, z^2
$\mathbf{A}_{2g}=\Sigma_g^-$	1	1	…	-1	1	1	…	-1	R_z	
$\mathbf{E}_{1g}=\Pi_g$	2	$2\cos(\phi)$	…	0	2	$-2\cos(\phi)$	…	0	(R_x, R_y)	(xz, yz)
$\mathbf{E}_{2g}=\Delta_g$	2	$2\cos(2\phi)$	…	0	2	$2\cos(2\phi)$	…	0		(x^2-y^2, xy)
$\mathbf{E}_{3g}=\Phi_g$	2	$2\cos(3\phi)$	…	0	2	$-2\cos(3\phi)$	…	0		
…	…	…	…	…	…	…	…			
$\mathbf{A}_{1u}=\Sigma_u^+$	1	1	…	1	-1	-1	…	-1	z	
$\mathbf{A}_{2u}=\Sigma_u^-$	1	1	…	-1	-1	-1	…	1		
$\mathbf{E}_{1u}=\Pi_u$	2	$2\cos(\phi)$	…	0	2	$-2\cos(\phi)$	…	0	(x, y)	
$\mathbf{E}_{2u}=\Delta_u$	2	$2\cos(2\phi)$	…	0	2	$2\cos(2\phi)$	…	0		
$\mathbf{E}_{3u}=\Phi_u$	2	$2\cos(3\phi)$	…	0	2	$-2\cos(3\phi)$	…	0		
…	…	…	…	…	…	…	…			

Table E.6: O_h point group character and product table (e.g. SF_6).

	E	$8C_3$	$6C_2$	$6C_4$	$3C_2 = (C_4)^2$	i	$6S_4$	$8S_6$	$3\sigma h$	$6\sigma d$	linear rotations	quadratic
A_{1g}	1	1	1	1	1	1	1	1	1	1		$x^2+y^2+z^2$
A_{2g}	1	1	-1	-1	1	1	-1	1	1	-1		
E_g	2	-1	0	0	2	2	0	-1	2	0		$(2z^2-x^2-y^2, x^2-y^2)$
T_{1g}	3	0	-1	1	-1	3	1	0	-1	-1	(R_x, R_y, R_z)	
T_{2g}	3	0	1	-1	-1	3	-1	0	-1	1		(xz, yz, xy)
A_{1u}	1	1	1	1	1	-1	-1	-1	-1	-1		
A_{2u}	1	1	-1	-1	1	-1	1	-1	-1	1		
E_u	2	-1	0	0	2	-2	0	1	-2	0		
T_{1u}	3	0	-1	1	-1	-3	-1	0	1	1	(x, y, z)	
T_{2u}	3	0	1	-1	-1	-3	1	0	1	-1		

	A_{1g}	**A_{2g}**	**E_g**	**T_{1g}**	**T_{2g}**	**A_{1u}**	**A_{2u}**	**E_u**	**T1u**	**T_{2u}**
A_{1g}	A_{1g}	A_{2g}	E_g	T_{1g}	T_{2g}	A_{1u}	A_{2u}	E_u	T_{1u}	T_{2u}
A_{2g}	A_{2g}	A_{1g}	E_g	T_{2g}	T_{1g}	A_{2u}	A_{1u}	E_u	T_{2u}	T_{1u}
E_g	E_g	E_g	$A_{1g}+A_{2g}+Eg$	$T_{1g}+T_{2g}$	$T_{1g}+T_{2g}$	E_u	E_u	$A_{1u}+A_{2u}+E_u$	$T_{1u}+T_{2u}$	$T_{1u}+T_{2u}$
T_{1g}	T_{1g}	T_{2g}	$T_{1g}+T_{2g}$	$A_{1g}+E_g+T_{1g}+T_{2g}$	$A_{2g}+E_g+T_{1g}+T_{2g}$	T_{1u}	T_{2u}	$T_{1u}+T_{2u}$	$A_{1u}+E_u+T_{1u}+T_{2u}$	$A_{2u}+E_u+T_{1u}+T_{2u}$
T_{2g}	T_{2g}	T_{1g}	$T_{1g}+T_{2g}$	$A_{2g}+E_g+T_{1g}+T_{2g}$	$A_{1g}+E_g+T_{1g}+T_{2g}$	T_{2u}	T_{1u}	$T_{1u}+T_{2u}$	$A_{2u}+E_u+T_{1u}+T_{2u}$	$A_{1u}+E_u+T_{1u}+T_{2u}$
A_{1u}	A_{1u}	A_{2u}	E_u	T_{1u}	T_{2u}	A_{1g}	A_{2g}	E_g	T_{1g}	T_{2g}
A_{2u}	A_{2u}	A_{1u}	E_u	T_{2u}	T_{1u}	A_{2g}	A_{1g}	E_g	T_{2g}	T_{1g}
E_u	E_u	E_u	$A_{1u}+A_{2u}+E_u$	$T_{1u}+T_{2u}$	$T_{1u}+T_{2u}$	E_g	E_g	$A_{1g}+A_{2g}+E_g$	$T_{1g}+T_{2g}$	$T_{1g}+T_{2g}$
T_{1u}	T_{1u}	T_{2u}	$T_{1u}+T_{2u}$	$A_{1u}+E_u+T_{1u}+T_{2u}$	$A_{2u}+E_u+T_{1u}+T_{2u}$	T_{1g}	T_{2g}	$T_{1g}+T_{2g}$	$A_{1g}+E_g+T_{1g}+T_{2g}$	$A_{2g}+E_g+T_{1g}+T_{2g}$
T_{2u}	T_{2u}	T_{1u}	$T_{1u}+T_{2u}$	$A_{2u}+E_u+T_{1u}+T_{2u}$	$A_{1u}+E_u+T_{1u}+T_{2u}$	T_{2g}	T_{1g}	$T_{1g}+T_{2g}$	$A_{2g}+E_g+T_{1g}+T_{2g}$	$A_{1g}+E_g+T_{1g}+T_{2g}$

Longue résumé en français

Révéler la dynamique ultrarapide sous-jacente à toute réaction chimique exige des techniques d'imagerie capable de suivre un processus moléculaire étape par étape. Dans ces processus élémentaires, le mouvement des noyaux et des électrons de valence de l'édifice moléculaire sont liés et l'importance de ces dynamiques est un point commun à la biologie, la chimie et la physique [1]. Divers outils sont apparus dans les dernières décennies qui ont permis de sonder directement la moyenne temporelle de la structure moléculaire, comme la diffraction électronique ou de neutrons, l'absorption et diffraction des rayons X , la RMN et la microscopie électronique [2]. L'utilisation de ces techniques a permis de déterminer les structures tridimensionnelles avec une résolution à l'échelle atomique. Cependant, pour former une compréhension complète de fonctions biologiques, des réactions chimiques ou des transitions de phase les processus élémentaires doivent être résolus en temps réel. Hors ces changements s'étalent sur différentes échelles de temps et différents états de transition et intermédiaires. Ces dynamiques et changements structurels sont naturellement liés par les lois de la mécanique quantique [1].

L'invention des chaines laser pulsées ultracourtes a fourni l'outil pour détecter ces processus en temps réel. Spectroscopie d'absorption et d'émission, spectrométrie de masse par photoionization, et les techniques de diffraction jouent le rôle moderne des photographies ultrahaute vitesse pour résoudre ces processus moléculaires élémentaires. L'une des premieres expériences de photographie prenant compte de la vitesse du processus est celle d'un cheval en mouvement en 1878 par Eadweard Muybridge. Il a réussi à capturer le mouvement d'un cheval galopant en mettant en place une rangée de caméras avec des cables de déclenchement. Ansi chaque camera prend une image capturant ainsi une fraction de seconde du mouvement. Ce premier film est considéré comme la naissance d'études photographiques du mouvement et de la projection cinématographique. Puisque l'échelle de temps typique des mouvements des noyaux dans une molécule est l'échelle femtoseconde, les impulsions laser femtosecondes sont les outils les plus pertinents pour saisir l'évolution des réarrangements nucléaires, tels que l'isomérisation et la dissociation (voir Chapitre 2). La spectroscopie femtoseconde est comme regarder un «film» où chaque séquence révèle l'étape élémentaire conduisant in fine aux produits de la réaction chimique. Résoudre dans le temps des dynamiques à l'échelle femtoseconde nécessite de déclencher une dynamique sur cette échelle. Ceci n'est possible que sur des évènements à déclenchement non-statistiques comme des réactions unimoleculaires. Ainsi une impulsion laser pompe ultracourte induit une excitation dans la molécule parent, définissant ainsi $t = 0$. Les détails du processus de relaxation, tel que le temps de décroissance, le bilan énergétique ou les rapports de branchement peuvent ainsi être mesurés par la spectroscopie résolue en temps, ce qui définit le domaine de la femtochimie .

La femtochimie tente de répondre par exemple aux questions suivantes : Comment l' énergie déposée dans le système est redistribuée dans les différents degrés de liberté de la molécule, et à quelle vitesse cela se produit-il? Quelles sont les vitesses des changements de liaisons entre les états quantiques des réactifs et ceux des produites? Quels sont les mouvements nucléaires qui déclenchent la réaction et définissent ainsi les états de transition? Quels sont les échelles de temps typiques de ces mouvement et quelle est la pertinence d'une description statistique de la relaxation? [3]. Cependant, répondre à ces questions n'est pas aussi simple qu'il y parait. En fait, pour comprendre ces étapes élémentaires il faut tout d'abord comparer les observables issues de l'expérience avec celles produites par les modèles théoriques basés sur des calculs ab initio. Seul cette confrontation expérience-théorie permet éventuellement de reconstruire la dynamique des états de transition, soit la cinétique des réactifs aux produits. Cette comparaison expérience-théorie est d'autant plus facile que les molécules sont libres d'un environnement. En effet, il est difficile de modéliser théoriquement environnement. Produire des molécules libres d'un environnement consiste principalement à les produire en phase gazeuse dans un jet moléculaire, permettant ainsi d'avoir des molécules initialement dans une distribution d'états internes (comme la rotation et la vibration), les plus froides possible. Ainsi l'impulsion pompe crée par absorption d'un ou plusieurs photons une excitation électronique, vibrationnelle et/ou rotationnelle. C'est le temps t = 0 défini par la durée de l'impulsion pompe. Maintenant, la question principale est comment détecter ces changements drastiques nucléaires et quelles seront les observables en phase gazeuse. Dans cette thèse deux techniques ont été utilisées, l'une basée sur la photoionization classique tandis que la seconde est basée sur des techniques tout optique. Différents systèmes moléculaires ont été étudiés par ces deux différentes techniques. Sur des échelles de temps encore plus courts que le mouvement des atomes et des molécules est le mouvement des électrons. Les distances des orbites stationnaires des électrons de valence sont de l'ordre de quelques Angtrom. Ainsi les périodes d'oscillation des paquets d'ondes d'électrons dans les systèmes atomiques ou moléculaires liés sont de quelques centaines d'attosecondes (as = 10^{18} sec.) [1]. Si la femtochimie est la science du mouvement des noyaux dans des édifices moléculaires, La physique attoseconde est la science du mouvement des électrons. Produire des impulsions de lumière dans le régime attoseconde implique, du fait de la transformée de Fourier temps-fréquence, de trouver une gamme de longueur d'onde supportant plus que 50 eV. Le domaine privilégé des impulsions attosecondes est donc celui de l'ultraviolet du vide (VUV) avec des énergies de photons allant jusqu'à 100 eV voir même jusqu'au keV. C'est là qu'intervient la génération d'harmoniques d'ordre élevé comme un outil de conversion de photons du proche infrarouge issus d'une chaine laser femtoseconde intense (10^{14} photons) vers quelques 10^8 photons dans le VUV voir même jusqu'à la région des rayons X mous.

Chapitre 1: De la imagerie femtoseconde à l'attoseconde

Chapitre 1 est une introduction aux deux principales configurations expérimentales utilisées dans cette thèse pour sonder la dynamique moléculaire, à savoir l'imagerie de vecteurs vitesse femtoseconde et la génération d'harmonique d'ordre élevé. Après avoir introduit le concept général de la dynamique moléculaire et la technique pompe-sonde dans la Section 1.1, Section 1.2 illustre les concepts fondamentaux de l'imagerie des vecteurs vitesse. Dans la Section 1.3 les concepts fondamentaux de la génération d'harmoniques d'ordre élevé sont introduits.

Chapitre 2: Photodissociation de chlore azoture (ClN_3)

Une expérience résolue à l'échelle femtoseconde est réalisée pour étudier la photodissociation du ClN_3 après excitation électronique dans deux régions énergétiquement différentes. Les résultats obtenus sont l'objet du Chapitre 2. Les principales observables sont les co-fragments N_3 et Cl. Le but de l'expérience est d'élucider la dynamique ultra-rapides qui conduit à la production d'un fragment cyclique-N_3. En effet à 4,5 eV (268 nm) d'excitation électronique, le fragment N_3 est produit dans une géométrie linéaire alors qu'autour de 6,17 eV (201 nm), N_3 est supposé être essentiellement produit sous forme cyclique. En fait la production d'un fragment cyclique N_3 est l'objet de controverse dans la littérature. La technique d'imagerie de vecteur vitesse permet pas seulement l'identification des co-fragments, et un bilan énergétique de la dissociation mais aussi elle donne également accès à leur distribution angulaire. Ainsi la résolution temporelle femtoseconde révèle l'échelle de temps de la dissociation. Grâce à une ionisation multiphotonique des fragments, nous sommes en mesure pour la première fois de détecter directement les fragments N_3 produits sur des temps ultracourts tels que la dizaine de femtoseconde. Détecter ce fragment est relativement important pour comprendre la difference entre les chemins menant à des fragments linéaires ou cycliques. Les études préalables ont en effet toute été réalisées sur des échelles de temps nanoseconde en détectant principalement le fragment de Cl dont la spectroscopie d'ionisation multiphotonique est bien établie. L'échelle de temps de la photodissociation de ClN_3 a pu être mesurée pour la première fois. Un bilan d'énergie résolu en temps du fragment Cl mais surtout du fragment N_3 a pu être obtenu par le spectromètre d'imagerie des vecteurs vitesse. Ceci a permis non seulement de confronter ce bilan d'énergie résolu en temps à ceux obtenus en régime nanoseconde, mais aussi de résoudre en temps les distributions angulaires d'émission des fragments dans les deux régions d'excitation électronique soit à une énergie de dissociation de 4,67 eV (268 nm), où le fragment N_3 est produit principalement linéairement et à 6.13 eV (201 nm), où N_3 cyclique est produit. L'emploi d'une impulsion sonde avec une polarisation perpendiculaire au laser de dissociation pompe permet d'obtenir un meilleur rapport signal sur bruit. Dans cette configuration, peu commune en imagerie de vecteur vitesse, des polarisations des impulsions pompe et sonde, les temps de dissociation mesurés sur le co-fragment chlore sont comparables, dans les barres d'erreurs, aux temps de dissociation mesurés sur le fragment N_3. Le temps de dissociation a été établie à 262 ± 38 fs et 178 ± 22 fs pour ces deux domaines d'énergie. Ces temps de dissociation sont en fait les temps d'apparition des fragments par sélection en masse et énergie (mais intégré en angle). Ces temps de dissociation sont en fait deux fois plus longs que les temps de décroissance mésurés sur le spectre de masse (intégré en énergie et angle) collecté directement en sortie du temps de vol (soit sur les galettes de microcanaux). Notons que ce spectre de masse est constitué principalement des fragments d'ionisation dissociative et révèlent ainsi le temps de décroissance de l'état électronique d'ordre zéro préparé par l'impulsion pompe. De ces différences sur le temps de dissociation et le temps de décroissance, nous pouvons conclure que la dissociation n'est pas une dissociation directe comme suggéré auparavant [4] et qu'au moins un état de transition est atteint avant d'accéder au continuum de dissociation. Une dissociation directe se produirait à peu près sur la moitié de la période de vibration de la liaison Cl–N_3 qui n'est que de 30 fs ($\nu_{stretch}$ = 545 cm^1 = 61 fs). Le fait que la dynamique de dissociation n'est pas totalement révélée dans les signaux intégrés en énergie et angle révèle que l'ionisation dissociative est sensible à la nature électronique ou la structure nucléaire. Des expériences d'ionisation, enregistrant en coïncidence les fragments et les photoélectrons associés pourraient révéler éventuellement les états électroniques rencontrés. La distribution angulaire du fragment N_3 mesurée en fonction du temps révèle à de longs délais un paramètre d'anistropie β_2 de 1.64 ± 0.06 et 0.27 ± 0.05 pour les canaux de dissociation menant à un N_3 linéaire et ceux menant à un N_3 cyclique. Ces valeurs sont en accord avec les seules mesures publiée en régime ns mesurant uniquement la distribution angulaire du fragment Cl. En effet l'ionisation multiphotonique résonante de N_3 n'a pas encore été étudiée. Ainsi aucune valeur d'anistropie angulaire de ce fragment n'a été publiée En outre, la dépendance temporelle de cette distribution angulaire montre que ces valeurs asymptotiques d'émission des fragments ne sont pas atteints immédiatement . Il faut 170 ± 45 fs et 136 ± 7 fs pour le fragment N_3 linéaire et cyclique pour atteindre les limites asymptotiques d'émission anisotropique. Malheureusement, la détection d'ionisation multiphotonique non résonante n'est pas adaptée pour détecter le fragment Cl avec un bon rapport signal sur bruit, spécialement aux délais courts où peu de fragments sont produits. Cependant, à de longs retards pompe-sonde le paramètre β_2 mesuré à partir des images de Cl est en bon accord avec les valeurs obtenues à partir des images N_3.

Chapitre 3: Relaxation électronique et dissociation du tétrathiafulvalène (TTF)

La relaxation électronique du tétrathiafulvalène (TTF, $C_6H_4S_4$) est étudiée dans le Chapitre 3, en variant l'excitation électronique initiée par l'impulsion pompe autour de 4 eV. Les observables sont un spectre de masse et la spectroscopie de photoélectrons, toutes deux résolus en temps. Pour améliorer la sensibilité , la photo-ionisation est réalisée à différentes longueurs d'onde de sonde (266 nm , 400 nm et 800 nm). La longueur d'onde de la pompe a été variée de 322 nm à 307 nm pour révéler éventuellement sur les temps de décroissance, un changement possible du caractère électronique ou vibrationnel. Avec une impulsion de 800 nm intense la photo-ionisation au dessus du seuil (ATI) du TTF est étudiée. Le spectre de photoélectrons par photoionisation femtoseconde de TTF révèle une ionisation multiphotonique par absorption de douze photons à 808 nm, soit une énergie interne de l'ion de 12.1 eV. La dépendance angulaire des photoélectrons éjectés montre que ce processus multiphotonique est plus susceptible de survenir dès le premier état excité de l'ion. Dans l'intervalle de ces énergies internes d'ion élevées, une variété de canaux de dissociation sont accessibles. A cette gamme d'énergie une variété de canaux de dissociation sont accessibles dans le continuum d'ions. Afin de démêler cette dissociation ionique complexe, l'imagerie de photoélectrons en coïncidence avec les photoion (iPEPICO) est utilisée. Au-dessus du seuil de dissociation, les résultats iPEPICO montrent que l'ion moléculaire (m/z = 204) dissocie en sept ions produits, dont six sont en concurrence dans une fenêtre de l'énergie 1,0 eV avec une même énergie de seuil de 10 eV. Ceci montre que la dissociation de l'ion TTF est régi par un état de transition relativement serré menant à un produit de réaction intermédiaire non spécifié, qui par la suite dissocie via plusieurs canaux de dissociation, menant ainsi à une multitude de fragment. Des calculs ab initio sur les structures d'ions fragments possibles de dissociation via cinq canaux montre tous la perte de C_2H_2 et C_2H_2S pour les cations TTF d'énergie interne élevée. Un modèle de dissociation à trois canaux de dissociation est utilisé pour ajuster les données iPEPICO. Deux canaux de dissociation sont traités comme des dissociations simples (dont une avec un renversement de barrière), tandis que le reste impliquent une barrière partagée. Ces canaux ne peuvent pas rivaliser avec des énergies internes supérieures où des voies plus entropiques deviennent dominantes. Le fragment S en photoionization VUV semble apparaître à 12,6 eV à partir d'une dissociation secondaire du fragment réorganisé S_2. Cela confirme que, dans les études pompe-sonde femtoseconde de la deuxième bande UV de TTF, une vibration d'énergie particulière caractérise la production du fragment ionisé S. Cela expliquerait le profil temporel du fragment S présentant un décalage de 95 fs sur sa fonction de décroissance.

Chapitre 4: Quantum battements dans l'hexafluorure de soufre (SF_6)

Dans le Chapitre 4, le spectre XUV diffracté produit par génération d'harmoniques d'ordre élevé sur des molécules SF_6 vibrationnellement excitée est étudié par deux techniques toutes deux sensibles à la phase des harmoniques. L'émission XUV de SF_6 devrait prendre place principalement depuis la HOMO (orbitale moléculaire occupée la plus haute en énergie) comme précédemment observé dans tous les atomes de gaz rares et les petits systèmes moléculaires tels que N_2, CO_2, NO_2 et N_2O_4. Ceci résulte de la probabilité dune ionisation tunnel par abaissement du potentiel coulombien qui dépend exponentiellement de l'énergie des orbitales (ou encore du potentiel d'ionisation). En fait la très haute symétrie de SF_6, les résonances de forme et l'autoionization qui caractérise son continuum de l'ion à basse énergie font que les harmoniques dans SF_6 sont en fait produites à partir de l'émission d'un électron depuis les HOMO-2 et HOMO-3. En variant de manière cohérente la géométrie de SF_6 dans l'état fondamental, nous visons à faire la lumière sur le processus de génération d'harmoniques d'ordre élevé dans SF_6. Cette modification de la géométrie de SF_6 est réalisée en créant un paquet d'ondes vibrationnelles préparé par une transition Raman. Deux montages expérimentaux sophistiqués, tous deux basés sur une détection hétérodyne sont mis en oeuvre pour mesurer non seulement l'amplitude mais également la phase de l'émission harmonique d'ordre élevé. Un montage utilise deux impulsions de pompage pour créer un réseau de diffraction de l'excitation vibrationnelle dans le jet de gaz. Ainsi l'impulsion sonde génère des harmoniques d'ordre élevé sur ce réseau d'excitation. La lumière diffractée XUV est l'observable principale avec son efficacité de diffraction variant en fonction de la géométrie du SF_6. La deuxième expérience utilise quant à elle deux impulsions sonde séparées spatialement en introduisant simplement une lame de phase de pi dans le faisceau sonde intense. Ces deux impulsions génèrent chacune un faisceau XUV, qui interfèrent tout deux en champ lointain, soit aux niveaux du détecteur. L'impulsion pompe n'est superposée spatialement qu'avec une seule des impulsions sonde, venant ainsi modifier le diagramme d'interference XUV à la fois en amplitude et en phase. Les variations temporelles (soit pompe sonde) d'amplitude et de phase contiennent ainsi des informations sur les excitations vibrationnelles induites par l'impulsion pompe. Les deux configurations ont montré qu'elles sont toute deux sensibles aux excitations vibrationnelles caractérisant le milieu de production. Les trois modes Raman actifs de SF_6, ν_1 (775 cm^1), ν_2 (638 cm^1), ν_5 (528 cm^1), ont pu être observés dans l'amplitude de l'émission harmonique mais aussi dans les variations en phase. Pour la configuration du réseau transitoire (deux pompes et une sonde), les harmoniques produites s'étalent de la 9ième à la 17ieme alors que dans l'expérience à deux sources, le spectre harmonique s'étale de H9 jusqu'à H35. Dans les deux expériences, les principaux modes révélés sont les modes ν_1 et ν_5 similairement à la spectroscopie Raman traditionnelle. Pour la configuration à deux sources XUV, l'amplitude du mode ν_5 montre un minimum clair autour de l'harmonique 17, tandis que dans la phase un saut est observé autour de l'harmonique 15. Le mode ν_5 montre aucune tendance claire en amplitude mais sa phase présente un minimum autour de l'harmonique 17. Ces minima ne peuvent pas venir des précédents minima observés dans l'émission harmonique de SF_6 statique à H15 et H17, minima statique qui concluent sur l'implication des HOMO-2 et HOMO-3. En effet, nous sommes dans une détection hétérodyne. Ceci nous laisse conclure que les caractéristiques observées ici ne sont introduites que par la modification de la distance S–F propre au le paquets d'ondes vibrationnelles. En outre, il semble que l'émission harmonique n'est pas optimisée pour les molécules entièrement étirée ou compressée comme observé dans des expériences similaires sur N_2O_4. Une interprétation complète de ces résultats expérimentaux nécessite le développement d'un modèle théorique pour reproduire l'amplitude et la phase. Néanmoins, cette étude est la première résolue en phase, ce qui constitue une première étape dans la compréhension de l'origine de la modulation dans le spectre harmonique de SF_6.

Chapitre 5: fs-VUV-VMI – HHG comme impulsion couplé à un VMI

Le Chapitre 5 établit un lien entre le Chapitre 2/Chapitre 3 et Chapitre 4, car ici l'émission harmonique d'ordre élevé est utilisé comme une source secondaire XUV permettant de réaliser un système de détection universelle. Pour cela, un nouveau spectromètre XUV a été construit et couplé à un spectromètre d'imagerie de vecteur vitesse. Après une description et une caractérisation de la nouvelle configuration de l'ionisation pompe sonde est réalisée sur argon et C_2H_2. Ici, les observables sont les photoélectrons de bandes latérales produits par deux chemins quantiques impliquant différentes résonances. Nous avons tenté d'étudier la photodissociation de l'acétylène à 9.3 eV en utilisant la nouvelle configuration fs-VUV-VMI. Deux approches différentes ont été utilisées. Au départ, nous avons utilisé une transition pompe à trois photons centré à 401.3 nm et une étape de la sonde VUV à partir du spectre harmonique pour ioniser les fragments de dissociation. Cependant, aucune dissociation des fragments n'a été détectée par cette méthode. On ignore encore les raisons pour lesquelles ce schéma pompe-sonde d'excitation n'a pas fonctionné. D'une part, il est possible que notre flux de photons harmonique soit insuffisante pour sonder les fragments de dissociation du fait des sections efficaces d'absorption trop faibles, comme c'est le cas pour les fragments d'hydrogène (qui d'ailleurs peuvent être produits eux même en faible quantité du fait d'une faible efficacité dissociation). En revanche, il n'est pas exclut pas que nous ne contrôlons pas suffisament l'excitation pompe assez précis. En effet, même si on excite la molécule a une bande d'absorption avec une section efficace très forte (résonance à trois photons), il est possible que nous ne laissons pas suffisamment de population dans l'état excité en raison d'une ionization à un photon trop efficace depuis l'état excité. Le taux de dissociation de l'état $F0_0^0$ pourrait également ne pas être suffisant pour étudier la photodissociation de cet état. Utiliser une excitation multiphotonique est particulièrement problématique, surtout lorsque la transition résonant implique un nombre relativement élevé de photons (ici 3) par rapport à la transition menant à l'ionisation (ici 4). Ceci illustre la pertinence des sources de photons dans le domaine VUV. En effet, effectuer une transition à un photon de l'état fondamental à l'état excité apporte un intérêt sur l'excitation sans risquer d'ionisation la molécule par une transition impliquant un deuxième photon. C'est cet aspect que nous avons essayé de développer dans la deuxième approche expérimentale, en excitant la molécule d'acétylène par une transition à un photon utilisant la troisième harmonique générée à 400 nm. Une seconde impulsion à 400 nm a alors été utilisé pour sonder la dissociation de la molécule. Ce montage ne permet pas cependant d'ioniser des fragments car trop peu de photons sont utilises pour la sonde afin de garder un signal pompe-sonde sur le parent de bon contraste. L'analyse des spectres de photoélectrons en fonction du delai pompe-sonde a révélé une dynamique femtoseconde de la relaxation des états excités mis en jeu. Toutefois, compte tenu de la large bande spectrale de la 3ème harmonique, il est difficile d'attribuer les états concernés. Cette grande largeur de bande spectrale est l'inconvénient majeur de HHG comme une source de photons VUV pompe pour la spectroscopie atomique et moléculaire.

Conclusion et perspectives

Ces différentes observations expérimentales nous conduisent à la conclusion que nous devons étudier expérimentalement ce qu'est réellement une grosse molécule polyatomique habillée par un fort champ électromagnétique. La plupart des expériences sur les champs forts dans le passé, sont des détection de la quantité de fragments ionisés produites en fonction soit du champ électrique ou de la longueur d'onde [5–10]. Mais récemment, avec les progrès de la détection de coïncidence avec 4π stéradian de collection (COLTRIMS) [11], du controle de la phase de l'enveloppe porteuse (CEP) [12, 13] et la fusion de la science de l'attoseconde avec la femtochimie, l'une des principale question qui se pose maintenant est quelle est l'importance de l'interaction cohérente entre différentes orbitales moléculaire [14–20]. Évidemment, bien que les effets de champ fort ont été étudiés depuis longtemps, pour comprendre l'ionisation séquentielle ou la formation de nouvelles espèces [18, 21], il est nécessaire de suivre la dynamique non-adiabatique d'électrons au niveau des oscillations du champ électrique [22].

Deux techniques totalement différentes semblent émerger pour investir cette question, toutes deux nécessitant un contrôle de la CEP. La premiere est une détection en coincidence couplée à de l'explosion Coulomb [23]. Ce montage de coincidence permet la détermination de l'orientation du système moléculaire [24, 25], ce qui est exactement ce que nous souhaitons réaliser pour confirmer l'isomérisation de N_3 suite à la dissociation des ClN_3 à 6 eV. En outre, dans le cas de l'ionisation tunnel, il permet de déterminer à partir de quelle orbitale moléculaire les électrons sont émis [15, 26], En effet en se basant sur l'ionisation dissociation en VUV, les seuils d'apparition des fragment issus de l'ionisation dissociative sont connus (expérience I-PEPICO telle que réalisée sur TTF au SLS-Villegen). Souvent ces seuils coincident énergétiquement avec des états excités de l'ion. Ainsi collecter les spectres d'électrons ATI en coincidence avec les fragments ionisés permet de déterminer a partir de quels états excités ils ont été émis et donc de quelle orbitale. Ce type d'expérience pour l'instant réalisée seulement au NRC (Albert Stolow, Steaci Institute, Ottawa) est appelée CRATI pour channel resolved above threshold ionisation. Il est important de noter que ce type d'experience ne donne une information que sur l'orbitale moléculaire d'émission et non sur l'étape de recombinaison dans la génération d'harmonique. De plus la validité de la comparaison champ forts/HHG ne tient qu'a une équivalence entre la spectroscopie VUV et la spectroscopie en champ fort. Hors sur un système tel que SF6, la comparaison présente déjà ses limites puisque le fragment souffre est dominant en ionisation dissociative en champ fort au contraire de l'ionisation VUV. Les ATI spectres d'énergie cinétique de photoélectrons dans CRATI sont enregistrés donc en co-variance avec l'ion parent et les ions fragments. Cette mesure CRATI qui est fortement dépend de la spectroscopie VUV de l'ionisation dissociative, révèle directement la population de multiple continua électronique et les déplacements par effet Stark de ces états [22]. Mesures CRATI sur SF_6 sont en cours à Ottawa. Le développement technologique le plus important pour la physique des champs forts est des impulsions laser de quelques cycles optiques avec un contrôle de la phase de la porteuse (CEP- carrier envelop phase) et ce tir à tir [27]. Cette prouesse technologique énorme permet, par exemple, de découpler les déformations de potentiel, les excitations électroniques résonantes, et l'ionisation séquentielle par recollision électronique en faisant simplement varier la CEP et collectant l'anisotropie des fragments et le changement dans la distribution de l'énergie cinétique [28, 29]. La seconde technique de détection est totalement différente; c'est la spectroscopie absorption XUV. Cette technique émergente est principalement utilisé sur les systèmes atomiques et connue sous le nom d'absorption transitoire attosecond spectroscopie (ATAS). ATAS combine une impulsion IR et une impulsion XUV attosecondes, qui se chevauchent dans le temps. Le signal est le spectre d'absorption de l'impulsion attoseconde XUV en fonction du retard de cette impulsion par rapport à l'impulsion IR intense de quelques cycle (typiquement 10 à 20 fs). Les premières expériences ont été effectuées avec des trains d'impulsions attosecondes révélant ainsi l'interférence de paquets d'ondes d'électrons dans les atomes initiées par les impulsions individuelles dans le train [30, 31]. Récemment, ces expériences ont été étendues à des impulsions XUV attosecondes simples, donnant accès à la réponse instantanée du système excité à la fois sur des échelles de temps femtoseconde et attoseconde. Cette expérience a permis, par exemple, de déterminer si la cohérence existe dans la photo-ionisation d'un atome et ce en fonction de la durée de l'impulsion IR en champ intense utilisée. [32]. Au meilleur de notre connaissance, aucune étude n'a été réalisée expérimentalement sur des systèmes polyatomiques. Cependant, des expériences ATAS peuvent, ouvrir de nouvelles perspectives pour révéler la dynamique électronique non adiabatique des électrons de valence peu liés dans les systèmes moléculaires.

References

[1] Krausz, F. *Attosecond physics*. Rev. Mod. Phys. **81**:1 163–234 (2009) (cited p. 229, 230).

[2] Zewail, AH. *The new age of structural dynamics*. Acta Cryst. **66**:2 135–136 (2010) (cited p. 229).

[3] Zewail, AH. *Femtochemistry: Atomic-scale dynamics of the chemical bond*. J. Phys. Chem. A **104**:24 5660–5694 (2000) (cited p. 230).

[4] Hansen, N and Wodtke, AM. *Velocity Map Ion Imaging of Chlorine Azide Photolysis: Evidence for Photolytic Production of Cyclic-*N_3^+. J. Phys. Chem. A **107**:49 10608–10614 (2003) (cited p. 232).

[5] Corkum, PB, Ivanov, MY, and Wright, JS. *Subfemtosecond processes in strong laser fields*. Ann. Rev. Phys. Chem. **48**:1 387–406 (1997) (cited p. 235).

[6] DeWitt, MJ and Levis, RJ. *Concerning the ionization of large polyatomic molecules with intense ultrafast lasers*. J. Chem. Phys. **110**:23 11368 (1999) (cited p. 235).

[7] Hankin, S, Villeneuve, D, Corkum, P, and Rayner, D. *Nonlinear Ionization of Organic Molecules in High Intensity Laser Fields*. Phys. Rev. Lett. **84**:22 5082–5085 (2000) (cited p. 235).

[8] Lezius, M, Blanchet, V, Ivanov, MY, and Stolow, A. *Polyatomic molecules in strong laser fields: Nonadiabatic multielectron dynamics*. J. Chem. Phys. **117**:4 1575–1588 (2002) (cited p. 235).

[9] Lezius, M, Blanchet, V, Rayner, DM, Villeneuve, DM, Stolow, A, and Ivanov, MY. *Nonadiabatic multielectron dynamics in strong field molecular ionization*. Phys. Rev. Lett. **86**:1 51–54 (2001) (cited p. 235).

[10] Harada, H, Tanaka, M, Murakami, M, Shimizu, S, Yatsuhashi, T, Nakashima, N, Sakabe, S, Izawa, Y, Tojo, S, and Majima, T. *Ionization and Fragmentation of Some Chlorinated Compounds and Dibenzo- p-dioxin with an Intense Femtosecond Laser Pulse at 800 nm*. J. Phys. Chem. A **107**:34 6580–6586 (2003) (cited p. 235).

[11] Ullrich, J, Moshammer, R, Dorn, A, Dörner, R, Schmidt, LPH, and Schmidt-Böcking, H. *Recoil-ion and electron momentum spectroscopy: reaction-microscopes*. Rep. Prog. Phys. **66**:9 1463–1545 (2003) (cited p. 235).

[12] Feng, X, Gilbertson, S, Mashiko, H, Wang, H, Khan, SD, Chini, M, Wu, Y, Zhao, K, and Chang, Z. *Generation of Isolated Attosecond Pulses with 20 to 28 Femtosecond Lasers*. Phys. Rev. Lett. **103**:18 183901 (2009) (cited p. 235).

[13] Kienberger, R, Goulielmakis, E, Uiberacker, M, Baltuska, A, Yakovlev, V, Bammer, F, Scrinzi, A, Westerwalbesloh, T, Kleineberg, U, Heinzmann, U, Drescher, M, and Krausz, F. *Atomic transient recorder*. Nature **427**:6977 817–821 (2004) (cited p. 235).

[14] Akagi, H, Otobe, T, Staudte, A, Shiner, A, Turner, F, Dörner, R, Villeneuve, DM, and Corkum, PB. *Laser Tunnel Ionization from Multiple Orbitals in HCl*. Science **325**:5946 1364–1367 (2009) (cited p. 235).

[15] Boguslavskiy, AE, Mikosch, J, Gijsbertsen, A, Spanner, M, Patchkovskii, S, Gador, N, Vrakking, MJJ, and Stolow, A. *The Multielectron Ionization Dynamics Underlying Attosecond Strong-Field Spectroscopies*. Science **335**:6074 1336–1340 (2012) (cited p. 235, 236).

[16] Kelkensberg, F, Lefebvre, C, Siu, W, Ghafur, O, Nguyen-Dang, T, Atabek, O, Keller, A, Serov, V, Johnsson, P, Swoboda, M, Remetter, T, L'Huillier, A, Zherebtsov, S, Sansone, G, Benedetti, E, Ferrari, F, NISOLI, M, Lépine, F, Kling, M, and Vrakking, M. *Molecular Dissociative Ionization and Wave-Packet Dynamics Studied Using Two-Color XUV and IR Pump-Probe Spectroscopy*. Phys. Rev. Lett. **103**:12 123005 (2009) (cited p. 235).

[17] Znakovskaya, I, Hoff, P von den, Zherebtsov, S, Wirth, A, Herrwerth, O, Vrakking, M, Vivie-Riedle, R de, and Kling, M. *Attosecond Control of Electron Dynamics in Carbon Monoxide*. Phys. Rev. Lett. **103**:10 103002 (2009) (cited p. 235).

[18] Markevitch, A, Romanov, D, Smith, S, and Levis, R. *Coulomb Explosion of Large Polyatomic Molecules Assisted by Nonadiabatic Charge Localization*. Phys. Rev. Lett. **92**:6 063001 (2004) (cited p. 235).

[19] Patchkovskii, S, Zhao, Z, Brabec, T, and Villeneuve, D. *High Harmonic Generation and Molecular Orbital Tomography in Multielectron Systems: Beyond the Single Active Electron Approximation*. Phys. Rev. Lett. **97**:12 123003 (2006) (cited p. 235).

[20] Smirnova, O, Mairesse, Y, Patchkovskii, S, Dudovich, N, Villeneuve, D, Corkum, P, and Ivanov, MY. *High harmonic interferometry of multi-electron dynamics in molecules*. Nature **460**:7258 972–977 (2009) (cited p. 235).

[21] Furukawa, Y, Hoshina, K, Yamanouchi, K, and Nakano, H. *Ejection of triatomic hydrogen molecular ion from methanol in intense laser fields*. Chem. Phys. Lett. **414**:1-3 117–121 (2005) (cited p. 235).

[22] Spanner, M, Mikosch, J, Gijsbertsen, A, Boguslavskiy, AE, and Stolow, A. *Multielectron effects and nonadiabatic electronic dynamics in above threshold ionization and high-harmonic generation*. New Jour. Phys. **13**:9 093010 (2011) (cited p. 235, 236).

[23] Eremina, E, Liu, X, Rottke, H, Sandner, W, Schätzel, M, Dreischuh, A, Paulus, G, Walther, H, Moshammer, R, and Ullrich, J. *Influence of Molecular Structure on Double Ionization of* N_2 *and* O_2 *by High Intensity Ultrashort Laser Pulses*. Phys. Rev. Lett. **92**:17 173001 (2004) (cited p. 236).

[24] Itakura, R, Yamanouchi, K, Yasuike, T, and Someda, K. *Formation of* $[C_5H_6(NH_3)_2]^+$ *and* $[NH_4(NH_3)_m]^+$ *(m=1–3) from size-selected aniline–ammonia cluster cations in intense laser fields*. Chem. Phys. Lett. **396**:1-3 208–212 (2004) (cited p. 236).

[25] Legare, F, Lee, K, Litvinyuk, I, Dooley, P, Wesolowski, S, Bunker, P, Dombi, P, Krausz, F, Bandrauk, A, Villeneuve, D, and Corkum, P. *Laser Coulomb-explosion imaging of small molecules*. Phys. Rev. A **71**:1 013415 (2005) (cited p. 236).

[26] Kotur, M, Weinacht, TC, Zhou, C, and Matsika, S. *Strong-Field Molecular Ionization from Multiple Orbitals*. Physical Review X **1**:2 021010 (2011) (cited p. 236).

[27] Kremer, M, Fischer, B, Feuerstein, B, Jesus, VLB de, Sharma, V, Hofrichter, C, Rudenko, A, Thumm, U, Schröter, CD, Moshammer, R, and Ullrich, J. *Electron Localization in Molecular Fragmentation of* H_2 *by Carrier-Envelope Phase Stabilized Laser Pulses*. Phys. Rev. Lett. **103**:21 213003 (2009) (cited p. 236).

[28] Kling, MF, Siedschlag, C, Verhoef, AJ, Khan, JI, Schultze, M, Uphues, T, Ni, Y, Uiberacker, M, Drescher, M, Krausz, F, and Vrakking, MJJ. *Control of Electron Localization in Molecular Dissociation*. Science **312**:5771 246–248 (2006) (cited p. 236).

[29] Xie, X, Doblhoff-Dier, K, Roither, S, Schöffler, MS, Kartashov, D, Xu, H, Rathje, T, Paulus, GG, Baltuška, A, Gräfe, S, and Kitzler, M. *Attosecond-Recollision-Controlled Selective Fragmentation of Polyatomic Molecules*. Phys. Rev. Lett. **109**:24 243001 (2012) (cited p. 236).

[30] Loh, ZH, Khalil, M, Correa, R, Santra, R, Buth, C, and Leone, S. *Quantum State-Resolved Probing of Strong-Field-Ionized Xenon Atoms Using Femtosecond High-Order Harmonic Transient Absorption Spectroscopy*. Phys. Rev. Lett. **98**:14 143601 (2007) (cited p. 236).

[31] Holler, M, Schapper, F, Gallmann, L, and Keller, U. *Attosecond Electron Wave-Packet Interference Observed by Transient Absorption*. Phys. Rev. Lett. **106**:12 123601 (2011) (cited p. 236).

[32] Goulielmakis, E, Loh, ZH, Wirth, A, Santra, R, Rohringer, N, Yakovlev, VS, Zherebtsov, S, Pfeifer, T, Azzeer, AM, Kling, MF, Leone, SR, and Krausz, F. *Real-time observation of valence electron motion*. Nature **466**:7307 739–743 (2010) (cited p. 237).

List of Publications

[1] Thiré, N, Cireasa, R, Staedter, D, Blanchet, V, and Pratt, ST. *Time-resolved predissociation of the vibrationless level of the B state of CH_3I*. Phys. Chem. Chem. Phys. **13**:41 18485–18496 (2011).

[2] Ruf, H, Handschin, C, Ferre, A, Thire, N, Bertrand, JB, Bonnet, L, Cireasa, R, Constant, E, Corkum, PB, Descamps, D, Fabre, B, Larregaray, P, Mevel, E, Petit, S, Pons, B, Staedter, D, Worner, HJ, Villeneuve, DM, Mairesse, Y, Halvick, P, and Blanchet, V. *High-harmonic transient grating spectroscopy of NO_2 electronic relaxation*. J. Chem. Phys. **137**: 224303 (2012).

[3] Mayer, PM, Staedter, D, Blanchet, V, Hemberger, P, and Bodi, A. *Comparing Femtosecond Multiphoton Dissociative Ionization of Tetrathiafulvene with Imaging Photoelectron Photoion Coincidence Spectroscopy*. J. Phys. Chem. A **117**:13 2753–2759 (2013).

[4] Piecuch, P, Hansen, JA, Staedter, D, Faure, S, and Blanchet, V. *Communication: Existence of the doubly excited state that mediates the photoionization of azulene*. J. Chem. Phys. **138**:20 201102–4 (2013).

[5] Staedter, D, Thiré, N, Baynard, E, Samartzis, PC, and Blanchet, V. *268 nm photodissociation of ClN3: a femtosecond velocity-map imaging study*. Phys. Chem. Chem. Phys. **16**:2 540–549 (2014).

Publications in preparation at the time of printing this manuscript:

[6] Staedter, D, Samartzis, PC, and Blanchet, V. *Photodissociation dynamics in ClN_3 probed by femtosecond time-resolved velocity-map imaging at 202 nm*. in preparation for Phys. Rev. Lett. (2013).

[7] Thiré, N, Staedter, D, Polizzi, L, Marsden, C, and Blanchet, V. *Time-resolved Electronic Relaxation Dynamics in Tetrathiafulvalene probed by velocity-map imaging*. in preparation for J. Chem. Phys. (2013).

Abstract

Revealing the underlying ultrafast dynamics in molecular reaction spectroscopy demands state-of-the-art imaging techniques to follow a molecular process step by step.

Femtosecond time-resolved velocity-map imaging is used to study the photodissociation dynamics of chlorine azide (ClN_3). Here especially the co-fragments chlorine and N_3 are studied on the femtosecond timescale in two excitation energy regions around 4.67 eV and 6.12 eV, leading to the formation of a linear N_3 fragment and a cyclic N_3 fragment, respectively. This work is the first femtosecond spectroscopy study revealing the formation of cyclic N_3. Tetrathiafulvalene (TTF, $C_6H_4S_4$) electronic relaxation is studied, while scanning the electronic excitation around 4 eV, by time resolved mass and photoelectron spectroscopy. As only few is known about the ion continuum about TTF the imaging photoelectron photoion coincidence (iPEPICO) technique is used in order to disentangle the complex ionic dissociation.

The second part of the thesis is based on the generation and application of XUV light pulses by high-order harmonic generation with an intense femtosecond laser pulse in a molecular target. Two types of phase sensitive attosecond spectroscopy experiments were conducted to study the vibrational dynamics of SF_6: one using strong field transient grating spectroscopy, where high-order harmonic generation takes place in a grating of excitation, and the second experiment using high-order harmonic interferometry using two intense XUV probe pulses. The temporal dependencies in phase and amplitude reveal the vibrational dynamics in SF_6 and demonstrate that high-order harmonic generation is sensitive to the internal excitations. Last but not least, the use of high-order harmonics as a XUV photon source for the velocity-map imaging spectrometer is investigated. Using time-resolved photoelectron imaging, the relaxation dynamics initiated with 15.5 eV in argon and 9.3 eV in acetylene are revealed.

Keywords spectroscopy, molecular dynamics, photodissociation, femtosecond, attosecond, velocity-map imaging, high-order harmonic generation, strong field transient grating, two source high-order harmonic interferometry, chlorine azide, ClN_3, tetrathiafulvalene, TTF, sulfur hexafluoride, SF_6, acetylene, C_2H_2, extreme ultraviolet, XUV

Résumé

Dans cette thèse, la dynamique de photodissociation de l'azoture de chlore (ClN_3) est étudiée dans le domaine temporel par imagerie de vecteur vitesse des photofragments, spécialement du chlore et de N_3. Cette imagerie résolue à l'échelle femtoseconde permet d'extraire les temps de dissociation, l'établissement temporel de la balance d'énergie de la réaction ainsi que la conservation des moments. Cette étude a permis de différencier deux domaines d'énergie: l'un menant à la formation d'un fragment N_3 linéaire (étude autour de 4.5 eV d'excitation électronique) et le plus intéressant aboutissant à la formation d'un fragment N_3 cyclique (autour de 6 eV).

Dans une seconde étude, la dynamique de relaxation électronique du tétrathiafulvalène ($C_6H_4S_4$-TTF) est étudiée autour de 4 eV par spectroscopie de masse résolue en temps ainsi que par spectroscopie de photoélectron. Les seuils d'ionisation dissociative sont extraits d'une détection en coïncidence entre les photoélectrons de seuil et les fragments ionisés réalisée sur rayonnement synchrotron.

Les deux dernières expériences sont basées sur la génération d'harmoniques d'ordre élevé dans l'XUV d'une impulsion femtoseconde à 800 nm ou à 400 nm. Dans la première expérience, les harmoniques sont couplées à un imageur de vecteur vitesse en tant que rayonnement secondaire VUV. Par imagerie de photoélectron résolue en temps, nous avons révélé ainsi les dynamiques de relaxation des états de Rydberg initiée par une impulsion femtoseconde XUV à 15.5 eV dans l'argon et à 9.3 eV dans l'acétylène. Dans la seconde expérience, couramment nommée spectroscopie attoseconde, les harmoniques constituent le signal pompe sonde. Deux types de spectroscopie attoseconde ont été réalisés pour étudier la dynamique vibrationnelle de SF_6: une expérience en réseau transitoire créé par deux impulsions pompe Raman avec une impulsion sonde intense générant les harmoniques à partir du réseau d'excitation et une expérience d'interférence de deux rayonnement XUV en champ lointain créés par deux impulsions sonde intenses.

Mots Clefs: spectroscopie, dynamique moléculaire, photodissociation, femtoseconde, attoseconde, l'imagerie de vecteur vitesse, génération d'harmoniques d'ordre élevé, réseau transitoire d'excitation, two source high-order harmonic interferometry, azoture de chlore, ClN_3, tétrathiafulvalène, TTF, sulfur hexafluoride, SF_6, acétylène, C_2H_2, extreme ultraviolet, XUV